UNIVERSITÀ DELLA CALABRIA

UNIVERSITA' DELLA CALABRIA

Dipartimento di Fisica

Dottorato di Ricerca in

Scienze e Tecnologie Fisiche, Chimiche e dei Materiali

CICLO XXXV

Measurements of single, double and triple differential cross-sections of top-quark pair production, in the lepton+jets channel, in *pp* collisions at $\sqrt{s}$=13 TeV using the data collected by the ATLAS detector during the full Run 2.

Settore Scientifico Disciplinare FIS/01

Coordinatore: Ch.ma Prof. ssa Gabriella Cipparrone

Firma [redacted]

Supervisore/Tutor: Ch.mo Prof. ENR[redacted]

Firma [redacted]

Firma oscurata in base alle linee guida del Garante della privacy

Supervisore/Tutor Dott. MICHELE FAUCCI GIANNELLI

Firma [redacted]

Firma oscurata in base alle linee guida del Garante della privacy

Dottorando: Dott. FRANCESCO CURCIO

Firma [redacted]

Firma oscurata in base alle linee guida del Garante della privacy

UNIVERSITÀ DELLA CALABRIA

UNIVERSITA' DELLA CALABRIA

Dipartimento di Fisica

Dottorato di Ricerca in

Scienze e Tecnologie Fisiche, Chimiche e dei Materiali

CICLO XXXV

Measurements of single, double and triple differential cross-sections of top-quark pair production, in the lepton+jets channel, in *pp* collisions at √s=13 TeV using the data collected by the ATLAS detector during the full Run 2.

Settore Scientifico Disciplinare FIS/01

Coordinatore: Ch.ma Prof. ssa Gabriella Cipparrone

Firma _____

Supervisore/Tutor: Ch.mo Prof. ENRICO TASSI

Firma_____

Supervisore/Tutor Dott. MICHELE FAUCCI GIANNELLI

Firma_____

Dottorando: Dott. FRANCESCO CURCIO

Firma _____

Acknowledgements

I would like to acknowledge and give my warmest thanks to my supervisor, Prof. Tassi, who made this work possible and carried me through the stages of writing this thesis.

I would also like to thank the other members of the analysis on which this thesis is based on. In particular, Dr. Davide Malito, whose professionalism and friendship were priceless during the whole three years of my PhD. Another huge thank you goes to Dr. Michele Faucci Giannelli and Dr. Marino Romano, who never spared themselves in giving me help and advice when needed.

For his help in whatever circumstance, and despite never even meeting in person, I would also like to greatly thank Dr. Francesco Giuli, who was always able to give me good advice.

My uttermost thanks also to all my friends that endured my rants, both PhD- and non-PhD-related. Most of all, (in no particular order) Ismaele, for being my fellow student despite being 1600 km away, Luciano and Greg, for our countless flights of fancy, Mara, for always being there and making me sleep on her couch, Domenico, who lowered my hearing and made me know what a truly fat cat is, and Betta, who now has a degree of her own but still does not answer my texts before 72 hours have passed.

I would not have made it this far without the help of my family, therefore I ought them a really big thanks.

Last, but not least, I would like to thank Dan K. M. Emes for always showing me that a laugh can indeed change how you see things.

Abstract

In this thesis the differential cross-sections for the inclusive production of $t\bar{t}$ pairs have been measured at a center-of-mass energy of $\sqrt{s} = 13$ TeV. The data were collected by the ATLAS detector during the period spanning from 2015 to 2018, also known as Run 2, and correspond to an integrated luminosity of 140 fb^{-1}. The top-quark pair events were selected in the lepton (either electron or muon) plus jets channel.
The single, double and triple differential cross-sections have been measured as a function of the kinematic variables of the $t\bar{t}$ system or the hadronically decaying top-quark and extrapolated to the full phase-space.
The large amount of $t\bar{t}$ pairs produced at LHC gives the opportunity to perform stringent tests of pQCD by comparing the measured spectra with the theoretical fixed-order NNLO and Monte Carlo predictions.

Abstract

In questo lavoro di tesi sono state misurate le sezioni d'urto differenziali per la produzione inclusiva di coppie $t\bar{t}$ con un'energia del centro di massa di $\sqrt{s} = 13$ TeV. I dati sono stati raccolti con il rivelatore ATLAS durante il periodo dal 2015 al 2018, chiamato anche Run 2, e corrispondono ad una luminosità integrata di 140 fb^{-1}. Gli eventi di produzione di coppie $t\bar{t}$ sono stati selezionati nel canale "lepton+jets".
Le sezioni d'urto singolo, doppio e triplo differenziali sono state misurate in funzione di variabili cinematiche del sistema $t\bar{t}$ e del quark top che decade nel canale adronico e sono state estrapolate in tutto lo spazio delle fasi.
Il gran numero di coppie $t\bar{t}$ prodotte ad LHC dà l'opportunità di testare in maniera stringente la QCD perturbativa confrontando gli spettri misurati sia con predizioni teoriche NNLO che con predizioni Monte Carlo.

Contents

List of Figures

List of Tables

Introduction

Studying the properties of the top-quark is an important part of the ATLAS physics programme. One of its most notable properties is its mass: the highest between the known fundamental particles. This implies that the top-quark decays before undergoing the hadronization step, allowing a unique way of probing the Standard Model. The cross-section for the production of top-antitop pairs is one of the largest between the processes studied at the LHC, ~ 800 pb at a center of mass energy of $\sqrt{s} = 13$ TeV, therefore using the large amount of data collected by the ATLAS experiment during the full Run 2 to measure differential cross-sections for $t\bar{t}$ production is an excellent way to thoroughly test QCD. For this reason, the differential cross-sections measured in this analysis are compared to the latest fixed-order and Monte Carlo predictions, produced respectively using the `MATRIX` open-source code and the `MiNNLOPS` Monte Carlo generator. Other Monte Carlo predictions are also compared to the measured cross-sections. This allows for a careful comparison of the compatibility between data and available generators, while also allowing for tuning of the generator themselves. Moreover, precise measurements of differential cross-sections allow to conduct phenomenological studies, such as the extraction of the proton parton distribution functions, as well as extracting information on fundamental quantities of nature, such as the top-quark pole mass and the strong coupling constant α_s.

This thesis is structured as follows: in the first chapter the Quantum Chromodynamics theory is introduced, together with the parton distribution functions and the properties of the top-quark; in Chapter 2, the Large Hadron Collider and the ATLAS detector are described; in the third chapter, the description of both data and Monte Carlo generators used in this analysis is given; Chapter 4 is dedicated to the description of the reconstruction of physical objects and how they are defined; Chapter 5 focuses on the selection criteria used to separate $t\bar{t}$ signal from background events; in Chapter 6 the unfolding procedure used in this analysis to extract the parton-level cross-sections is presented; systematic uncertainties affecting the measurements are presented in Chapter 7; finally, Chapter 8 describes the unfolded parton-level

cross-sections measured in this analysis, compared with fixed-order pQCD predictions and Monte Carlo event generators.

Chapter 1

Quantum Chromodynamics

The Standard Model (SM) [1–4] is a relativistic quantum field theory that describes elementary particles and their interactions. A large number of experimental results have confirmed the validity of this model with outstanding precision, helping us to understand the world of elementary particles. Nevertheless, it is not a complete theory, since it fails to explain some phenomena such as the asymmetry between matter and antimatter, gravity or dark matter. In this chapter the theoretical framework from which the SM stems is described, in particular the theory of strong interactions. The first part of this chapter will be dedicated to derive the theory of Quantum Chromodynamics (QCD), then its divergences and their renormalization will be discussed. A description of basic collider processes and the factorization of their cross-sections is given in the second part, followed by a brief discussion of DGLAP (Dokshitzer-Gribov-Lipatov-Altarelli-Parisi) equations and parton distribution functions (PDFs). In the last part of the chapter, a summary of $t\bar{t}$ production processes in the framework of perturbative QCD (pQCD) is given, which is a crucial point of this thesis.

1.1 Quantum Chromodynamics

Quantum Chromodynamics is the field theory describing the strong interaction between gluons and quarks, collectively known as partons. They interact with a coupling constant usually written as $g_s = \sqrt{4\pi\alpha_s}$. Partons have a charge-like quantum number called colour which implies a gauge symmetry based on the non-abelian group SU(N_c) with $N_c = 3$ indicating the number of colour states. As a starting point the Lagrangian density (hereafter referred

to only as Lagrangian) can be written As

$$\mathscr{L}_q = \sum_{q=u,d,s,\ldots} \sum_{i,j} \bar{q}_i (i\partial\!\!\!/ - m_q)_{ij} q_j. \tag{1.1}$$

Here q is a quark colour-triplet and $\bar{q}$ is its adjoint, meaning

$$q = \begin{pmatrix} q_r \\ q_g \\ q_b \end{pmatrix}, \ \bar{q} = (\bar{q}_r, \bar{q}_g, \bar{q}_b) \tag{1.2}$$

whose elements are indicated in Eq. (1.1) by the subscripts $i, j = 1, 2, 3$ (for $N_c = 3$). The sum over different quark flavours will be omitted from now on.

The Lagrangian should be invariant under SU(N_c) non-abelian local group transformations: in fact, it can be shown that it does not change under transformations of the type

$$q \to q' = U(\theta) q = e^{i\theta_a T^a} q, \ a = 1, 2, \ldots, N_c^2 - 1, \tag{1.3}$$

where θ_a is an $N_c^2 - 1$-dimensional vector and T_a is one of the generators of the fundamental representation of the $SU(N_c)$ group, defined by:

$$[T^a, T^b] = i f^{abc} T^c. \tag{1.4}$$

Here f^{abc} are the structure constants of the $SU(N_c)$ group, these are totally antisymmetric under the exchange of two indices and their elements are numeric factors specific to the considered group. The Lagrangian Eq. (1.1) is clearly invariant under the transformation Eq. (1.3) as long as the θ_a represent a set of position-independent parameters. If, instead, $\theta_a \to \theta_a(x)$, giving

$$q \to q' = U(x) q = e^{i\theta_a(x) T^a} q, \tag{1.5}$$

the previous statement is not valid anymore. In fact, the derivative term in Eq. (1.1) transforms as

$$\partial_\mu q \to \partial_\mu q' = U(x) \partial_\mu q + [\partial_\mu U(x)] q, \tag{1.6}$$

spoiling the invariance of the Lagrangian. To fix this, one introduces as many boson fields as the group generators, say A^a_μ, which here represent gluons, and requires that the covariant derivative defined as

$$D_\mu = \partial_\mu + i g_s A^a_\mu T_a, \tag{1.7}$$

transforms as:

$$D'_\mu q' = D_\mu q. \tag{1.8}$$

This is only realised if the boson fields A^a_μ transform as:

$$A^a_\mu T_a \to U(x) A^a_\mu T_a U^{-1}(x) + \frac{i}{g_s}[\partial_\mu U(x)]U^{-1}(x) \tag{1.9}$$

or, since $0 = \partial_\mu(UU^{-1}) = (\partial_\mu U)U^{-1} + U(\partial_\mu U^{-1})$,

$$A^a_\mu T_a \to U(x)\left(A^a_\mu T_a - \frac{i}{g_s}\partial_\mu\right)U^{-1}(x). \tag{1.10}$$

Similar transformation laws are found for all the boson fields introduced in Yang-Mills [5] field theories based on non-abelian symmetry groups.

One interesting thing to note here is that, due to Eq. (1.9) configurations with non-zero A_μ can be obtained from $A_\mu = 0$ ones through a gauge transformation; this does not happen in abelian gauge theories, such as Quantum Electrodynamics (QED). When acting on quark fields, the T^a are $N_c^2 - 1$ generators in the fundamental representation of the group $\mathrm{SU}(N_c)$. In the case $N_c = 3$ these are simply $\frac{\lambda^a}{2}$ where λ^a are the 8 Gell-Mann matrices. The gauge fields A^a_μ transform according to the adjoint representation of the $\mathrm{SU}(N_c)$ group; in this representation the T^a matrices are constructed using the structure constants of the group, namely $(T^a)_{bc} = -if_{abc}$. Both the representations satisfy Eq. (1.4). The covariant derivative gives the possibility to calculate the field strength tensor, in fact

$$\begin{aligned}[D_\mu, D_\nu] &= ig_s G^a_{\mu\nu} T_a \\ G^a_{\mu\nu} &= \partial_\mu A^a_\nu - \partial_\nu A^a_\mu - g_s f^{abc} A^b_\mu A^c_\nu.\end{aligned} \tag{1.11}$$

Now all the pieces are in place to write the QCD Lagrangian in its full form, which is

$$\mathscr{L} = \bar{q}_i(i\not{D} - m_q)_{ij} q_j = \frac{1}{4} G^a_{\mu\nu} G^{\mu\nu}_a \tag{1.12}$$

It is easily seen that gluon fields have to be massless, since a massive term of the type $m^2 A^a_\mu A^\mu_a$ would not be gauge invariant due to how A_μ transforms. Useful identities involving the colour matrices, following the convention $\mathrm{Tr}\{T^a T^b\} = T_R \delta^{ab}$, $T_R = 1/2$ are:

$$\begin{aligned}\sum_a T^a_{ij} T^a_{jk} &= C_F \delta_{ik}, & C_F &= \frac{N_c^2 - 1}{2N_c} \\ \mathrm{Tr}\{T^c T^d\} &= \sum_{a,b} f^{abc} f^{abd} = C_A \delta^{cd}, & C_A &= N_c.\end{aligned} \tag{1.13}$$

These identities are valid for every symmetry group $SU(N_c)$.

From Eq. (1.12) the feynman rules for QCD can be extracted, these are:

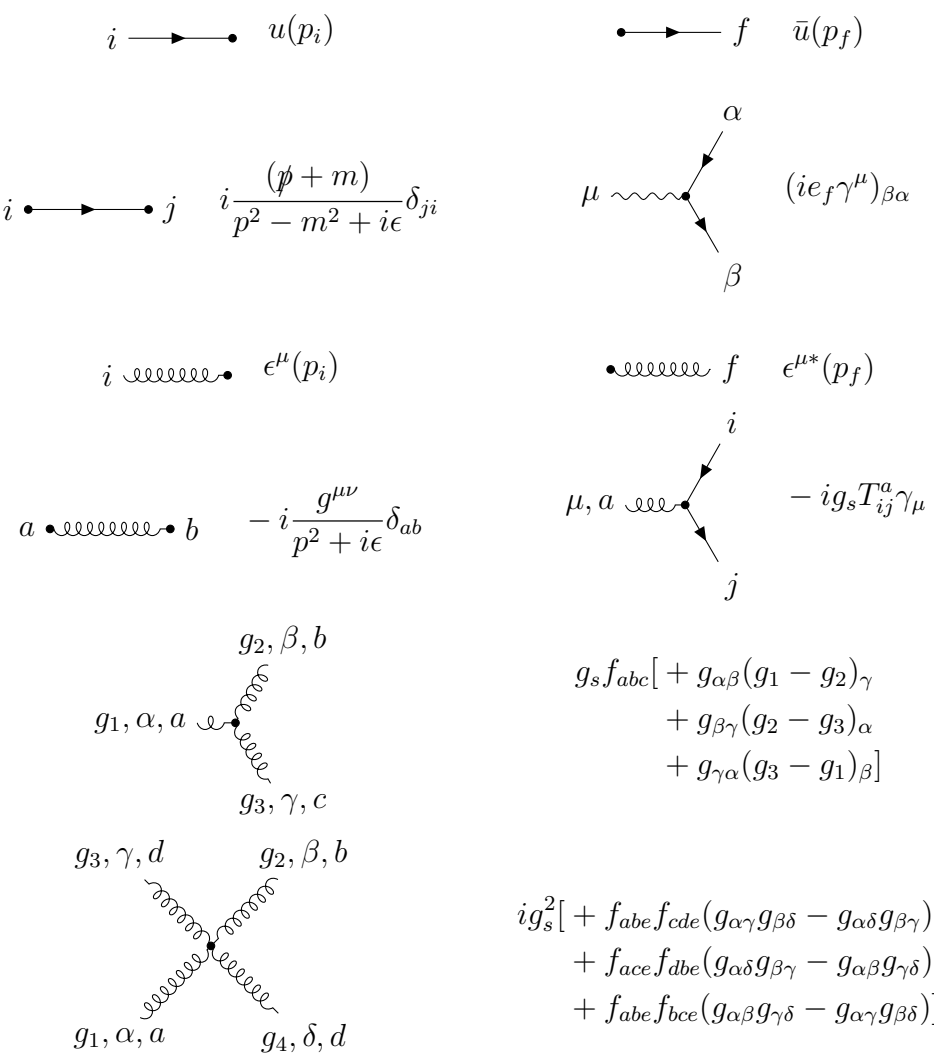

The gluon propagator is here written in the Feynman gauge, e_f is the charge of the considered fermion and all the Kronecker δs are referred to the colour indices. Initial and final momenta are represented by p_i and p_f respectively, while p is the momentum flowing in the propagator terms; the term m in the fermion propagator is the pole mass of the considered fermion. The four-vector e^μ and its complex conjugate represent the polarization of the gluons, $g^{\mu\nu}$ is the tensor diag$(1,-1,-1,-1)$. Greek letters indicate Lorentz indices, while latin ones are reserved for the colour indices.

1.2 QCD renormalization and divergences

When using pQCD every observable can be calculated as a perturbative (asymptotic) series in powers of α_s, in which the first non-zero contribution is called leading order (LO), while the higher powers are called next-to-leading order (NLO), next-to-next-to-leading-order (NNLO) etc. In Deep Inelastic Scattering, here taken as an example, when the initial state parton is a quark, the LO contribution is $\mathcal{O}(\alpha_s^0)$, since the sub-process $q + V \to q'$ (where V is a W, Z or γ boson) is purely electroweak and QCD effects enter the calculation only through higher order diagrams. In this case, the power series for an observable (e.g. a cross-section) will be $C_0 + C_1\alpha_s + C_2\alpha_s^2 + \cdots$. In this procedure, when higher order corrections are calculated, there usually are divergent contributions, these have to be regularized and removed using a prescription called renormalization. This technique consists in redefining the fields and couplings in order to cancel the divergences encountered order by order. One of the most important results of renormalization in QCD is asymptotic freedom, i.e. the possibility to treat quarks as free particles when the transferred momentum Q^2 is high enough.

1.2.1 UV divergences and renormalization

In the QCD framework, divergences present themselves in two forms, namely ultraviolet (UV) and infrared (IR) divergences. UV divergences arise in loop integrals, since the internal momentum of the loop is integrated to ∞. Infrared and collinear divergences, instead, arise when a particle is emitted in the limit in which $E \to 0$ (soft emission) or the angle between two emitted particles is small (collinear). Removing these divergences is paramount to produce reasonable results in perturbative theory, in particular UV divergences are removed using renormalization, while IR and collinear ones are treated using what is known as the Kinoshita, Lee, Nauenberg (KLN) theorem [6, 7]. The renormalization of the UV divergences also affects the coupling constant which, through the introduction of a *renormalization scale*, becomes a *running* coupling.

Integrals that present ultraviolet divergencies are treated using dimensional regularization: this technique consists in performing the integrals in $D = 4-2\epsilon$ dimensions and then considering the limit in which $\epsilon \to 0$ in order to obtain the analytical continuation as a series in powers of ϵ. An N-loop calculation will contain poles of increasing powers in ϵ, so a generic observable O could be written as:

$$O_N = \sum_{n=0}^{N} \left(\frac{\alpha_s}{4\pi}\right)^n \frac{C_n}{\epsilon} + \mathcal{O}(\epsilon). \tag{1.14}$$

When using dimensional regularization the coupling, dimensionless in $D = 4$, acquires a mass dimension. This is usually factorized, so that one can rewrite $g_s \to \mu^\epsilon g_s$. If one redefines the fields in the following way:

$$\begin{aligned} \psi_B &= Z_\psi^{1/2}\psi & A_B^\mu &= Z_A^{1/2}A^\mu \\ m_B &= Z_m m & g_{s0} &= \mu^\epsilon Z_g g_s, \end{aligned} \tag{1.15}$$

the Lagrangian assumes the form

$$\mathscr{L}_{\text{renorm}} = \mathscr{L} + \mathscr{L}_{\text{counter}}. \tag{1.16}$$

This can be understood looking at the Dirac part of the Lagrangian:

$$Z_\psi\bar{\psi}(i\partial\!\!\!/ - Z_m m)\psi = \bar{\psi}(i\partial\!\!\!/ - m)\psi + i(Z_\psi - 1)\bar{\psi}\partial\!\!\!/\psi - (Z_m Z_\psi - 1)m\bar{\psi}\psi, \tag{1.17}$$

which can be interpreted as $\mathscr{L}_{\text{Dirac}} + \mathscr{L}_{\text{Dirac,counter}}$. The same argument obviously applies to all other terms. The counter-terms Lagrangian contains new terms that are considered part of the interaction Lagrangian, and therefore contribute to the matrix elements. The point of redefining the fields and the Lagrangian in such a way is to obtain finite amplitudes, which is done imposing that the Zs cancel the divergences; this gives power series for these parameters.

If summing these infinite series was possible, one could obtain the exact values, devoid of any μ dependence or ambiguity. Being the world far from ideal, only a few orders can be calculated and since this means truncating the expansion series, some ambiguity remains in the definition of the Z parameters, such as which parts of the divergent amplitudes are cancelled by the counter-terms. Different definitions are referred to as *renormalization schemes*; one of the most used is the $\overline{\text{MS}}$ in which one imposes that the renormalization constants remove the ϵ poles and part of the finite piece of the amplitude. One of the perks of this approach is that no dependence on m/μ[1] is found in the Z functions, which renders calculations easier.

Since the dependence on μ is unphysical, an important request is that the *one particle irreducible* diagrams must be independent of it. If the amputated diagram (all the external lines are physical particles) contains n_ψ fermions and n_A gauge bosons, in the renormalization framework it will be written as

$$\Gamma_0(\alpha_{s0}, m_0, Q) = Z_\psi^{-\frac{n_\psi}{2}} Z_A^{-\frac{n_A}{2}} \Gamma(\mu, \alpha_s, m, Q). \tag{1.18}$$

The aforementioned request is realised if

$$0 = \frac{d\Gamma_0}{d\mu} = \left\{ \mu\frac{\partial}{\partial\mu} + \beta\frac{\partial}{\partial\alpha_s} + m\gamma_m\frac{\partial}{\partial m} - n_\psi\gamma_\psi - n_A\gamma_A \right\}\Gamma \tag{1.19}$$

[1]Since the Zs are dimensionless, any mass dependence would have to be in this form.

with γ and β functions defined as

$$\begin{aligned} \beta &= \mu\frac{\partial\alpha_s}{\partial\mu} & \gamma_\psi &= \frac{1}{2}\frac{\mu}{Z_\psi}\frac{\partial Z_\psi}{\partial\mu} \\ \gamma_m &= \frac{\mu}{m}\frac{\partial m}{\partial\mu} & \gamma_A &= \frac{1}{2}\frac{\mu}{Z_A}\frac{\partial Z_A}{\partial\mu} \end{aligned} \tag{1.20}$$

Eq. (1.19) is known as renormalization group equation (RGE) and, if solved, gives information on how the renormalized Γ varies with μ.

Independence of μ has, of course, to be valid for all the quantities that have been redefined, with an interesting case being $g_s = \sqrt{4\pi\alpha_s}$. A useful relation between the β functions for g_s and α_s is

$$\beta = \mu\frac{\partial\alpha_s}{\partial\mu} = \frac{\mu}{4\pi}\frac{\partial g_s^2}{\partial\mu} = \mu\frac{g_s}{2\pi}\frac{\partial g_s}{\partial\mu} = \frac{g_s}{2\pi}\beta_g \tag{1.21}$$

so that knowing one, the other is automatically available. Using the fact that $g_{s0} = \mu^\epsilon Z_g g_s$, the independence condition translate for g_s in

$$0 = \mu\frac{dg_{s0}}{d\mu} = \mu^\epsilon\left[\epsilon g_s Z_g + \beta_g\left(Z_g + g_s\frac{\partial Z_g}{\partial g_s}\right)\right]. \tag{1.22}$$

Using Eq. (1.22) together with the fact that Z_g can be written as a Laurent series in terms of inverse powers of ϵ and then requesting β to be a well defined function in the limit $\epsilon \to 0$, an expression for β can be derived. In QCD it has the form

$$\beta = -\alpha_s^2\sum_{n=0}^{\infty}\beta_n\alpha_s^n \tag{1.23}$$

where the coefficients β_n, in the $\overline{\text{MS}}$ scheme, take the form

$$\begin{aligned} \beta_0 &= \frac{33-2n_f}{12\pi} \\ \beta_1 &= \frac{153-19n_f}{24\pi^2} \\ \beta_2 &= \left(2857 - \frac{5033}{9}n_f + \frac{325}{27}n_f^2\right)\Big/128\pi^3 \\ &\vdots \end{aligned} \tag{1.24}$$

where n_f is the number of active flavours.

Using the expression Eq. (1.23) and choosing $\mu = Q^2$, we can calculate how the coupling constant α_s "runs" with the renormalization mass μ or equivalently with the scale Q, in fact

$$Q^2\frac{\partial\alpha_s}{\partial Q^2} = -\alpha_s^2\sum_{n=0}\beta_n\alpha_s^n \tag{1.25}$$

To solve this, the quantity $t = \ln(Q^2/Q_0^2)$ can be defined, so that $\alpha_s(Q^2)$ is implicitly defined by

$$t = \ln\left(\frac{Q^2}{Q_0^2}\right) = \int_{\alpha_s(Q_0^2)}^{\alpha_s(Q^2)} \frac{dx}{\beta(x)} \tag{1.26}$$

Neglecting terms in β higher than NLO and with the useful boundary condition $\alpha_s(Q_0^2 = \Lambda^2) = \infty$, $\alpha_s(Q^2)$ is given implicitly by the relation

$$\frac{1}{\alpha_s(Q^2)} = \beta_0 \ln\left(\frac{Q^2}{\Lambda^2}\right) - \frac{\beta_1}{\beta_0} \ln\left(\frac{\alpha_s(Q^2)}{\beta_0 + \beta_1 \alpha_s(Q^2)}\right). \tag{1.27}$$

This equation cannot be solved exactly, so either a numerical solution or an approximate one has to be found. In particular, if expanded in inverse powers of $\ln(\mu/\Lambda^2)$, α_s is found to be

$$\alpha_s(Q^2) = \frac{1}{\beta_0 \ln(Q^2/\Lambda^2)} \left[1 - \frac{\beta_1}{\beta_0^2} \frac{\ln\ln(Q^2/\Lambda^2)}{\ln(Q^2/\Lambda^2)} + \frac{\beta_1^2}{\beta_0^4 \ln^2(Q^2/\Lambda^2)} \left(\ln\ln(Q^2/\Lambda^2) - \frac{1}{2}\right)^2\right]. \tag{1.28}$$

Considering the case $\beta_1 = 0$, meaning that the calculation is done at LO, Eq. (1.27) can be inverted exactly to obtain

$$\alpha_s(Q^2) = \frac{1}{\beta_0 \ln(Q^2/\Lambda^2)}. \tag{1.29}$$

Λ is found experimentally to be $\sim$ 200 MeV which is of the order of the inverse length of a hadron, meaning that α_s becomes large, therefore spoiling the convergence of the perturbative expansion, when the energy scale is not high enough to probe the hadron internal structure.

Using the substitution $\Lambda^2 \to Q_0^2 \exp(-1/\beta_0 \alpha_s(Q_0^2))$ in Eq. (1.29), where Q_0^2 is an arbitrary reference scale, one obtains

$$\alpha_s(Q^2) = \frac{\alpha_s(Q_0^2)}{1 + \beta_0 \alpha_s(Q_0^2) \ln(Q^2/Q_0^2)}. \tag{1.30}$$

As long as $\beta_0 > 0$, meaning $n_f < 17$, Eq. (1.30) implies that α_s becomes smaller at scales higher than Q_0^2, therefore giving a proof of asymptotic freedom and of the validity of pQCD. Determinations of the strong coupling constant at different energies are reported in Fig. 1.1.

1.2.2 Infrared and collinear divergences

Turning now to infrared and collinear divergences, these can be treated using the KLN theorem. This proves that inclusive enough quantities are infrared

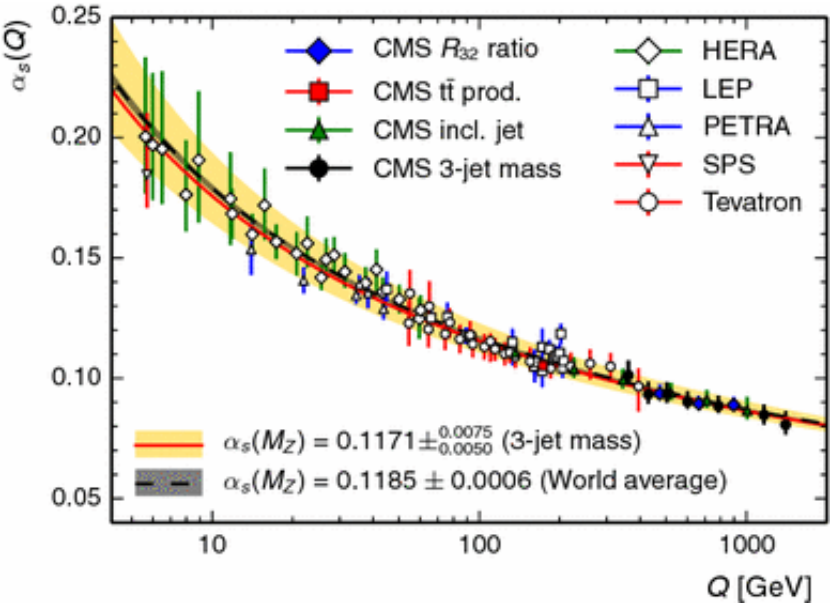

Figure 1.1: Measurements showing the running of the strong coupling constant. Figure taken from [8].

and collinear divergence-free, taking into account also the fact that in a true experimental setup, a process in which a soft gluon is emitted cannot be distinguished from one without a gluon emission. A similar argument can be applied to the case in which two particles are emitted collinearly, the detector cannot always distinguish between them. Following this way of thinking, when calculating cross-sections or every other quantity, contributions from these processes have to be included as well. The interference terms between soft/collinear contributions and the "pure" process will render the observables finite, getting rid of the divergences since they contribute with negative terms, while the squared ones are positive. Again dimensional regularization turns out to be useful to treat divergent integrals while all the contributions are being calculated and to see that, at the end, those divergences cancel out.

Calculating the cross-section for electron-positron annihilation into hadrons gives a finite result at $\mathcal{O}(\alpha_s)$, in fact the aforementioned KLN theorem guarantees that such an inclusive quantity is infrared and collinear safe. The key idea is that a quark and a quark with any number of soft and/or collinear gluons have to be treated as if they were the same. Generally a measured observable is described by an expression with the general form

$$I = \frac{1}{\text{flux}} \sum_n \frac{1}{n!} \int d\Phi^n \overline{\sum} \left| \mathcal{M}^{(n)}(p_i) \right|^2 \rho_n(p_i). \tag{1.31}$$

Here $\mathcal{M}^{(n)}$ is the Feynman amplitude for a process with an n-parton final state, p_i represents the momenta of the n partons, $p_1, \ldots, p_n$, $\overline{\sum}$ indicates sum over initial spin and colour configurations and the average on the final ones. The $1/n!$ factor stems from the assumption (not always valid) that the partons are indistinguishable from one another, while Φ_n is the n-particles phase space. The flux factor for a head-on collision of the type $p_a + p_b \to p_1 + \cdots + p_n$ is given by

$$\text{flux} = 4\sqrt{(p_a \cdot p_b)^2 - (m_a m_b)^2} \tag{1.32}$$

and for a process in which particle masses are negligible it can be approximated with $2s$. When I is the total cross-section, $\rho_n = 1$, while if interested in a differential cross-section $d\sigma/dX$, ρ_n takes the form

$$\rho_n = \delta(X - \mathcal{X}_n(p_i)), \tag{1.33}$$

where $\mathcal{X}_n(p_i)$ is a function (for n partons) of the variable X to which one is interested. This function has to verify the relations (based on the idea of infrared and collinear safety, meaning finiteness of I)

$$\left.\begin{array}{l} \mathcal{X}_{n+1}\left(p_1, \ldots, \lambda p_n, (1-\lambda)p_n\right) \\ \mathcal{X}_{n+1}(p_1, \ldots, p_n, 0) \end{array}\right\} = \mathcal{X}_n(p_1, \ldots, p_n). \tag{1.34}$$

Note that these requirements have both a theoretical and an experimental value. They are needed to accomplish the cancellation of the infinite parts in the theoretical calculation, but at the same time reflect the fact that real detectors have a finite resolution in both angle (collinear divergences) and energy (infrared divergences). Unfortunately this requirement cannot be satisfied by quantities that require the inclusive sum to contain a specific particle which is the case for some of the quantities entering the cross-section calculation.

We here give a brief and qualitative description of how the infrared and collinear singularities can be removed, in a way reminiscent of renormalization, following the discussion in [9]. When considering a hard subprocess with an incoming parton, the lowest order cross-section can be calculated, using the factorization theorem Eq. (1.48), to be discussed in the next section, so that one has

$$\sigma_0 = \int_0^1 dx\ \sigma_h(xp) q(x) \tag{1.35}$$

Corrections coming from higher order diagrams to the same hard process cross-section σ_h, in which an extra gluon is emitted in the final state can be written as (considering σ_{h+g} the cross-section for this process)

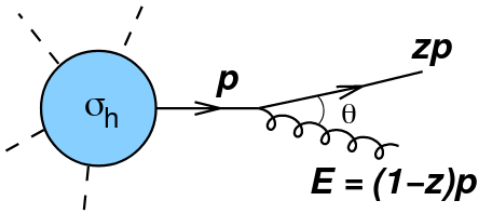

$$\sigma_{h+g} = \sigma_h \frac{\alpha_s C_F}{2\pi} \frac{1+z^2}{1-z} \frac{dk_t^2}{k_t^2}. \quad (1.36)$$

Here the transverse momentum $k_t = E \sin\theta$ has been introduced, with $E = (1-z)p$. Including the contribution from a virtual gluon in the final state (meaning that a state with a soft and/or collinear gluon plus a quark is considered as if it was just a one-quark state), one obtains a cancellation of the two singularities and therefore a finite result. In fact the cross-section contribution for a virtual gluon is of the form σ_{h+V}, which is of the form

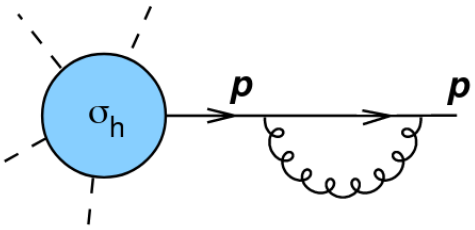

$$\sigma_{h+V} = -\sigma_h \frac{\alpha_s C_F}{2\pi} \frac{1+z^2}{1-z} \frac{dk_t^2}{k_t^2}. \quad (1.37)$$

If we now focus on gluon radiation in the *initial* state, the hard process takes place after the quark-gluon splitting, so that the momentum entering in σ_h is now $p \to zp$:

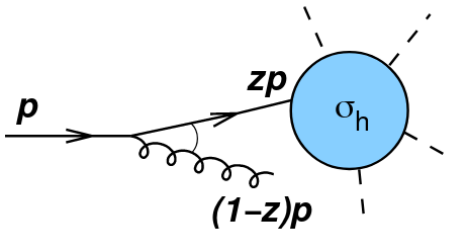

$$\sigma_{g+h} = -\sigma_h(zp) \frac{\alpha_s C_F}{2\pi} \frac{1+z^2}{1-z} \frac{dk_t^2}{k_t^2}. \quad (1.38)$$

Looking at the virtual process contribution the cross-section, since the moment entering the hard process this time is not changed, takes the form

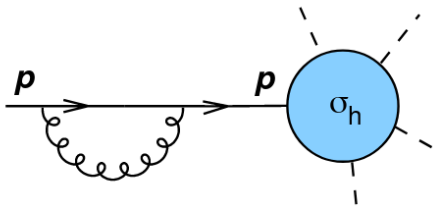

$$\sigma_{V+h} = -\sigma_h(p)\frac{\alpha_s C_F}{2\pi}\frac{1+z^2}{1-z}\frac{dk_t^2}{k_t^2}. \quad (1.39)$$

Summing now these two contributions and integrating over k_t and z, the total contribution for the process becomes

$$\sigma_{g+h} + \sigma_{V+h} \to \frac{\alpha_s C_F}{2\pi}\int_0^{Q^2}\frac{dk_t^2}{k_t^2}\int_0^1 dz\frac{1+z^2}{1-z}\left[\sigma_h(zp) - \sigma_h(p)\right]. \quad (1.40)$$

Note that the z integral is finite in the limit $z \to 1$, while the k_t integral diverges logarithmically when integrated to 0, this can be temporarily avoided introducing a regulator, μ_F^2. When calculating the cross-section the incoming parton has a fraction x of the hadron initial momentum, this has to be integrated over too, so that one obtains (σ_1 being the correction from one gluon emission, real and virtual)

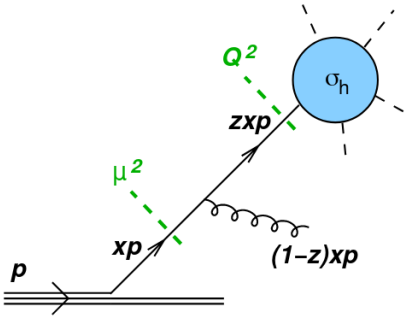

$$\begin{aligned}\sigma_0 &= \int dx\sigma_h(xp)q(x,\mu_F^2)\\ \sigma_1 &= \frac{\alpha_s}{2\pi}\int_{\mu_F^2}^{Q^2}\frac{dk_t^2}{k_t^2}\int dxdz\left(\frac{C_F(1+z^2)}{1-z}\right.\\ &\left.\times\left[\sigma_h(zxp) - \sigma_h(xp)\right]q(x,\mu_F^2)\right).\end{aligned} \quad (1.41)$$

The integral in k_t is now finite, even if it could still be large, while the contributions coming from $k_t < \mu_F$ have been absorbed into the PDFs, which now depend on the cut-off.

1.2.3 DGLAP equations

The process of redefining the PDFs and the introduction of a dependence on μ_F sketched in 1.2.2 is reminiscent of renormalization. In fact, even if a way to extract the PDFs from the QCD Lagrangian is yet to be found, equations for the evolution of the parton distribution functions can be found that describe how they change with this (unphysical) scale. These equations

are known as DGLAP [10–12] evolution equations:

$$Q^2 \frac{\partial q(x,Q^2)}{\partial Q^2} = \int_x^1 \frac{dz}{z} \frac{\alpha_s}{2\pi} P_{qq}(z) q\left(\frac{x}{z}, Q^2\right), \tag{1.42}$$

where $P_q q(z) = C_F((1+z^2)/(1-z))_+$ and the plus prescription has been introduced, and has to be understood as follows:

$$\begin{aligned} \int_x^1 dz\ [g(z)]_+ f(z) &= \int_x^1 dz\ g(z) f(z) - \int_0^1 dz\ g(z) f(1) \\ &= \int_x^1 dz\ g(z) \left[f(z) - f(1)\right] - \int_0^x dz\ g(z) f(1) \end{aligned} \tag{1.43}$$

The Altarelli-Parisi kernel P_{qq} can be perturbatively calculated as a series of α_s powers

$$P_{qq} = P_{qq}^{(0)} + \frac{\alpha_s}{2\pi} P_{qq}^{(1)} + \cdots . \tag{1.44}$$

These functions are, at the present time, known at NNLO [13, 14], this allows very precise comparison between measured cross-sections and theoretical ones calculated using PDFs extracted from other analyses, which in turn allows more precise parton distribution functions to be extracted and then used. DGLAP equations for quarks, antiquarks and gluons together, form a set of integro-differential equations that allow to calculate how a PDF evolves from one scale Q_0 to another, these equations are coupled since there are different kernels to use in Eq. (1.42), for example $P_{q\bar{q}}$ or P_{gq}. In its most general form and using the most common scale choice $\mu_F^2 = \mu_R^2 = Q^2$, the DGLAP system takes the form

$$\begin{aligned} Q^2 \frac{\partial}{\partial Q^2} \begin{pmatrix} q_i(x,Q^2) \\ g(x,Q^2) \end{pmatrix} =& \frac{\alpha_s}{2\pi} \sum_j \int_x^1 \frac{dz}{z} \\ & \begin{pmatrix} P_{q_i q_j}\left(\frac{x}{z}, \alpha_s\right) & P_{q_i g}\left(\frac{x}{z}, \alpha_s\right) \\ P_{g q_j}\left(\frac{x}{z}, \alpha_s\right) & P_{gg}\left(\frac{x}{z}, \alpha_s\right) \end{pmatrix} \begin{pmatrix} q_j(z,Q^2) \\ g(z,Q^2) \end{pmatrix} \end{aligned} \tag{1.45}$$

where q_i and q_j include both quark and antiquark contributions and α_s is to be considered as a function of the scale, $\alpha_s \equiv \alpha_s(Q^2)$. As a useful shorthand notation, the convolution between a PDF and a suitable Altarelli-Parisi kernel can be written as

$$[q \otimes P](x,Q^2) \equiv \int_x^1 \frac{dz}{z}\ q\left(\frac{x}{z}, Q^2\right) P(z) = \int_x^1 \frac{dz}{z}\ q(z,Q^2) P\left(\frac{x}{z}\right). \tag{1.46}$$

1.2.4 Hadron-hadron scattering

Hadronic interactions are quite vary, but can be, in broad outline, divided in two categories. The first class of processes is composed by soft interactions, in which the hadron is seen as a whole, due to the fact that transferred momenta are small compared to the center-of-mass (CoM) energy $\sqrt{s}$. The second group consists of hard processes, in which Q^2 is big enough to probe the hadrons' internal structure. While for the category of soft processes the cross-sections are quite large, for the latter category of hard processes the opposite situation is found, with small to tiny cross-sections that markedly depend on the CoM energy. Since pQCD can be only applied in the case of high Q^2, the only treatable problems with this approach are the second ones, while the first have to be treated using phenomenological arguments.

A formal result of quantum field theory applied to strong interactions is the *factorization theorem*, this states that the dependence on short and long distance interactions can be separated. In particular, long range physics is described by the PDFs and short range interactions are described by the pQCD cross-section for the hard (parton level) process. Therefore the cross-section for a proton-proton (or more generally hadron-hadron) scattering of the type

$$h_1(p_1) + h_2(p_2) \to X, \tag{1.47}$$

where p_1 and p_2 are the four-momenta of the protons h_1 and h_2 respectively. To calculate the cross-section the following equation is used (with $\mu_R = \mu_F = \mu$):

$$\sigma(p_1, p_2) = \sum_{a,b} \int_0^1 dx_1 \int_0^1 dx_2 f_{a/h_1}(x_1, \mu^2) f_{b/h_2}(x_2, \mu^2) \hat{\sigma}\left(x_1, x_2, \alpha_s(\mu^2), \tfrac{Q^2}{\mu^2}\right), \tag{1.48}$$

this is also schematically represented in Fig. 1.2. Here the CoM energy is reduced by a factor $s \to x_1 x_2 s$. In addition, the partons that do not take part in the hard subprocess, called the remnant, can interact and produce other reactions, with $s_{rem} = (1 - x_1 x_2)s$, even if the probability for two hard processes to take place is very small. The factorized form Eq. (1.48) is used in the calculation of theoretical predictions for the cross-section of hadron-hadron processes as top-antitop quark pairs production at the LHC, which is the focus of this analysis.

The characteristic scale of the hard scattering (here denoted by Q) could, for example, be the mass of a weak boson or heavy quark or the large transfer moment of a final state particle. The hard scattering cross-section σ_{ij}, since the coupling is small at high energy, can be calculated as a perturbative expansion in the running coupling α_s and can be, again, written as

$$\hat{\sigma} = \alpha_s^k \sum_{m=0}^{n} c_m \alpha_s^m \tag{1.49}$$

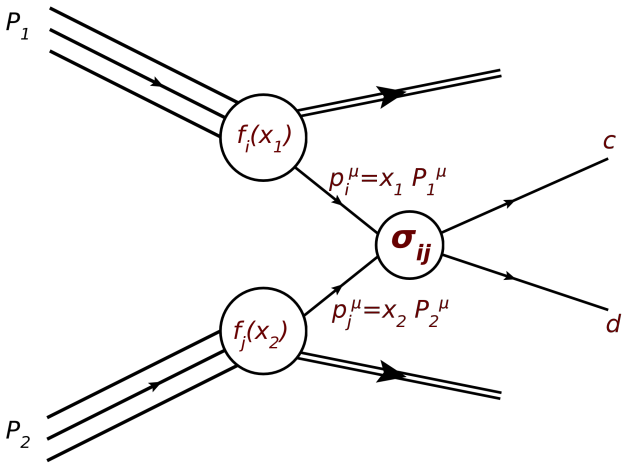

Figure 1.2: Schematic representation of a hadron-hadron scattering process in which two partons, i and j, interact through a hard process that gives as a result particles c and d.

where the coefficients c_m are functions of both the kinematic variables and the factorization scale. At every order in the series, different processes will contribute to the calculation of this cross-section. For example, at $\mathcal{O}(\alpha_s^0)$, the process is purely electromagnetic and therefore only quark-antiquark annihilation contributes. These coefficients usually include powers of $\ln(Q^2/\mu_F^2)$, these could become large if μ_F is not chosen to be of the order of Q, which is the standard choice. The more terms are in included the perturbative expansion, the weaker the dependence on the renormalization and factorization scales will be. In fact, the complete independence of the results from μ_F and μ_R would be true in an all order calculation. Because the series is truncated, a residual dependence on the scales remains in any fixed-order calculation. In fact, the relations

$$\frac{\partial\sigma}{\partial\mu_R} = \frac{\partial\sigma}{\partial\mu_F} = 0, \tag{1.50}$$

would hold only for a (ideal) situation in which all the terms of the expansion are calculated.

1.2.5 Cross-sections numerical evaluation

The calculation of cross-sections in pQCD is very CPU-intensive, therefore a fast way to re-evaluate the already derived cross-section is needed. In particular here the grid method used by both the `APPLgrid` and `fastNLO` programs is described; however for a more in-depth illustration of these two programs the reader is referred to their documentation [15, 16]. This method is based on the idea that once the CPU-intensive calculation has been made,

the results can be stored in a so-called grid that allows a fast re-evaluation of the cross-section for the considered process.

The main idea is that PDFs can be represented by storing their values in a two dimensional grid of points and using n-th order interpolations between them. To better cover the full range in x and Q^2 this variable change is made

$$y(x) = \ln\left(\frac{1}{x}\right) + a(1-x) \quad \text{and} \quad \tau(Q^2) = \ln\ln\left(\frac{Q^2}{\Lambda^2}\right) \tag{1.51}$$

where Λ is chosen of the order of Λ_{QCD} but is not necessarily the same. The parameter a's scope is to increase the density of points in the large-x region. A generic PDF $f(x, Q^2)$ is then represented by its values $f_{i,j}$ on two-dimensional grid points $(i\delta y, j\delta\tau)$, where δy and $\delta\tau$ are the grid spacings. For an $(x,\ Q^2)$ point which is not contained in the grid, the PDF is evaluated by the interpolation (based on Lagrange polynomials) formula:

$$f(x,Q^2) = \sum_{i=0}^{n}\sum_{j=0}^{n'} f_{k+i,k'+j} I_i^{(n)}\left(\frac{y(x)}{\delta y} - k\right) I_j^{(n')}\left(\frac{\tau(Q^2)}{\delta\tau} - k'\right). \tag{1.52}$$

Here n and n' are the interpolating orders and the functions $I_i^{(n)}(u)$ are 1 for $u = i$ and are defined as

$$I_i^{(n)}(u) = \frac{(-1)^{n-i}}{i!(n-i)!}\frac{u(u-1)\ldots(u-n)}{u-i} \tag{1.53}$$

otherwise. The indices k and k' are defined as

$$\begin{aligned} k(x) &= \text{int}\left(\frac{y(x)}{\delta y} - \frac{n-1}{2}\right) \\ k'(Q^2) &= \text{int}\left(\frac{\tau(Q^2)}{\delta\tau} - \frac{n'-1}{2}\right) \end{aligned} \tag{1.54}$$

and the function int(u) is defined to be the largest integer verifying int$(u)\leq u$. An example of usage for single-flavour DIS is here reported.

Assuming a Monte Carlo generator at next-to-next-to-leading order precision is available that produces events $m = 1, \ldots, N$. Every event m has x-value x_m, Q^2 value Q_m^2 and a weight w_m. Defining p_m to be number of powers of α_s in the event m, the result for the Monte Carlo would be

$$W = \sum_{m=1}^{N} w_m \left(\frac{\alpha_s(Q^2)}{2\pi}\right)^{p_m} f(x_m, Q_m^2) \tag{1.55}$$

where f is the PDF of the considered flavour. Using these grids, instead, the weights $W_{i,j}^{(p)}$ are used and for each event only a part of the grid is updated

$$W_{k+i,k'+j}^{(p_m)} \to W_{k+i,k'+j}^{(p_m)} + w_m I_i^{(n)} \left(\frac{y(x_m)}{\delta y} - k(x_m) \right) I_j^{(n')} \left(\frac{\tau(Q_m^2)}{\delta \tau} - k'(Q_m^2) \right). \tag{1.56}$$

The final result can then be obtained after the Monte Carlo run in the following way, for a generic α_s and PDF f

$$W = \sum_p \sum_i \sum_j W_{i,j}^{(p)} \left(\frac{\alpha_s(Q^{2^{(j)}})}{2\pi} \right)^p f(x^{(i)}, Q^{2^{(j)}}). \tag{1.57}$$

Here $Q^{2^{(j)}}$ and $x^{(i)}$ have been introduced and are such that

$$\begin{aligned} y(x^{(i)}) &= i\delta y \\ \tau(Q^{2^{(j)}}) &= j\delta\tau. \end{aligned} \tag{1.58}$$

In the previous discussion the relation $\mu_F^2 = \mu_R^2$ has been assumed, but knowing DGLAP evolution and the weight matrix order by order, the variation of these scales can be introduced in the calculation. This is done, taking ξ_R and ξ_F to be the scale factors for μ_F and μ_R respectively and considering NLO as the higher order in α_s, calculating

$$\begin{aligned} W(\xi_R, \xi_F) = \sum_i \sum_j \Bigg\{ & \left(\frac{\alpha_s(\xi_R^2 Q^2)}{2\pi} \right)^{p_{LO}} W_{i,j}^{(p_{LO})} f(x, \xi_F^2 Q^2) \\ & + \left(\frac{\alpha_s(\xi_R^2 Q^2)}{2\pi} \right)^{p_{NLO}} \\ & \times \Big[\left(W_{i,j}^{(p_{NLO})} + 2\pi\beta_{0,p_{LO}} \ln \xi_R^2 W_{i,j}^{(p_{LO})} \right) \\ & \times f(x, \xi_F^2 Q^2) - \ln \xi_F^2 W_{i,j}^{(p_{LO})} (P_0 \otimes f)(x, \xi_F^2 Q^2) \Big] \Bigg\}. \end{aligned} \tag{1.59}$$

Here x and Q^2 have to be regarded as $x^{(i)}$ and $Q^{2^{(j)}}$, P_0 is the LO matrix for the splitting functions and β_0 is the same as the one in Eq. (1.24). This method only works if ξ_R and ξ_F are constants, moreover even if this formula is given for an x-space approach, a similar form can be found for an N-space one. To obtain the full cross-section a sum of the weights and the PDFs over all the contributing sub-processes is needed.

This approach is easily generalized to the case of hadron-hadron collisions, in which case Eq. (1.57) can be rewritten as

$$W = \sum_p \sum_{l=0}^{n_{sub}} \sum_{i_1} \sum_{i_2} \sum_j W_{i_1,i_2,j}^{(p,l)} \left(\frac{\alpha_s(Q^2)}{2\pi} \right)^p F^{(l)}(x_1, x_2, Q^2). \tag{1.60}$$

Here n_{sub} is the number of subprocesses, while the functions F are subprocess-dependent combination of PDFs. These can sometimes be simplified exploiting the symmetries in the weights. It is again possible to find a formula to take arbitrary (but constant) scale variations into account, at NLO this takes the form:

$$\begin{aligned} W(\xi_R, \xi_F) = \sum_{l=0}^{n_{sub}-1} \sum_{i_1} \sum_{i_2} \sum_{j} \Bigg\{ & \left(\frac{\alpha_s(\xi_R^2 Q^2)}{2\pi} \right)^{p_{LO}} \\ & \times W_{i_1,i_2,j}^{(p_{LO},l)} F^{(l)} \left(x_1, x_2, \xi_F^2 Q^2 \right) \\ & + \left(\frac{\alpha_s(\xi_R^2 Q^2)}{2\pi} \right)^{p_{NLO}} \\ & \times \Bigg[\left(W_{i_1,i_2,j}^{(p_{NLO},l)} + 2\pi\beta_0 p_{LO} \ln \xi_R^2 W_{i_1,i_2,j}^{(p_{LO},l)} \right) \\ & \times F^{(l)} \left(x_1, x_2, \xi_F^2 Q^2 \right) \\ & - \ln \xi_F^2 W_{i_1,i_2,j}^{(p_{LO},l)} \left(F_{q_1 \to P_0 \otimes q_1}^{(l)} \left(x_1, x_2, \xi_F^2 Q^2 \right) \right. \\ & \left. + F_{q_2 \to P_0 \otimes q_2}^{(l)} \left(x_1, x_2, \xi_F^2 Q^2 \right) \right) \Bigg] \Bigg\} . \end{aligned} \tag{1.61}$$

Here the functions $F_{q_i \to P_0 \otimes q_i}^{(l)}$ are defined as $F^{(l)}$ but q_i is replaced with $P_0 \otimes q_i$, while x_k and Q^2 are to be viewed as $x_k^{(i)}$ and $Q^{2^{(j)}}$.

1.3 Top quark production

Between all the particles described by the Standard Model, the top (t) quark is the heavier. This implies that its decay time is less than its hadronization time. Studying processes in which top quarks are produced therefore gives a perfect instrument to test perturbative QCD and the predictions obtained in this framework. The top quark was first discovered in 1995 by the CDF and D0 collaborations at Tevatron; they studied $p\bar{p}$ collisions at a CoM energy of $\sqrt{s} = 1.8$ TeV [17–20]. Its mass was measured in various experiments and according to the Review of Particle Physics by the Particle Data Group (PDG) in 2022, $m_t = 172.69 \pm 0.30$ GeV [21], while recent measurements from LHC experiments are reported in Fig. 1.3. The existence of a third generation doublet of quarks such as the top-bottom doublet implies, taking into account also the existence of three lepton generations, the cancellation of the chiral gauge anomalies [22] and also allows the CKM mechanism to explain the CP violation [23].

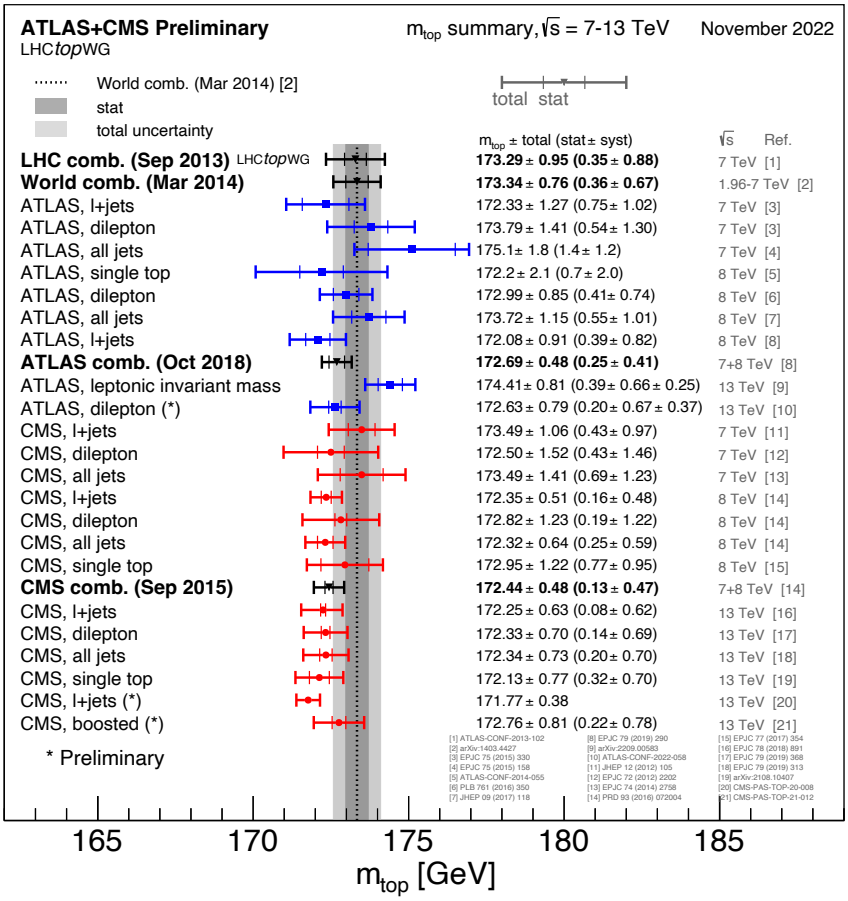

Figure 1.3: Summary of ATLAS and CMS determinations of the top mass. The results are compared with the LHC and Tevatron+LHC combined determinations [24].

1.3.1 Top quark production

Top quarks are produced in accelerators such as LHC, usually as a $t\bar{t}$ pair or, rarely, as a single top quark. The interactions in which top pairs are produced are mediated by the strong force, while the ones in which a single top quark is produced are mediated by the weak force. At leading-order (LO), top-antitop pairs are produced through two main processes: quark-quark annihilation and gluon-gluon fusion, shown in the diagrams in Fig. 1.4. In addition to the production of pairs, single top quarks can be produced through the diagrams show in Fig. 1.5. Production of $t\bar{t}$ pairs at the LHC occurs predominantly through the gluon-gluon channel. Since this analysis' goal is to measure differential cross-sections for the inclusive production of $t\bar{t}$ pairs, the single top events are treated as a background.

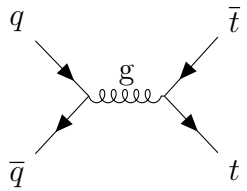

(a) $t\bar{t}$ production via quarks annihilation

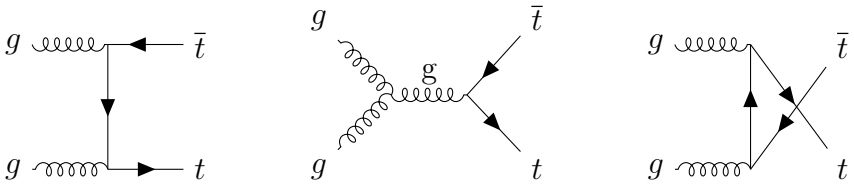

(b) $t\bar{t}$ production via gluon fusion

Figure 1.4: Examples of Feynman diagrams at LO for the creation of a $t\bar{t}$ pair via quarks annihilation in (a) or via gluons fusion (b).

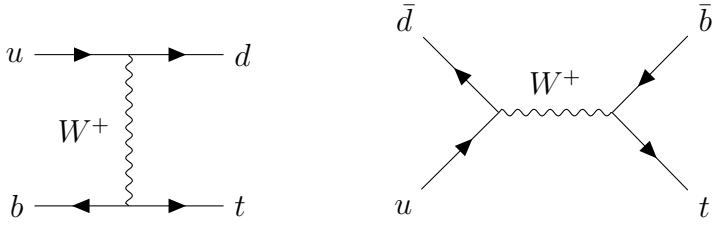

(a) t channel

(b) s channel

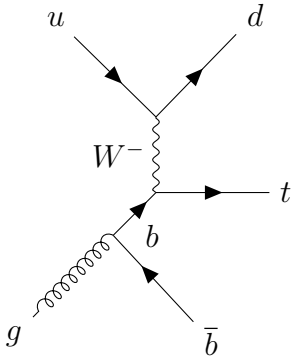

(c) Wt channel

Figure 1.5: LO diagrams for the production of single top via different channels.

1.3.2 Top decays

Top quarks decay via the weak interaction into a W boson and a quark, either d, s or b, the former two being suppressed due to the mixing elements of the

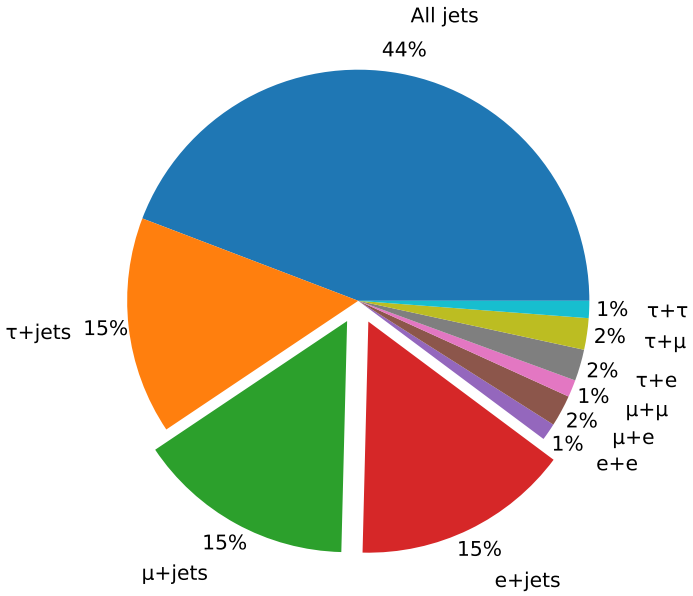

Figure 1.6: Branching ratios for $t\bar{t}$ production

CKM matrix. The branching ratios for these decays are:

$$\begin{aligned} \mathrm{BR}(t \to bW) &= 99.8\% \\ \mathrm{BR}(t \to sW) &= 0.16\% \\ \mathrm{BR}(t \to dW) &= 0.001\%. \end{aligned}$$

The W bosons can decay in two different ways, two quarks or a lepton and its associated neutrino. This implies that a $t\bar{t}$ pair can be identified by three different signatures:

- All hadronic channel: $t\bar{t} \to W^+b + W^-\bar{b} \to q\bar{q}'b + q''\bar{q}'''\bar{b}$. In this case both the W bosons decay into quarks, the b quarks have high transverse momentum and four light quarks are observed in the final state.
- Semileptonic channel: $t\bar{t} \to W^+b + W^-\bar{b} \to q\bar{q}'b + \ell^-\bar{\nu}_\ell\bar{b}/\ell^+\nu_\ell b + q\bar{q}'\bar{b}$. In this channel one of the W bosons decays leptonically, while the other produces two quarks. The signature for this channel is the presence of one lepton, one neutrino (therefore missing transverse energy), two b-quarks and two light quarks.
- Dileptonic channel: $t\bar{t} \to W^+b + W^-\bar{b} \to \ell^+\nu_\ell b + \ell^-\bar{\nu}_\ell\bar{b}$. Here both the Ws decay leptonically, therefore the final state is characterized by two

leptons, two b-quarks and large missing transverse energy, due to the presence of two neutrinos.

1.3.3 Top pair production

As shown in Eq. (1.48), the cross-section for a process involving hadrons can be written in a factorized form in which the PDFs are convoluted with the so-called "hard" cross-section. As seen in the previous sections, at the LHC and at leading-order, the main contribution to $t\bar{t}$ production comes from gluon-gluon fusion, Fig. 1.4(b). This can be seen looking at the gluon PDF in the naive parton-model interpretation, in fact the gluon PDF decreases as x increases, meaning that is less probable to find a gluon with a fraction x of its parent proton's momentum and to produce a $t\bar{t}$ pair, this fraction has to be $\sim \frac{m}{\sqrt{s}} \sim 0.02$.

The total cross-section for $t\bar{t}$ production can be written, using the factorization theorem, as [25]:

$$\sigma_{pp\to t\bar{t}} = \sum_{i,j=q,\bar{q},g} \int dx_1 dx_2 f_{i/p_1}(x_1,\mu_F^2) f_{j/p_2}(x_2,\mu_F^2) \hat{\sigma}_{ij\to t\bar{t}}(\hat{s},\alpha_s^2(\mu_R^2),\mu_F^2) \tag{1.62}$$

where $\hat{\sigma}_{ij\to t\bar{t}}$ is the hard cross-section for the process in which two partons, labelled i and j, interact producing a $t\bar{t}$ pair. This cross-section can be written as

$$\hat{\sigma}_{ij\to t\bar{t}}(\hat{s},\mu_R^2,\mu_F^2) = \frac{\alpha_s^2(\mu^2)}{m_t^2} h_{ij}\left(\rho, \frac{\mu^2}{m_t^2}\right) \tag{1.63}$$

where $\rho \equiv \frac{4m_t^2}{s}$, $\mu_R = \mu_F = \mu$ and m_t is the top quark mass. The perturbative part of the cross-section is h_{ij}, which can be therefore written as

$$h_{ij}\left(\rho, \frac{\mu^2}{m_t^2}\right) = h_{ij}^{(0)}(\rho) + \alpha_s(\mu^2)\left[h_{ij}^{(1)}(\rho) + \tilde{h}_{ij}^{(1)} \ln\left(\frac{\mu^2}{m_t^2}\right)\right] + \mathcal{O}(\alpha_s^2). \tag{1.64}$$

In particular $h_{ij}^{(0)}$ is:

$$\begin{aligned} h_{q\bar{q}}^{(0)} &= \frac{\pi\beta\rho}{27}[2+\rho] \\ h_{gg}^{(0)} &= \frac{\pi\beta\rho}{192}\left[\frac{1}{\beta}(\rho^2+16\rho)\ln\left(\frac{1+\beta}{1-\beta}\right) - 28 - 31\rho\right] \\ h_{gq}^{(0)} &= h_{g\bar{q}}^{(0)} = 0 \end{aligned}$$

where $\beta \equiv \sqrt{1-\rho}$. The higher orders in Eq. (1.64) can be written in the form of two terms, $\tilde{h}^{(1)}(\rho)$ which are the coefficients of terms proportional

to $\ln\left(\frac{\mu^2}{m_t^2}\right)$ and can be determined from the lower-order terms using renormalization group arguments; the $h^{(1)}(\rho)$ terms depend on the factorization and renormalization schemes and can only be obtained through a full $\mathcal{O}(\alpha_s^3)$ perturbative calculation. The $\tilde{h}^{(1)}$ can be analytically derived, while the $h^{(1)}$ is obtained via numerical integration [26]. Important contributions come from corrections near the parton process threshold. Another source of large corrections is the high s region in the gg and qg subprocesses, which allow gluon exchange in the t-channel at $\mathcal{O}(\alpha_s^3)$.

1.3.4 NNLO predictions

In the last years theoretical NNLO predictions have become available both for total [27–32] and differential [33–35], single and double, $t\bar{t}$ pairs production cross-section, for which the contributions in pQCD are shown in Fig. 1.7. These kind of calculation for partonic cross-sections have been recently implemented in the open source software `MATRIX` [36].

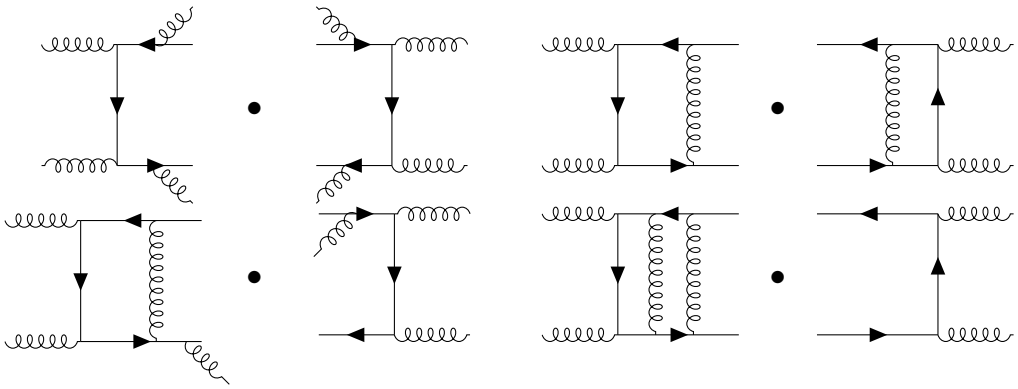

Figure 1.7: Four contributions to NNLO $t\bar{t}$ cross-section. The double real radiations $d\sigma^{RR}$, the 1-loop squared contribution $d\sigma^{SV}$, the 1-loop, 1-real part $d\sigma^{RV}$ and the double virtual contribution $d\sigma^{VV}$

In addition to fixed order predictions, a new Monte Carlo generator called `MiNNLOPS` [37, 38] has been developed to consistently combine NNLO calculations with a PS algorithm. This procedure consists of three steps, here sketched schematically:

1. Generation of a $t\bar{t}$ pair together with a light parton, following the Powheg [39–41] method, done at the NLO level, inclusive over the radiation of a second light parton.

2. In the limit in which the light partons of the previous step become unresolved, meaning that $t\bar{t}+$ light partons $\simeq t\bar{t}$, the need for a Sudakov

form factor and terms of higher orders arises. This is necessary to ensure the calculation remains finite while also being NNLO-accurate for the inclusive $t\bar{t}$ production.

3. The kinematic of the second radiated light parton, which was inclusively considered in step 1, is generated following the POWHEG method. This ensures the NLO accuracy of the $t\bar{t}$+jet cross-section.

After the third step, subsequently produced radiation is included by the PS, with the constraint that its transverse momentum be softer than the last POWHEG real emission's one.

Chapter 2

LHC and the ATLAS Experiment

2.1 LHC

The Large Hadron Collider (LHC) is the biggest superconducting hadron collider, located at CERN (European Center for Nuclear Research, in french Conseil Européen pour la Recherche Nucléaire). It's an underground structure, built beneath the border between Swiss and France, near the city of Geneva. This structure consists of a 27 km ring of superconducting magnets where bunches of hadrons are accelerated until they collide at a CoM energy $\sqrt{s} = 13$ TeV. In correspondence of the points where the bunches collide, four main experiments are located, ALICE [42] (A Large Ion Collider Experiment), ATLAS [43] (A ToroidaL ApparatuS), CMS [44] (Compact Muon Spectrometer) and LHCb [45] (Large Hadron Collider beauty). The proton bunches are accelerated in the LHC using sixteen radio-frequency cavities. These bunches are bent by an 8 T magnetic field, created by a series of dipole and quadrupole magnets kept at a temperature of 2 K. Before entering the main ring, the particles pass through a series of pre-accelerators. The main goal of the LHC is to test SM predictions and investigate physics Beyond the Standard Model (BSM). The number of events per unit time can be written as

$$\frac{dN}{dt} = \underbrace{\frac{N_b^2 n_b \gamma_r f}{4\pi\epsilon_n \beta^*} F}_{L_{\text{inst}}} \sigma, \tag{2.1}$$

here σ is the cross-section for the considered process, N_b is the number of particles per bunch, n_b is the number of bunches composing the beams, γ_r is the relativistic gamma factor, f is the revolution frequency, ϵ is the (normalized) transverse beam emittance and F is a factor that takes into account the geometry of the beam collisions at the interaction points. The

integrated luminosity, which is a measure of how many interactions took place in a certain amount of time, can be calculated as:

$$L = \int_{t_1}^{t_2} L_{\text{inst}} dt, \tag{2.2}$$

here $\Delta t = t_2 - t_1$ is the total data acquisition time.

2.1.1 LHC Experiments

Experiments taking place at CERN have different goals and investigate different fields of High Energy Physics. In particular, the four main experiments are:

- ALICE, which studies quark-gluon plasma produced in Pb nuclei collisions. This is a state of matter which is believed to be what the universe was made of in its early stage, when hadrons hadn't formed, yet.
- ATLAS is a multi-purpose detector. Its goals are to perform precise measurements of SM processes and searches for BSM physics. A detailed description will be given in the following sections, since the work presented in this thesis has been done using data coming from the ATLAS experiment.
- CMS is the second multi-purpose detector and, although with different technologies, has similar physics goals as ATLAS.
- LHCb is an experiment specifically designed to investigate and measure the CP-violation of b-hadrons, as the name suggests.

Apart from these main four experiments, there are three more:

- LHCf [46] (Large Hadron Collider forward) simulates cosmic rays using forward particles generated from LHC.
- MoEDAL [47] (Monopole and Exotics Detector at the LHC) searches for the magnetic monopole.
- TOTEM [48] (TOTal Elastic and diffractive cross-section Measurement) measures total cross-sections, elastic scattering and diffraction processes studying particles produced at very small angles.

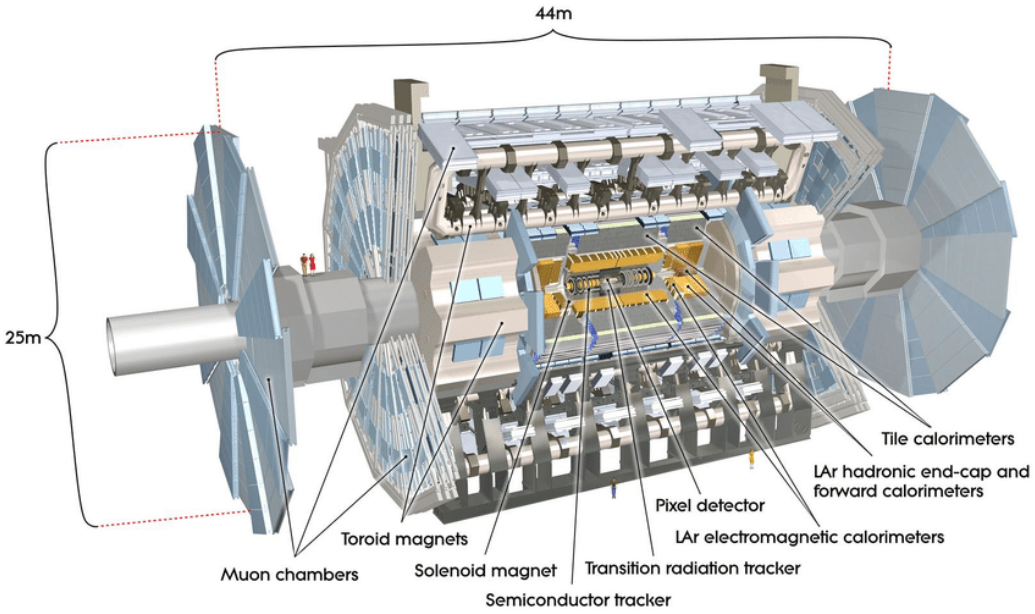

Figure 2.1: A view of ATLAS sub-detectors [43].

2.2 ATLAS

ATLAS is a multi-purpose detector that aims to perform stringent SM measurements. At the moment, ATLAS is the largest detector at LHC, with its 44 m in length, 25 m in height and a weight of over 7000 t. The detector has the typical onion-shell structure used in collider experiments, cylindrically symmetric with respect to the beam pipe. The ATLAS detector can be divided in two main parts: the central part, also called the *barrel*, and two side parts, called *endcaps*. ATLAS is composed of several sub-detectors [49] as shown in Fig. 2.1. In particular, these are a toroidal magnet system and five main sub-detectors, which are (from closer to further from the beam-pipe) the inner detector (ID), the electromagnetic liquid argon calorimeter (LAr), the hadronic calorimeter (Tile), the muon spectrometer (MS) and the forward detectors. The way in which these sub-detectors are arranged is crucial in reconstructing the produced particles. The magnetic field make the charged particles' trajectories curve, allowing their reconstruction and the measurement of the particles' momenta in the ID, which is a tracker system. The middle section is composed of calorimeters, which absorb most of the particles and measure their energies. The MS is used to identificate muons, which are not absorbed by the calorimeters.

2.2.1 Coordinate System

Due to the cylindrical symmetry with respect to the IP, ATLAS uses a right-handed coordinate system with its origin at the nominal IP in the center of the detector and the z-axis along the beam pipe. The x-axis points from the IP to the center of the LHC ring, and the y-axis points upwards, defining the transverse plane with respect to the beam. It is also useful to introduce the natural units system, in which the fundamental physics constants, $\hbar$ and c, are set to 1 and therefore all the kinematics variables can be expressed in units of energy (electronvolts eV). Cylindrical coordinates (r, ϕ) are used in the transverse plane, ϕ being the azimuthal angle around the z-axis. The polar angle θ is the angle from the z-axis, as shown in Fig. 2.2. The azimuthal differences $\Delta\phi$ are invariant under Lorentz transformations, while the polar differences $\Delta\theta$ are not, so defining a new Lorentz-invariant quantity to use in place of the polar angle is useful: this is the rapidity, defined as

$$y = \frac{1}{2} \ln \left(\frac{E + p_z}{E - p_z} \right). \tag{2.3}$$

Rapidity is used for massive particles, since for massless particles it reduces to just

$$\eta = -\ln \tan \frac{\theta}{2}, \tag{2.4}$$

called pseudorapidity. The differences Δy and $\Delta\eta$ are Lorentz-invariant. Distances between particles ΔR can be expressed in terms of the pseudorapidity and the azimuthal angle in the following way:

$$\Delta R \equiv \sqrt{\Delta\phi^2 + \Delta\eta^2}. \tag{2.5}$$

If the momentum of a particle becomes a relevant quantity, it is useful to define the *transverse momentum* (p_T) of that particle, which is the projection of the 4-momentum on the x-y plane.
If some of the particles are not revealed by the detector – either because their trajectories are outside the ATLAS detector or they have a low interaction rate with matter, like neutrinos – a useful quantity to take into account is the missing transverse energy E_T^{miss}, defined as

$$E_T^{\text{miss}} = \left| \sum_i p_{T,i} \right|. \tag{2.6}$$

Here $p_{T,i}$ is the transverse momentum of the i-th particle. From the conservation law of the momentum, this sum has to be 0 if all the particles have been revealed, if instead $E_T^{\text{miss}} \neq 0$, it means some of them have not.

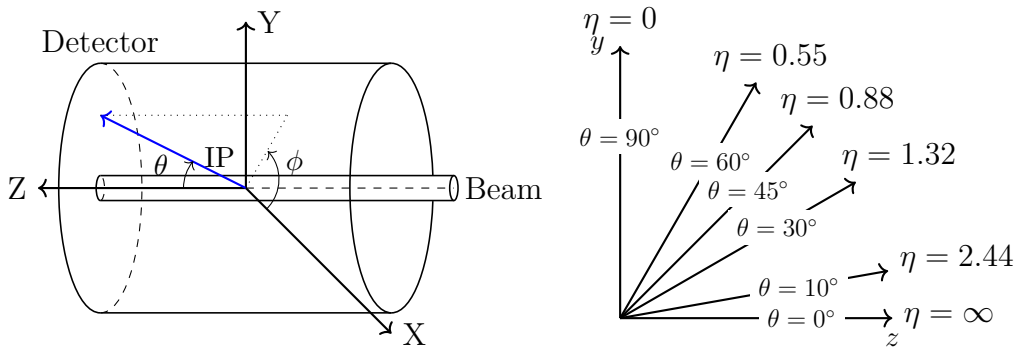

(a) Illustration of the ATLAS coordinate system.

(b) A graphic of the relation between η and θ.

Figure 2.2: Scheme of the coordinate system used in ATLAS. In Figure 2.2(a) is shown a scheme of the ATLAS detector with the Cartesian axes and the angle used, while in Figure 2.2(b) is shown the dependence of the pseudorapidity η from the polar angle θ.

2.2.2 Magnet System

ATLAS has two magnetic field systems which are used to bend the trajectories of charged particles for momentum and charge measurements: one system is the Central Solenoid (CS) and the other is composed of the Barrel Toroid (BT) and the two End-cap Toroids (ECT), both shown in Fig. 2.3. The CS produces a magnetic field of 2 T in the direction of the beam line and its design was devised in order to minimize the impact on the energy measurements in the calorimeters. The CS is 5.3 m long and has a diameter of 2.4 m. The toroidal magnets generate a magnetic field up to 4 T and are used to bend the trajectories of the muons in the muon spectrometer; these magnets are arranged with a eight-fold azimuthal symmetry around the calorimeters. The Barrel measures 25 m in length, with an inner core of 9.4 m and an outer diameter of 20.1 m. It bends the trajectories of particles located in the region $|\eta| < 1$. The two ECTs are 5 m long, with an inner core of 1.64 m and an outer diameter of 10.7 m. They operate in the region $1.4 \leq |\eta| \leq 2.7$. In the region between the aforementioned ones ($1 \leq |\eta| \leq 1.4$), the magnetic field is provided by both barrel and end-cap toroids.

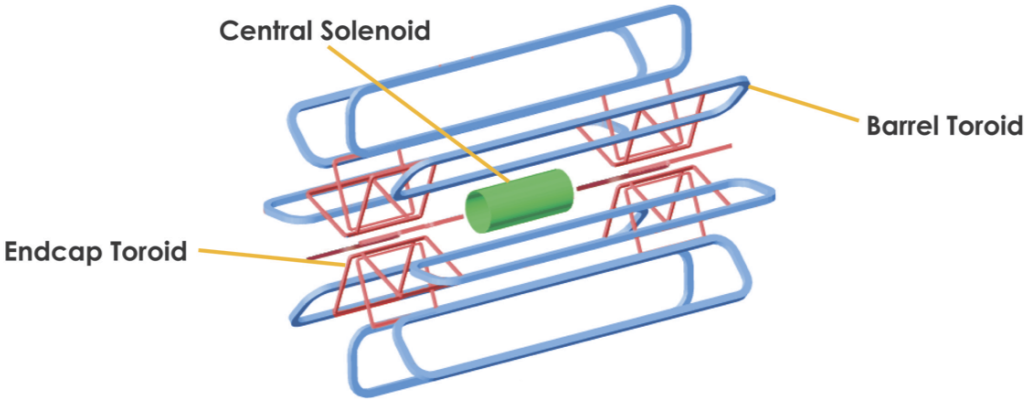

Figure 2.3: A schematic view of the ATLAS magnetic systems [50].

2.2.3 Inner Detector

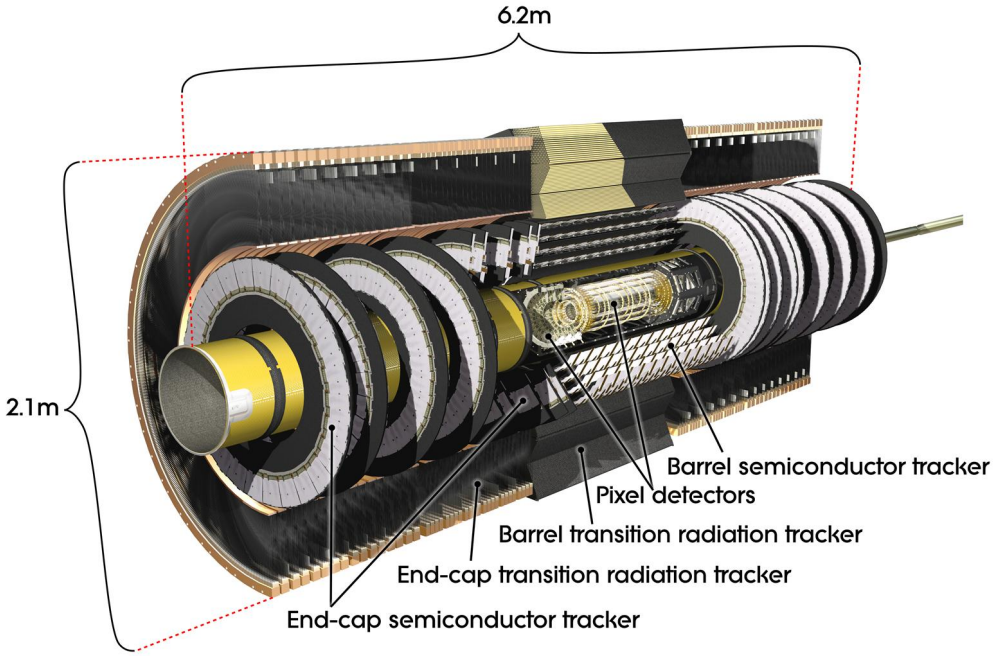

Figure 2.4: An overview of ATLAS Inner Detector [43].

The first layer of the ATLAS Inner Detector is the Inner Tracker, it is the closest one to the IP and the one responsible for the reconstruction of particles in the range $|\eta| \leq 2.5$. The aim of the Inner Detector is to track and discriminate particles produced in the pp collisions at the LHC, thousands every 25

ns. The reconstructed tracks are used to identify and reconstruct interaction vertices. The ID has a cylindrical shape with a diameter of 2.1 m and a length of 7 m, it is completely immersed in the 2 T magnetic field generated by the central solenoid. There are four sub-detectors composing the Inner Detector: the Insertable B-Layer (IBL), the Pixel Detector, the Semi-Conductor Tracker (SCT) and the Transition Radiation Tracker (TRT); all these components are shown in Fig. 2.4. The SCT and the Pixel Detector are the ones giving the most precise and granular readings, they are built with this in mind, being the ones closer to the beams. They are based on silicon technology. The IBL was added to provide precise measurements for secondary vertices reconstruction. Together with the TRT, the most external part of the Inner Detector, these provide very precise tracks and high momentum resolution. The intrinsic resolution of the ID in the central barrel without the IBL is around $\sigma\left(\frac{1}{p_T}\right) p_T = 0.036\% \oplus \frac{1.3\%}{\sqrt{\sin\theta}}$ [49].

Insertable B-layer

The Insertable B-Layer [51] (IBL) was added to the ATLAS detector in the shutdown between Run 1 (2009-2012) and Run 2 (2015-2018). It is the sub-detector which is closest to the beam pipe and consists of a single 3.5 m long cylindrical layer of silicon pixels. Its main task is to provide high-quality track reconstructions, which in turn has an impact on the identification of b-jets, as shown in Fig. 2.5.

Pixel Detector

The Pixel Detector [53] is composed of silicon pixel tiles and goes from 5 to 15 cm from the interaction point, being the second sub-detector in the Inner Detector. It has a central part composed of three concentric cylindrical layers containing 67 million pixel tiles, while three disks are located at each end-cap which increase the tile count by 13 million. Every layer has 1744 modules that provide about 80 million readout channels. Each pixel is 50×400 μm^2 in the $R - \phi \times z$ plane and 250 μm thick. The pixels cover the region $|\eta| < 2.5$, the full range in ϕ and provide three points for track reconstruction. This sub-detector has a resolution of about 75 μm in the z direction and 12 μm in the $R - \phi$ one.

Semi-Conductor Tracker

The SCT [54] is the third sub-detector in the Inner Tracker, coming after the Pixel Detector. It is composed by a barrel piece consisting of four

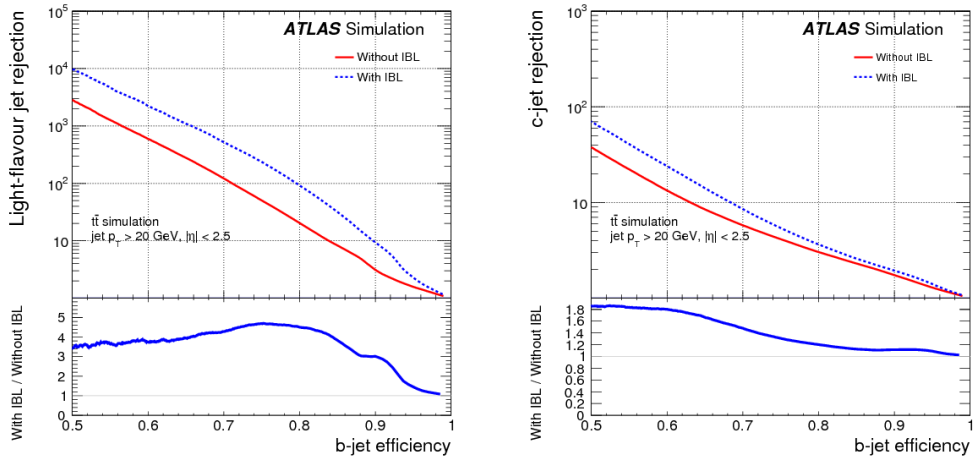

(a) (b)

Figure 2.5: c-jets (a) and light-jets (b) rejections as a function of the b-tagging efficiency with the IBL (in blue) and without (in red) [52].

detector layers and nine disks at each end-cap. Each piece of the Tracker is built from double-sided silicon strips parallel/perpendicular to the beam in the barrel/discs. The SCT provides measurements of tracks perpendicular to the beam in a larger area than, but as accurate as the Pixel Detector. This detector is also fundamental in both the measurement of the impact parameters and vertexing for heavy-flavour and τ-lepton tagging.

Transition Radiation Tracker

The most external sub-detector is the TRT [55]. This detector gives significant information when identifying particles thanks to the detection of the transition radiation generated from X-ray photons. It combines a Transition Radiation detector with a drift tube tracker, consisting of kapton+carbon drift tubes of 4 mm in diameter and gold-plated tungsten wires with a diameter of 31 μm. The tube is filled with a gaseous mixture composed by 70% Xe, 27% CO_2 and 3% O_2. When ionizing particles cross the TRT, it produces a low energy signal which is revealed by the wires. If, instead, the particle is a high-energy one, transition radiation in the X-ray spectrum is produced, which is then absorbed by the gaseous mixture. This kind of signal is generally higher than the one from ionizing particles, therefore giving a way to distinguish between the two. The TRT encloses the region with $|\eta| < 2$ and has a resolution of 130 μm in the R-ϕ direction when measuring tracks.

2.2.4 Calorimeters

Calorimeters aim to measure the energy of produced particles, in particular these part of the detector covers the region $|\eta| < 4.9$. Typically this is done thanks to the shower of secondary particles released in the calorimeters. Two sets of calorimeters can be found in the ATLAS detector: an ElectroMagnetic Calorimeter (EMC) and an Hadronic Calorimeter (HC), shown in Fig. 2.6. The Electromagnetic Calorimeter detects showers typically composed of photons, electrons and positrons, and is usually completely absorbed by the calorimeter. The Hadronic Calorimeter reveals different types of particles, with different decays and also particles that can escape detection, like neutrinos and muons. To measure the energy of these particles, the calorimeters need to absorb them, so they have a layered structure in which layers of active material alternate with absorbing material. The absorbing layers are made of a high-density material which passively slows particles down and favours the production of electromagnetic showers, while the active layers are capable of producing an electrical signal when a particle interacts with them, in order to measure the energy of that particle. Fully containing the showers and measuring their energy is essential in the reconstruction of missing transverse energy E_T^{miss}. In an ideal world, only muons and neutrinos would escape detection in this layer, arriving in the most external layer of the ATLAS detector, the Muon Spectrometer.

Electromagnetic Calorimeter

EMCs are situated around the ID and the solenoid magnet and are composed of lead and Liquid Argon (LAr), maintained at a temperature of 88 K. These are built with an accordion geometry that gives a full ϕ coverage. The lead layers are used as passive material, increasing the probability of interaction, while the Argon is the active medium.
Two main parts compose the LAr calorimeter, the ElectroMagnetic Barrel (EMB) and the two ElectroMagnetic end-caps (EMEC), which cover the regions $|\eta| < 1.475$ and $1.375 < |\eta| < 3.2$ respectively.
Each end-cap has an outer wheel and an internal wheel, covering the regions $1.375 < |\eta| < 2.5$ and $2.5 < |\eta| < 3.2$ respectively.
The transition region between the barrel and the end-caps, covering the pseudorapidity region $1.37 < |\eta| < 1.52$, is called the *crack region*. This name comes from the fact that it is expected to perform more poorly because of the increased quantity of active passive material in front of the calorimeters. The EMC was designed to achieve an energy resolution of $\frac{\sigma_E}{E} = \frac{10\%}{\sqrt{E}} \oplus \frac{150\ \text{MeV}}{E} \oplus 0.7\%$ [56].

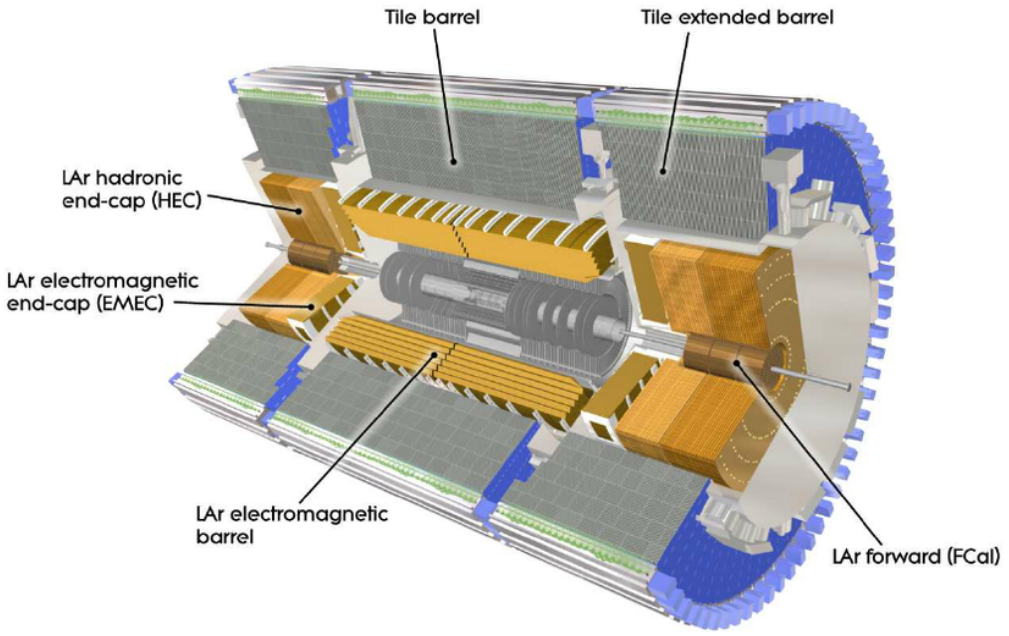

Figure 2.6: Cut-away view of the ATLAS calorimeters [43].

Hadronic Calorimeter

The goal of Hadronic Calorimeters is to absorb particles that manage to escape the EMCs. In particular, as shown in Fig. 2.7, hadrons are the one absorbed here, while muons are revealed by the most external layer in the detector. ATLAS has a Hadronic Calorimeter system composed of three different calorimeters: the Tile Calorimeter, the LAr Hadronic End-Cap Calorimeter (HEC) and the LAr Forward Calorimeter (FCAL).
The Tile Calorimeter measures particle energy in the region $|\eta| < 1.7$, outside the LAr EM calorimeter. The active material here is plastic polystyrene in the form of tiles, while the absorbing material is steel. It consists of a central barrel, 5.8 m long and the extended barrels of 2.6 m. The region between the barrel and the extended barrels is built with modules that allow partial recovery of the missing energy due to the crack regions.
The LAr Hadronic Calorimeter covers the region immediately after the Tile Calorimeter, $1.5 < |\eta| < 3.2$, and is very similar to the EMCs since it is a liquid Argon calorimeter. In fact, it shares the cryostat with both the EMEC and the FCAL. It is composed of two wheels for each end-cap cryostat, in particular a front wheel (HEC1), closest to the IP and composed of 25 mm parallel copper plates and a rear wheel (HEC2), made of 50 mm parallel copper plates.

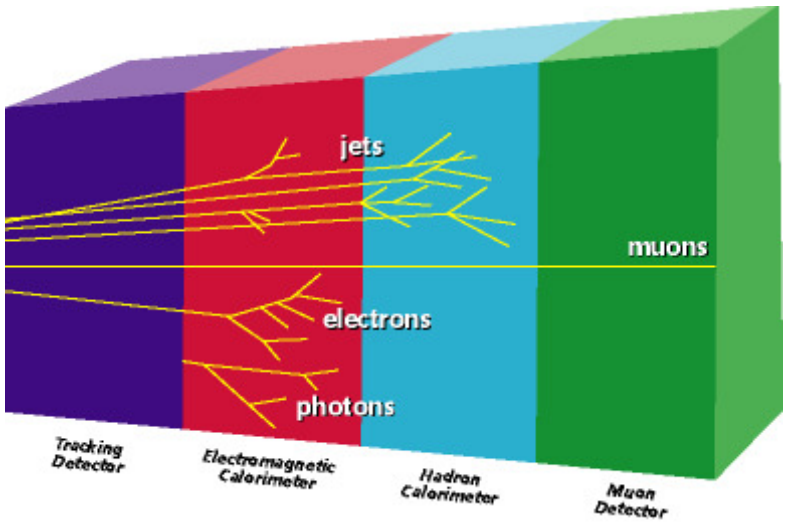

Figure 2.7: A scheme of how the particles interact with the ATLAS detector: the straight lines are the track that get reconstructed, while the branches at the end of some lines indicate where the particles decay and get absorbed.

The resolution of the hadronic calorimeter is $\frac{\sigma_E}{E} = \frac{50\%}{\sqrt{E}} \oplus 3\%$ [56].

Forward Calorimeter

The Forward Calorimeter (FCAL) works as both an electromagnetic and hadronic calorimeter. It is divided in three sections in each endcap: a copper section used for electromagnetic measurements and two sections in which tungsten is used as passive material, used to measure the energy of hadronic showers. It covers the region $3.1 < |\eta| < 4.9$, which is really close to the beam pipe. The FCAL is exposed to high particle flux and is therefore built with an electrode structure of small diameter rods, centered in tubes parallel to the beam axis.
The target resolution for the FCAL is $\frac{\sigma_E}{E} = \frac{0.285}{\sqrt{E/\text{GeV}}} \oplus 0.035$ [57].

2.2.5 Muon Spectrometer

Since muons have a very low interaction rate, they go through both the ID and the calorimeters without losing much of their energy, so a different detector is needed to reveal them: the Muon Spectrometer (MS) fulfils this need. It is the biggest and most external detector in ATLAS and its goals are identificating muons, measuring momentum, and triggering of particles not fully absorbed by the calorimeters, like the ones produced in hadron showers. The magnetic field produced by the barrel solenoid and the end-cap toroidal

magnets is used to reveal muons in the regions $|\eta| < 1.4$ and $1.6 < |\eta| < 2.7$ respectively. These magnetic fields are designed to be orthogonal to the muon trajectories.
There are four systems in the Muon Spectrometer: the Monitored Drift Tube, the Cathode Strip Chambers, the Resistive plate chamber and the Thin Gap Chambers.
The MS's overall resolution is $\frac{\sigma_{p_T}}{p_T} = 4\%$ at 5 GeV and $\frac{\sigma_{p_T}}{p_T} = 1\%$ at 1 TeV [58].

Monitored Drift Tube

The Monitored Drift Tube (MDT) chambers are used to precisely measure momentum in the regions $|\eta| < 1.1$ (barrel) and $1.1 < |\eta| < 2.7$ (end-caps). They are built with aluminium tubes with a 3 cm diameter, filled with a pressurized mixture of 93% Ar and 7% CO_2. At the center of these tubes, a 50 μm tungsten-rhenium acts as an anode that collects the electrons generated by the muons passing inside the gas. Momentum measurements are obtained by precisely measuring the drift time (and consequently the drift distance). Each MDT chamber consists of two multilayers of tubes, three in the barrel and four in the end-caps, for a total of 1150 modules.
The MTD has a 80 μm spatial resolution per tube layer, while the typical drift time is about 700 ns. Because of the magnitude of the drift time, the MDT is not suitable for triggering, but a great precision is achieved in momentum measurements obtained using this detector.

Cathode Strip Chambers

The Cathode Strip Chambers (CSCs) cover the region $2.0 < |\eta| < 2.7$ and provide more precise track measurements when compared to the MDT. The CSC system is composed of two disks, each containing eight chambers, which in turn contain four CSC planes. CSCs are multi-wired proportional chambers where the wires are positioned in the radial direction with respect to the beam axis. These are composed of arrays of positively charged wires, crossed with negatively charged strips, acting as anodes and cathodes respectively, immersed in a gas mixture (30% Ar, 50% CO_2, 20% CF_4).
The track position is obtained interpolating the electron avalanche originated by the passing muons when they ionize the gas mixture. The CSCs have a spatial resolution of 60 μm.

Resistive Plate Chambers

The Resistive Plate Chambers (RPCs) provide the trigger for muons in the barrel region. These are gaseous detectors (94.7% $C_2H_2F_4$, 5% Iso-C_4H_{10}, 0.3% SF_6) that consist of two parallel plates, one positively charged and one negatively charged, which act as anodes and cathodes respectively. The plates are made of resistive bakelite and distanced by polycarbonate spacers at 2 mm. When a particle passes through the gas, the mixture is ionized, which in turn causes an electron avalanche since the detector is immersed in a 4.9 kV/mm electric field. These electrons are then collected by external metallic strips.
RPC trigger chambers consist of two rectangular detector layers, each of which has two orthogonal series of strips to collect electrons: strips parallel to the MTD wires are used for η measurements, while the ones which are orthogonal to the MTD strips provide ϕ measurements.
The spatial resolution of the RPCs is of ~ 1 cm, while their time resolution is 1 ns.

Thin Gap Chambers

The Thin Gap Chambers (TGCs) are situated in the end-cap regions and are used to obtain trigger information and ϕ measurements. There are four chambers in each end-cap, providing measures in the $1 < |\eta| < 2.7$ region. Each of these chambers consists of two grounded planes which act as cathodes inside which a positively charged plane of closely spaced wires is located. The wires are distanced by 1.8 mm, while the distance between the anode and the cathodes is 1.4 mm. The gas in which the plates are immersed is a highly quenching mixture (55% CO_2 and 45% n-C_5H_12). The TGCs have a spacial resolution of ~ 5 mm and a time resolution of 4 ns.

2.2.6 Forward Detectors

Apart from the main detectors just described, ATLAS has some special-purpose detectors in the forward region:

- LUminosity measurement using Cherenkov Integrating Detector (LUCID) [59] is a Cherenkov detector that covers the region $5.6 < |\eta| < 6$. This is placed at 17 m from the interaction point. Since LUCID consists of aluminium tubes filled with C_4F_{10} that emit Cherenkov radiation when they are crossed by particles, it is used to monitor the luminosity of ATLAS. An estimate of the instantaneous luminosity is obtained from the average number of interactions per bunch crossing, which in

turn is measured when the Cherenkov photons are collected by the photomultipliers at the end of each tube.

- Beam Conditions Monitor (BCM) [60] is used to check the beam conditions and potential detector damage caused by anomalies. It is composed of two stations placed symmetrically around the beam at $\eta = \pm 4.2$.
- Zero Degree Calorimeter (ZDC) [61] detects forward ($|\eta| > 8.3$) neutrinos which are used to determine the centrality of heavy-ion collisions. It is placed at a distance of 140 m from the interaction point.
- Absolute Luminosity For ATLAS (ALFA) [62] measures the absolute luminosity using measurements of elastic scattering at small angles. It is located at a distance of 240 m from the IP.

2.2.7 Trigger and Data Acquisition System

In ATLAS protons collide with a frequency of 40 MHz, which corresponds to roughly 60 TB/s of raw data acquired. For an amount of data this big, the LHC storage system is not enough. Moreover, the processes studied at the LHC hav lower cross-sections when compared to other processes that could happen in pp collisions, as Fig. 2.8 shows. Therefore a triggering mechanism has been put in place to filter the raw data and lower the amount of data that is ultimately saved.

Triggers

The ATLAS trigger system is composed of two levels, one hardware-based trigger called L1 and a software-based trigger system called High Level Filter, which are used to reduce the event rate from 40 MHz to 1 kHz. More in detail:

- The L1 layer uses information from the calorimeters and the muon spectrometer, triggering only if an event with high p_T is detected. This operation reduces the event rate to 100 kHz. The L1 is also used to gain information about the Regions of Interest (RoIs) used in the HLF;
- The High Level Filter (HLF) uses algorithms on a computer farm that reduce the event rate to $\sim$ 1 kHz, allowing the data to be stored.

The L2 trigger and the Event Filter (EF) are used together and form the High Level Trigger (HLT), which optimizes the use of resources.

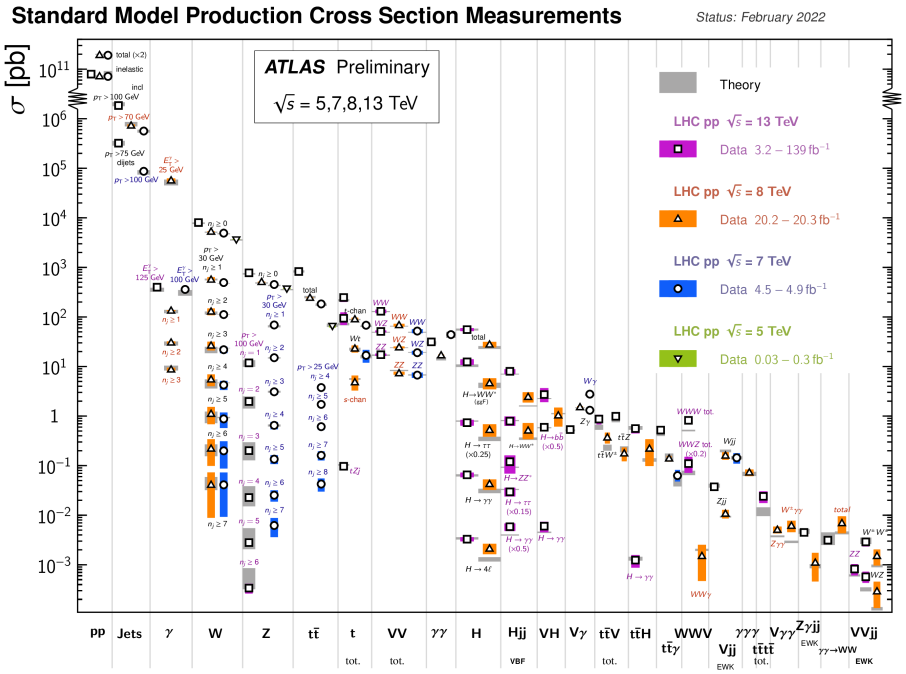

Figure 2.8: Measured cross-sections for different processes at LHC. The most probable is the inelastic scattering of the protons. The most interesting processes have cross-section of about 10 order of magnitude lower [63].

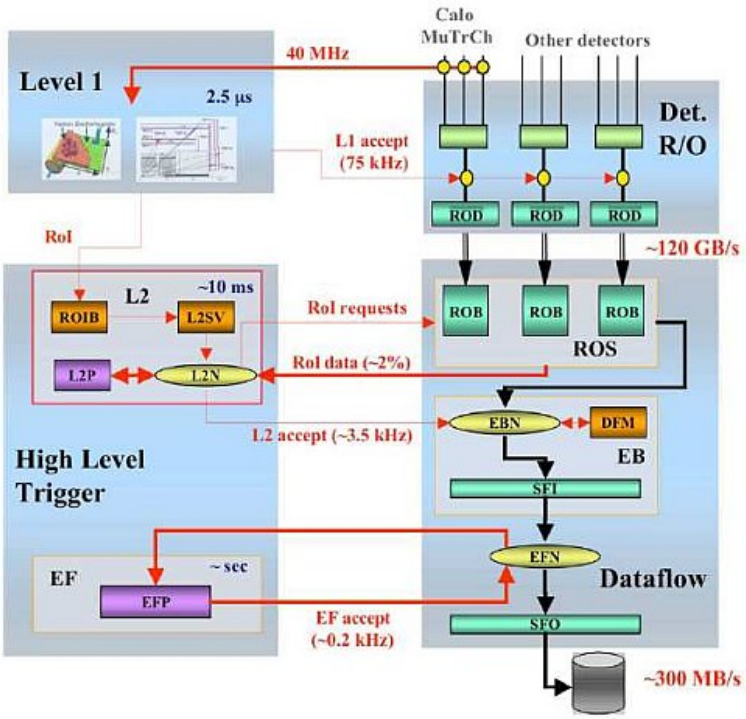

Figure 2.9: Scheme of the data flow from the detector to the storage [64].

Data Acquisition System

When an event passes the L1 trigger, the ReadOut System (ROS) buffers the data for the time needed by the HLF to run. During this period, the HLF will exchange data with the ROS. After an event also passes the EF, the data is stored permanently in the Sub-Farm Output (SFO). Data flow is shown in Fig. 2.9.

Computing Model

The ATLAS Computing Model [65] is what stores, transfers and processes recorded data, while also producing and distributing simulated data and modelling the detector. It is based on the Grid [66] paradigm and built with high decentralization and resource sharing in mind. Decentralization is achieved using a tiered model [67], where CERN is the production center (Tier-0) that distributes data in quasi-real time to 13 Tier-1 centers. These, in turn, provide services for many associated Tier-2 centers.
Both storage and reprocessing are provided by Tier-1 centers, while also allowing for scheduled analysis of the processed data by the analysis groups. Tier-2 facilities are used for analysis and simulation. Tier-3 centers provide

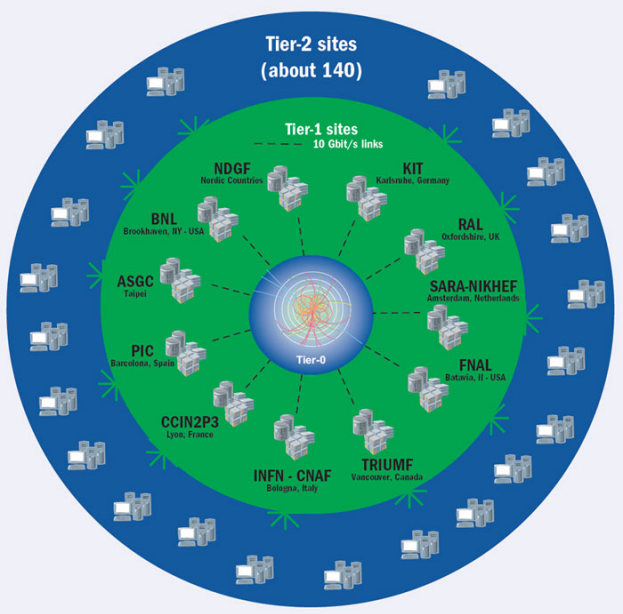

Figure 2.10: Scheme of the ATLAS Tier system [68].

additional computing resources. The structure of the ATLAS computing model is schematically represented in Fig. 2.10 The workflow for data (real and simulated) processing and analysis can be divided in four steps, to allow easier access and storage:

- Raw Data (RAW) are the unprocessed data, directly stored in the Tier-0 center for processing.
- Event Summary Data (ESD) contain detailed output of the detector reconstruction.
- Analysis Object Data (AOD) are designed to reduce the size of the samples for storage and to allow easier physics analyses. These also contain summaries of the reconstruction and are obtained using the `ATHENA` [69] software.
- Derived Analysis Object Data (DAOD) are generated from the xAOD format and share a similar layout, but contain less information to further reduce the file size.

2.2.8 ATLAS performance during Run2

During the 2015-2018 data-taking period, known as Run2, LHC delivered 156 fb^{-1} of pp collisions data at a center of mass energy of $\sqrt{s} = 13$ TeV.

Out of these, only 147 fb^{-1} were recorded by ATLAS to be used for physics analyses, corresponding to a data taking efficiency of $\sim 94\%$, and 140 fb^{-1} were actually used to run physics analyses, as shown in Fig. 2.11.

The difference between delivered and recorded luminosities are due to two

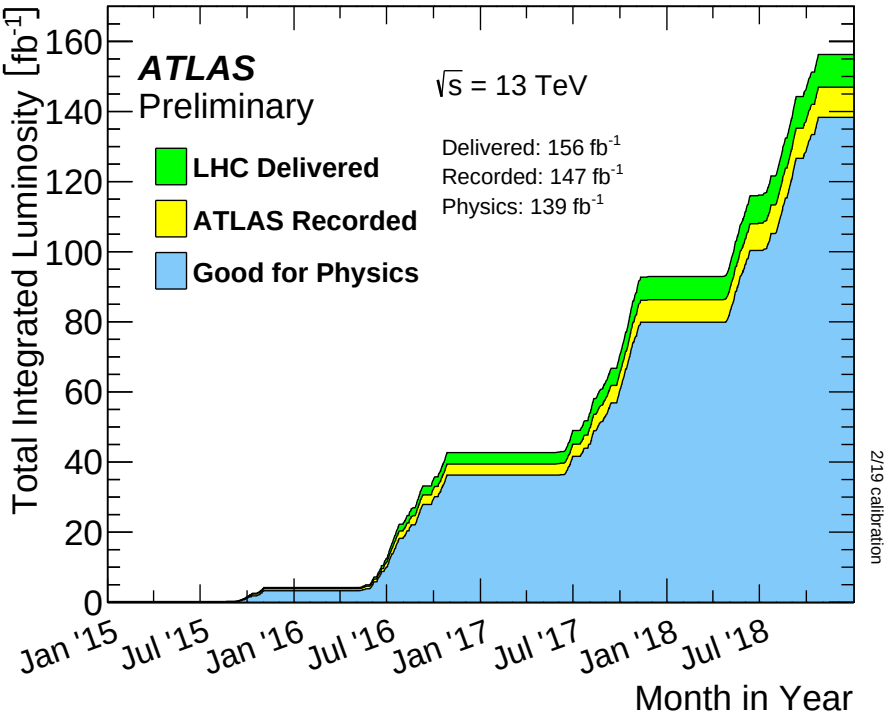

Figure 2.11: Cumulative luminosity delivered to ATLAS (green), recorded by ATLAS (yellow), and certified to be good quality data (blue) during stable beams for *pp* collisions at 13 TeV centre-of-mass energy in 2015-2018 [70].

main factors which have to be considered: the Data Acquisition System has a less-than-one efficiency and ATLAS needs time to reach the operative voltage, due to the so-called *warm start*.

Pileup Effect

When proton bunches collide multiple *pp* interactions take place and trying to reconstruct all these collisions as a single event causes the so-called pileup effect.

The main source of pileup are:

- In-time pileup: additional *pp* collisions occur in the same bunch-crossing as the collision of interest. This is due to the high delivered luminosity, meaning that the higher the luminosity, the higher the pileup.

- Out-of-time pileup: the probability of multiple pp collisions depends on the spacing between two subsequent bunches. In particular, if the bunch spacing is shorter than the detectors' response time, the measurements for one bunch crossing are affected by the second.

The mean number of interactions per bunch crossing, calculated from the instantaneous per-bunch luminosity, is

$$\langle \mu \rangle = \frac{L_{\text{inst}} \cdot \sigma_{\text{inel}}}{n_b \cdot f_r} \tag{2.7}$$

where L_{inst} is the instantaneous luminosity over a large time, typically larger than 600 ns, σ_{inel} is the total cross-section for inelastic scattering (80 mb for 13 TeV collisions), n_b is the number of proton bunches and f_r is the frequency of the circulating beam at LHC, corresponding to 11 kHz. This number is used to estimate the pileup. The distribution of the mean number of interactions per bunch crossing (weighted by the luminosity) for the full Run2 is shown in Fig. 2.12.

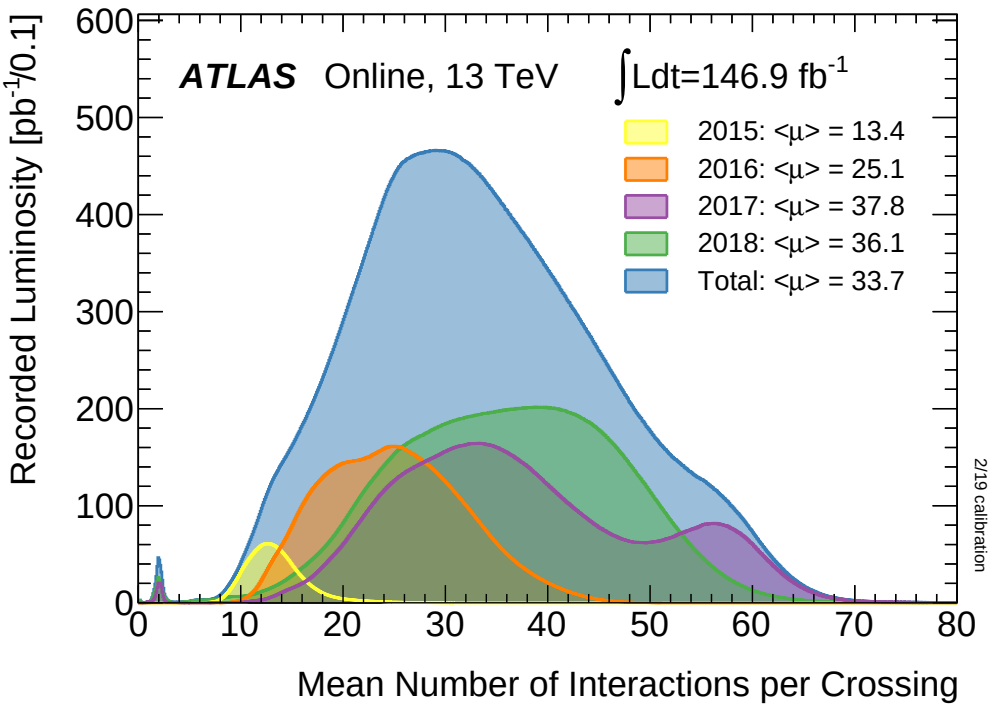

Figure 2.12: Luminosity-weighted distribution of the mean number of interactions per crossing for the Run2 (2015-2018) pp collision data at $\sqrt{s} = 13$ TeV. The mean number of interactions per crossing corresponds to the mean of the poisson distribution of the number of interactions per crossing calculated for each bunch [70].

Chapter 3

Monte Carlo Simulations and Data Samples

3.1 Data Sample

To conduct the analysis described in this thesis, data from the so-called Run 2 have been used. In particular these data were collected by the ATLAS collaboration between 2015 and 2018, at a center-of-mass energy of 13 TeV and an integrated luminosity of 140 fb^{-1}. All the collected data is divided in so-called luminosity blocks, spanning about 2 minutes of data-taking; the portions of these data that may be affected by detector problems are excluded from the Good Run List (GRL). The data are further partitioned based on trigger configurations and beam settings.

3.2 Monte Carlo Simulations

Monte Carlo (MC) simulations are an indispensable tool when conducing an high-energy analysis. In particular, they are used to estimate the detector's efficiency and acceptance and evaluate the signal and the background processes that can give the same final state as the signal.

MC simulations use theoretical predictions together with phenomenological models to model the interactions that take place in the LHC. The short distance interactions are well described by perturbative QCD, but when hadronization and other large distance phenomena have to be taken into account, only phenomenological models can be used.

An MC simulation consists of different steps: simulation of the hard scattering, parton shower, hadronization, decay of the unstable particles and evaluation of the underlying events. These steps will be described in more

detail in the following sections.

3.2.1 Hard Scattering and Matrix Element generators

The first step in the generation of MC events is evaluating the Matrix Element (ME) for the considered process, which is then convoluted with the PDFs to evaluate the hard scattering cross-section. The ME is calculated at a fixed order in perturbation theory, in the case of LHC this is the NLO in α_s and the considered process is the interaction of two partons going into n particles. This cross-section can be written as:

$$\sigma = \int_n \sigma^B + \int_n \sigma^R + \int_n \sigma^V \tag{3.1}$$

where σ^B is the Born level diagram, which contains only the diagrams with exactly n particles in the final state, σ^R contains the diagrams describing a final state with n+1 particles, indicating the real contribution, while σ^V describes the virtual contribution. The Born level and real emission cross-sections contribute both at LO and NLO, while the virtual emission piece is only included in the NLO diagrams.

When matrix elements are calculated at higher orders, higher precision is achieved in the description of the considered processes. In the present thesis, the ME generator used a calculation at the NLO level, but recently a new NNLO ME generator has been developed [37] and used for $t\bar{t}$ production processes.

3.2.2 Parton Shower

After the evaluation of the Matrix Element, the Parton Shower (PS) takes place, which is a way to simulate QCD radiation. In this step the involved partons radiate other partons with an energy that spans the range from hard-scattering scales up to hadronization scale; this is due to higher-order QCD effects. The process of partons emitting radiation is known as *splitting* and its description comes from the Altarelli-Parisi splitting functions $P_{ij}(\alpha_s, \mu^2)$ mentioned in Section 1.2.3.

3.2.3 Underlying Events and Additional Processes

After the hard-scattering, the remaining pieces of the interacting hadrons, called remnants, can interact and therefore generate distinct scatters, together with multiple parton interactions; these interactions generate soft processes, collectively known as Underlying Event (UE). The UE can interfere with the

hard processes, and therefore needs to be modeled to obtain a precise estimate of the signal for the considered process. Since the UE cannot be modeled using perturbative QCD, describing it requires the use of phenomenological models in which a data-driven [71] process is used to tune the parameters.

Another factor that has to be accounted for is the pile-up described in Section 2.2.8, caused by secondary interactions or effects such as beam halo, cavern background and overlapping detector responses.

3.2.4 Hadronization

After the simulation of the parton shower and the underlying event, the partons that have been produced are bound together in colorless particles called hadrons, divided in baryons and mesons. This process is called hadronization. Since the partons considered in this step have low energy and are separated by large distances, pQCD cannot be used, therefore requiring the use of non-perturbative methods and models. The most known and successful of such models are the *cluster fragmentation model* [72] and the *Lund string model* [73], for which a schematical representation can be seen in Fig. 3.1(a) and Fig. 3.1(b), respectively:

- Cluster fragmentation model: assuming that color confinement exists, perturbative QCD predicts [74, 75] that in hard processes, confinement of partons is local in colour and independent of the the hard scale Q. This means that there is a "preconfinement" of the partons. After the parton shower stage, all the remaining gluons are split non-perturbatively in colour-singlet couples of quark and anti-quarks, which follow the "preconfinement". The obtained cluster are then decomposed into hadrons; if the cluster is too light to decay into two hadrons, it is considered to be the lightest hadron with its flavour and, through a momentum exchange with the closest cluster, its mass is set to the appropriate value. The other clusters are iteratively decayed into hadrons until only stable clusters remain.

- Lund string model: in this model, quarks and gluons are represented as points moving along a one-dimensional string-like object, which is called *flux tube*. The interactions between quarks and gluons are described by the dynamics of this tube, which can stretch, bend, and break as the quarks and gluons move; when the tube breaks, a new $q\bar{q}$ couple is formed. The model also includes a "string tension", which represents the strong force that holds quarks together inside hadrons. This is again an iterative procedure which stops when the strings are too light to create new $q\bar{q}$ pairs.

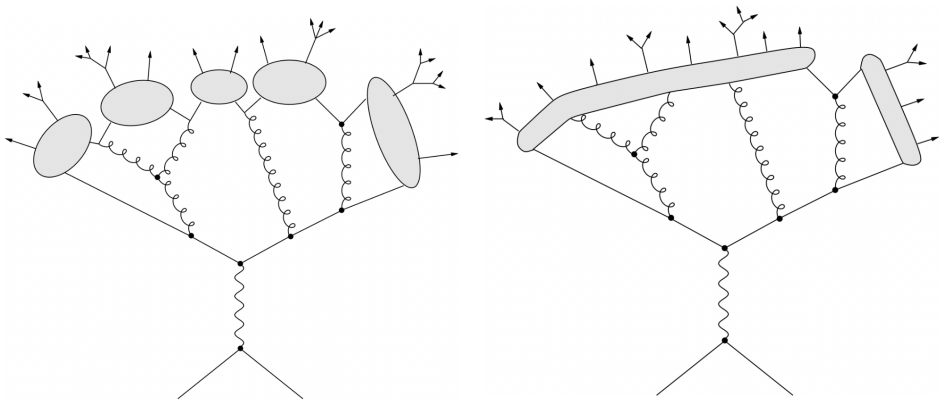

(a) (b)

Figure 3.1: Representation of the cluster model (a) and the string model (b) used to describe the hadronization process.

3.2.5 Detector Simulation

After the hadronization step, the interactions of the final state particles with the ATLAS detector have to be simulated. This is performed using the `Geant4` [76] toolkit, which provides an accurate way to model the ATLAS detector, taking into account the materials with which the detector is built and the geometry of the sub-detectors.

The `Geant4` toolkit requires a considerable amount of time to run, therefore the samples can be both produced with the full detector simulation (ATLASFullSim) or using what is known as ATLASFastII (AFII), in which the calorimeters showers are generated using a parametrization.

Multiplicative scale factors (SF) are applied to the MC generated events in order to obtain a more precise description of the reconstructed quantities. These are defined as:

$$\mathrm{SF} = \frac{\epsilon_{\mathrm{data}}}{\epsilon_{\mathrm{MC}}} \tag{3.2}$$

where ϵ_{data} is the efficiency in reconstruction and identification of physics objects measured in data, while ϵ_{MC} is the same quantity, evaluated for the simulated events. The per-event correction procedure in which the SF are applied is known as calibration.

3.2.6 Production Campaign

The production of Monte Carlo samples is divided into so-called campaigns, in which LHC and ATLAS configurations during a data-taking run such as geometry and center-of-mass energy are used. Usually different campaigns

cover different years, but the difference can also be in trigger, pile-up simulation and reconstruction software. In this analysis, the MC16a, MC16d and MC16e campaigns have been used, corresponding respectively to the data-taking periods 2015-2016, 2017 and 2018.

3.3 Monte Carlo Generators

Different Monte Carlo generators are aimed at different part of the generation, in particular they are used to calculate either the hard subprocess or the parton shower and hadronization, as described in the following paragraphs.

Hard Subprocess Generators

- PowhegBox [77] uses POWHEG (Positive Weight Hardest Emission Generator) [39, 41] to generate the hard subprocess through an NLO calculation. A large number of physics processes are supported. To obtain a complete event simulation, a procedure called matching has to be implemented between the hard process and the parton shower. This is to avoid possible double counting when going from one step of the generation to the other. Two of the most important parameters that can be changed (the best values are found through a procedure known as MC tuning) are h_{damp} which governs the p_T of the first additional emission and p_T^{hard}, which regulates the definition of the vetoed region of the showering, which is important to avoid hole/overlap in the phase space filled by PowhegBox and Pythia 8.

- MadGraph5_aMC@NLO [78] is capable of automatically calculate the matrix element up to NLO. This also need a matching procedure with a parton shower generator, this follows the MC@NLO method [41]

Multi-purpose Generators

- Pythia 8 [79] can simulate the hard scattering at LO for a multitude of physics processes. It can be interfaced with a hard-scattering generator to simulate parton shower, hadronization and decay of the emitted particles. PYTHIA uses a PS model based on the Lund string model, in which the emissions are ordered by their p_T.

- Herwig [80] too can provide PS and hadronization model when interfaced with a hard process generator. The parton shower model used

follows the cluster model and orders the emissions by their opening angle.

Multi-purpose Generators includin NLO Matrix Element

- SHERPA [81] (Simulation of High-Energy Reactions of PArticles) can provide calculations up to NLO for the hard process and perform the PS and hadronization steps. The hadronization model used is the cluster model.

3.3.1 MC samples used in the analysis

In the following section the MC samples used in the analysis will be described. MC samples were used both to study the signal and to generate background events. Only the so-called fakes background is determined in a different way, using a data-driven approach, described in later chapters.

The corrections due to pile-up were estimated using a variable number of simulated inelastic pp collisions, generated using PYTHIA 8 (v8.186) with the ATLAS set of tuned parameters for minimum-bias events (A3 tune) [82] and the NNPDF2.3 LO PDF set [83]; these samples were overlayed with the nominal one and then reweighed as to match the average number of pp collisions per bunch crossing observed in the data.
All the samples used in this analysis and their tunings have been summarized in Table 3.1.

Process	Generator + fragmentation/hadronization	Tune	PDF set	Cross-section normalisation
Nominal samples				
$t\bar{t}$	POWHEGBOX v2 + PYTHIA 8.230	A14	NNPDF3.0NLO	NNLO+NNLL
single-top	POWHEGBOX v2 + PYTHIA 8.230	A14	NNPDF3.0NLO	NLO+NNLL
V+jets	SHERPA 2.2.1	SHERPA	NNPDF3.0NNLO	NNLO
Dibosons	SHERPA 2.2.2	SHERPA	NNPDF3.0NNLO	NLO
$t\bar{t}+V$	MADGRAPH5_aMC@NLO + PYTHIA 8.230	A14	NNPDF2.3LO	NLO
$t\bar{t}+H$	MADGRAPH5_aMC@NLO + PYTHIA 8.230	A14	NNPDF2.3LO	NLO
Alternative samples				
$t\bar{t}$	POWHEGBOX v2 + HERWIG 7.7.1.3	H7.1-Default	NNPDF3.0NLO	NNLO+NNLL
$t\bar{t}$	MADGRAPH5_aMC@NLO v2.3.3.1 + PYTHIA 8.230	A14	NNPDF3.0NLO	NNLO+NNLL
$t\bar{t}$	POWHEGBOX v2 + PYTHIA 8.230	A14+pthard=1	NNPDF3.0NLO	NNLO+NNLL
$t\bar{t}$	POWHEGBOX v2 + PYTHIA 8 MiNNLOPS	A14	NNPDF3.0NLO	NNLO+NNLL

Table 3.1: Summary of the nominal and alternative simulated event samples used for this analysis.

Nominal $t\bar{t}$ sample

The PowhegBox v2 generator with the `NNPDF3.0NLO` [84] PDF set was used to simulate the NLO ME for the $t\bar{t}$ signal, which was used as the nominal sample. Parton shower, hadronization and underlying events were generated using Pythia 8 (v8.230) [85] with the `NNPDF2.3LO` [86] PDF sets and the A14 tune [87]. Events in which both the top quark and the anti-top decay hadronically were excluded.

The mass of the top-quark was set to 172.5 GeV, while its decay width to 1.32 GeV [39]. The h_{damp} parameter, which controls the p_T of the first emitted quark or gluon when going beyond the Born level diagrams, is set to $1.5m_t$ [88].

Using a $k-$factor, the sample was normalized to NNLO+NNLL in pQCD. In particular, the cross-section used to evaluate the $k-$factor is $\sigma_{t\bar{t}} = 832^{+20}_{-30}$ (scale) ± 35 (PDF, α_s) ± 23 (m_t) pb, and was calculated using the `Top++2.0` program at NNLO in pQCD, including resummation at NNLL [29, 89–94] with a top-quark mass of $m_t = 172.5$ GeV.

Alternative $t\bar{t}$ signal samples

To estimate the impact of the tuning of the MC parameters, as well as PDF choice, underlying events, hadronization and parton shower, together with the variations in the amount of additional radiation, additional MC $t\bar{t}$ samples have been generated. All these alternative samples have been normalized to the same k-factor as the nominal one.

These are:

- Events generated using the same PowhegBox v2 setup, but interfaced with Herwig 7.7.1.3 [80, 95], which includes an angle-ordered parton shower model. In this sample the H7.1-Default tune [96] was used together with the `MMHT2014LO` PDF set [97].
- Events generated with the nominal settings, but the `pthard` parameter set to 1, instead of 0.
- Events generated with the nominal settings, but the h_{damp} parameter set to $3m_t$.
- Events generated with the nominal settings, but with $m_t = 169$ GeV and $m_t = 176$ GeV.
- Events generated using the MiNNLOPS event generator with the setup described in [37, 38].

Background samples

Since some physics processes share a similar final state with $t\bar{t}$ production and due to the possibility of misreconstruction of some objects, which could satisfy the selection criteria, it is important to estimate background processes, in order to remove events that are not part of the signal.

The best MC-estimated backgrounds are single top quark production, the production of a vector boson together with a jet, the diboson final state and the production of a $t\bar{t}$ pair with an associated Higgs boson or vector boson.

A more detailed description of these backgrounds follows:

- Single Top: single top-quarks in the t-channel, s-channel or together with a W boson were modelled using PowhegBox (NLO in pQCD). The parton shower and hadronization steps were modelled using Pythia 8 8.230 using the A14 tune and the `NNPDF2.3LO` PDF set. The diagram-removal (DR) [98] scheme was used in the tW samples to account for the interference with $t\bar{t}$ production [88]. The cross-section in the tW channel was normalized to its NLO+NNLL predictions, while t- and s-channel predictions were normalized to the corresponding NLO prediction[99–103].

- V+jets: Events in which W and Z bosons were produced together with jets were simulated using Sherpa 2.2.1 [81], using NLO matrix elements for events containing up to two jets, while LO MEs for the ones containing up to four jets were calculated using the Comix [104] and OpenLoops [105] libraries. The aforementioned libraries were interfaced with the Sherpa parton-shower [106] model using the MEPS@NLO prescription [107]. The tune developed by the Sherpa authors with the `NNPDF3.0NNLO` PDF set were used. These samples were normalized to their NNLO cross-sections [108, 109].

- Diboson: Sherpa 2.2.2 was used to model diboson samples in which one of the bosons decayed hadronically and the other in the leptonic channel. The matrix elements were computed at NLO in pQCD for up to one additional parton and at LO for up to three extra partons. The PDF set used was `NNPDF3.0NNLO`. The cross-section evaluated by the generator was used to normalize these samples.

- $t\bar{t}V$: The samples for the production of a $t\bar{t}$ pair associated with a W or Z boson were modelled at NLO using the MadGraph5_aMC@NLO 2.3.3 generator and the `NNPDF3.0NNLO` PDF set. The parton shower step was modelled using Pythia 8 8.230 with the A14 tune and the

NNPDF2.3LO PDFs. The cross-section calculated by the generator was used for the normalization of these samples.

- $t\bar{t}H$: PowhegBox v2 was used to simulate the samples in which a $t\bar{t}$ pair is produced together with a H boson. The NNPDF3.0ME PDF set was used. The parton shower step was modelled using Pythia 8 8.230 with the A14 tune and the NNPDF2.3LO PDFs. The cross-section calculated by the generator was used for the normalization of these samples.

To evaluate systematic uncertainties, alternative samples were generated for some of the backgrounds:

- Single Top: An alternative sample was generated using the diagram subtraction method [110] (DS) instead of the diagram-removal one.
- Diboson: Samples with $4\ell, 3\ell\nu, \ell\ell\nu\nu$ and $\ell 3\nu$ were also produced.
- $t\bar{t}V$: Samples with $tZ, t\bar{t}t\bar{t}, t\bar{t}WW$ and tWZ were also produced.

Chapter 4

Object Definition

To distinguish the final state of the considered process from all the similar ones it is paramount to identify the physics objects characterizing the interaction of the particles with the ATLAS detector.

In this analysis, the final state consists of both heavy- and light-flavour jets, leptons and neutrinos coming from hadronization and decay of the particles produced in a $t\bar{t}$ event, respectively. These objects are represented schematically in Fig. 4.1.

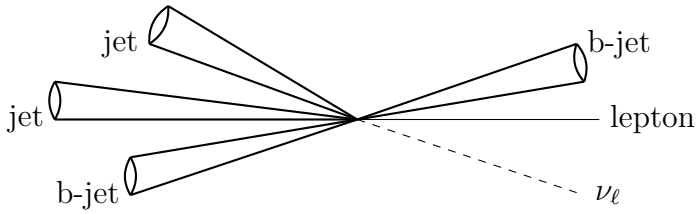

Figure 4.1: Sketch of the objects produced in a $t\bar{t}$ event in the ℓ+jets channel.

4.1 Tracks and Primary Vertices

When particles pass through the Inner Tracker (IT), they interact with the detector giving information on where exactly they have passed, the reconstructed paths are called tracks. These objects are used by the tracking reconstruction algorithm [111, 112] to reconstruct the particles' trajectories.

The trajectory of a charged particle in the magnetic field of the ATLAS detector can be parametrized using five observables: (d_0, z_0, ϕ, θ, $q/|\vec{p}|$), where d_0 and z_0 are the longitudinal and transverse impact parameters, ϕ and θ are the azimuthal and polar angles respectively, while $q/|\vec{p}|$ is the ratio

of the particle's charge and the absolute value of its momentum. A pattern recognition algorithm is applied to the hits in the IT. Clusters of hits are created using timing information and deposits in both the Pixel Detector and the SCT. An algorithm called *inside-out* [111] is then used on the IT hits which finds the tracks and extend them to the TRT. A similar approach, called *outside-in* procedure, is then used to perform back-tracking, which takes into account all the remaining hits, starting from the TRT and going towards the Pixel Detector.

Tracks compatible with the interaction region, are used in the reconstruction of the Primary Vertex (PV), through a so-called *vertex finder* [113, 114]. In this algorithm the only tracks taken into account are the ones with an associated $p_T > 400$ MeV, in order to improve the resolution. To be chosen as a PV, the candidate vertex has to have at least two associated tracks and the highest $\sum p_T^2$. Remaining vertices are considered pile-up, while the vertices not associated with the beam-collision region are considered Secondary Vertices.

4.2 Electrons

In ATLAS, electrons are reconstructed tracks with deposits in the EM calorimeter in the region with $|\eta| < 2.47$ but neglecting the transition region between the end-cap and the barrel EM calorimeter ($1.37 \leq |\eta| \leq 1.52$). The reconstruction process can be divided in three main steps:

- Identification and clustering, which produces electrons *superclusters* [115] and it is performed in two steps: the first step is testing EM topo-clusters as candidates for seed cluster, which are the base of the superclusters; in the second step the topo-cluster near the seed candidates are identified as satellite clusters candidates, which can be due to bremsstrahlung radiation or topo-cluster splitting. After the satellite candidates have been identified they are added to the seed clusters to form superclusters if they pass the selection criteria.

- Matching of the tracks, in which the clusters are matched to the previously reconstructed tracks in the ID. The last reconstructed point in the ID and the clusters in the EM are used to extrapolate the tracks, while the angular coordinates of the deposits in the electromagnetic calorimeter are compared to the extrapolated η and ϕ. If the distance between the impact point of the track and the barycenter of the cluster satisfies the requirement $|\eta| < 0.05$, the track si considered matched. If no matching happens the cluster is considered to have come from a

converted or unconverted photon, whether it comes from the primary or the secondary vertices. Additional requirements are used to further improve the matching, in particular for track parameters it is required that $|d_0|/\sigma_{d_0} < 5$ and $|z_0 \sin\theta| < 0.5$. To take into account the possibility of bremsstrahlung loss effects, clusters are extended in the ϕ direction.

- Reconstruction of the electrons. In particular, identifying the so-called *prompt* electrons, the ones coming from the hard scattering interaction, is paramount in order to reduce background contamination. To separate between real and fake electrons, an identification algorithm [116] is used. This is based on a likelihood (LH) method in which a multivariate analysis is run using information on the candidate electrons (track quality, information on calorimeters and TRT, track-cluster matching) as input and combining them into a discriminant. Following this approach, three sets of cuts have been chosen to identify *loose*, *medium* and *tight* electrons, going from lower to higher background-rejection power, and therefore higher to lower identification efficiency. In this analysis, a *tightLH* operating point has been used.

  A further requirement on isolation, based on both calorimeter and tracking, is used to reduce background contamination coming from jets misidentified as prompt leptons or semileptonic decays of heavy-flavour hadrons [117]. These requirement use two variables: E_T^{cone}, which is the sum of the transverse energy of the clusters in the electromagnetic calorimeter within a radius of $\Delta R = 0.2$ from the electron candidate, which is required to be $E_T^{\text{cone}} < 0.06$; the second variable is related to track isolation, p_T^{varcone}, defined as the sum of transverse momenta of all the tracks within a cone of $\Delta R = \min(0.2, 10)$ GeV $/E_T$ from the track of the electron candidate coming from the PV, with a requirement of $p_T^{\text{varcone}}/p_T < 0.06$. These criteria are collectively referred to as *FCtight*. Electron reconstruction efficiency depends on the transverse energy of the electrons, varying from 97% at $E_T = 15$ GeV to 99% at $E_T > 50$ GeV. For this analysis, the isolation efficiency varies from 90% to 99% when $p_T > 25$ GeV and $p_T > 60$ GeV respectively. A per-event scale factor is used to account for differences between MC-estimated isolation efficiencies and data-measured ones.

4.3 Muons

Muons are reconstructed in a similar way to what is done with electrons, using information coming from the ID and the Muon Spectrometer. First the tracks are reconstructed separately in the ID and in the Muon Spectrometer. The reconstruction of tracks in the inner detector follow the same steps as the electron ones. In the Muon Spectrometer, tracks that may form a pattern are matched in every muon chamber. A Hough transformation [118] is used to search for hits aligned to a trajectory in the bending plane of the detectors in the MDTs. Hits in the RPC and TGC are used to measure the coordinate orthogonal to the bending plane. Segments of tracks in the planes identified by the polar coordinates η and ϕ are reconstructed using hits in the CSC. As a final step, all the hits are fitted together to form the muon candidates. Tracks are built requiring at least two matching segments, except for the transition region between the barrel and the end-cap in which a single, high-quality, segment can be used together with η and ϕ information. To maintain the efficiency high also for close muons, the tracks are chosen using the following prescription: if they have segments in three different layers of the muon spectrometer, they are kept if identical in two out of the three layers only if they don't share any hits in the outermost layer [119]. Several algorithms have been developed to combine muon tracks that differ based on the subsector is used in the reconstruction:

- Combined Muons (CB): tracks are separately reconstructed in the ID and the MS, and then combined trough a global fit procedure. The majority of the muons are reconstructed starting from the hits in the Muon Spectrometer and moving inward to the inner detector hits.

- Segment-Tagged Muons (ST): Usually used when there is only one track segment in the MS, due to low p_T of the muon or the fact it passed through the reduced acceptance region. In this algorithm, a track in the inner detector is classified as a muon if it can be matched to at leas one segment in either the MDT or CSC chambers.

- Calorimeter-Tagged Muons (CT): if an energy deposit in the calorimeters can be matched to a track in the inner detector, this is classified as a muon. This algorithm gives the lowest purity, but it is reliable when considering low-p_T muons or muons passing through the region with reduced acceptance.

- Extrapolated Muons (ME): muons are reconstructed using only information on the MS tracks with a loose requirement on compatibility with

the origin being the interaction point. This particular algorithm is used to include the region $2.5 < |\eta| < 2.7$, not covered by the ID.

A representation of the four algorithms used to reconstruct the muons is shown in Figure 4.2.

Similarly to what is done for the electrons, the muons are then identified in order to improve the separation between prompt and fake muons. This process is done using these variables:

- q/p compatibility $= \dfrac{|q/p_{\mathrm{ID}} - q/p_{\mathrm{MS}}|}{\sqrt{\sigma^2(q/p_{\mathrm{ID}}) + \sigma^2(q/p_{\mathrm{MS}})}}$, where q is the charge determined from the track curvature, p is the muon momentum, measured both in the ID and in the MS.
- $\rho' = \dfrac{|p_{T,\mathrm{ID}} - p_{T,\mathrm{MS}}|}{p_{T,\mathrm{CB}}}$, where $p_{T,\mathrm{ID}}$ and $p_{T,\mathrm{MS}}$ are the transverse momenta measured in the ID and the MS, respectively, while $p_{T,\mathrm{CB}}$ is the value resulting from the combined track fit.
- the normalized χ^2 of the combined track fit [119].

Identification requirements are defined using the variables just mentioned, in particular in the present analysis the muons are required to satisfy a *LHMedium* working point.

Similarly to what is done with electrons, to increase the discrimination between prompt and non-prompt muons, further requirement are used: an isolation requirement on $E_T^{\mathrm{cone}}/p_T < 0.15$ in the calorimeter and a track isolation requirement, which is $p_T^{\mathrm{varcone}}/p_T < 0.04$ with $\Delta R = \min(0.3, 10\ \mathrm{GeV}/E_T)$ when $p_T^{\mathrm{muon}} < 50$ GeV and $\Delta R = \min(0.2, 10\ \mathrm{GeV}/E_T)$ otherwise. The reconstruction efficiency for the muons is at least 95% and goes up to 99% with increasing p_T [119].

4.4 Jets

Jets formed after the hadronization of gluons and quarks are observed as narrow cones of hadrons and other particles. These objects can be used to thoroughly investigate the kinematics of the partons that generated them.

4.4.1 Jet Reconstruction

A good definition of a jet, should give similar results when it is applied to data, MC and parton-level calculations. Some general properties that allow

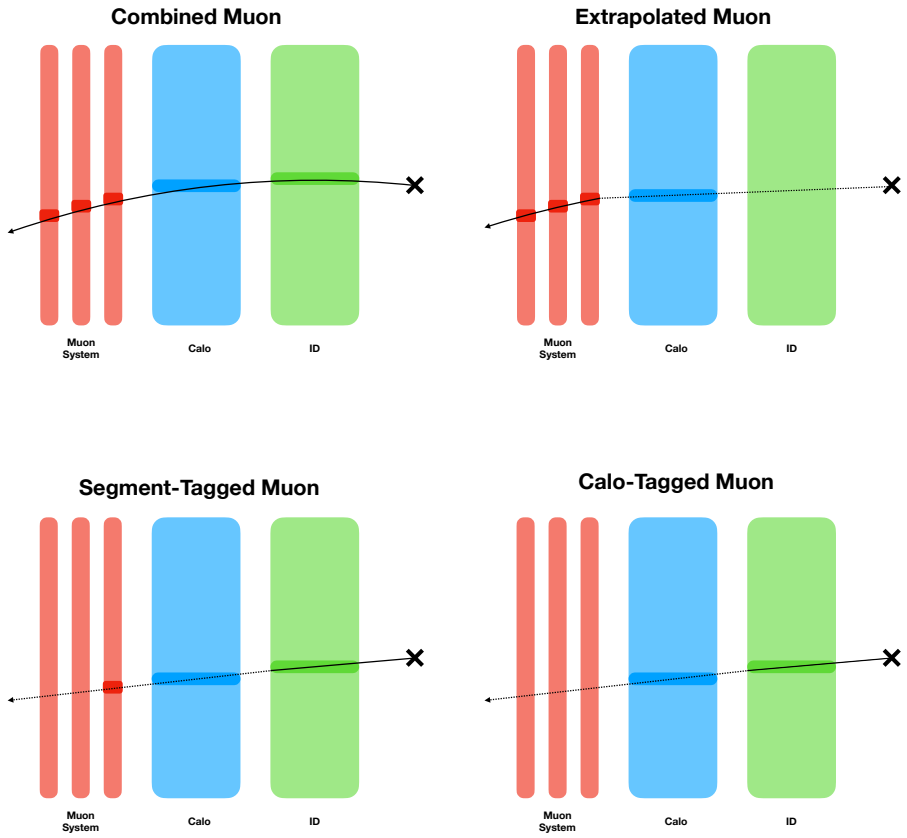

Figure 4.2: Reconstruction of the muons using different algorithms.

a jet reconstruction algorithm to follow this rule are known as *Snowmass accord* [120]:

- Simple to implement in an experimental analysis;
- Simple to implement in theoretical calculations;
- Defined at all orders in perturbation theory;
- cross-sections calculated using the algorithm should be finite;
- cross-sections calculated using the algorithm should be relatively insensitive to hadronization.

A good jet algorithm should also be Infrared and Collinear (IRC) safe, this means that it should be invariant under $\vec{p}_i \to \vec{p}_j + \vec{p}_k$ whenever $\vec{p}_j$ and $\vec{p}_k$

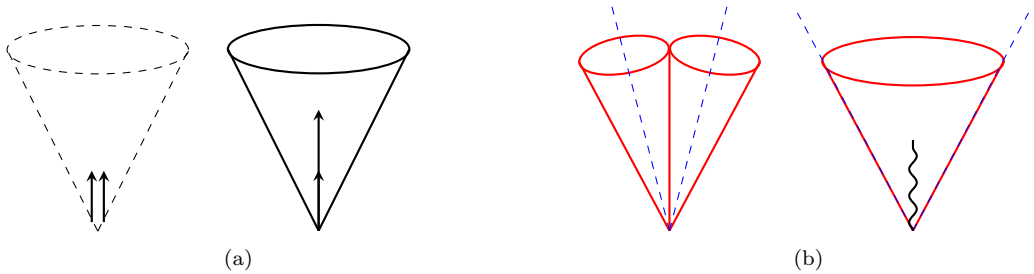

Figure 4.3: Pictorical depiction of collinear safety (a) and infra-red safety (b).

are parallel (collinear) or one of them is small (infrared), see Fig. 4.3. This property is important for a number of reasons:

- Non-perturbative effects and fragmentation of the hadrons always involve the production of collinear particles. Moreover, soft particles can be produced both in perturbative and non-perturbative QCD processes.

- As explained in Section 1.2.2, when infrared or collinear divergences arise in fixed order pQCD calculations, these are cancelled if the observable is inclusive enough. The same is not true for jet algorithms that are IRC unsafe. This happens because tree-level splitting and loop diagrams may result in two different sets of jets that do not cancel out, resulting in infinite cross-sections.

- The fact that the experimental apparatus used to measure physical observables has a finite resolution provides a natural cut-off to the (minimum) measurable energy and separation between particles. This means that results obtained using IRC unsafe algorithms cannot be compared to experimental measurements.

To reconstruct the jets in the ATLAS detector, the energy deposits in the calorimeters are clustered together using an iterative procedure [121], starting from the most significant one and combining the nearby cells. At the end of this procedure the so-called topo-clusters (topological clusters) are obtained. These are the starting point, the proto-jets, for jet reconstruction algorithms.

In this analysis, the anti-k_t jet reconstruction algorithm [122] has been used, which satisfies all the aforementioned requirements for IRC safety. This algorithm iteratively combines the proto-jets based on their properties, in

particular:

$$d_{ij} = \min\left(\frac{1}{k_{T,i}^2}, \frac{1}{k_{T,j}^2}\right)\frac{\Delta_{ij}}{R^2} \tag{4.1}$$

$$d_{iB} = \frac{1}{k_{T,i}^2} \tag{4.2}$$

$$\Delta_{ij} = (\eta_i - \eta_j)^2 + (\phi_i - \phi_j)^2 \tag{4.3}$$

where d_{ij} is the distance between proto-jets i and j, d_{iB} is the distance of proto-jet i from the beam pipe, $k_{T,i}$ is the transverse momentum of proto-jet i and R is the jet radius, a parameter used by the algorithm to control the size of the jets. The steps of the anti-k_t algorithm are as follows:

- compare d_{ij} and d_{iB} for every pair of jets;
- if $d_{iB} > d_{ij}$ the two proto-jets are combined in a new proto-jet;
- if $d_{iB} < d_{ij}$ the proto-jet is considered a jet.

In this analysis R is set to 0.4.

4.4.2 Jet Calibration and Jet Energy Resolution

A jet calibration procedure [123] has to be carried out in order to correct the measurements taking place in the hadronic calorimeters so that they can be traced back to their generating partons. The procedure to calibrate the reconstructed jets consists of several steps. The first one consists in the correction of the jet's direction so that it points toward the primary vertex. Right after this step, the jet energy is corrected to account for pileup effects, so the extra energy deposits are removed. This is done using a method [124] that uses ρ, the per-event pileup density in the $\eta \times \phi$ plane, and the area of the projection of the jet in this plane, A^{jet}. The correction is defined in terms of the jet momentum as follows:

$$p_T^{\text{corr}} = p_T^{\text{jet}} - \rho \times A^{\text{jet}}.$$

After correcting for pileup effects, jet energy scale (JES) and η corrections are applied using MC simulations. In particular the JES correction consists in correcting the reconstructed energy to the scale of the particle-level jets. This is done parametrizing the ratio of the energies of particle-level jets matched to the reconstructed ones and of the reconstructed jets as a function of p_T and η. After this function is extracted, its inverse is applied as a correction factor to

the energy of the reconstructed jets. After the JES calibration a step called Global Sequential Calibration (GSC), which is a track-based correction aimed at reducing the difference between quark-initiated jets and gluon-initiated ones. The calibration procedure ends with data-related corrections, which are called *in-situ* corrections. These corrections aim to remove all the remaining pseudorapidity differences in the jets after the MC calibration, correct the absolute p_T in the central region and to calibrate high-p_T jets. This is done deriving the η-intercalibration with dijet events, the balance of γ and Z bosons recoiling against the jets and using events in which low-p_T jets recoil against a high-p_T jet respectively.

Using the width of the distribution of the asymmetry between jets and photons or Z bosons it is possible to measure the Jet Energy Resolution (JER) using data. For high-p_T jets or jets falling in the very forward $|\eta|$ regions, asymmetry in dijet events is used.

4.4.3 Jet Vertex Trigger

To separate jets coming from the hard interactions from the ones originated by pileup activity, a likelihood discriminant called the Jet Vertex Tagger (JVT) [125] is used. This is obtained in a multivariate analysis in which dijet events are used to extract kinematic variables which in turn enter into the discriminant. In the present analysis, the cut JVT>0.59 is applied to jets with $p_T < 60$ GeV and $|y| < 2.4$.

4.5 *b*-tagging

Since the final state of $t\bar{t}$ events contains two jets originated by b-quarks, identification of the b-jets, the so-called *b-tagging*, is of major importance in order to separate top-quark pair events from background ones.

Algorithms aimed at identifying b-jets make extensive use of the property of b-hadrons of being long-lived ($\tau \simeq 1.5$ ps) when differentiating them from c-jets or light-flavour jets (containing u, d, s). The long lifetime of these particles results in a long flight distance and therefore a secondary vertex is observed, as shown in Fig. 4.4.

In this analysis, the `DL1r`[1] [126] has been used. This algorithm uses a deep neural network to combine the outputs of three different sets of low-level b-tagging algorithms into a single discriminant. The first set of algorithms combines transverse and longitudinal impact parameters, together

[1] `DL1r` is an extension of the `DL1` algorithm, in which a new low-level tagger has been added that uses the correlations between track impact parameters.

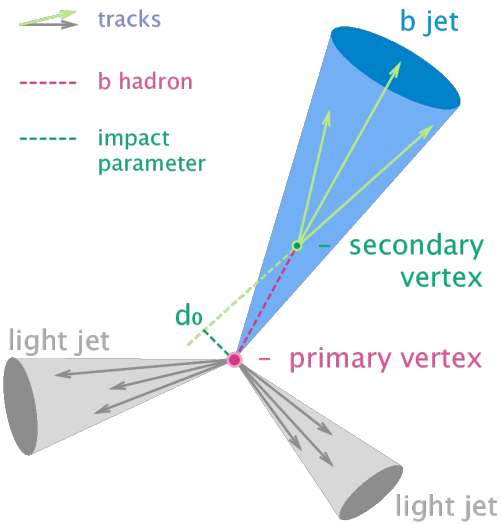

Figure 4.4: A scheme of the typical topology of a decaying b-hadron.

with their correlations, into a single likelihood discriminant. The second low-level tagger takes into account the reconstruction and identification of a displaced secondary vertex and its properties. In the last algorithm, using the Kalman filter [127] implemented in the JetFitter [128] algorithm, the topological structure of b-hadrons and c-hadrons is exploited. The output of these three low-level taggers, together with the p_T and $|\eta|$ of the jet, are given as input to the `DL1r` neural network, which combines these information in a discriminant used to separate different jet flavours. Working points are defined using the efficiency of b-tagging in $t\bar{t}$ events, with a single cut-value on the discriminant. This analysis uses a working point of 70%.

A procedure called b-tagging calibration has to be carried over to correct for differences between simulated and measured data. This is done using scale factors derived from the observed differences in efficiency (as a function of p_T) between the two, and take the form of a scale factor, applied on a per-event basis to the MC:

$$\mathrm{SF} = \frac{\epsilon_b^{\mathrm{data}}}{\epsilon_b^{\mathrm{MC}}} \tag{4.4}$$

where $\epsilon_b^{\mathrm{data}}$ is the efficiency measured in the data, while ϵ_b^{MC} is the predicted efficiency obtained with the MC.

The b-tagging calibration is mainly done using $t\bar{t}$ samples in the dileptonic channel, since it gives the lowest background contamination. The methods used to perform the calibration are the likelihood method (LH) and the tag-and-probe method (T&P) [129]. In order to extend the p_T range, semileptonic $t\bar{t}$ samples are used [130], due to their increased statistics with respect to the

dileptonic ones. Even higher p_Ts can be reached extrapolating the SFs from MC simulations [131].

4.6 Missing Transverse Energy

Since the total momentum has to be conserved, the sum of all the transverse momenta should be zero. If this sum is not exactly zero, the missing part is known as *missing transverse momentum* E_T^{miss} [132]. The presence of missing transverse momentum implies the presence of particles that have not been detected; in the SM these are represented by neutrinos.

The missing energy is measured taking the absolute value of the sum of the momenta of all calibrated and reconstructed objects, with additional terms coming from tracking [133]. The missing transverse energy in the x and y directions is calculated in the following way:

$$E_{x(y)}^{\text{miss}} = E_{x(y)}^{\text{miss,e}} + E_{x(y)}^{\text{miss},\mu} + E_{x(y)}^{\text{miss},\tau} + E_{x(y)}^{\text{miss},\gamma} + E_{x(y)}^{\text{miss,jets}} + E_{x(y)}^{\text{miss,soft}} \tag{4.5}$$

where every term, except the soft one, is the sum of the momenta for the corresponding calibrated object projected in the considered direction (x or y). The soft term is reconstructed from transverse momentum deposits in the detector that are not associated with any reconstructed hard object. This is done using two types of methods: Calorimeter Soft Term (CST), based on calorimeter information, and track-based methods known as Track Soft Term (TST).

The total missing energy is then calculated in the following manner:

$$E_T^{\text{miss}} = \sqrt{(E_x^{\text{miss}})^2 + (E_y^{\text{miss}})^2} \tag{4.6}$$

4.7 Overlap Removal

It may happen that a reconstructed object satisfies multiple selection criteria. Since every object needs to be associate with only one physics object, a procedure known as *overlap removal* was devised:

- If a muon and an electron share the same track, there is a high probability the electron has originated from bremmstrhalung effects and is therefore discarded.
- If an electron and a jet are close, it could happen that the energy deposits due to the electron in the calorimeters are double counted as a jet. To remove this double counting, the jet closest to the electron is discarded if $\Delta R(\text{jet}, \text{e}) < 0.2$.

- Moreover, if $\Delta R(\text{jet}, \text{e}) < 0.4$, the electron is discarded, to reduce non-prompt electron contamination.
- If $\Delta R(\text{jet}, \mu) \leq 0.4$ and the number of tracks for the jet is less than three, the jet is discarded, otherwise is the muon that is removed.

Chapter 5

Event Selection and Reconstruction

5.1 Event Selection

After detector-level objects have been reconstructed, as explained in Chapter 4, a set of requirements is applied to these same objects, this is called *event selection*.

In order to pass the selection, the events are required to have at least two tracks matched to the primary vertex and additionally a lepton with $p_T > 27$ GeV. Single-lepton triggers are used in the selection, where the read-out in the detector is triggered by either an electron or a muon in the HLT, as described in Section 2.2.7. Three triggers are used for e+jets events and two for μ+jets ones. Different sets of triggers are used for the 2015 and 2016-2018 data-taking periods and are listed in Table 5.1. The final selection is done using a logical `OR` between all the triggers. A further request is made for the events to be selected: it has to have at least four jets with $p_T > 25$ GeV and $|y| < 2.5$ of which at least two have to be b-tagged using the `DL1r` tagger with a WP of 70%. The Pseudo-Top algorithm is the one used to reconstruct $t\bar{t}$ events and it will be described in the following sections.

Object	2015	2016-2018
electron	HLT_e24_lhmedium_L1EM20VH HLT_e60_lhmedium HLT_e120_lhloose	HLT_e26_lhtight_nod0_ivarloose HLT_e60_lhmedium_nod0 HLT_e140_lhloose_nod0
muon	HLT_mu20_iloose_L1MU15 HLT_mu50	HLT_mu26_ivarmedium HLT_mu50

Table 5.1: Single lepton triggers used in the analysis. The identification operating points are represented by *lhtight*, *lhmedium*, *lhloose* and *loose*, while the isolation operating points are represented by *ivarloose* and *ivarmedium*

5.2 Parton-level definition

At parton-level, the objects are defined for MC simulations. At this level, the selection of the top and anti-top quarks happens, based on their decay products, a W boson and a b-quark. Another requirement is that one of the top quarks decays in the leptonic channel, while the other does so in the hadronic channel. Dileptonic events are excluded in the parton-level selection.

5.3 Background Determination

It can happen that events that are not originated by a $t\bar{t}$ pair pass the selection. This is because their final state is similar to the signal final state. These events have to be accounted for as a background. Most of these events include a lepton in the final state and their number is estimated using MC simulations. A much smaller fraction of background events is due to objects misreconstructed as leptons, these are estimated using data-driven methods due to the lack of precise simulations. Events in which both the top quarks decay leptonically could also pass the selection and are therefore, at this stage, considered as signal. The total estimated background is then subtracted from the data samples.

5.3.1 MC-based Background

The biggest contribution to backgrounds are single-top events, since the associated final state is similar to the one for the $t\bar{t}$ production. Other background sources are events in which a W or Z boson is produced together with jets. W+jets events give a bigger contribution than Z+jets ones. Diboson events can also contribute to backgrounds if one of the bosons decays leptonically, while the other one generates hadrons. Lastly, the smallest background contributions, due to their small cross-sections, are given by events in which a $t\bar{t}$ pair is produced in association with a vector boson or H boson.

5.3.2 Data-driven Background

Processes in which a number of jets are produced, called multijet, which include the hadronic channel for $t\bar{t}$ production, have final states that could pass the selection criteria for the ℓ+jets channel. In particular, this is due to the presence of objects misidentified as leptons or non-prompt real leptons. This background is called multijet/fakes background and is estimated from data using the Matrix Method [134].

This method consists in three steps:

- Two requirements on leptons are defined: loose and tight, which is the one used in this analysis, as explained in Chapter 4.
- Data samples are then split in two subsets, T and L, depending on whether they pass or not the tight selection criteria. Another way to divide the data sample S is to identify the two subsets R and F, containing real and fake leptons, respectively. Now the data sample can be decomposed as $S = T + L = R + F$, with the intersection between T and F being the fake leptons that contribute to the background. A matrix relation between the subsets can therefore be written as

$$\begin{pmatrix} \langle n_T \rangle \\ \\ \langle n_L \rangle \end{pmatrix} = \begin{pmatrix} \epsilon_r & \epsilon_f \\ \\ \overline{\epsilon_r} & \overline{\epsilon_f} \end{pmatrix} \begin{pmatrix} n_R \\ \\ n_F \end{pmatrix} \tag{5.1}$$

  where $\langle n \rangle$ is the expected number of events in the subset, while the ϵ coefficients are the probabilities for a lepton of a determinate subset to pass the tight criteria. The $\bar{\epsilon}$ coefficients are defined as $\bar{\epsilon} = 1 - \epsilon$.
- Assuming $\epsilon_r \neq \epsilon_f$, Eq. (5.1) can be inverted, therefore obtaining an estimate for the number of fake leptons passing the tight selection:

$$\begin{pmatrix} n_R \\ \\ n_F \end{pmatrix} = \frac{1}{\epsilon_r - \epsilon_f} \begin{pmatrix} \overline{\epsilon_f} & -\epsilon_f \\ \\ -\overline{\epsilon_r} & \epsilon_r \end{pmatrix} \begin{pmatrix} \langle n_T \rangle \\ \\ \langle n_L \rangle \end{pmatrix} \tag{5.2}$$

  obtaining therefore an estimate for n_{TF}:

$$\hat{n}_{TF} = \epsilon_f \hat{n}_F = \frac{\epsilon_f}{\epsilon_r - \epsilon_f}(\epsilon_r(n_T + n_L) - n_T). \tag{5.3}$$

In this analysis, the fake lepton efficiency was estimated using control regions in which the dominant background was the multijet one, after the background due to non-prompt real leptons was subtracted using MC-generated events. In particular the real-lepton efficiency was extracted using leptons coming from the decay of Z bosons and applying a tag-and-probe technique.

5.4 Event Yields and Control Plots

In the present analysis both data and MC samples are split, depending on the final state lepton, in an e+jets and a μ+jets sample. The selection is

sample	e+jets	μ+jets
$t\bar{t}$	2041959 (91.14%)	2052925 (90.45%)
SingleTop	96279 (4.3%)	95916 (4.23%)
Wjets	49185 (2.2%)	52855 (2.33%)
fakes	21131 (0.94%)	44498 (1.96%)
Zjets	22330 (1.0%)	14290 (0.63%)
ttV	6630 (0.3%)	6432 (0.28%)
Diboson	3043 (0.14%)	2886 (0.13%)
Total Prediction	2240557	2269802
Data	2232302	2219459
Data/Prediction	0.996	0.978

Table 5.2: Observed and expected number of events in the e+jets and μ+jets channels. The percentage impact of each sample to the total MC prediction is also shown.

done separately on these two samples and they are then combined in a ℓ+jets sample. This is only consistent if the yields of both samples are similar, which is true for this analysis, as shown in Table 5.2. In Table 5.3, the cumulative yields for the ℓ+jets sample are shown.

Control plots for the combined ℓ+jets channel are shown in Figs. 5.1 and 5.2. The same kind of control plots for the separate e+jets and μ+jets channels can be found in Appendix A. A reasonable agreement between data and MC prediction can be observed in all the distributions. A tendency of the MC nominal sample to overestimate the data is found both in the high p_T and high-E_T^{miss} distributions: this could be due to missing higher order corrections in the simulation, since the used MC generator is NLO in pQCD.

5.5 Reconstruction of top-quark kinematic properties

Once all the objects have been reconstructed and after the selection is applied, they are used in the reconstruction of top-quarks, which are the focal point of this analysis. There are several algorithms capable of reconstructing the kinematic properties of the top-quarks produced in a pp interaction. These make use of the kinematic properties of the objects in the final state. A description of the algorithm used in the present analysis is given in the following section.

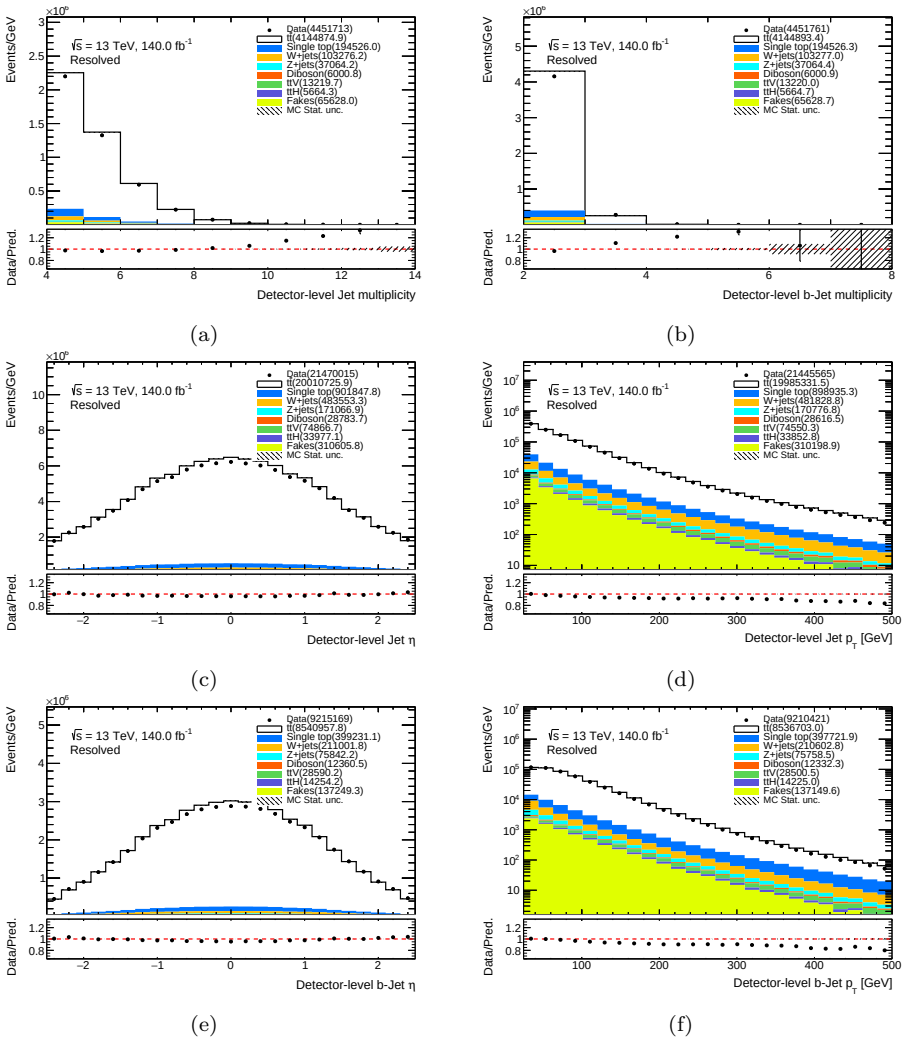

Figure 5.1: Comparison of measured data and Monte Carlo simulations for basic kinematic observables in the l+jets channel at detector level: (a) multiplicity of jets, (b) multiplicity of $b-$jets, (c) pseudorapidity of the jets, (d) transverse momentum of the jets, (e) pseudorapidity of the $b-$jets, (f) transverse momentum of the $b-$jets. The data, represented by the dots in the plots, is directly compared with the total Monte Carlo simulations, represented by the different colors stacked histograms. The uncertainty band represents the statistical uncertainty in the MC sample, while bars on data points represent the uncertainty on data.

sample	ℓ+jets
$t\bar{t}$	4094884 (90.79%)
SingleTop	192196 (4.26%)
Wjets	102040 (2.26%)
fakes	65629 (1.46%)
Zjets	36620 (0.81%)
ttV	13062 (0.29%)
Diboson	5929 (0.13%)
Total Prediction	4510359
Data	4451761
Data/Prediction	0.987

Table 5.3: Observed and expected number of events in the l+jets channel. The percentage impact of each sample to the total MC prediction is also shown.

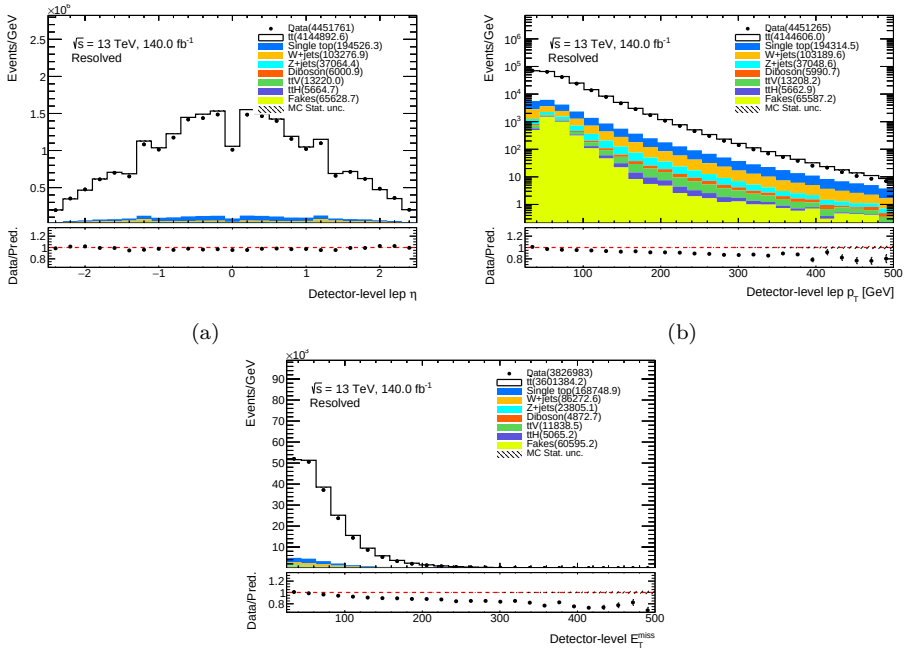

Figure 5.2: Comparison of measured data and Monte Carlo simulations for basic kinematic observables in the l+jets channel at detector level: (a) pseudorapidity of the produced lepton, (b) transverse momentum of the produced lepton, (c) missing transverse energy. The data, represented by the dots in the plots, is directly compared with the total Monte Carlo simulations, represented by the different colors stacked histograms. The uncertainty band represents the statistical uncertainty in the MC sample, while bars on data points represent the uncertainty on data.

5.5.1 Pseudo-Top reconstruction algorithm

The Pseudo-Top algorithm [135] is the one used in this analysis for the reconstruction of top-quarks. This algorithm uses information on the final state objects, meaning the charged lepton (electron or muon), the E_T^{miss} and the four jets, of which two b-tagged, to reconstruct the top-quarks' full decay chain. The steps performed by the algorithm are the following:

- Exactly two b-jets are chosen. If more than two jets have been identified as being originated by a b-quark, only the hardest two jets, the ones with higher p_T are chosen, while the others are considered light jets.
- Between the remaining jets, the ones coming from the decay of the W boson are chosen. This is done comparing the invariant mass of each pair of jets and comparing it to the mass of the W boson, then choosing the pair with the invariant mass closest to it.
- Using the constraint $m_W = m_{\ell\nu}$, the z component of the neutrino's four-momentum is calculated. If the quadratic equation obtained imposing this constraint has two real solutions, the one with the smallest p_z is chosen. If the solutions are complex, only the real part is considered. The E_T^{miss} is used to calculate the other four-momentum components, while the mass is approximated to zero.
- The W boson that decays in the leptonic channel is reconstructed from the system composed by the lepton and the neutrino.
- To reconstruct the top-quark that decayed leptonically, the leptonically decaying W is used together with the closest (in $\Delta R = \sqrt{(\Delta\eta)^2 + (\Delta\phi)^2}$) b-jet to the lepton, chosen from the two highest-p_T b-jets.
- The two non-b-tagged jets whose invariant mass is closer to the mass of the W boson are used to reconstruct the hadronically decaying W.
- The hadronically decaying top-quark is reconstructed using the hadronic W boson and the b-jet that was not chosen in the reconstruction of the leptonic top.

A comparison between data and the nominal Monte Carlo generator sample is shown for the kinematic observables of the hadronically and leptonically decaying top quarks, reconstructed using the Pseudo-Top algorithm, in Fig. 5.3. A similar comparison for the kinematic observables of the $t\bar{t}$ pairs is shown in Fig. 5.4.

A good agreement between MC and data is observed for all the distributions, with the exception of the transverse momentum of both hadronic tops and $t\bar{t}$ pairs. In these distributions, in fact, Monte Carlo simulations overestimate data in the high-p_T range. The source of this excess is a consequence of non-optimal modelling of the top-quark p_T spectrum, which in turn affects all observed distributions due to an explicit p_T cut in event selection. As a result the ratio between data and MC lies in the range between 5 and 20% in almost all the bins for the measured distributions, although the shape agreement is generally good. A similar trend is observed in previous analyses [136].

The shape agreement is worse at high jet and b-jet multiplicities, as shown in figure Figs. 5.1(a) and 5.1(b) where there is a noticeable positive slope in data/MC ratios. Poorer modelling is somewhat anticipated in higher multiplicity regions. The underestimation of events with high numbers of b-jets, observed in Fig. 5.1(b), is also consistent with other $t\bar{t}$ measurements that include multiple b-jets in the final state [137].

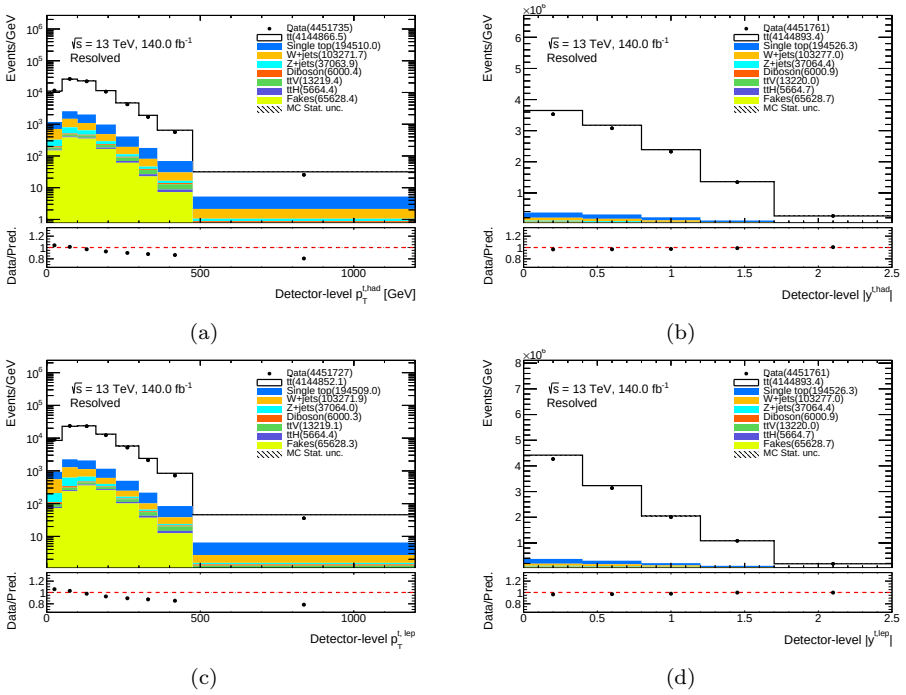

Figure 5.3: Kinematic observables for the leptonically and hadronically decaying top quarks reconstructed with the Pseudo-Top algorithm: (a) transverse momentum and (b) rapidity of the hadronic top; (a) transverse momentum and (b) rapidity of the leptonic top. The data, represented by the dots in the plots, is directly compared with the total Monte Carlo simulations, represented by the different colors stacked histograms. The uncertainty band represents the statistical uncertainty in the MC sample, while bars on data points represent the uncertainty on data.

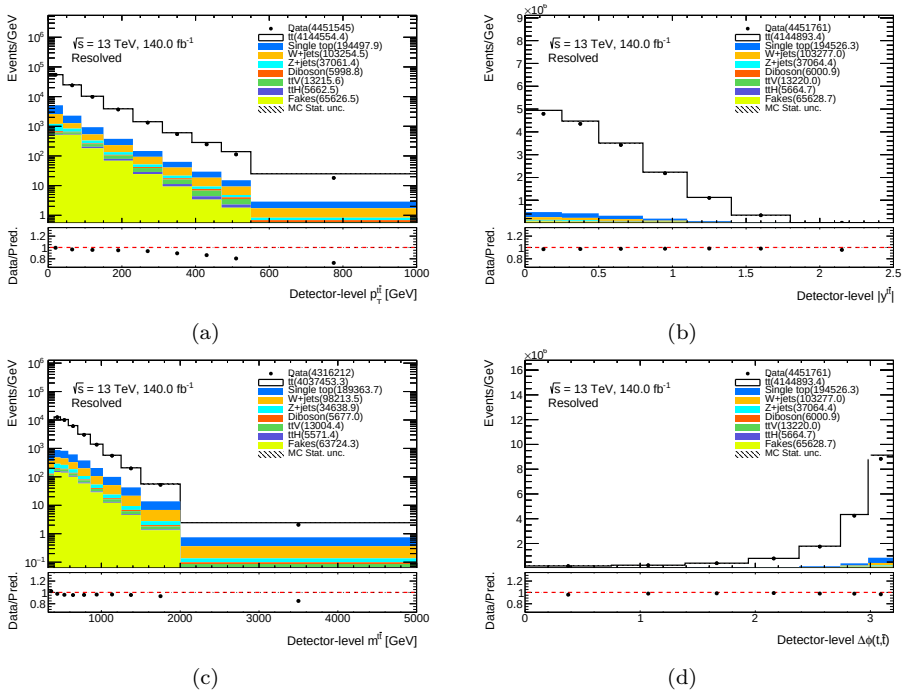

Figure 5.4: Kinematic observables for the $t\bar{t}$ system reconstructed with the Pseudo-Top algorithm: transverse momentum (a), rapidity (b), invariant mass (c) and the azimuthal angle difference (d). The data, represented by the dots in the plots, is directly compared with the total Monte Carlo simulations, represented by the different colors stacked histograms. The uncertainty band represents the statistical uncertainty in the MC sample, while bars on data points represent the uncertainty on data.

Chapter 6

Cross-Section Measurement

6.1 Unfolding

Measurements made in high-energy physics suffer from distortion effects due to the detectors, which don't allow a direct comparison with theoretical predictions. The procedure devised to correct for these effects is called *unfolding*. In particular, the finiteness of the detector's resolution causes a smearing in the measurements. A way to model this problem mathematically is the *Fredholm integral equation* [138]:

$$g(y) = \int A(x,y)f(x)dx + b(y) \tag{6.1}$$

where $g(y)$ represents the measured distribution, while $f(x)$ corresponds to the true one. $A(x,y)$ is known as resolution function and represents the aforementioned distortion effects. The function $b(y)$ represents background contributions to the measurement. The unfolding procedure aims to extract the function $f(x)$ by inverting this equation and, therefore, obtaining the inverse of the resolution function, $A^{-1}(x,y)$.

All these distributions are estimated using Monte Carlo simulations, therefore they assume the form of histograms, while $A(x,y)$ is represented by a matrix, called Migration Matrix if it normalized, Response Matrix otherwise. Thus, the problem becomes an algebraic system of equations:

$$y = Ax + b \tag{6.2}$$

where y and b are now vectors of n elements and represent the histograms of measured and background distributions. A is now an $n \times m$ Response Matrix that multiplies the true vector x, with dimension m.

The Response Matrix is seldom diagonal, since events in bin j can be reconstructed in the ith bin, with $i \neq j$, which is known as *migration*. Since

the inverse of the matrix A might not exist, different techniques have been devised to get around this problem. There are four main unfolding methods used in HEP:

- Bin-by-bin: Correction factors are extracted bin-by-bin from the ratio of number of reconstructed events in the bin over the number of true-level events. Using this techniques does not account for migration effects.
- Simple matrix inversion: The matrix is numerically inverted with conventional methods.
- Single Value Decomposition (SVD) [139]: The migration matrix is decomposed in three sub-matrices, which makes the inversion problem simpler to solve. It is an extension of the simple matrix inversion.
- Iterative Bayesian [140]: Technique based on the Bayes theorem. This is the way the matrix are inverted in the present analysis and it is treated more in-depth in the following sections.

6.1.1 Iterative Bayesian Unfolding

The Iterative Bayesian Unfolding (IBU) is an unfolding approach based on the Bayes theorem [141] and it gives a cause-effect interpretation to the unfolding in which the causes are the true events C_i, while the effects are represented by the measured events E_j. Effects are measured, but it is impossible to say which cause generated a particular effect, so this has to be estimated using MC generators. In order to do this, the probability $P(C_i|E_j)$ that a C_i was the cause of E_j can be estimated in the following way:

$$P(C_i|E_j) = \frac{P(E_j|C_i) \cdot P_0(C_i)}{\sum_{k=1}^{n_C} P(E_j|C_k) \cdot P_0(C_k)} \tag{6.3}$$

where $P_0(C_i)$ is the prior (a-priori) probability for the cause C_i, n_C is the number of possible causes and $P(E_j|C_i)$ is the conditional probability of the E_j being caused by cause C_i. An estimator for the number of causes in the i-th bin can be written as

$$\hat{n}(C_i) = \frac{1}{\epsilon_i} \sum_{j=1}^{n_E} n(E_j) \cdot P(C_i|E_j) \tag{6.4}$$

where $n(E_j)$ is the number of events in the j-th bin and ϵ_i is the efficiency for each bin

$$\epsilon_i = \sum_{j=1}^{n_E} \frac{n(E_j)^{\mathrm{MC}}}{n(C_j)^{\mathrm{MC}}}, \tag{6.5}$$

both measured in MC simulations. The inverse of the migration matrix can be then written as

$$\mathcal{M}_{ij}^{-1} = \frac{P(E_j|C_i) \cdot P_0(C_i)}{\sum_{h=1}^{n_E} P(C_i|E_h) \sum_{k=1}^{n_C} P(E_j|C_k) \cdot P_0(C_k)}, \tag{6.6}$$

so that Eq. (6.4) assumes the form:

$$\hat{n}(C_i) = \sum_{j=1}^{n_E} \mathcal{M}_{ij}^{-1} n(E_j). \tag{6.7}$$

The *a posteriori* probability for a cause C_i is therefore

$$\hat{P}(C_i) \frac{\hat{n}(C_i)}{\sum_j \hat{n}(C_j)}. \tag{6.8}$$

The bayesian unfolding is an iterative procedure. This is necessary in order to obtain a stable solution. The starting point is a polynomial fit of the posterior distribution, which is then used as a prior for the next iteration. Every iteration will make the solution better, and the procedure stops when no improvement is observed in subsequent iterations.

6.1.2 Unfolding-related biases

The use of IBU, as with any unfolding technique, can introduce biases if certain assumptions are not satisfied. One of the main sources of bias in IBU is the choice of prior, which can affect the reconstructed distribution, especially in regions where the data are sparse or where the prior is poorly constrained. Another source of bias is the modeling of the detector response, which can introduce systematic effects and distort the measured distribution. The iterative nature of IBU can also lead to biases if the iterations are not converged or if the stopping criterion is not well-defined. Based on the experience gained in previously performed analyses [136], these effects are small and under control.

6.2 Binning Choice

The measurements presented in this thesis follow a similar binning strategy as the one used in a previously published analysis [136] in which the same observables were measured with a luminosity of 36 fb^{-1}. The binning optimization strategy for the previous analysis and for the present one are described in the following sections.

6.2.1 Binning optimization in the previous analysis

The binning optimization was done using the following formula:

$$\delta \cdot R(p_{n-1}) \geq \frac{x_n - x_{n-1}}{2} \tag{6.9}$$

where $R(p_{n-1})$ is the resolution function of the considered observable in the middle point of the bin whose edges are x_{n-1} and x_n. The parameter δ accounts for the non-gaussian shape of the resolution distribution usually chosen to be grater than 1. A further request is applied to the statistical uncertainty associated with each bin, which should be smaller than 5%.

6.2.2 Binning optimization strategy for the present analysis

For the measurements presented in this thesis, a similar choice of binning as the one used in the partial Run 2 analysis has been used in the case of single and double differential cross-sections, expanding however the limit in the high-mass and high-momenta regions.

In the case of triple differential cross-sections, the approach was to require a less-than-5% statistical uncertainty in regions already covered by the published analysis, while minimizing the other systematic uncertainties.

6.3 Correction Evaluation

Kinematic properties related to physics objects are measured with an associated uncertainty, due to the finiteness of the detector's resolution and coverage. Moreover, as explained in Chapter 5, some kinematic cuts are applied in order to reduce background contamination. Due to the less-than-100% accuracy in the measurements, the yields have to be corrected. The correction factors can be estimated using MC simulations. It is therefore paramount to have a well-defined truth-level, in which particles have not yet interacted with the detector.

6.3.1 Parton-level

When defining the truth-level, to which the measurement is unfolded, there are different aspects that have to be accounted for. In order to correctly identify both the leptonic and hadronic top-quarks, the contribution of the dileptonic $t\bar{t}$ events is discarded. This is done using a correction factor, f_{dilep}, defined as:

$$f_{\text{dilep}} \equiv \frac{N_{\text{reco}\wedge\ell+\text{jets}}}{N_{\text{reco}}}. \tag{6.10}$$

This represents the fraction of detector-level $t\bar{t}$ events that decay in the ℓ+jets decay channel ($N_{\text{reco}\wedge\ell+\text{jets}}$) in the total detector-level sample (N_{reco}). The produced lepton can be either an electron, a muon or a τ lepton. W bosons producing τ leptons are treated as signal, independent of what the τ decays into. The cross-sections are measured using the kinematic properties of the top-quarks before the decay process and after the QCD radiation. The hadronic top properties are used to measure top-quark-related properties.

Another thing that has to be taken into account is the efficiency of the detector. This is done using a correction factor, ϵ, that corrects for events generated at truth-level, which don't pass the selection at the detector-level. This is again estimated using Monte Carlo simulations:

$$\epsilon \equiv \frac{N_{\text{reco}\wedge\ell+\text{jets}}}{N_{\ell+\text{jets}}} \tag{6.11}$$

where $N_{\ell+\text{jets}}$ is the number of events generated at truth-level.

Lastly, using information on parton-level events that pass the detector-level selection, the migration matrix is built, considering only semileptonic events. Correction factors derived from $t\bar{t}$ MC simulations for single differential spectra are shown in Figs. 6.1 to 6.5, together with migration matrices. Figs. 6.6 to 6.9 show the migration matrices for the double differential spectra.

6.4 Unfolding Procedure

After the correction have been applied and the background has been subtracted, data are unfolded using the iterative bayesian unfolding as implemented in the `RooUnfold` package [142].

After the response matrix has been built, using events that passed both the truth-level and reco-level selections in the nominal sample, the matrix is normalized so that the entries on every row sum up to 1. The result of this procedure is called migration matrix.

In order to estimate the statistical uncertainty in the MC samples, due to the finiteness of their size, pseudo-experiments are performed by smearing every bin with a gaussian shift and then taking the envelope of the results. The total statistical uncertainty for the Monte Carlo samples is found to be below 0.5% in all the measured spectra.

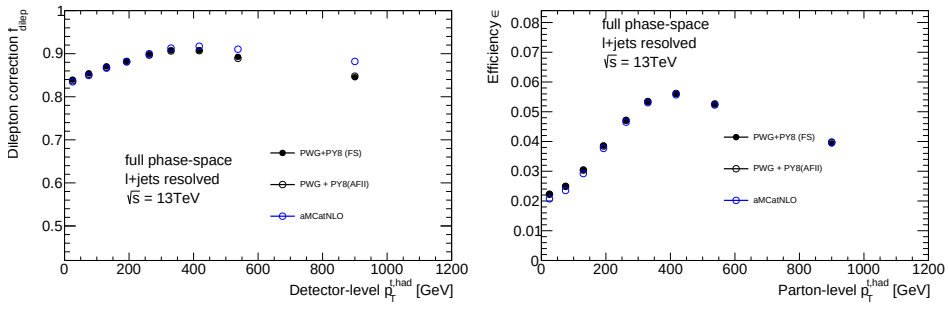

(a) (b)

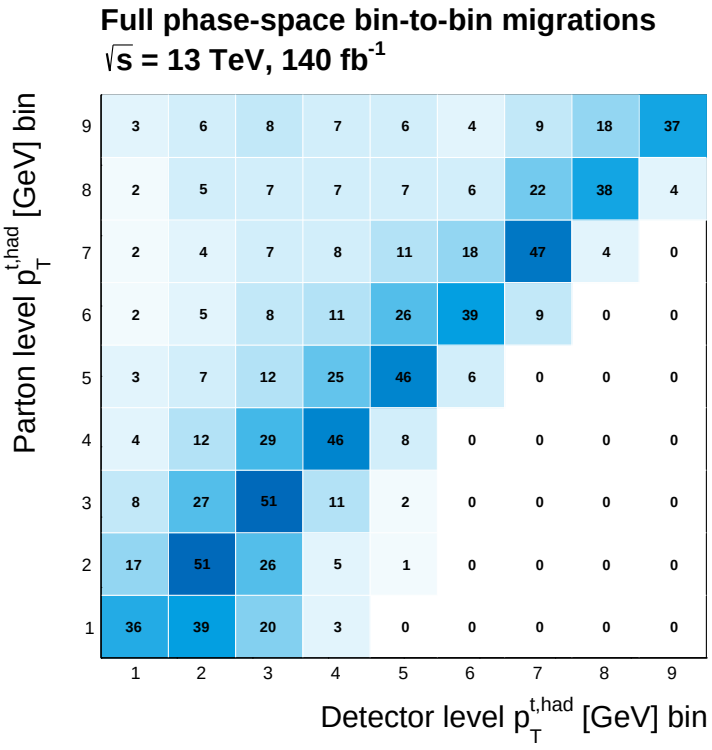

(c)

Figure 6.1: The (a) dilepton and (b) efficiency corrections, and the (c) detector-to-parton level migration matrix for the hadronic top-quark transverse momentum in the resolved topology at parton level.

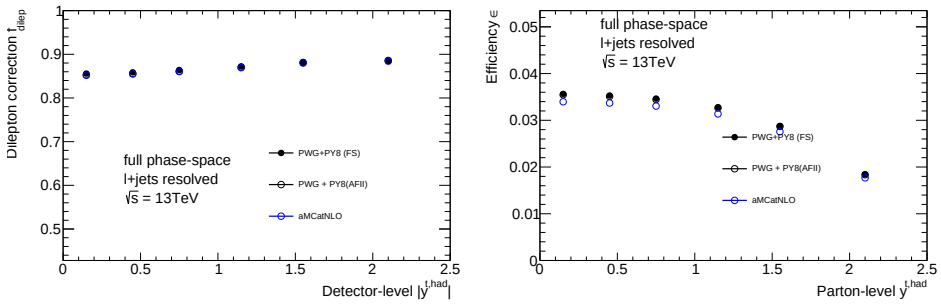

(a) (b)

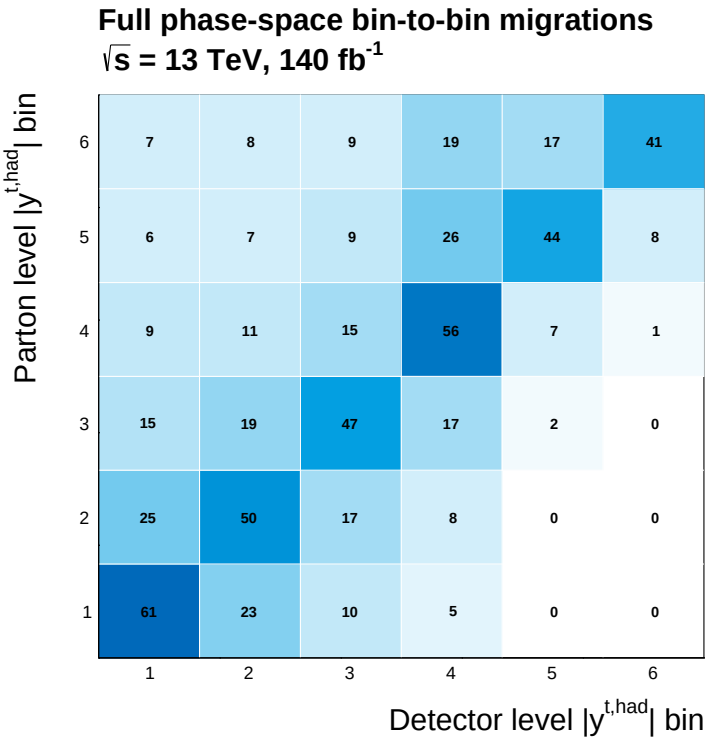

(c)

Figure 6.2: The (a) dilepton and (b) efficiency corrections, and the (c) detector-to-parton level migration matrix for the hadronic top-quark absolute rapidity in the resolved topology at parton level.

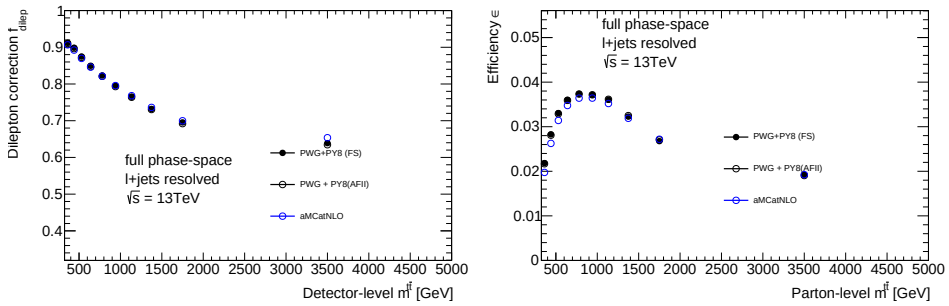

(a) (b)

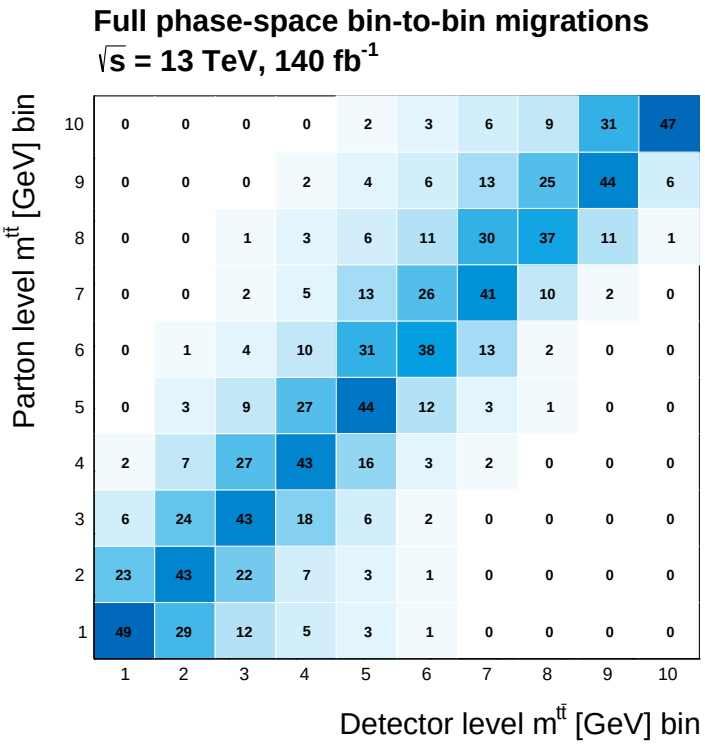

(c)

Figure 6.3: The (a) dilepton and (b) efficiency corrections, and the (c) detector-to-parton level migration matrix for the $t\bar{t}$ invariant mass in the resolved topology at parton level.

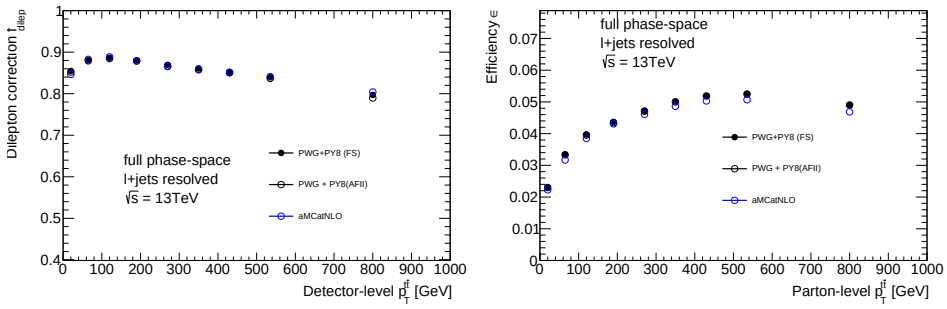

(a) (b)

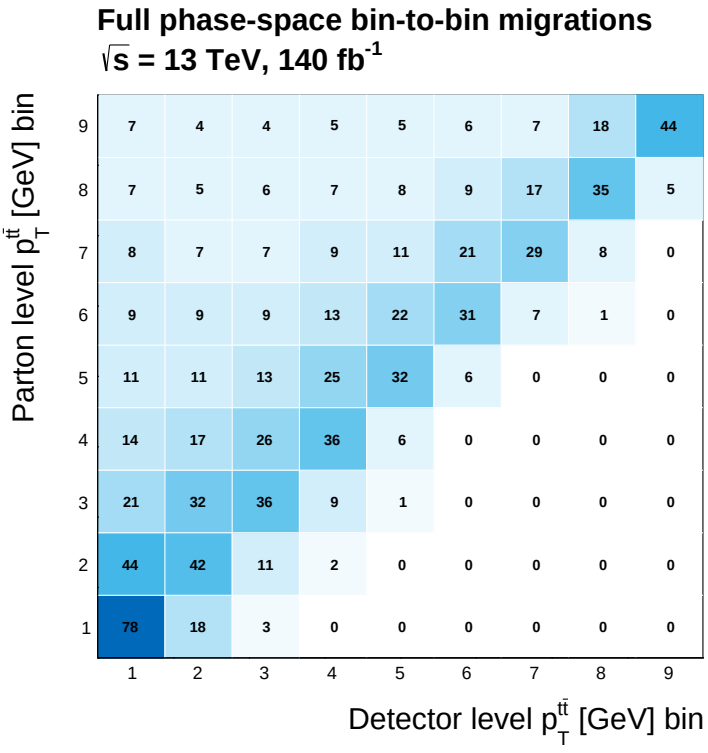

(c)

Figure 6.4: The (a) dilepton and (b) efficiency corrections, and the (c) detector-to-parton level migration matrix for the $t\bar{t}$ transverse momentum in the resolved topology at parton level.

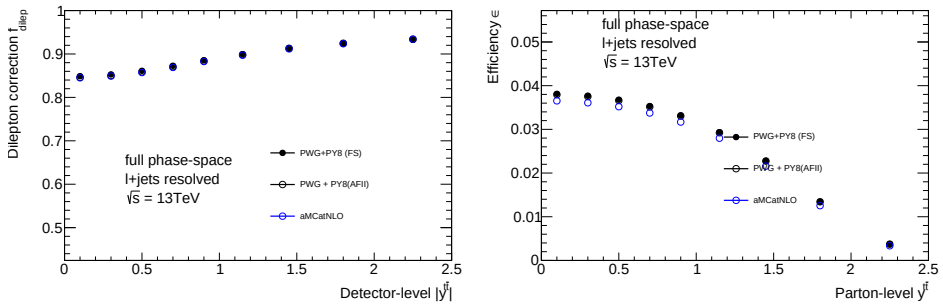

(a) (b)

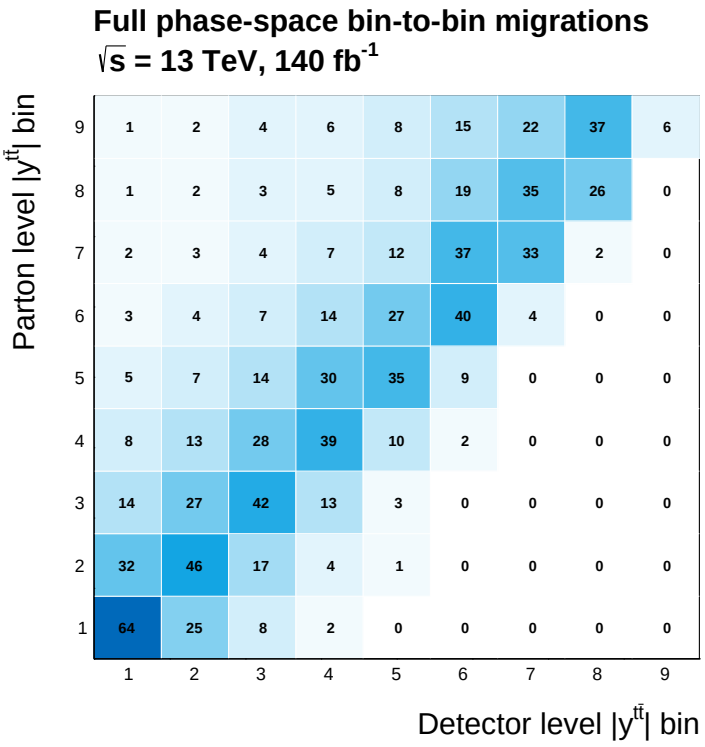

(c)

Figure 6.5: The (a) dilepton and (b) efficiency corrections, and the (c) detector-to-parton level migration matrix for the absolute $t\bar{t}$ rapidity in the resolved topology at parton level.

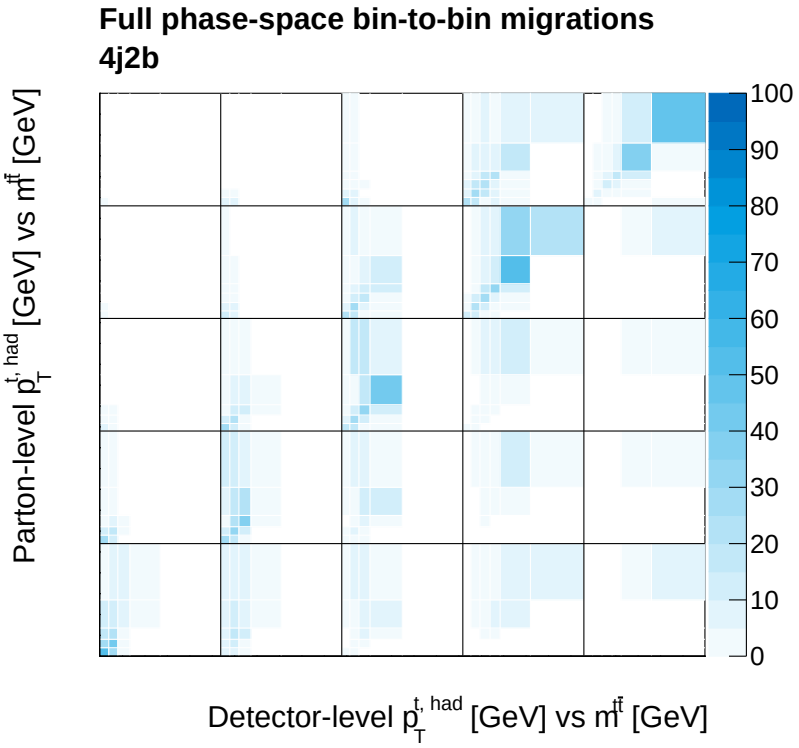

Figure 6.6: Detector-to-parton level migration matrix for the double differential cross-section as a function of the transverse momentum of the hadronic top in bins of the mass of the $t\bar{t}$ system.

6.5 Cross-section extraction

The extraction of the cross-sections can be divided into two main steps:

1. The following formula

$$N_i^{\text{unf}} = \frac{1}{\text{BR}} \frac{1}{\epsilon_i} \sum_j \mathcal{M}_{ij}^{-1} f_{\text{dilep}}^j \left(N_{\text{reco}}^j - N_{\text{bkg}}^j \right) \tag{6.12}$$

   is used to obtain the number of events in bin i at truth-level. The index j runs over bins at reco-level and the matrix $\mathcal{M}_{ij}^{-1}$ is the inverse of the migration matrix, obtained using the IBU. BR represents the branching ratio for the ℓ+jets channel, used to extrapolate the results to the full phase-space.

2. Eq. (6.12) can be used to extract single, double and triple differential

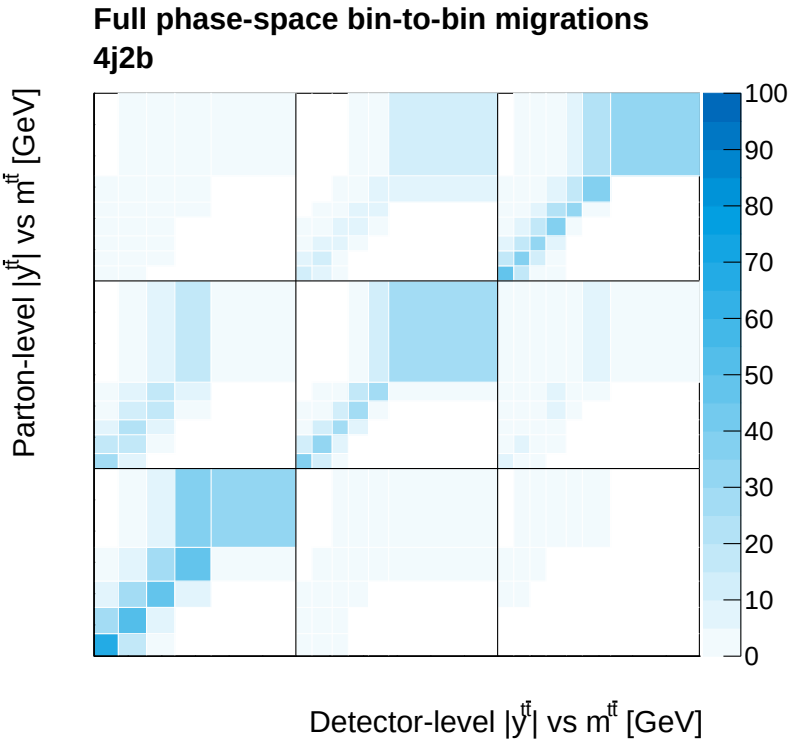

Figure 6.7: Detector-to-parton level migration matrix for the double differential cross-section as a function of the absolute rapidity of the $t\bar{t}$ system in bins of the mass of the $t\bar{t}$ system.

cross-sections using the following formulas:

$$\frac{d\sigma}{dX_i} \equiv \frac{1}{\mathcal{L}\Delta X_i} N_i^{\text{unf}} \tag{6.13}$$

$$\frac{d^2\sigma}{dX_i dY_j} \equiv \frac{1}{\mathcal{L}\Delta X_i \Delta Y_j} N_{ij}^{\text{unf}} \tag{6.14}$$

$$\frac{d^3\sigma}{dX_i dY_j dZ_k} \equiv \frac{1}{\mathcal{L}\Delta X_i \Delta Y_j \Delta Z_k} N_{ijk}^{\text{unf}} \tag{6.15}$$

where the index i (j, k) runs over bins of X (Y, Z) at reco-level, ΔX_i (ΔY_j, ΔZ_k) is the bin width and $\mathcal{L}$ is the integrated luminosity.

The procedure just described is used for single, double and triple differential distributions. The only difference in the cross-section extraction between these cases is that in the double and triple differential case, the N^{unf} vector is obtained concatenating all the bins, starting from the internal variables, and

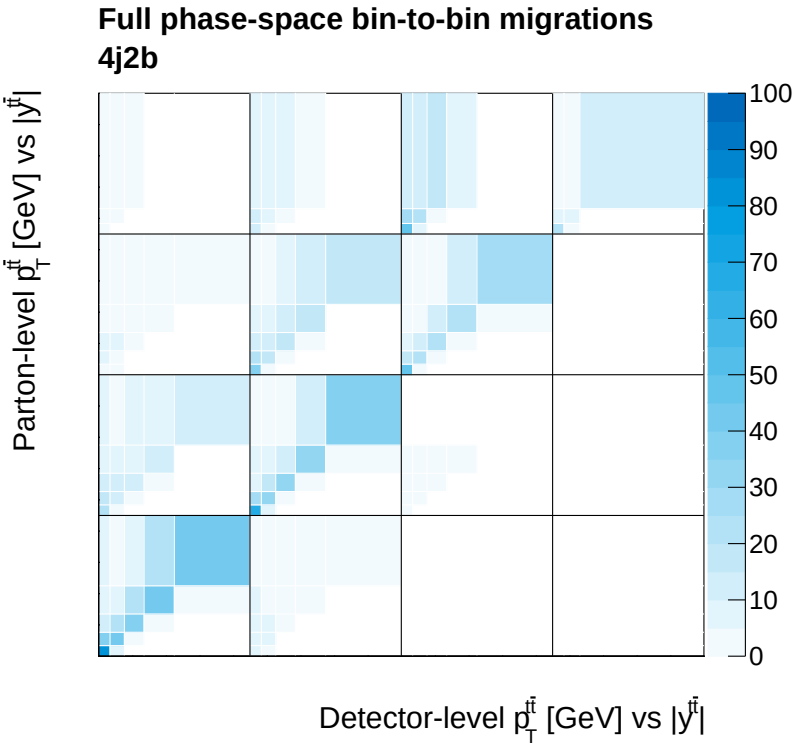

Figure 6.8: Detector-to-parton level migration matrix for the double differential cross-section as a function of the transverse momentum of the $t\bar{t}$ system in bins of the absolute rapidity of the $t\bar{t}$ system.

going up to the most external variable. The size of this vector will therefore be $m = \sum_{i=1}^{n_X} n_{Y,i}$ in the case of double differential cross-sections, where n_X is the number of bins of the variable X and $n_{Y,i}$ is the number of Y bins in the i-th bin of the variable X. The dimension of the vector is $l = \sum_{i=1}^{n_X} \sum_{j=1}^{n_{Y_i}} n_{Z,j}$ in the triple differential case, with a similar meaning as before for n_X, $n_{Y,i}$ and $n_{Z,j}$.

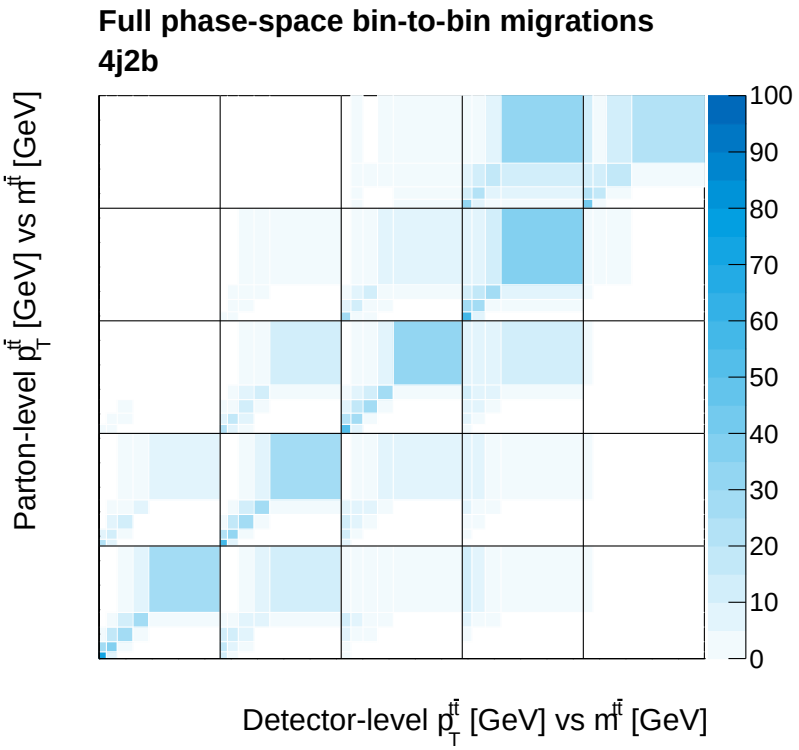

Figure 6.9: Detector-to-parton level migration matrix for the double differential cross-section as a function of the transverse momentum of the $t\bar{t}$ system in bins of the mass of the $t\bar{t}$ system.

Chapter 7

Systematic Uncertainties

The measured cross-sections are affected by different sources of systematic uncertainty, the main ones coming from background and signal modelling and from the detector.

For every observable, the uncertainties are evaluated after the unfolding procedure has been carried out. This is done varying the reconstructed nominal MC sample bin-by-bin for each source of systematic uncertainty. This varied samples are then used as if they were the nominal ones during the unfolding procedure. After the unfolding, the nominal cross-section and the one obtained with the varied sample are subtracted and their difference is used as uncertainty. In some cases only a $+1\sigma$ variation is available and in that case the procedure is carried out with this single variation and then symmetrized to obtain a $\pm 1\sigma$ uncertainty estimate.

For uncertainties due to modelling, alternative MC samples are used as nominal in a procedure similar to the one described above.

In the following sections, a more thorough description of the uncertainty sources is given.

7.1 Detector Systematics

Detector-related systematics are evaluated using Monte Carlo samples that model the way in which the detector responds to different reconstructed objects. These uncertainties are evaluated using samples containing varied signal and backgrounds. After the nominal background is subtracted ($N^j_{\text{reco}} - N^j_{\text{bkg}}$ in Eq. (6.12)) from the varied sample, it is unfolded using nominal correction factors.

7.1.1 Lepton Reconstruction

Uncertainties such as triggering, momentum resolution, reconstruction efficiency and identification energy of the electrons and muons are estimated using $Z \to ee/\mu\mu$, $J/\psi \to ee/\mu\mu$ and $W \to e\nu$ samples, with the procedure described in [119, 143]. These uncertainties are observed to have an impact of less than 1% across all the measured spectra.

7.1.2 Jet Reconstruction

The uncertainty related to the Jet Energy Scale (JES) is estimated using the uncertainties derived from simulation and in-situ calibration [144] and varying the jet energies accordingly. This systematic uncertainty consists of 30 uncorrelated components, coming from jet flavour composition, pile-up, single-particle response, and effects due to jets not contained in the calorimeters.

One of the main uncertainty source is the one related to Jet Energy Resolution (JER) differences between data and MC events. In order to evaluate this uncertainty, the MC jet transverse momentum is smeared according to the jet resolution as a function of the jet p_T and η [145]. The estimated uncertainty is about 5% in all the spectra, with slight reduction with increasing mass and p_T of the $t\bar{t}$ system.

7.1.3 *b*-tagging

The uncertainties related to *b*-tagging algorithms are divided in three different categories: *b*-tagging efficiency and mis-tag efficiencies for *c*- and light-jets tagged as *b*-jets [146–148]. These are parametrized with a set of 19 parameters depending on jet η and p_T. These uncertainties are estimated from data, in particular from correction factors that correct data-to-simulation differences. The *b*-tagging uncertainty is about 4% across all the spectra.

7.1.4 Missing Transverse Energy

E_T^{miss} measurements are affected by uncertainties in reconstructed objects and the so-called *soft-terms*, i.e. presence of low-p_T jets and calorimeter cells not included in the object reconstruction. These uncertainties are estimated from data using $Z \to \mu\mu$ events and from the symmetry between hard and soft component of the E_T^{miss} [149]. The uncertainty related to E_T^{miss} is found to be less than 1%.

7.1.5 Luminosity

The uncertainty in the combined 2015–2018 integrated luminosity is 0.83% [150], obtained using the LUCID-2 detector [151] for the primary luminosity measurements, complemented by measurements using the inner detector and calorimeters.

7.2 Signal Modelling Uncertainties

7.2.1 MC generator

Uncertainties related to the MC generator used to calculate the ME and to model the Parton Shower are described in the following paragraphs, component-by-component. In order to estimate these uncertainties, the MC samples described in Section 3.3.1 have been used.

Hard Scattering

The uncertainty due to the choice of the MC generator used for the implementation of the hard scattering model is computed by comparing the parton level distributions of an alternative signal sample generated with PowhegBox interfaced with Pythia 8, where the p_T^{hard} parameter is set to 1 following the prescription described in [152]. Both the nominal and alternative samples used for this uncertainty are simulated with the AFII settings, in order to save computation and storage resources. The uncertainty due to the hard scattering model is the dominant uncertainty in these measurements. It is found to increase with increasing $m^{t\bar{t}}$ values.

Hadronization and Parton Shower

The uncertainties coming from the choice of the hadronization and parton-shower model are assessed in a similar way of the Matrix Element uncertainty. The alternative sample used is generated with PowhegBox interfaced with Herwig. Also for this uncertainty the fast simulation samples have been used.

The uncertainty related to the parton shower is calculated using samples obtained with Powheg+Pythia 8 where the p_T^{hard} parameter is set to 1 instead of 0, like in the nominal sample.

7.2.2 Initial- and final-state QCD radiation for the signal sample

The amount of ISR/FSR changes the number of jets in the event as well as the transverse momemtum of the $t\bar{t}$ system. In order to evaluate the uncertainty linked to the modeling of the ISR/FSR, $t\bar{t}$ MC samples with modified ISR/FSR modeling were used. This is evaluated using a prediction obtained with POWHEG+PYTHIA 8 , where μ_R and μ_F in the hard scatter are varied simultaneously by a factor 0.5 and 2.0 and the scales in the showering are varied accordingly to the `Var3c` eigentune of the A14 tune [153]. These variations affects mainly ISR. Another parameter affecting ISR is h_{damp}. The uncertainty due to the choice of this parameter is estimated independently from the other ISR components using a dedicated POWHEG+PYTHIA 8 sample where h_{damp} is multiplied by a factor 1.5 with respect to the nominal value.

The uncertainty due to the FSR simulation is obtained using a sample obtained using POWHEG+PYTHIA 8 where the renormalization scale used in the final-state shower is varied by a factor 2 and 0.5 with respect to the nominal value.

7.2.3 Parton distribution functions

The impact of the choice of different PDF sets has been assessed by applying an event-by-event reweighting procedure to a $t\bar{t}$ sample generated with POWHEG+PYTHIA 8 using the 30 PDF set of the PDF4LHC15 prescription [154].

The effect of a different PDF choice modifies the efficiency, acceptance and potentially also the response matrix, i.e. the corrections used to correct the spectrum at the detector level to the particle and parton levels levels. The PDF choice effect has been evaluated by unfolding the nominal POWHEG+PYTHIA 8 sample using differently PDF-reweighted corrections. The so-called "intra-PDF" variations using the PDF4LHC15 were combined to define a relative uncertainty as

$$\delta_{\text{intra}} \equiv \frac{\sqrt{\sum_{i \in \text{sets}} (U_i \cdot R_0 - T_0)^2}}{T_0}$$

where the 0 (i) subscripts denotes the PDF4LHC15 central (varied) PDF set, R represents the distribution at the detector level while T symbolizes the distribution at the particle level, and the unfolding procedure is shortened into the U factor, with subscript on each characterizing the PDF set used

to evaluate the spectrum or the corrections. The resulting uncertainties are found to be at the sub-percent level.

7.2.4 Top-quark mass uncertainty

Since the kinematics of the decay products (and therefore the probability of passing the selection) depend on the the mass of the top-quark, which is known with a precision of around 0.5 GeV [155], a corresponding uncertainty is estimated. This is done using two additional MC samples, in which the value of the top-quark mass is set to 169 and 176 GeV. The setup of these two samples is, except for the mass of the top-quark, the same as the nominal one. The uncertainty is evaluated using the unfolded distributions obtained with the varied mass samples, in the same way as the other modelling uncertainties. The obtained result is then scaled by 1/7 to match the effect of the ± 0.5 GeV shift in the top-quark mass.

7.3 Background Modelling Systematics

The background in Monte Carlo simulations is also affected by both theoretical and experimental uncertainties. These uncertainties affect the unfolding procedure too, since the background is subtracted from the data.

To estimate these uncertainties, varied background samples are used, in samples that contain the nominal signal and the varied background, from which the nominal background is subtracted and then are unfolded using the nominal correction factors.

7.3.1 W+jets and Z+jets

The uncertainty on W+jets and Z+jets events is a conservative 50% variation that takes into account uncertainties coming from PDFs, α_S, μ_R and μ_F. The varied sample is unfolded and compared with the nominal one to estimate a one-sided uncertainty, which is then symmetrized. Uncertainties for W+jets samples are found to be larger in the mass of the $t\bar{t}$ system cross-sections, with respect to other spectra. This is due to the large fractional contribution of these samples in this kinematic region.

7.3.2 Single Top

Since the tW production channel is the who contributes most to the single top background, an uncertainty on the method used to handle interference

between tW and $t\bar{t}$ production was determined by comparing simulated tW sample that uses the DS method with the nominal one based on the DR scheme. Furthermore an overall uncertainty is applied separately to the s-, t- and tW-channels in order to take into account the uncertainties on PDFs, α_S, μ_R and μ_F.

7.3.3 Diboson and $t\bar{t}V$

A 40% uncertainty is considered for Diboson samples, so as to cover both the cross-section uncertainty and the uncertainty due to two extra jets being present.

A 14% uncertainty is considered for the $t\bar{t}V$ samples, so as to cover uncertainties coming from scale, α_s and the PDFs.

Both the samples undergo a procedure similar to the one used for the V+jets ones in order to estimate their uncertainties.

A more detailed breakup of the systematic uncertainties which affect the measurements is given in Chapter 8.

Chapter 8

Results

In this chapter the measurements are presented in the form of single, double and, for the very first time, triple differential cross-sections. These are presented as a function of several kinematic variables related to the top-quark and the $t\bar{t}$ system. In particular, the chosen observables are the mass, transverse momentum and rapidity of the $t\bar{t}$ system ($m^{t\bar{t}}$, $p_T^{t\bar{t}}$ and $y^{t\bar{t}}$), while for the hadronically decaying top quark, the transverse momentum and rapidity have been chosen ($p_T^{\mathrm{t,had}}$, $y^{\mathrm{t,had}}$).

The measured cross-sections have been compared with event generator MC predictions, in particular with Powheg+Pythia 8 and `MiNNLOPS` predictions. In order to compare the results with available fixed-order predictions, a slightly different binning choice has been used. These predictions are NNLO in pQCD and are obtained using the `MATRIX` [36] program or provided by Czakon, Mitov and Papanastasiou [156]. The `MATRIX` calculations have been performed at NNLO with a numerical precision of 0.1%, using the `NNPDF3.1` set. The renormalization and factorization scales have been set to $\mu_R = \mu_F = H_T/4$, where H_T is the scalar sum of the transverse momenta of all the final state objects. For the p_T of the hadronically decaying top, the scales were set to $\mu_R = \mu_F = m_T^{t\bar{t}}$, where $m_T^{t\bar{t}}$ is the transverse mass of the $t\bar{t}$ system. This choices were made to reflect the setting of the previously provided theoretical predictions.

8.1 Full phase-space cross-sections

8.1.1 Single differential cross-sections

Single differential cross-sections are reported in Fig. 8.1 as a function of top-quark-related kinematic observables, and in Fig. 8.3 as a function of

kinematic observables related to the $t\bar{t}$ system. In Figs. 8.2 and 8.4 the fractional uncertainties for the same cross-sections are shown, with a complete breakdown of the systematic uncertainty components; the same results are shown, in tabular form in Appendix B. A good agreement with MC generators predictions is observed overall. A tendency of all NLO MC predictions to overestimate the data in the high-p_T and high-m regions is observed, which is somewhat mitigated (especially in the $p_T^{t\bar{t}}$ spectrum, Fig. 8.3(a)) when using the `MiNNLOPS` predictions. The largest contribution to systematic uncertainties comes from background estimation, b-tagging, jet energy scale and resolution and initial and final state radiation.

A novelty aspect of this analysis is that, for the first time, single differential cross-sections have been measured in the high-$m^{t\bar{t}}$ region (2 TeV $< m^{t\bar{t}} <$ 5 TeV). The upper limit for both the transverse momentum of the $t\bar{t}$ system and the hadronic top-quark have also been extended with respect to a previously published analysis [136]. MC predictions show a very good agreement with data and between themselves in both rapidity distributions.

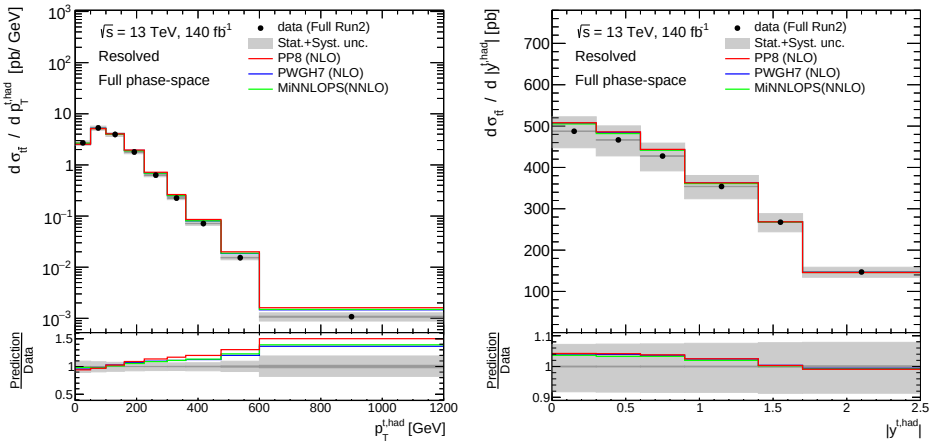

(a) (b)

Figure 8.1: Parton-level differential cross-sections as a function of (a) the transverse momentum and (b) the rapidity of the top quark, compared with the POWHEG+PYTHIA 8 (PP8), POWHEG+HERWIG7 (PWGH7) and MiNNLOPS Monte Carlo generators. The gray bands indicate the total uncertainty on the data in each bin. Data points are placed at the center of each bin.

Comparison with NNLO fixed order and MC predictions

The same single differential cross-sections are here presented in comparison with fixed order NNLO predictions and the nominal signal sample in Figs. 8.5 and 8.6. A different binning was used in order to compare the results with

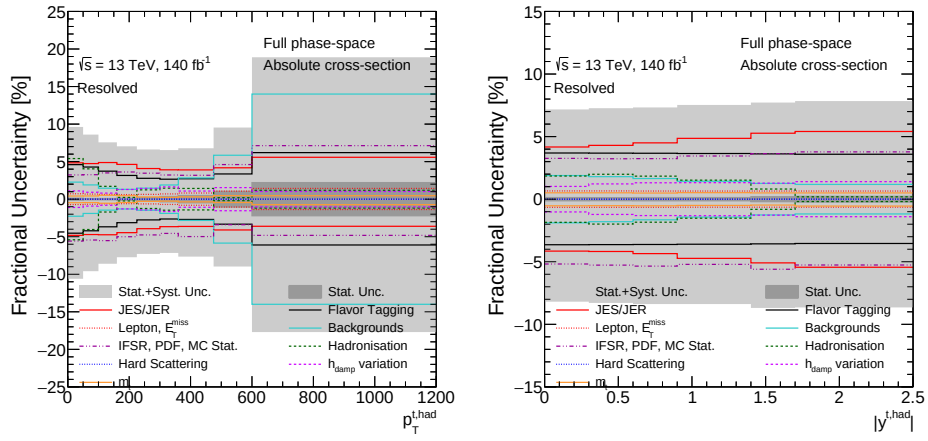

(a) (b)

Figure 8.2: Fractional uncertainties for parton-level differential cross-sections as a function of (a) the transverse momentum and (b) the rapidity of the top quark. The gray bands indicate the total uncertainty on the data in each bin.

available fixed order predictions. The overall agreement is good, between uncertainties, with both fixed order predictions, which are in better agreement with data than NLO MC samples in the high-mass and high-momentum region. The uncertainties due to choices of the factorization and renormalization scales, μ_F and μ_R, in the perturbative QCD calculations are evaluated by calculating the cross-sections varying these scales independently by a factor of 2 or 0.5. This procedure results in seven variations: $(\mu_R, \mu_F) = ((1,1),(2,1),(1,2),(0.5,1),(1,0.5),(0.5,0.5),(2,2))$. The envelope of all the variation is used as uncertainty.

8.1.2 Double differential cross-sections

The double differential cross-sections are shown in Figs. 8.7 to 8.10. These are presented as a function of the aforementioned kinematic observables relative to the $t\bar{t}$ system and the hadronic top-quark.

The measured double differential cross-sections show a good overall agreement with the MC predictions, in particular in the distributions presented as a function of the rapidity of the $t\bar{t}$ system. In the distributions including the transverse momentum of the $t\bar{t}$ system, it can be seen that the `MiNNLOPS` MC predictions describe data much better than the other (NLO) MC generators. A similar, less pronounced, effect is observed in the distributions expressed as functions of the transverse momentum of the hadronic top. All the MC predictions show a general tendency to overestimate the data in the high-mass

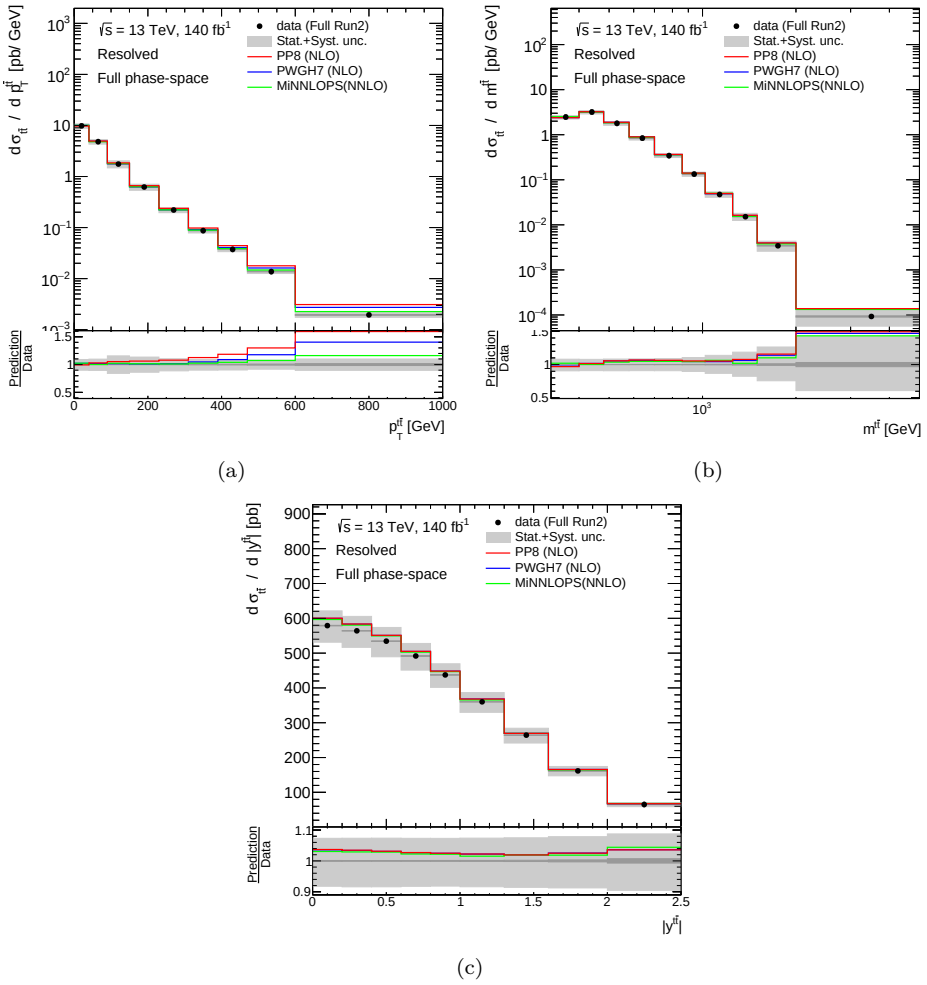

Figure 8.3: Parton-level differential cross-sections as a function of (a) the transverse momentum, (b) the invariant mass and (c) the absolute rapidity of the $t\bar{t}$ system, compared with the POWHEG+PYTHIA 8 (PP8), POWHEG+HERWIG7 (PWGH7) and MiNNLOPS Monte Carlo generators. The gray bands indicate the total uncertainty on the data in each bin. Data points are placed at the center of each bin.

region, which increases with increasing mass and increasing p_T.

8.1.3 Triple differential cross-sections

The triple differential cross-sections as a function of the hadronic top p_T and rapidity and as functions of the mass, rapidity and momentum of the $t\bar{t}$ system are shown in Figs. 8.11 to 8.13, while Figs. 8.14 and 8.15 show the ratio of various MC predictions with respect to the measured data and the breakdown of the uncertainties for the triple differential cross-section as a

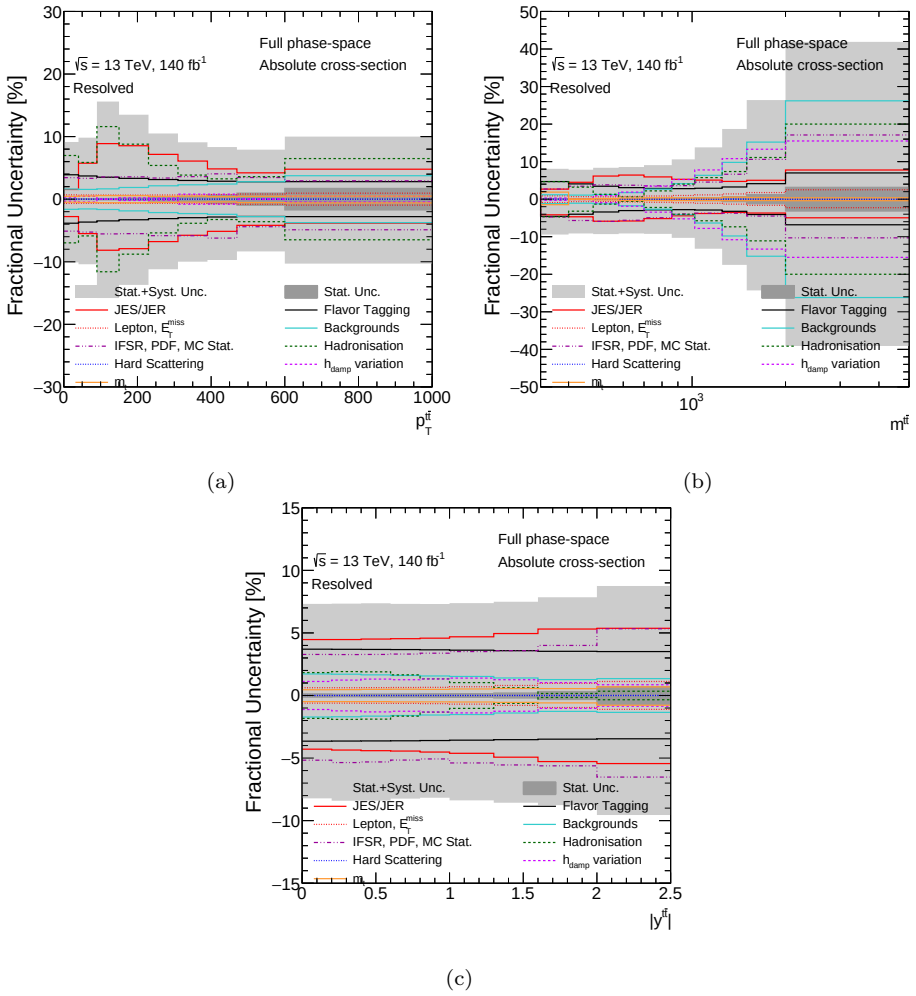

Figure 8.4: Fractional uncertainties for parton-level differential cross-sections as a function of (a) the transverse momentum, (b) the invariant mass and (c) the absolute rapidity of the $t\bar{t}$ system. The gray bands indicate the total uncertainty on the data in each bin.

function of $m^{t\bar{t}}$ in bins of $p_T^{\mathrm{t,had}}$ in bins of $|y^{\mathrm{t,had}}|$, respectively.

A good agreement is observed between the measured triple differential cross-sections and predictions obtained using MC event generators, both NLO and NNLO. In these distributions, differences with MC predictions tend to increase with increasing $m^{t\bar{t}}$, increasing $p_T^{\mathrm{t,had}}$, and increasing $|y^{\mathrm{t,had}}|$. This effect could be due to low statistics of the MC samples in these regions of the phase space. The total uncertainty assess to less than 20% in most of the bins, and less than 40% everywhere, with a statistical uncertainty well below 5% in all the regions of the phase space.

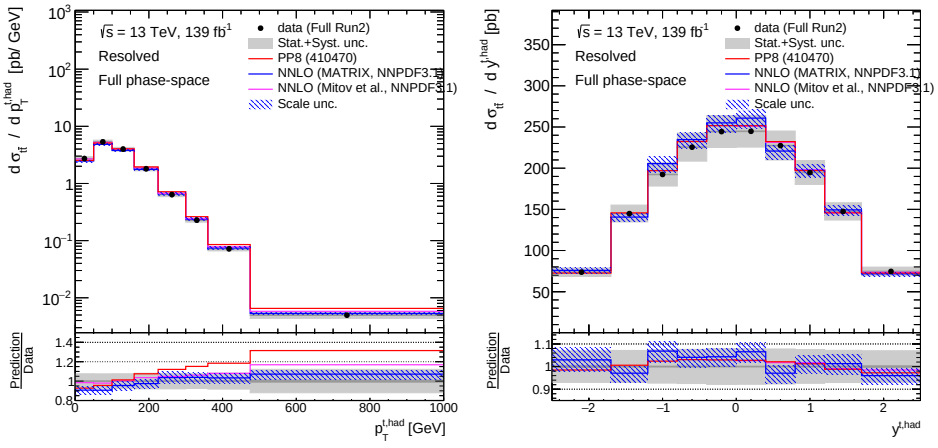

(a) (b)

Figure 8.5: Parton-level differential cross-sections as a function of (a) the transverse momentum and (b) the rapidity of the top quark, compared with the NNLO predictions and the POWHEG+PYTHIA 8 (PP8) Monte Carlo generator. The gray bands indicate the total uncertainty on the data in each bin and the blue etched band is the uncertainty on the choice of the scales for the `MATRIX` predictions. Data points are placed at the center of each bin.

8.2 Future developments

The measurements performed in this analysis probe some (until now) unexplored regions of the phase space, while also being very precise. Both these aspects could be exploited in future phenomenological analyses.

In particular, a global PDF fit could greatly benefit from such a precise measurement, especially from using triple differential cross-sections. The information contained in $t\bar{t}$ data could be particularly useful in constraining the gluon PDF, helping in reducing PDF uncertainties.

An analysis focusing on the extraction of a fundamental quantity of the SM such as the top-quark mass, m_t, could also exploit these data. This would be done performing a χ^2 fit in which the preferred value for this parameter would be inferred from data.

While this thesis focuses on the measurements performed at parton-level, a similar particle-level one is being performed by the ATLAS collaboration.

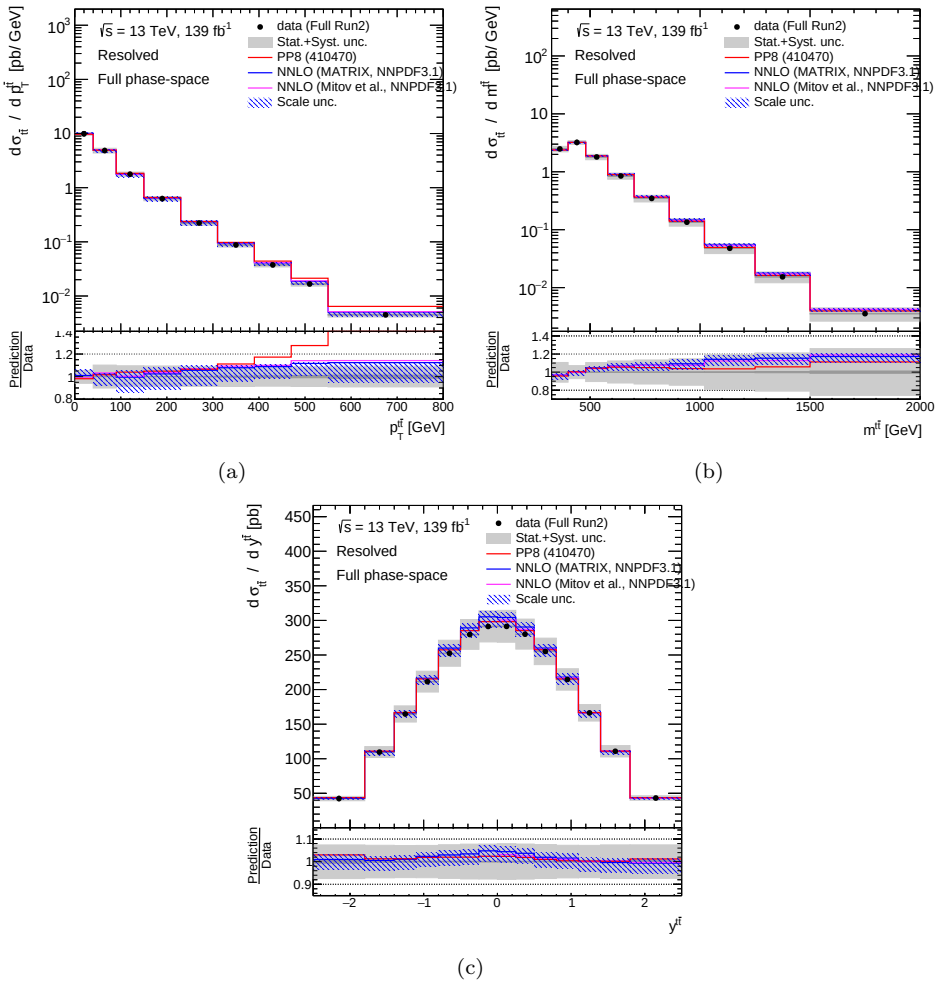

Figure 8.6: Parton-level differential cross-sections as a function of (a) the transverse momentum, (b) the invariant mass and (c) the rapidity of the $t\bar{t}$ system, compared with the NNLO predictions and the POWHEG+PYTHIA 8 (PP8) Monte Carlo generator. The gray bands indicate the total uncertainty on the data in each bin and the blue etched band is the uncertainty on the choice of the scales for the `MATRIX` predictions. Data points are placed at the center of each bin.

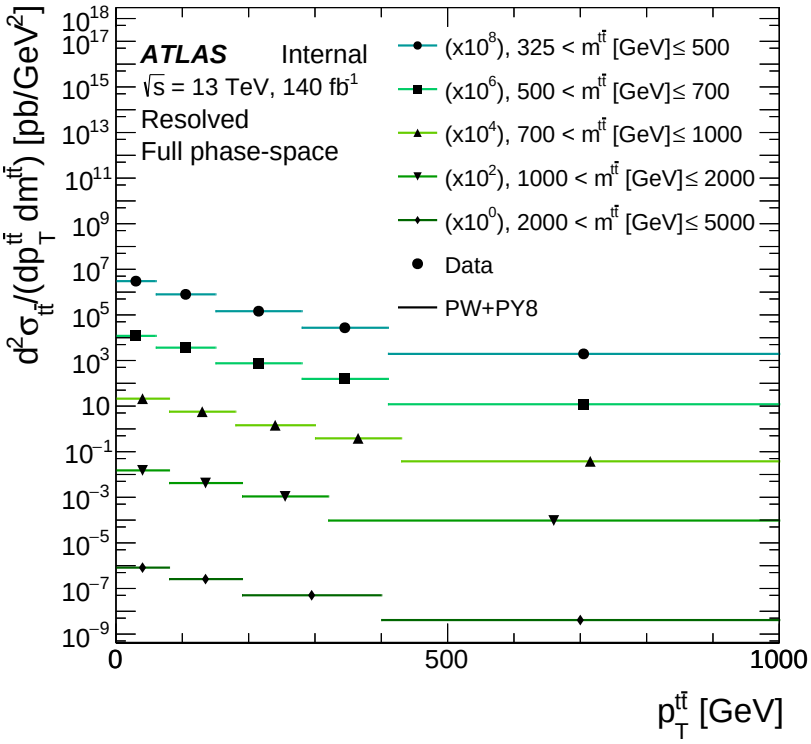

(a)

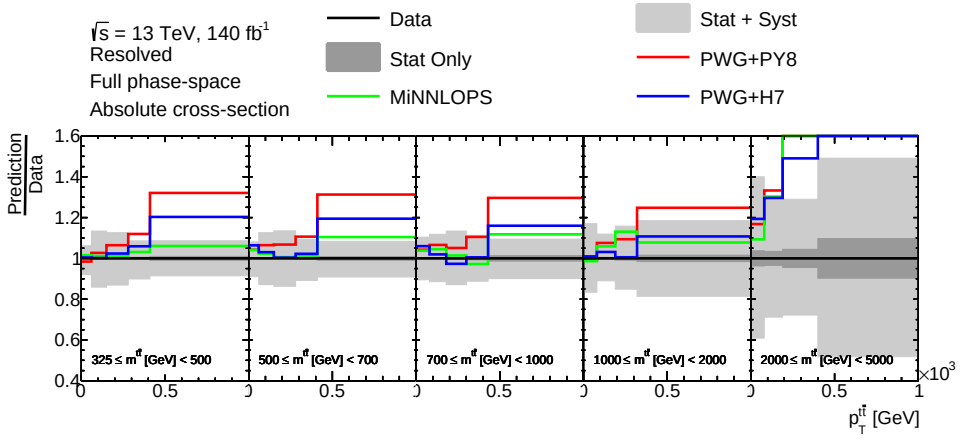

(b)

Figure 8.7: Parton-level double differential cross-sections as a function of the transverse momentum of the $t\bar{t}$ system in bins of the invariant mass of the $t\bar{t}$ system. The cross-sections shown in (a) are scaled for plotting purposes. The cross-sections are compared to the nominal MC prediction. The plot in (b) is the ratio of various MC predictions with respect to the measured cross-sections for each $m^{t\bar{t}}$ bin.

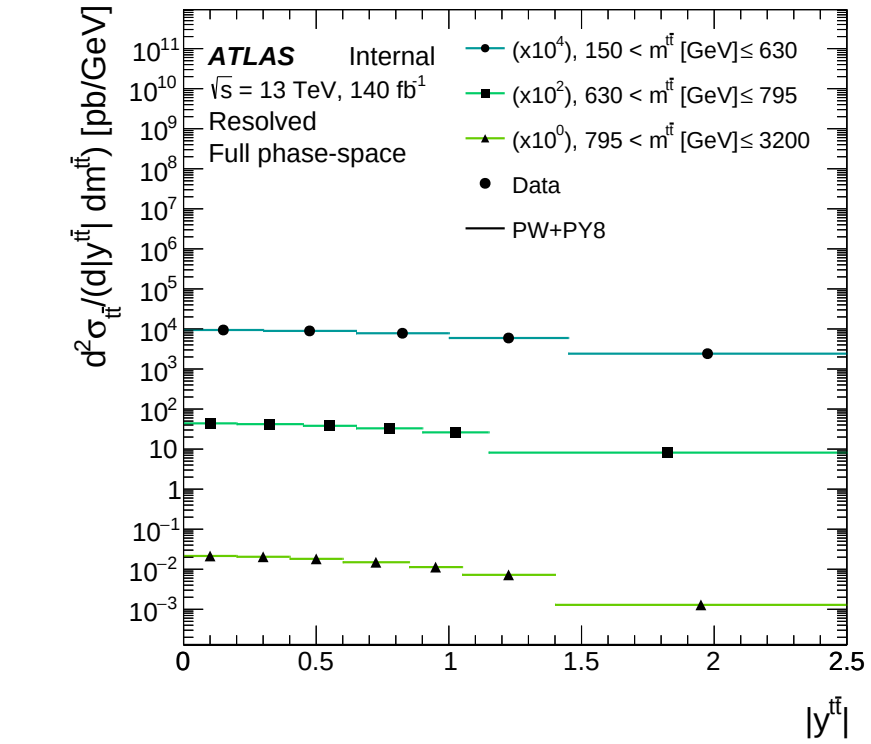

(a)

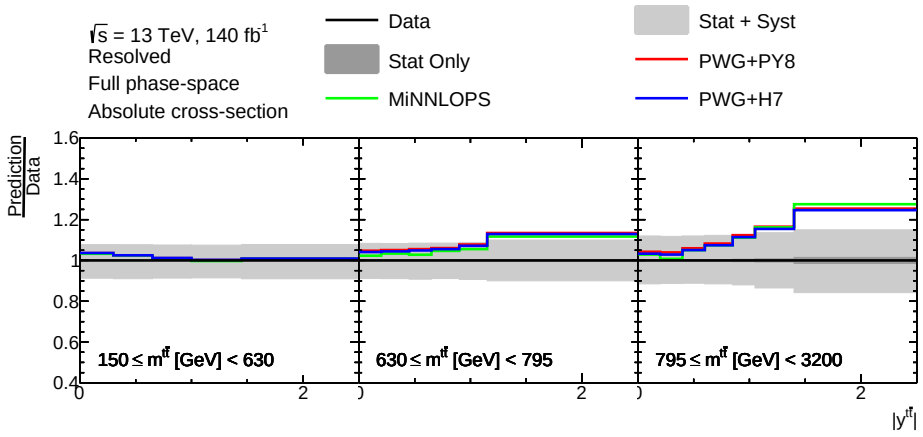

(b)

Figure 8.8: Parton-level double differential cross-sections as a function of the absolute rapidity of the $t\bar{t}$ system in bins of the invariant mass of the $t\bar{t}$ system. The cross-sections shown in (a) are scaled for plotting purposes. The cross-sections are compared with nominal MC prediction. The plot in (b) is the ratio of various MC predictions with respect to the measured cross-sections for each $m^{t\bar{t}}$ bin. The gray bands indicate the total uncertainty on the data in each bin.

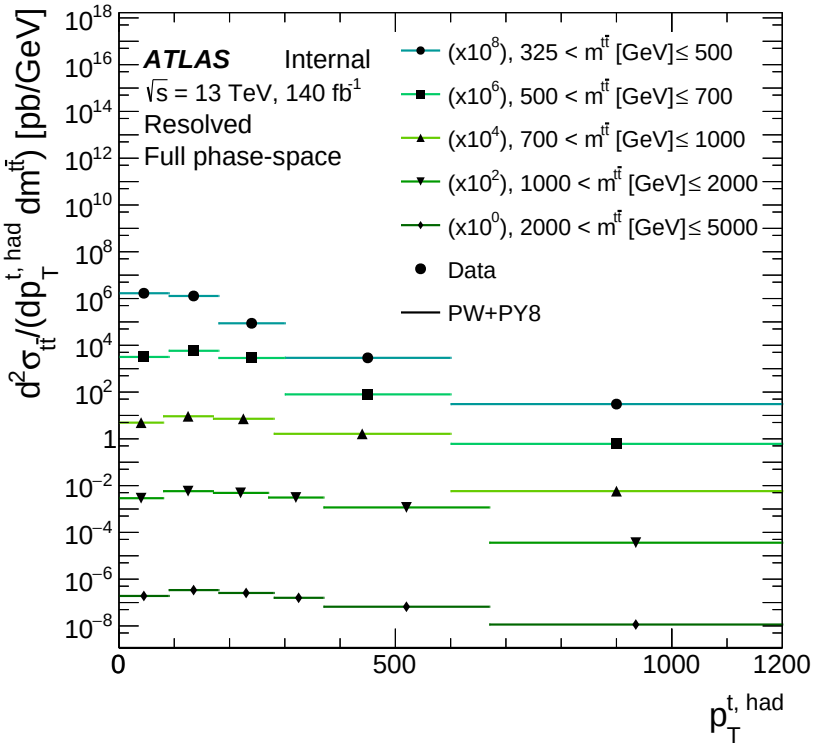

(a)

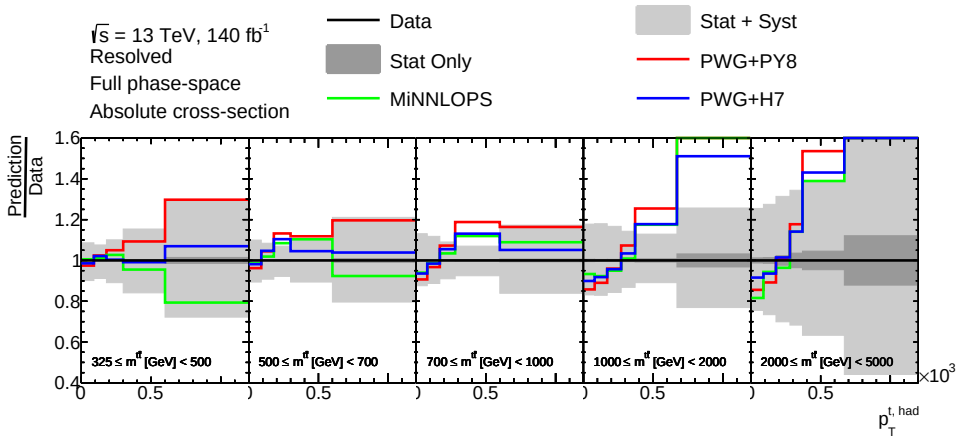

(b)

Figure 8.9: Parton-level double differential cross-sections as a function of the transverse momentum of the hadronic top in bins of the invariant mass of the $t\bar{t}$ system. The cross-sections shown in (a) are scaled for plotting purposes. The cross-sections are compared with the nominal MC prediction. The plot in (b) is the ratio of various MC predictions with respect to the measured cross-sections for each $m^{t\bar{t}}$ bin. The gray bands indicate the total uncertainty on the data in each bin.

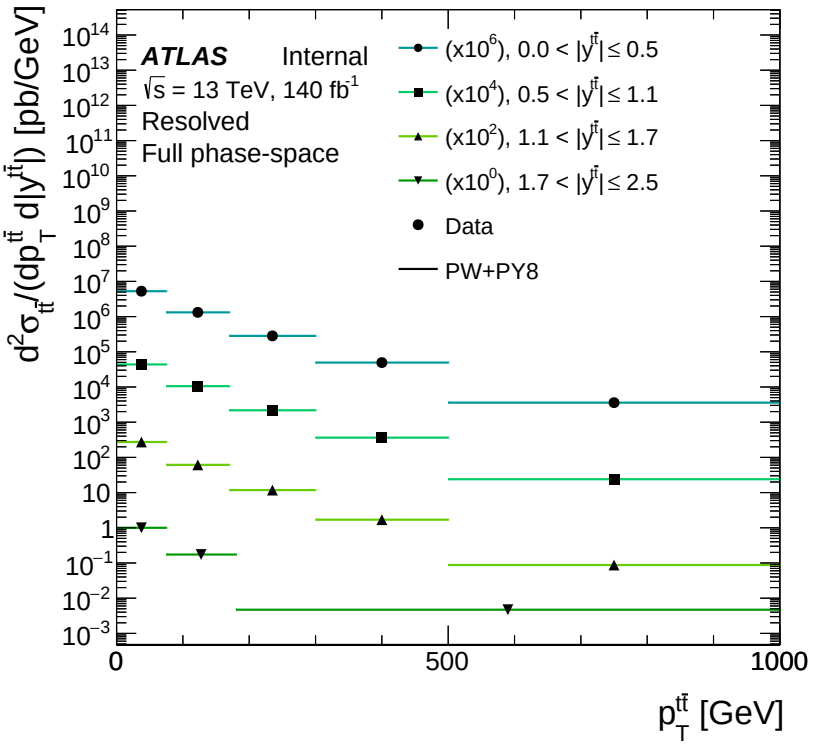

(a)

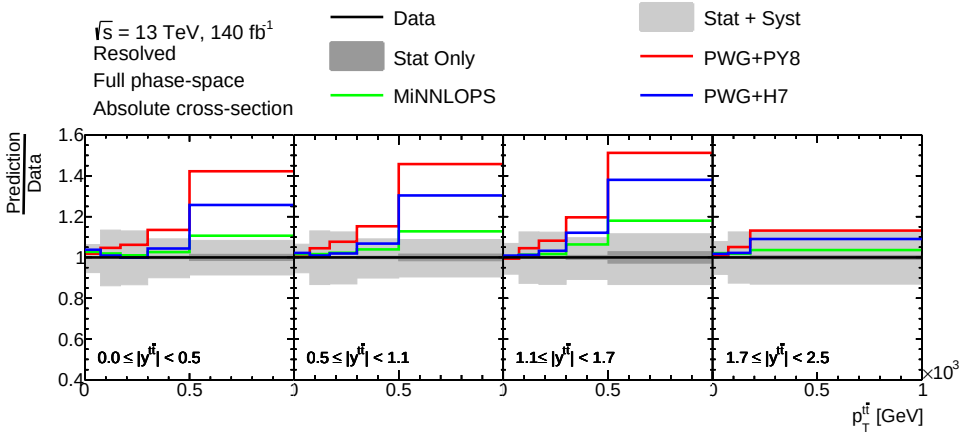

(b)

Figure 8.10: Parton-level double differential cross-sections as a function of the transverse momentum of the $t\bar{t}$ system in bins of the absolute rapidity of the $t\bar{t}$ system. The cross-sections shown in (a) are scaled for plotting purposes. The cross-sections are compared with the nominal MC prediction. The plot in (b) is the ratio of various MC prediction with respect to the measured cross-sections for each $|y^{t\bar{t}}|$ bin. The gray bands indicate the total uncertainty on the data in each bin.

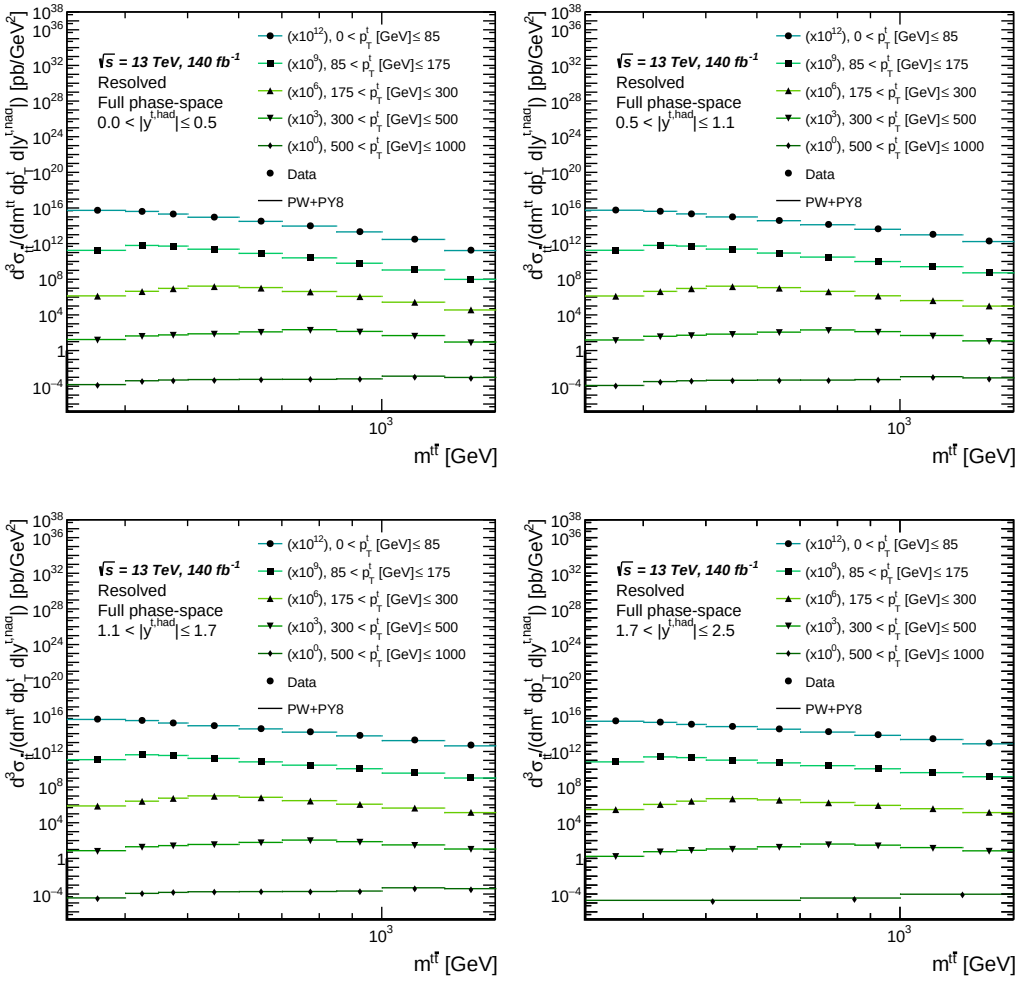

Figure 8.11: Parton-level triple differential cross-sections as a function of $m^{t\bar{t}}$ in bins of $p_T^{\mathrm{t,had}}$ in bins of $|y^{\mathrm{t,had}}|$. The cross-sections shown are scaled for plotting purposes.

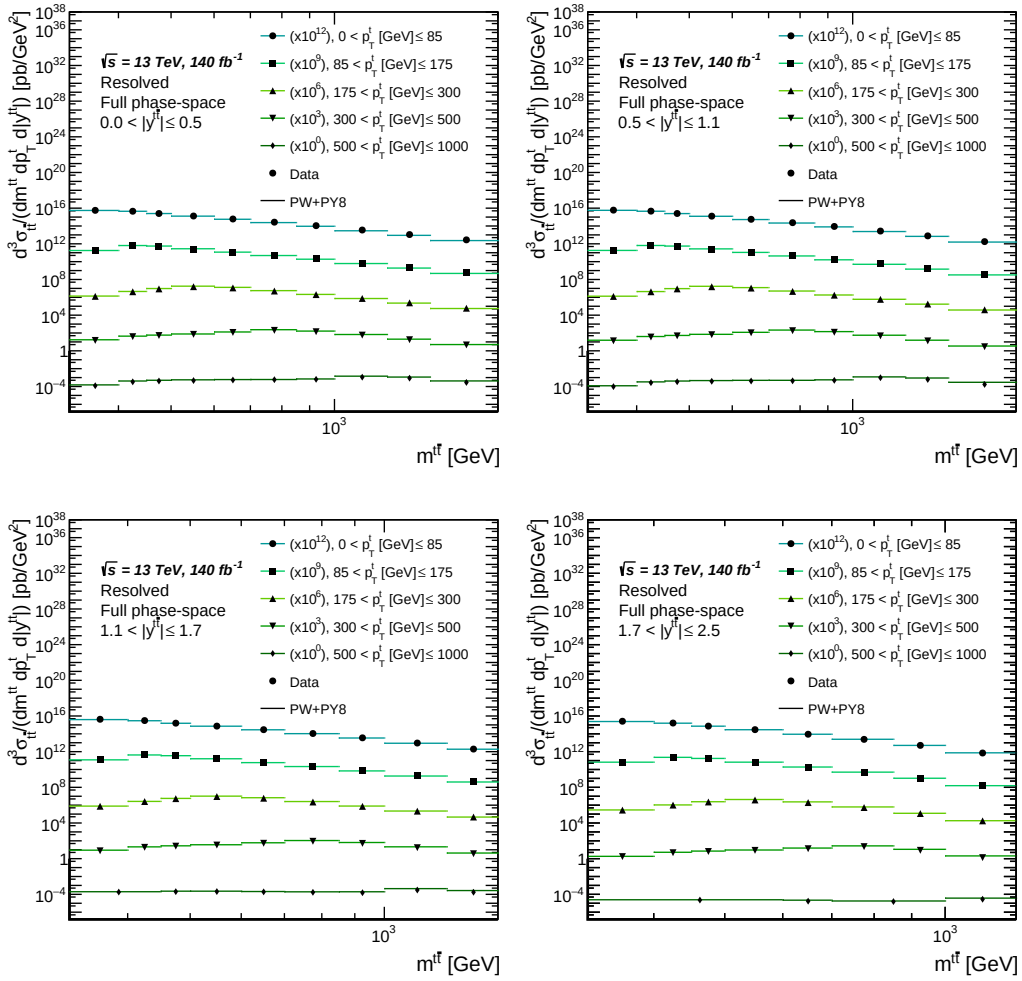

Figure 8.12: Parton-level triple differential cross-sections as a function of $m^{t\bar{t}}$ in bins of $p_T^{\mathrm{t,had}}$ in bins of $|y^{t\bar{t}}|$. The cross-sections shown are scaled for plotting purposes.

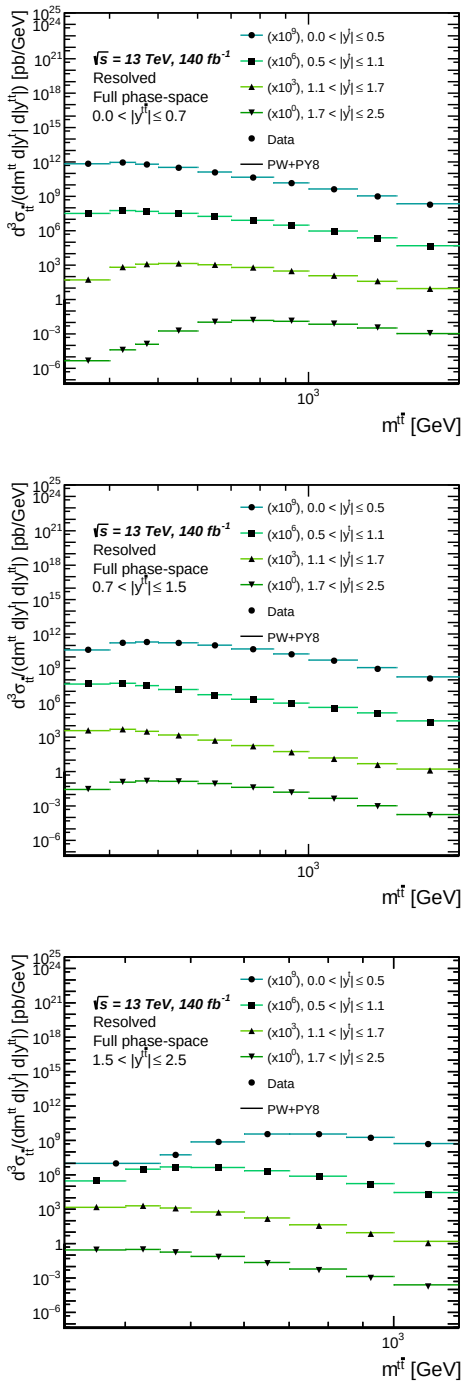

Figure 8.13: Parton-level triple differential cross-sections as a function of $m^{t\bar{t}}$ in bins of $|y^{\mathrm{t,had}}|$ in bins of $|y^{t\bar{t}}|$. The cross-sections shown are scaled for plotting purposes.

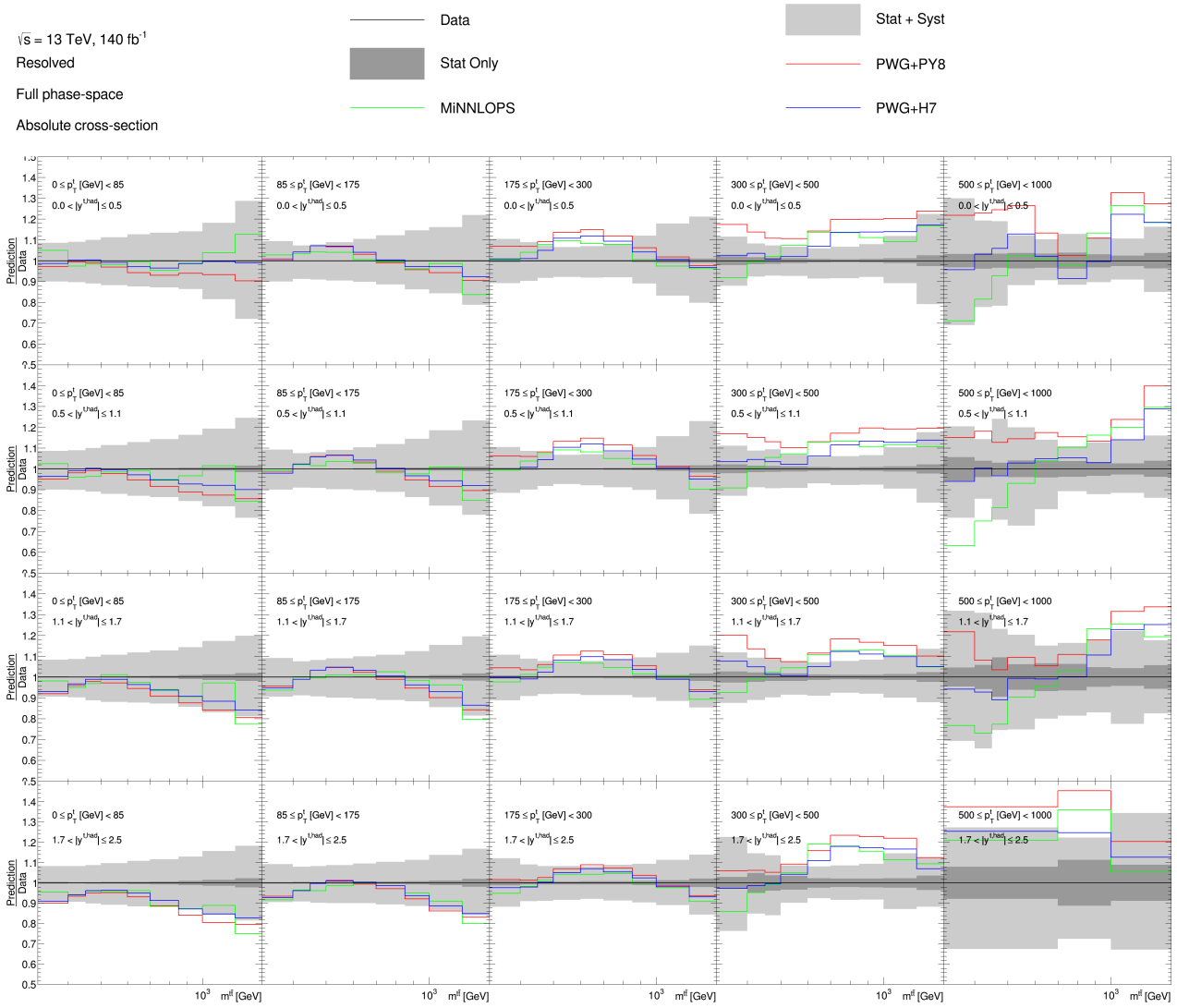

Figure 8.14: Ratio of various MC predictions with respect to the parton-level triple differential cross-section as a function of $m^{t\bar{t}}$ in bins of $p_T^{\mathrm{t,had}}$ in bins of $|y^{\mathrm{t,had}}|$. The gray bands indicate the total uncertainty on the data in each bin.

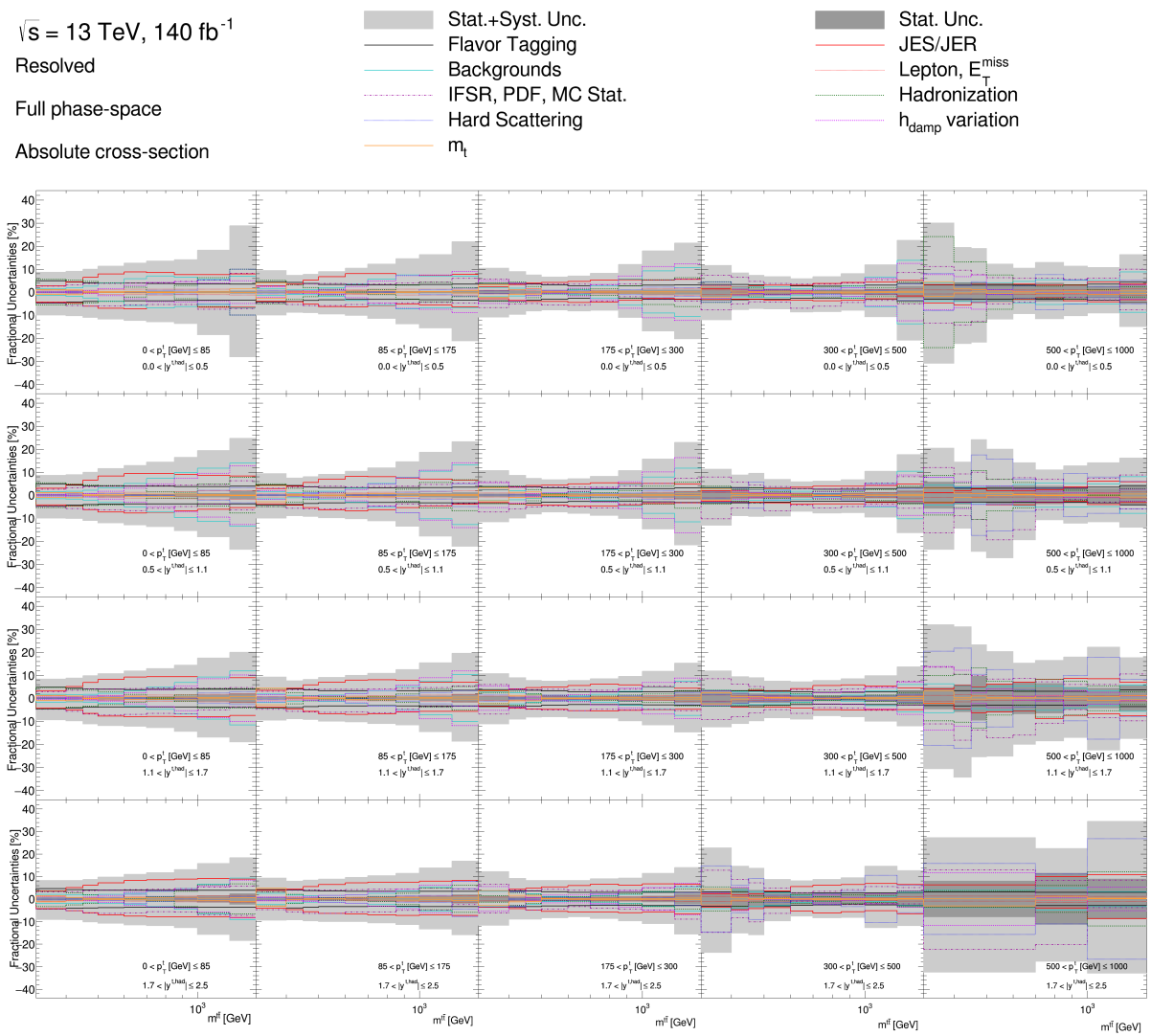

Figure 8.15: Breakdown of the uncertainties for the triple differential cross-section as a function of $m^{t\bar{t}}$ in bins of $p_T^{\mathrm{t,had}}$ in bins of $|y^{\mathrm{t,had}}|$. The gray bands indicate the total uncertainty on the data in each bin.

Conclusions

In this thesis, single, double and triple differential cross-sections have been measured for $t\bar{t}$ production at a CoM of $\sqrt{s} = 13$ TeV using data collected during the full Run 2 by the ATLAS detector. These correspond to an integrated luminosity of 140 fb^{-1}. The analysis was performed using semileptonic $t\bar{t}$ events, i.e. events in which one of the produced top quarks decays leptonically, while the other decays hadronically. To select these events, at least four jets were required to pass the selection, together with the requirement of exactly one lepton in the final state. A further b-tagging-based requirement was applied to improve the purity of the semileptonic events.

Single, double and triple differential cross-sections were measured in the full phase-space and are presented in this thesis as a function of kinematic observables related to the hadronic top or the $t\bar{t}$ system. Double and triple differential cross-sections give more detailed information on the properties of the top-quark and its production.

The main goal of this analysis is to provide a precise measurement suitable for the extraction of parton distribution functions of the proton and fundamental properties of the top-quark, while also providing a stringent test of pQCD fixed-order and new MC predictions.

The measured observables were compared with predictions obtained the most recent open-source program `MATRIX` and the state-of-the-art Monte Carlo generator at the NNLO level `MiNNLOPS`. The same measurements were also compared with other available MC predictions. These comparisons show a good overall agreement with both fixed-order and Monte Carlo predictions, with some of the single differential distributions, namely the mass of the $t\bar{t}$ system and the transverse momenta, showing trends that are however generally covered by the uncertainties except in the very high-mass and high-p_T regions. The differences with MC predictions are generally improved by using the `MiNNLOPS` generator. Similar trends are observed in double and triple differential cross-sections, to which the same considerations apply.

Finally, differences between standard ATLAS decay tables for the EvtGen MC generator and new ones made available by the BELLE II collaboration

were studied (Appendix C). The biggest differences were observed in distributions related to the multiplicity of decay products coming from heavy flavour hadrons. Differences up to 40% were also observed when comparing the results with different MC event generators. In order to validate the changes in the decay tables and compare the results with other Monte Carlo simulations, a Rivet routine was prepared that contains all the relevant distributions.

Appendix A

e+jets and μ+jets control plots

In this appendix the data-to-Monte Carlo control plots are presented separately for the e+jets channel, Figures A.1, A.2, A.3, A.4, and for the μ+jets channel, Figures A.5, A.6, A.7, A.8.

The data-Monte Carlo agreement is the same in both the channel, with the exception of the angular observables in which there is the contribution due to the crack region.

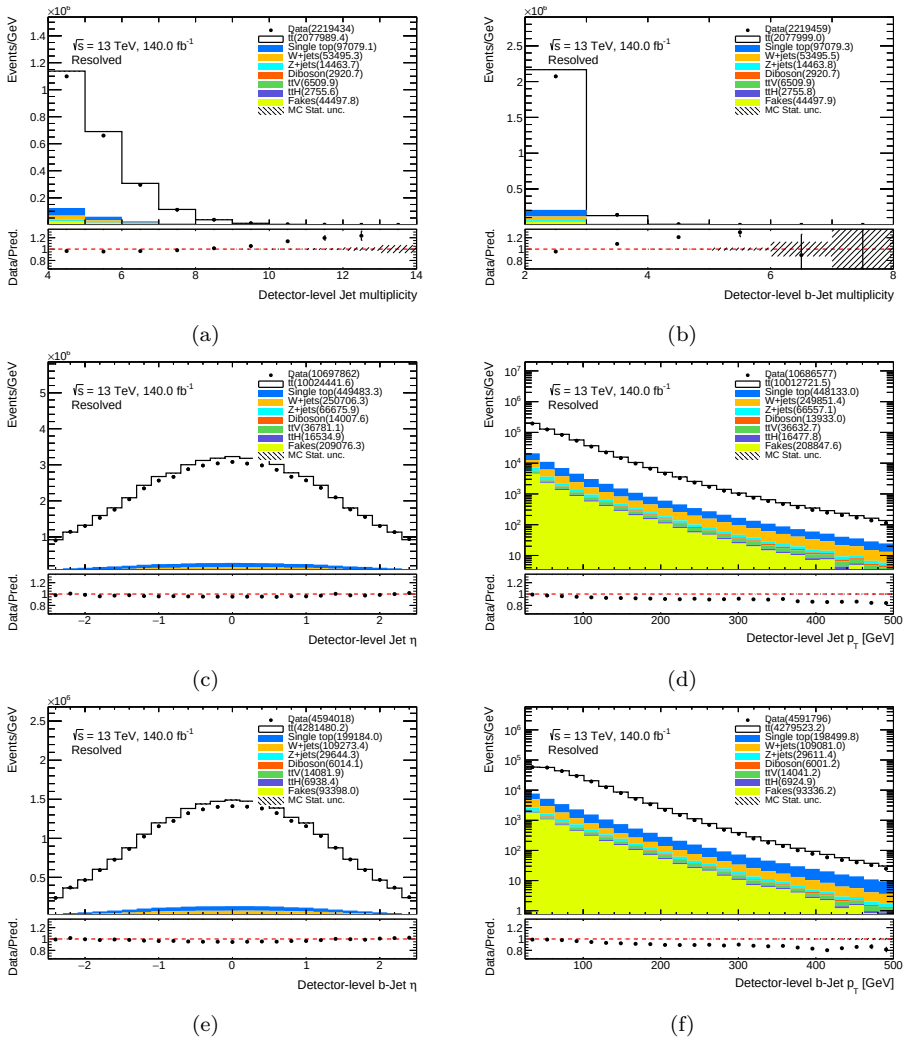

Figure A.1: Comparison of measured data and Monte Carlo simulations for basic kinematic observables in the e+jets channel at detector level: (a) multiplicity of jets, (b) multiplicity of $b-$jets, (c) pseudorapidity of the jets, (d) transverse momentum of the jets, (e) pseudorapidity of the $b-$jets, (f) transverse momentum of the $b-$jets. The data, represented by the dots in the plots, is directly compared with the total Monte Carlo simulations, represented by the different colors stacked histograms. The uncertainty band represents the statistical uncertainty in the MC sample, while bars on data points represent the uncertainty on data.

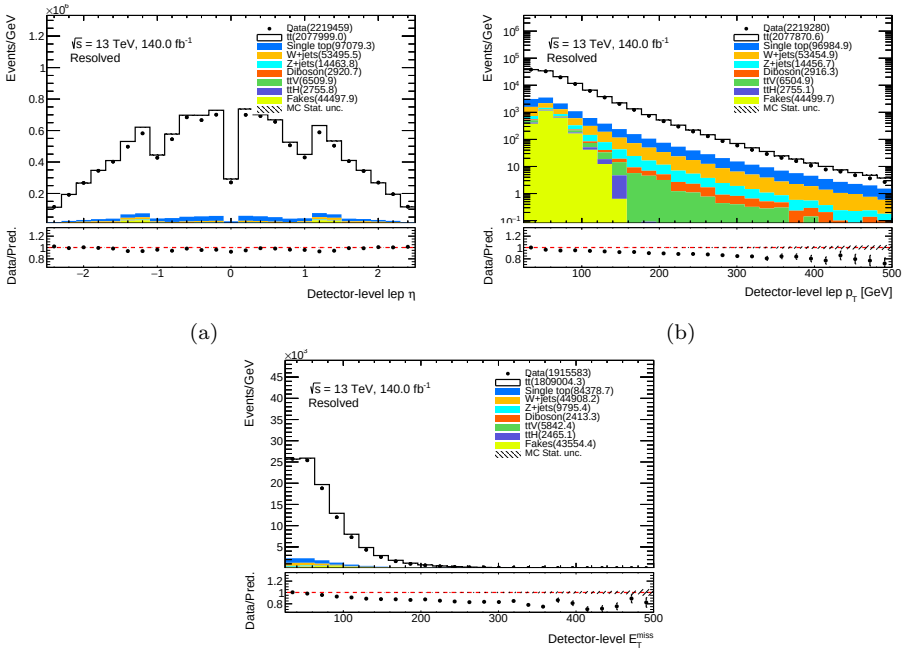

Figure A.2: Comparison of measured data and Monte Carlo simulations for basic kinematic observables in the e+jets channel at detector level: (a) pseudorapidity of the produced lepton, (b) transverse momentum of the produced lepton, (c) missing transverse energy. The data, represented by the dots in the plots, is directly compared with the total Monte Carlo simulations, represented by the different colors stacked histograms. The uncertainty band represents the statistical uncertainty in the MC sample, while bars on data points represent the uncertainty on data.

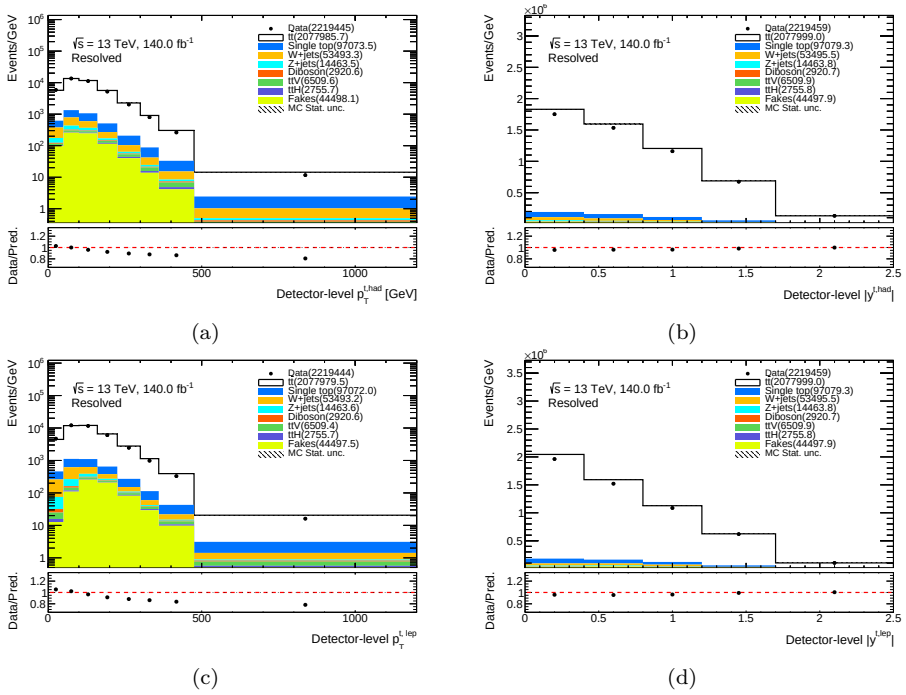

Figure A.3: Kinematic observables for the leptonically and hadronically decaying top quarks reconstructed with the Pseudo-Top algorithm: (a) transverse momentum and (b) pseudorapidity of the hadronic top; (a) transverse momentum and (b) pseudorapidity of the leptonic top. The data, represented by the dots in the plots, is directly compared with the total Monte Carlo simulations, represented by the different colors stacked histograms. The uncertainty band represents the statistical uncertainty in the MC sample, while bars on data points represent the uncertainty on data.

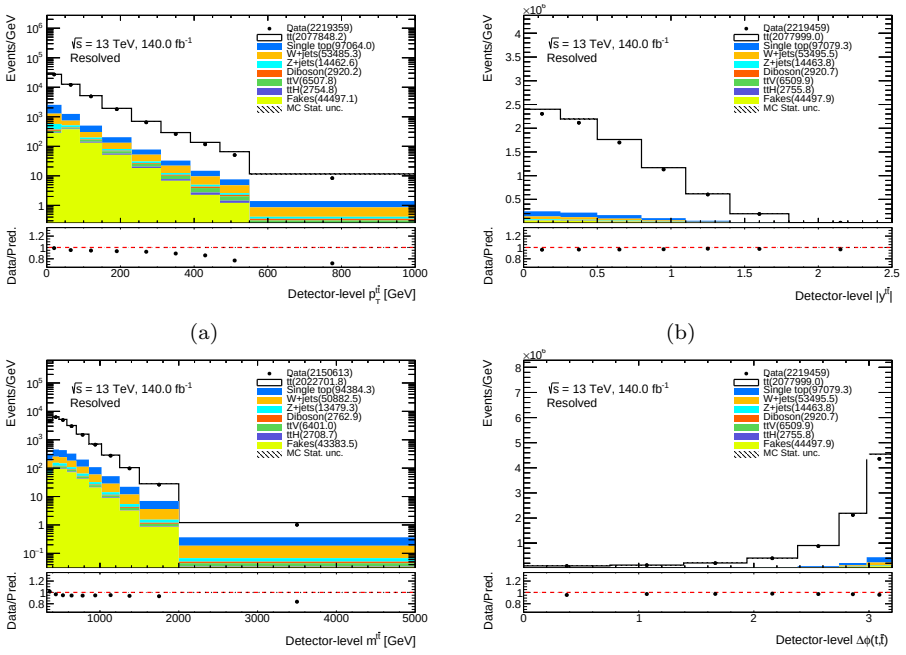

Figure A.4: Kinematic observables for the $t\bar{t}$ system reconstructed with the Pseudo-Top algorithm: transverse momentum (a), rapidity (b), invariant mass (c) and the azimuthal angle difference (d). The data, represented by the dots in the plots, is directly compared with the total Monte Carlo simulations, represented by the different colors stacked histograms. The uncertainty band represents the statistical uncertainty in the MC sample, while bars on data points represent the uncertainty on data.

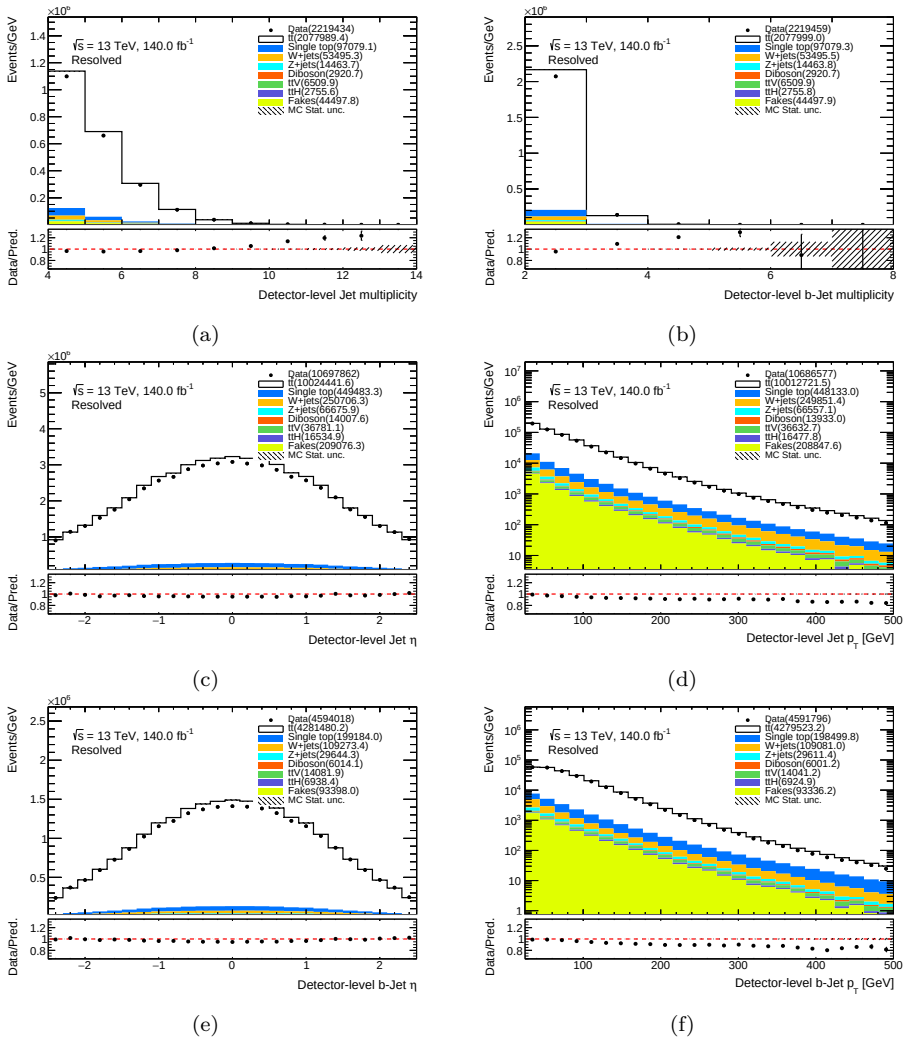

Figure A.5: Comparison of measured data and Monte Carlo simulations for basic kinematic observables in the μ+jets channel at detector level: (a) multiplicity of jets, (b) multiplicity of $b-$jets, (c) pseudorapidity of the jets, (d) transverse momentum of the jets, (e) pseudorapidity of the $b-$jets, (f) transverse momentum of the $b-$jets. The data, represented by the dots in the plots, is directly compared with the total Monte Carlo simulations, represented by the different colors stacked histograms. The uncertainty band represents the statistical uncertainty in the MC sample, while bars on data points represent the uncertainty on data.

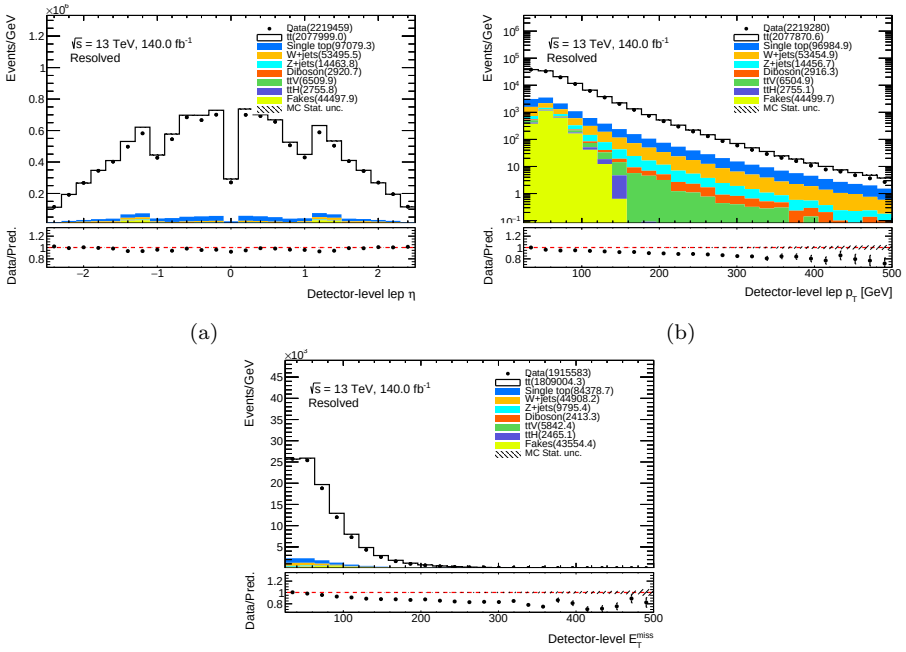

Figure A.6: Comparison of measured data and Monte Carlo simulations for basic kinematic observables in the μ+jets channel at detector level: (a) pseudorapidity of the produced lepton, (b) transverse momentum of the produced lepton, (c) missing transverse energy. The data, represented by the dots in the plots, is directly compared with the total Monte Carlo simulations, represented by the different colors stacked histograms. The uncertainty band represents the statistical uncertainty in the MC sample, while bars on data points represent the uncertainty on data.

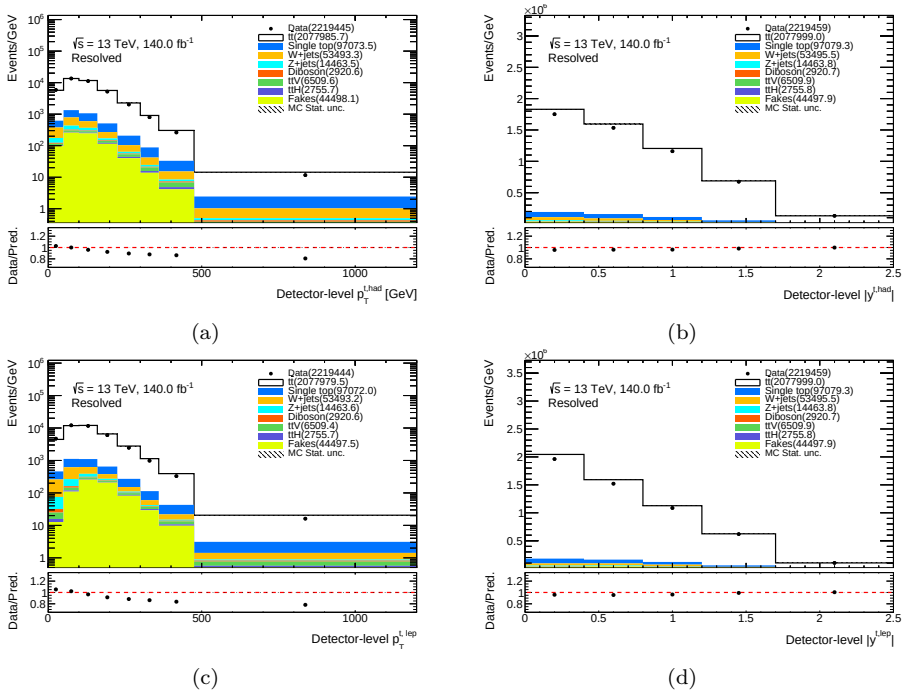

Figure A.7: Kinematic observables for the leptonically and hadronically decaying top quarks reconstructed with the Pseudo-Top algorithm: (a) transverse momentum and (b) rapidity of the hadronic top; (a) transverse momentum and (b) rapidity of the leptonic top. The data, represented by the dots in the plots, is directly compared with the total Monte Carlo simulations, represented by the different colors stacked histograms. The uncertainty band represents the statistical uncertainty in the MC sample, while bars on data points represent the uncertainty on data.

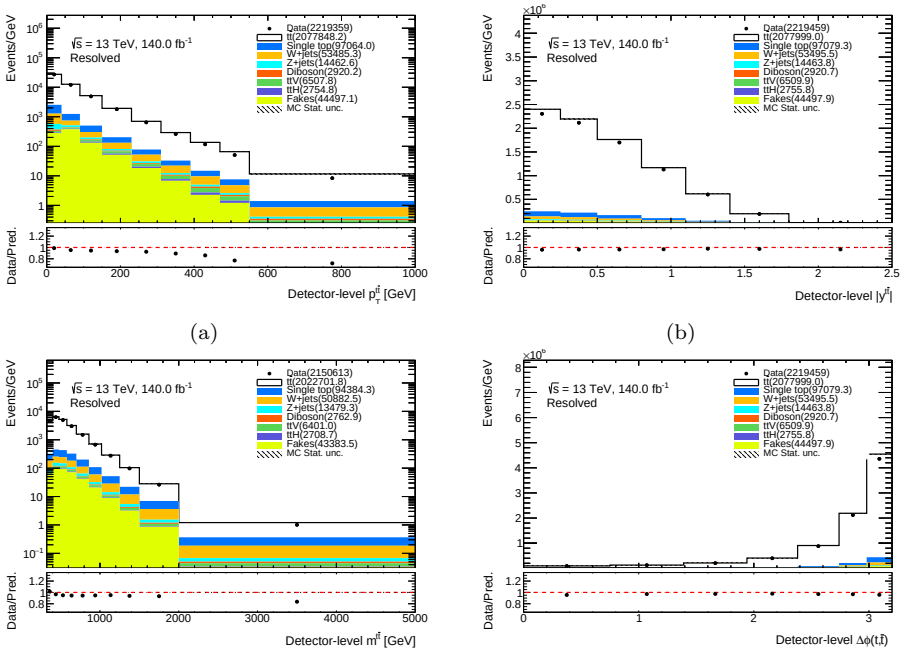

Figure A.8: Kinematic observables for the $t\bar{t}$ system reconstructed with the Pseudo-Top algorithm: transverse momentum (a), rapidity (b), invariant mass (c) and the azimuthal angle difference (d). The data, represented by the dots in the plots, is directly compared with the total Monte Carlo simulations, represented by the different colors stacked histograms. The uncertainty band represents the statistical uncertainty in the MC sample, while bars on data points represent the uncertainty on data.

Appendix B

Systematic tables

In this appendix, the systematic tables with the impact of the uncertainties for the single and double differential cross-sections are presented. Each table describes the impact of each group of uncertainties with their three largest components in the correspondant bin.

B.1 Single differential cross-sections

Bins [GeV]	0–50	50–100	100–160	160–225	225–300	300–360	360–475	475–600	600–1200
$d\sigma$ / dp_T^t [pb/GeV]	$2.70 \cdot 10^{0}$	$5.29 \cdot 10^{0}$	$3.94 \cdot 10^{0}$	$1.79 \cdot 10^{0}$	$6.34 \cdot 10^{-1}$	$2.26 \cdot 10^{-1}$	$7.15 \cdot 10^{-2}$	$1.53 \cdot 10^{-2}$	$1.07 \cdot 10^{-3}$
Total Uncertainty [%]	$^{+9.62}_{-10.6}$	$^{+8.60}_{-9.59}$	$^{+7.57}_{-8.60}$	$^{+7.04}_{-7.73}$	$^{+6.62}_{-7.29}$	$^{+6.54}_{-7.16}$	$^{+6.78}_{-7.65}$	$^{+9.54}_{-8.97}$	$^{+18.9}_{-17.7}$
Statistics [%]	±0.1	±0.0	±0.0	±0.1	±0.2	±0.3	±0.4	±1.0	±2.2
Systematics [%]	$^{+9.62}_{-10.5}$	$^{+8.60}_{-9.59}$	$^{+7.57}_{-8.60}$	$^{+7.04}_{-7.73}$	$^{+6.61}_{-7.28}$	$^{+6.53}_{-7.15}$	$^{+6.76}_{-7.63}$	$^{+9.48}_{-8.91}$	$^{+18.8}_{-17.5}$
Background [%]	±2.27	±1.90	±1.46	±1.31	±1.47	±1.89	±2.83	±5.85	±14.0
SingleTop_tW_DS [%]	< 0.05	< 0.05	∓0.17	∓0.48	∓0.94	∓1.48	∓2.47	∓5.45	∓13.5
Wjets_norm [%]	±2.00	±1.58	±1.07	±0.83	±0.83	±0.93	±1.18	±1.89	±3.37
SingleTop_norm [%]	±0.24	±0.23	±0.22	±0.23	±0.26	±0.29	±0.35	±0.56	±1.06
IFSR + PDF [%]	$^{+3.23}_{-3.58}$	$^{+3.26}_{-3.44}$	$^{+3.50}_{-3.52}$	$^{+3.62}_{-3.60}$	$^{+3.46}_{-3.76}$	$^{+3.22}_{-3.56}$	$^{+3.18}_{-3.98}$	$^{+4.61}_{-3.40}$	$^{+7.13}_{-4.82}$
fsr_muR_syst [%]	$^{+3.09}_{-5.47}$	$^{+3.14}_{-5.35}$	$^{+3.39}_{-5.46}$	$^{+3.50}_{-4.95}$	$^{+3.33}_{-4.72}$	$^{+3.06}_{-4.54}$	$^{+2.92}_{-4.95}$	$^{+3.63}_{-3.30}$	$^{+3.74}_{-4.20}$
scale_muR_syst [%]	-	−0.22	−0.37	−0.39	−0.29	−0.23	−0.31	−0.72	−2.19
isr_alphaS_Var3c_syst [%]	$^{-0.19}_{+0.68}$	$^{+0.15}_{+0.56}$	$^{+0.45}_{+0.36}$	$^{+0.65}_{+0.21}$	$^{+0.71}_{+0.17}$	$^{+0.76}_{-}$	$^{+1.00}_{-0.06}$	$^{+2.36}_{+0.95}$	$^{+5.31}_{+1.17}$
JES/JER [%]	$^{-0.81}_{+4.84}$	$^{-0.67}_{+4.74}$	$^{-0.40}_{+4.88}$	$^{-0.12}_{+4.63}$	$^{-}_{+4.08}$	$^{+0.34}_{+3.91}$	$^{+0.49}_{+3.90}$	$^{-}_{+4.18}$	$^{-}_{+5.58}$
CategoryReduction_JET_Pileup_RhoTopology [%]	$^{-4.82}_{+3.78}$	$^{-4.71}_{+3.72}$	$^{-4.74}_{+3.72}$	$^{-4.46}_{+3.26}$	$^{-3.93}_{+2.54}$	$^{-3.66}_{+2.07}$	$^{-3.63}_{+1.78}$	$^{-4.10}_{+1.60}$	$^{-3.61}_{+1.53}$
CategoryReduction_JET_EtaIntercalibration_Modelling [%]	$^{-3.67}_{+1.21}$	$^{-3.62}_{+1.20}$	$^{-3.57}_{+1.28}$	$^{-3.16}_{+1.24}$	$^{-2.48}_{+1.12}$	$^{-2.03}_{+1.05}$	$^{-1.70}_{+0.97}$	$^{-1.72}_{+1.03}$	$^{-1.14}_{+1.28}$
CategoryReduction_JET_Flavor_Response [%]	$^{-1.25}_{+1.87}$	$^{-1.22}_{+1.70}$	$^{-1.26}_{+1.59}$	$^{-1.19}_{+1.46}$	$^{-1.06}_{+1.46}$	$^{-0.94}_{+1.36}$	$^{-0.92}_{+1.79}$	$^{-1.00}_{+1.98}$	$^{-0.96}_{+0.49}$
Flavour tagging [%]	$^{+1.67}_{+4.60}$	$^{+1.53}_{+4.28}$	$^{+1.49}_{+3.73}$	$^{+1.48}_{+3.16}$	$^{+1.48}_{+2.78}$	$^{+1.64}_{+2.66}$	$^{+1.87}_{+2.72}$	$^{+1.86}_{+3.36}$	$^{+0.87}_{+6.20}$
weight_bTagSF_DL1r_70_extrapolation [%]	$^{-4.53}_{< 0.05}$	$^{-4.21}_{< 0.05}$	$^{-3.68}_{< 0.05}$	$^{-3.13}_{< 0.05}$	$^{-2.76}_{< 0.05}$	$^{-2.64}_{< 0.05}$	$^{-2.70}_{\pm 0.19}$	$^{-3.33}_{\pm 1.34}$	$^{-6.10}_{+4.92}$
weight_bTagSF_DL1r_70_eigenvars_B_1 [%]	∓0.64	$^{-0.72}_{+0.73}$	∓0.89	∓1.13	$^{-1.41}_{+1.42}$	$^{-1.68}_{+1.69}$	$^{-2.00}_{+2.02}$	$^{-2.51}_{+2.54}$	$^{-4.83}_{-3.07}$ $^{+3.11}$
weight_bTagSF_DL1r_70_eigenvars_B_0 [%]	$^{-4.34}_{+4.42}$	$^{-4.01}_{+4.08}$	$^{-3.43}_{+3.48}$	$^{-2.77}_{+2.81}$	$^{-2.24}_{+2.26}$	$^{-1.94}_{+1.95}$	$^{-1.75}_{+1.76}$	$^{-1.66}_{+1.67}$	$^{-1.87}_{+1.88}$
Modelling [%]	±5.44	±4.07	±1.79	$^{+0.59}_{-0.58}$	±1.37	±1.51	$^{+1.47}_{-1.48}$	$^{+1.03}_{-1.02}$	$^{+5.89}_{-5.91}$
HardScattering [%]	±0.33	±0.22	< 0.05	∓0.28	∓0.51	∓0.23	±0.11	∓0.90	∓5.75
Hadronization [%]	±5.41	±4.04	±1.71	∓0.24	∓1.24	∓1.47	∓1.43	∓0.20	±1.18
mtop [%]	$^{+0.42}_{-0.47}$	$^{+0.43}_{-0.45}$	$^{+0.52}_{-0.54}$	$^{+0.46}_{-0.44}$	$^{+0.39}_{-0.29}$	$^{+0.25}_{-0.26}$	$^{+0.31}_{-0.36}$	$^{+0.47}_{-0.44}$	$^{+0.46}_{-0.73}$
Leptons [%]	±0.72	±0.68	$^{+0.63}_{-0.62}$	$^{+0.61}_{-0.60}$	$^{+0.64}_{-0.63}$	±0.70	$^{+0.82}_{-0.81}$	$^{+1.07}_{-1.05}$	$^{+1.43}_{-1.38}$
weight_leptonSF_EL_SF_ID [%]	±0.38	±0.37	±0.37	±0.40	±0.45	±0.53	±0.67	±0.92	±1.24
weight_leptonSF_MU_SF_Trigger_SYST [%]	$^{-0.35}_{+0.36}$	$^{-0.34}_{+0.35}$	$^{-0.33}_{+0.34}$	$^{-0.32}_{+0.33}$	$^{-0.31}_{+0.32}$	∓0.31	∓0.31	∓0.32	∓0.35
weight_leptonSF_MU_SF_Isol_SYST [%]	±0.45	±0.40	±0.31	±0.24	±0.21	±0.20	±0.21	±0.23	±0.27

Table B.1: Table of systematics for the differential cross-section at the parton level for the $p_T^{t,had}$ observable.

Bins [Unit $\lvert y^{\mathrm{t,had}}\rvert$]	0–0.30	0.30–0.60	0.60–0.90	0.90–1.40	1.40–1.70	1.70–2.50
$\mathrm{d}\sigma$ / $\mathrm{d}\lvert y^{\mathrm{t,had}}\rvert$ [pb/ Unit $\lvert y^{\mathrm{t,had}}\rvert$]	$4.88 \cdot 10^2$	$4.67 \cdot 10^2$	$4.27 \cdot 10^2$	$3.54 \cdot 10^2$	$2.68 \cdot 10^2$	$1.47 \cdot 10^2$
Total Uncertainty [%]	$^{+7.17}_{-8.19}$	$^{+7.27}_{-8.29}$	$^{+7.33}_{-8.38}$	$^{+7.53}_{-8.38}$	$^{+7.72}_{-8.69}$	$^{+7.84}_{-8.65}$
Statistics [%]	±0.1	±0.1	±0.1	±0.1	±0.2	±0.2
Systematics [%]	$^{+7.17}_{-8.19}$	$^{+7.27}_{-8.29}$	$^{+7.33}_{-8.37}$	$^{+7.52}_{-8.37}$	$^{+7.72}_{-8.69}$	$^{+7.83}_{-8.65}$
JES/JER [%]	$^{+4.17}_{-4.15}$	$^{+4.30}_{-4.18}$	$^{+4.50}_{-4.35}$	$^{+4.86}_{-4.73}$	$^{+5.27}_{-5.09}$	$^{+5.41}_{-5.44}$
CategoryReduction_JET_Pileup_RhoTopology [%]	$^{+3.30}_{-3.25}$	$^{+3.37}_{-3.25}$	$^{+3.44}_{-3.30}$	$^{+3.52}_{-3.37}$	$^{+3.51}_{-3.37}$	$^{+3.45}_{-3.39}$
CategoryReduction_JET_Flavor_Response [%]	$^{-1.29}_{+1.18}$	$^{-1.34}_{+1.28}$	$^{-1.48}_{+1.44}$	$^{-1.79}_{+1.73}$	$^{-2.07}_{+2.03}$	$^{-2.30}_{+2.17}$
CategoryReduction_JET_EtaIntercalibration_Modelling [%]	$^{+0.55}_{-0.56}$	$^{+0.71}_{-0.69}$	$^{+1.02}_{-0.99}$	$^{+1.58}_{-1.55}$	$^{+2.23}_{-2.16}$	$^{+2.49}_{-2.54}$
Flavour tagging [%]	$^{+3.69}_{-3.64}$	$^{+3.68}_{-3.63}$	$^{+3.67}_{-3.62}$	$^{+3.65}_{-3.60}$	$^{+3.62}_{-3.57}$	$^{+3.59}_{-3.54}$
weight_bTagSF_DL1r_70_eigenvars_B_0 [%]	$^{-3.37}_{+3.42}$	$^{-3.36}_{+3.41}$	$^{-3.35}_{+3.41}$	$^{-3.34}_{+3.39}$	$^{-3.31}_{+3.36}$	$^{-3.27}_{+3.32}$
weight_bTagSF_DL1r_70_eigenvars_B_1 [%]	∓ 0.99	$^{-0.98}_{+0.99}$	∓ 0.98	∓ 0.97	$^{-0.96}_{+0.97}$	∓ 0.97
weight_bTagSF_DL1r_70_eigenvars_B_2 [%]	±0.85	±0.85	±0.85	±0.85	±0.86	±0.86
IFSR + PDF [%]	$^{+3.26}_{-5.18}$	$^{+3.23}_{-5.27}$	$^{+3.24}_{-5.35}$	$^{+3.45}_{-5.21}$	$^{+3.64}_{-5.60}$	$^{+3.78}_{-5.26}$
fsr_muR_syst [%]	$^{+3.22}_{-5.14}$	$^{+3.19}_{-5.23}$	$^{+3.20}_{-5.32}$	$^{+3.40}_{-5.19}$	$^{+3.57}_{-5.58}$	$^{+3.58}_{-5.17}$
IntraPDF [%]	±0.25	±0.22	±0.17	±0.16	±0.21	±0.94
isr_alphaS_Var3c_syst [%]	$^{+0.34}_{-0.42}$	$^{+0.34}_{-0.41}$	$^{+0.38}_{-0.41}$	$^{+0.40}_{-0.34}$	$^{+0.43}_{-0.25}$	$^{+0.45}_{-0.15}$
Background [%]	±1.89	±1.80	±1.65	±1.43	±1.26	±1.18
Wjets_norm [%]	±1.50	±1.43	±1.30	±1.08	±0.90	±0.81
Zjets_norm [%]	±0.53	±0.50	±0.46	±0.40	±0.33	±0.31
SingleTop_tW_DS [%]	∓ 0.48	∓ 0.44	∓ 0.36	∓ 0.33	∓ 0.26	∓ 0.18
Modelling [%]	$^{+1.94}_{-1.95}$	±2.05	$^{+1.91}_{-1.92}$	±1.61	$^{+0.95}_{-0.94}$	$^{+0.54}_{-0.59}$
Hadronization [%]	±1.85	±1.99	±1.84	±1.52	±0.81	±0.19
mtop [%]	$^{+0.51}_{-0.53}$	$^{+0.51}_{-0.52}$	$^{+0.49}_{-0.53}$	$^{+0.52}_{-0.50}$	$^{+0.50}_{-0.47}$	$^{+0.50}_{-0.55}$
HardScattering [%]	∓ 0.27	< 0.05	±0.10	< 0.05	< 0.05	±0.09
Leptons [%]	$^{+0.66}_{-0.65}$	$^{+0.66}_{-0.65}$	±0.65	$^{+0.65}_{-0.64}$	$^{+0.65}_{-0.64}$	$^{+0.65}_{-0.64}$
weight_leptonSF_EL_SF_ID [%]	±0.40	±0.40	±0.40	±0.40	±0.40	±0.40
weight_leptonSF_MU_SF_Trigger_SYST [%]	$^{-0.33}_{+0.34}$	$^{-0.33}_{+0.34}$	$^{-0.33}_{+0.34}$	$^{-0.33}_{+0.34}$	$^{-0.33}_{+0.34}$	$^{-0.33}_{+0.34}$
weight_leptonSF_MU_SF_Isol_SYST [%]	±0.33	±0.32	±0.32	±0.32	±0.31	±0.31

Table B.2: Table of systematics for the differential cross-section at the parton level for the $|y^{t,had}|$ observable.

Bins [GeV]	325–400	400–480	480–580	580–700	700–860	860–1020	1020–1250	1250–1500	1500–2000	2000–5000
$d\sigma$ / $dm^{t\bar{t}}$ [pb/GeV]	$2.46 \cdot 10^0$	$3.19 \cdot 10^0$	$1.79 \cdot 10^0$	$8.39 \cdot 10^{-1}$	$3.44 \cdot 10^{-1}$	$1.33 \cdot 10^{-1}$	$4.72 \cdot 10^{-2}$	$1.52 \cdot 10^{-2}$	$3.43 \cdot 10^{-3}$	$9.26 \cdot 10^{-5}$
Total Uncertainty [%]	$^{+8.09}_{-9.42}$	$^{+7.85}_{-9.13}$	$^{+8.36}_{-9.30}$	$^{+8.56}_{-9.13}$	$^{+9.07}_{-9.24}$	$^{+10.6}_{-10.3}$	$^{+13.8}_{-13.2}$	$^{+18.7}_{-17.5}$	$^{+26.4}_{-24.3}$	$^{+41.9}_{-39.1}$
Statistics [%]	±0.1	±0.0	±0.1	±0.1	±0.1	±0.2	±0.4	±0.6	±1.2	±3.1
Systematics [%]	$^{+8.09}_{-9.42}$	$^{+7.85}_{-9.13}$	$^{+8.36}_{-9.30}$	$^{+8.56}_{-9.13}$	$^{+9.07}_{-9.24}$	$^{+10.5}_{-10.3}$	$^{+13.8}_{-13.1}$	$^{+18.6}_{-17.5}$	$^{+26.4}_{-24.3}$	$^{+41.7}_{-38.9}$
Background [%]	±1.18	±1.08	±1.24	±1.75	±2.67	±4.13	±6.35	±9.80	±15.2	±26.2
SingleTop_tW_DS [%]	±0.24	±0.13	∓ 0.07	∓ 0.46	∓ 1.24	∓ 2.53	∓ 4.50	∓ 7.64	∓ 12.6	∓ 22.7
Wjets_norm [%]	±0.90	±0.79	±0.91	±1.31	±1.94	±2.82	±4.03	±5.68	±8.02	±12.3
SingleTop_norm [%]	±0.15	±0.16	±0.20	±0.27	±0.38	±0.53	±0.72	±0.98	±1.37	±2.09
Modelling [%]	$^{+5.05}_{-4.91}$	±3.23	±1.32	$^{+0.79}_{-0.87}$	±2.29	$^{+4.06}_{-4.07}$	±5.82	$^{+7.43}_{-7.42}$	±11.2	±20.0
Hadronization [%]	±4.68	±3.20	±1.30	∓ 0.58	∓ 2.21	∓ 4.01	∓ 5.75	∓ 7.36	∓ 11.1	∓ 20.0
HardScattering [%]	< 0.05	±0.37	< 0.05	∓ 0.43	∓ 0.46	∓ 0.56	∓ 0.82	∓ 0.85	∓ 1.31	∓ 1.09
mtop [%]	$^{+1.88}_{-1.47}$	$^{-0.12}_{+0.11}$	$^{+0.19}_{-0.20}$	$^{+0.32}_{-0.35}$	±0.37	$^{+0.34}_{-0.39}$	$^{+0.34}_{-0.37}$	$^{+0.52}_{-0.39}$	$^{+0.34}_{-0.37}$	$^{+0.37}_{-0.41}$
IFSR + PDF [%]	$^{+2.71}_{-4.73}$	$^{+3.45}_{-5.68}$	$^{+3.82}_{-5.92}$	$^{+3.71}_{-5.62}$	$^{+3.25}_{-4.94}$	$^{+3.91}_{-3.94}$	$^{+4.35}_{-3.73}$	$^{+6.64}_{-3.74}$	$^{+10.6}_{-4.49}$	$^{+17.1}_{-10.3}$
scale_muR_syst [%]	$^{+0.08}_{-0.32}$	$^{-0.28}_{+0.22}$	$^{-0.17}_{+0.16}$	$^{+0.11}_{+0.00}$	$^{+0.38}_{+0.00}$	$^{-0.28}_{+1.19}$	$^{-1.06}_{+2.84}$	$^{-2.12}_{+5.04}$	$^{-3.85}_{+8.26}$	$^{-7.92}_{+13.7}$
fsr_muR_syst [%]	$^{+2.64}_{-4.69}$	$^{+3.08}_{-5.63}$	$^{+3.74}_{-5.86}$	$^{+3.69}_{-5.55}$	$^{+3.37}_{-4.88}$	$^{+3.92}_{-3.87}$	$^{+5.09}_{-3.50}$	$^{+8.20}_{-2.91}$	$^{+14.8}_{-1.21}$	$^{+24.76}_{-5.22}$
scale_muF_syst [%]	$^{-0.28}_{+0.11}$	$^{-0.19}_{-}$	< 0.05	$^{+0.14}_{-0.11}$	$^{+0.27}_{-}$	$^{+0.36}_{-}$	$^{-0.09}_{+1.30}$	$^{-0.60}_{+2.58}$	$^{-1.74}_{+4.73}$	$^{-4.58}_{+8.66}$
JES/JER [%]	$^{+2.68}_{-4.17}$	$^{+4.50}_{-4.69}$	$^{+6.16}_{-5.87}$	$^{+6.42}_{-5.81}$	$^{+5.93}_{-5.17}$	$^{+5.29}_{-4.42}$	$^{+5.08}_{-3.82}$	$^{+4.73}_{-3.53}$	$^{+5.03}_{-3.69}$	$^{+7.77}_{-4.96}$
CategoryReduction_JET_EtaIntercalibration_Modelling [%]	$^{+0.16}_{-0.25}$	$^{+0.92}_{-0.95}$	$^{+1.56}_{-1.53}$	$^{+1.80}_{-1.73}$	$^{+1.90}_{-1.81}$	$^{+1.99}_{-1.84}$	$^{+2.17}_{-1.89}$	$^{+2.35}_{-2.07}$	$^{+2.70}_{-2.28}$	$^{+3.17}_{-2.46}$
CategoryReduction_JET_Pileup_RhoTopology [%]	$^{+2.00}_{-2.11}$	$^{+3.63}_{-3.06}$	$^{+4.52}_{+4.31}$	$^{+4.15}_{-3.94}$	$^{+3.29}_{-3.11}$	$^{+2.29}_{-2.18}$	$^{+1.44}_{-1.23}$	$^{+0.38}_{-0.21}$	$^{-0.93}_{+1.02}$	$^{-2.63}_{+3.43}$
CategoryReduction_JET_EtaIntercalibration_NonClosure_2018data [%]	$^{-0.29}_{+0.33}$	< 0.05	$^{+0.33}_{-0.30}$	$^{+0.53}_{-0.47}$	$^{+0.69}_{-0.63}$	$^{+0.84}_{-0.76}$	$^{+1.07}_{-0.90}$	$^{+1.25}_{-1.16}$	$^{+1.61}_{-1.32}$	$^{+2.10}_{-1.47}$
Flavour tagging [%]	$^{+4.69}_{-4.60}$	$^{+4.07}_{-4.01}$	$^{+3.45}_{-3.41}$	$^{+3.07}_{-3.04}$	$^{+2.86}_{-2.84}$	$^{+2.81}_{-2.79}$	$^{+2.91}_{-2.89}$	$^{+3.25}_{-3.23}$	$^{+4.13}_{-4.09}$	$^{+6.99}_{-6.82}$
weight_bTagSF_DL1r_70_extrapolation [%]	< 0.05	< 0.05	< 0.05	< 0.05	< 0.05	±0.05	±0.22	±0.72	$^{+1.82}_{-1.81}$	$^{+4.98}_{-4.81}$
weight_bTagSF_DL1r_70_eigenvars_B_1 [%]	∓ 0.57	∓ 0.75	∓ 0.98	$^{-1.20}_{+1.21}$	$^{-1.44}_{+1.45}$	$^{-1.73}_{+1.75}$	$^{-2.08}_{+2.10}$	$^{-2.52}_{+2.54}$	$^{-3.10}_{+3.14}$	$^{-4.11}_{+4.19}$
weight_bTagSF_DL1r_70_eigenvars_B_0 [%]	$^{-4.45}_{+4.54}$	$^{-3.81}_{+3.87}$	$^{-3.11}_{+3.15}$	$^{-2.63}_{+2.65}$	$^{-2.26}_{+2.30}$	$^{-2.09}_{+2.05}$	$^{-1.85}_{+1.86}$	∓ 1.70	∓ 1.59	∓ 1.48
Leptons [%]	$^{+0.90}_{-0.89}$	± 0.67	$^{+0.63}_{-0.62}$	$^{+0.74}_{-0.73}$	$^{+0.85}_{-0.83}$	$^{+0.98}_{-0.95}$	$^{+1.14}_{-1.09}$	$^{+1.40}_{-1.32}$	$^{+1.76}_{-1.64}$	$^{+2.50}_{-2.27}$
weight_leptonSF_EL_SF_ID [%]	±0.34	±0.35	±0.37	±0.41	±0.50	±0.62	±0.81	±1.06	$^{+1.42}_{-1.41}$	$^{+2.06}_{-2.05}$
EG_SCALE_ALL [%]	< 0.05	< 0.05	< 0.05	$^{+0.09}_{-0.05}$	$^{+0.19}_{-0.08}$	$^{+0.22}_{-0.12}$	$^{+0.30}_{-0.18}$	$^{+0.39}_{-0.22}$	$^{+0.53}_{-0.27}$	$^{+0.86}_{-0.40}$
weight_leptonSF_MU_SF_Trigger_SYST [%]	$^{-0.33}_{+0.34}$	$^{-0.32}_{+0.33}$	$^{-0.32}_{+0.33}$	∓ 0.33	$^{-0.34}_{+0.35}$	∓ 0.37	$^{-0.39}_{+0.40}$	$^{-0.43}_{+0.44}$	$^{-0.48}_{+0.49}$	$^{-0.96}_{+0.57}$

Table B.3: Table of systematics for the differential cross-section at the parton level for the $m^{t\bar{t}}$ observable.

Appendix B. Systematic tables

Bins [GeV]	0–40	40–90	90–150	150–230	230–310	310–390	390–470	470–600	600–1000
$d\sigma$ / dp_T^{tt} [pb/GeV]	$9.82 \cdot 10^{0}$	$4.81 \cdot 10^{0}$	$1.75 \cdot 10^{0}$	$6.22 \cdot 10^{-1}$	$2.21 \cdot 10^{-1}$	$8.71 \cdot 10^{-2}$	$3.74 \cdot 10^{-2}$	$1.37 \cdot 10^{-2}$	$1.95 \cdot 10^{-3}$
Total Uncertainty [%]	$^{+9.14}_{-10.1}$	$^{+9.83}_{-10.4}$	$^{+15.6}_{-15.8}$	$^{+13.5}_{-13.7}$	$^{+10.5}_{-11.2}$	$^{+9.09}_{-9.99}$	$^{+8.33}_{-9.72}$	$^{+7.91}_{-8.35}$	$^{+10.0}_{-10.3}$
Statistics [%]	±0.0	±0.0	±0.1	±0.1	±0.3	±0.4	±0.6	±0.9	±1.7
Systematics [%]	$^{+9.14}_{-10.1}$	$^{+9.83}_{-10.4}$	$^{+15.6}_{-15.8}$	$^{+13.5}_{-13.7}$	$^{+10.4}_{-11.2}$	$^{+9.08}_{-9.98}$	$^{+8.30}_{-9.70}$	$^{+7.84}_{-8.29}$	$^{+9.89}_{-10.2}$
Modelling [%]	±7.05	±5.89	±11.6	±9.00	±5.61	±4.01	±3.58	$^{+3.86}_{-3.87}$	$^{+6.51}_{-6.52}$
Hadronization [%]	∓6.98	±5.87	±11.6	±8.79	±5.39	±3.85	±3.25	±3.60	±6.49
HardScattering [%]	±0.85	±0.11	∓0.92	∓1.87	∓1.47	∓1.02	∓1.44	∓1.29	< 0.05
mtop [%]	$^{+0.46}_{-0.48}$	±0.51	$^{+0.56}_{-0.57}$	$^{+0.55}_{-0.58}$	$^{+0.46}_{-0.51}$	$^{+0.49}_{-0.47}$	$^{+0.40}_{-0.43}$	$^{+0.46}_{-0.55}$	$^{+0.49}_{-0.60}$
JES/JER [%]	$^{+1.55}_{-2.78}$	$^{+5.75}_{-5.50}$	$^{+8.88}_{-8.16}$	$^{+8.54}_{-7.91}$	$^{+7.16}_{-6.78}$	$^{+6.09}_{-5.77}$	$^{+4.84}_{-5.14}$	$^{+4.21}_{-4.18}$	$^{+4.79}_{-3.83}$
CategoryReduction_JET_Pileup_RhoTopology [%]	$^{+0.63}_{-0.83}$	$^{+4.32}_{-4.14}$	$^{+6.23}_{-5.79}$	$^{+5.73}_{-5.33}$	$^{+4.48}_{-4.23}$	$^{+3.58}_{-3.38}$	$^{+2.75}_{-2.87}$	$^{+2.27}_{-2.29}$	$^{+2.20}_{-1.90}$
CategoryReduction_JET_Flavor_Response [%]	$^{-0.31}_{+0.19}$	$^{-1.68}_{+1.60}$	$^{-2.83}_{+2.79}$	∓3.22	$^{-3.23}_{+3.20}$	$^{-3.05}_{+3.16}$	$^{-2.82}_{+2.65}$	$^{-2.10}_{+2.08}$	$^{-1.00}_{+1.32}$
CategoryReduction_JET_EtaIntercalibration_Modelling [%]	$^{-0.63}_{+0.52}$	$^{+1.76}_{-1.70}$	$^{+2.92}_{-2.78}$	$^{+2.80}_{-2.69}$	$^{+2.40}_{-2.30}$	$^{+2.02}_{-1.91}$	$^{+1.58}_{-1.77}$	$^{+1.42}_{-1.49}$	$^{+1.55}_{-1.34}$
IFSR + PDF [%]	$^{+3.44}_{-3.11}$	$^{+3.33}_{-3.26}$	$^{+3.55}_{-3.55}$	$^{+3.57}_{-3.51}$	$^{+3.38}_{-3.83}$	$^{+3.60}_{-3.84}$	$^{+4.05}_{-6.22}$	$^{+3.46}_{-3.40}$	$^{+2.94}_{-3.89}$
fsr_muR_syst [%]	$^{+3.34}_{-5.04}$	$^{+3.26}_{-5.21}$	$^{+3.32}_{-5.42}$	$^{+3.21}_{-5.30}$	$^{+2.99}_{-5.61}$	$^{+3.30}_{-5.65}$	$^{+3.79}_{-6.06}$	$^{+3.20}_{-4.21}$	$^{+2.58}_{-4.71}$
scale_muR_syst [%]	∓0.06	$^{+0.09}_{-0.11}$	$^{+0.32}_{-0.38}$	$^{+0.68}_{-0.82}$	$^{+0.92}_{-1.07}$	$^{+0.93}_{-1.03}$	$^{+1.03}_{-1.05}$	$^{+1.01}_{-0.96}$	$^{+0.99}_{-0.93}$
isr_alphaS_Var3c_syst [%]	$^{-0.55}_{+0.48}$	$^{+0.28}_{-0.31}$	$^{+1.10}_{-1.01}$	$^{+1.35}_{-1.20}$	$^{+1.23}_{-1.11}$	$^{+1.00}_{-0.94}$	$^{+0.86}_{-0.79}$	$^{+0.64}_{-0.62}$	$^{+0.55}_{-0.48}$
Flavour tagging [%]	$^{+3.90}_{-3.84}$	$^{+3.71}_{-3.66}$	$^{+3.51}_{-3.47}$	$^{+3.33}_{-3.29}$	$^{+3.14}_{-3.11}$	$^{+2.99}_{-2.96}$	$^{+2.87}_{-2.85}$	$^{+2.78}_{-2.76}$	$^{+2.80}_{-2.79}$
weight_bTagSF_DL1r_70_eigenvars_B_0 [%]	$^{-3.58}_{+3.64}$	$^{-3.40}_{+3.45}$	$^{-3.21}_{+3.25}$	$^{-3.02}_{+3.05}$	$^{-2.79}_{+2.82}$	$^{-2.58}_{+2.60}$	$^{-2.40}_{+2.42}$	$^{-2.20}_{+2.22}$	$^{-1.93}_{+1.95}$
weight_bTagSF_DL1r_70_eigenvars_B_1 [%]	∓0.97	∓0.95	∓0.94	∓0.99	$^{-1.09}_{+1.10}$	∓1.22	∓1.36	$^{-1.55}_{+1.56}$	$^{-1.89}_{+1.91}$
weight_bTagSF_DL1r_70_eigenvars_B_2 [%]	$^{+0.92}_{-0.91}$	$^{+0.87}_{-0.86}$	$^{+0.81}_{-0.80}$	$^{+0.77}_{-0.76}$	$^{+0.74}_{-0.73}$	±0.69	±0.61	±0.48	±0.19
Background [%]	±1.62	±1.56	±1.65	±1.87	±2.14	±2.30	±2.42	±2.79	±3.75
Wjets_norm [%]	±1.45	±1.03	±0.96	±1.30	±1.66	±1.84	±1.89	±1.92	±2.18
SingleTop_tW_DS [%]	∓0.07	∓0.35	∓0.59	∓0.72	∓0.82	∓0.96	∓1.29	∓1.87	∓2.98
Zjets_norm [%]	±0.56	±0.43	±0.33	±0.33	±0.34	±0.34	±0.32	±0.30	±0.31
Leptons [%]	$^{+0.69}_{-0.68}$	$^{+0.67}_{-0.66}$	±0.66	$^{+0.65}_{-0.64}$	$^{+0.67}_{-0.66}$	$^{+0.70}_{-0.69}$	±0.74	$^{+0.82}_{-0.81}$	$^{+0.96}_{-0.95}$
weight_leptonSF_EL_SF_ID [%]	±0.40	±0.39	±0.39	±0.42	±0.46	±0.51	±0.57	±0.66	±0.82
weight_leptonSF_MU_SF_Trigger_SYST [%]	∓0.34	$^{-0.33}_{+0.34}$	∓0.33	∓0.33	$^{-0.32}_{+0.33}$	∓0.32	∓0.32	$^{-0.31}_{+0.32}$	∓0.31
weight_leptonSF_MU_SF_Isol_SYST [%]	±0.34	±0.33	±0.31	±0.29	±0.27	±0.25	±0.24	±0.23	±0.23

Table B.4: Table of systematics for the differential cross-section at the parton level for the $p_T^{t\bar{t}}$ observable.

Bins [Unit $\lvert y^{tt}\rvert$]	0–0.20	0.20–0.40	0.40–0.60	0.60–0.80	0.80–1	1–1.30	1.30–1.60	1.60–2	2–2.50
$d\sigma$ / $d\lvert y^{tt}\rvert$ [pb/ Unit $\lvert y^{tt}\rvert$]	$5.79 \cdot 10^{2}$	$5.64 \cdot 10^{2}$	$5.34 \cdot 10^{2}$	$4.92 \cdot 10^{2}$	$4.37 \cdot 10^{2}$	$3.60 \cdot 10^{2}$	$2.64 \cdot 10^{2}$	$1.62 \cdot 10^{2}$	$6.51 \cdot 10^{1}$
Total Uncertainty [%]	$^{+7.32}_{-8.22}$	$^{+7.34}_{-8.41}$	$^{+7.37}_{-8.40}$	$^{+7.32}_{-8.24}$	$^{+7.31}_{-8.17}$	$^{+7.38}_{-8.38}$	$^{+7.49}_{-8.57}$	$^{+7.85}_{-8.76}$	$^{+8.75}_{-9.55}$
Statistics [%]	±0.1	±0.1	±0.1	±0.1	±0.1	±0.1	±0.2	±0.3	±0.7
Systematics [%]	$^{+7.32}_{-8.22}$	$^{+7.34}_{-8.41}$	$^{+7.37}_{-8.39}$	$^{+7.32}_{-8.24}$	$^{+7.30}_{-8.17}$	$^{+7.38}_{-8.38}$	$^{+7.48}_{-8.57}$	$^{+7.85}_{-8.75}$	$^{+8.71}_{-9.52}$
JES/JER [%]	$^{+4.47}_{-4.29}$	$^{+4.47}_{-4.36}$	$^{+4.51}_{-4.41}$	$^{+4.54}_{-4.44}$	$^{+4.58}_{-4.52}$	$^{+4.69}_{-4.62}$	$^{+4.95}_{-4.93}$	$^{+5.31}_{-5.28}$	$^{+5.37}_{-5.44}$
CategoryReduction_JET_Pileup_RhoTopology [%]	$^{+3.44}_{-3.28}$	$^{+3.43}_{-3.32}$	$^{+3.43}_{-3.33}$	$^{+3.41}_{-3.31}$	$^{+3.37}_{-3.30}$	$^{+3.38}_{-3.29}$	$^{+3.44}_{-3.33}$	$^{+3.51}_{-3.36}$	$^{+3.41}_{-3.36}$
CategoryReduction_JET_Flavor_Response [%]	$^{-1.47}_{+1.42}$	$^{-1.50}_{+1.43}$	$^{-1.54}_{+1.47}$	$^{-1.60}_{+1.51}$	$^{-1.65}_{+1.56}$	$^{-1.71}_{+1.63}$	$^{-1.87}_{+1.80}$	$^{-2.05}_{+2.02}$	$^{-2.10}_{+2.00}$
CategoryReduction_JET_EtaIntercalibration_Modelling [%]	$^{+0.87}_{-0.83}$	$^{+0.92}_{-0.91}$	$^{+1.03}_{-1.02}$	$^{+1.17}_{-1.15}$	$^{+1.34}_{-1.32}$	$^{+1.55}_{-1.54}$	$^{+1.91}_{-1.92}$	±2.38	$^{+2.63}_{-2.59}$
IFSR + PDF [%]	$^{+3.28}_{-5.17}$	$^{+3.27}_{-5.36}$	$^{+3.28}_{-5.31}$	$^{+3.31}_{-5.16}$	$^{+3.38}_{-5.07}$	$^{+3.51}_{-5.39}$	$^{+3.98}_{-5.55}$	$^{+4.00}_{-5.62}$	$^{+5.33}_{-6.52}$
fsr_muR_syst [%]	$^{+3.21}_{-5.12}$	$^{+3.20}_{-5.32}$	$^{+3.22}_{-5.27}$	$^{+3.27}_{-5.13}$	$^{+3.35}_{-5.05}$	$^{+3.49}_{-5.38}$	$^{+3.54}_{-5.53}$	$^{+3.84}_{-5.54}$	$^{+4.04}_{-5.59}$
IntraPDF [%]	±0.34	±0.31	±0.26	±0.19	±0.12	±0.14	±0.40	±0.91	±3.33
isr_alphaS_Var3c_syst [%]	$^{+0.45}_{-0.50}$	$^{+0.45}_{-0.49}$	$^{+0.42}_{-0.43}$	$^{+0.38}_{-0.37}$	$^{+0.33}_{-0.31}$	$^{+0.27}_{-0.20}$	$^{+0.26}_{-0.10}$	$^{+0.19}_{-}$	$^{+0.34}_{-}$
Flavour tagging [%]	$^{+3.70}_{-3.65}$	$^{+3.69}_{-3.64}$	$^{+3.68}_{-3.63}$	$^{+3.67}_{-3.62}$	$^{+3.65}_{-3.60}$	$^{+3.62}_{-3.57}$	$^{+3.58}_{-3.53}$	$^{+3.53}_{-3.49}$	$^{+3.51}_{-3.46}$
weight_bTagSF_DL1r_70_eigenvars_B_0 [%]	$^{-3.39}_{+3.44}$	$^{-3.38}_{+3.43}$	$^{-3.37}_{+3.42}$	$^{-3.36}_{+3.41}$	$^{-3.33}_{+3.39}$	$^{-3.30}_{+3.35}$	$^{-3.26}_{+3.30}$	$^{-3.20}_{+3.25}$	$^{-3.17}_{+3.22}$
weight_bTagSF_DL1r_70_eigenvars_B_1 [%]	$^{-0.97}_{+0.98}$	$^{-0.97}_{+0.98}$	$^{-0.97}_{+0.98}$	$^{-0.97}_{+0.98}$	$^{-0.97}_{+0.98}$	∓0.98	$^{-0.98}_{+0.99}$	$^{-0.99}_{+1.00}$	∓1.00
weight_bTagSF_DL1r_70_eigenvars_B_2 [%]	$^{+0.85}_{-0.84}$	±0.85	±0.85	±0.85	$^{+0.86}_{-0.85}$	$^{+0.86}_{-0.85}$	±0.86	$^{+0.87}_{-0.86}$	$^{+0.87}_{-0.86}$
Background [%]	±1.72	±1.70	±1.65	±1.60	±1.56	±1.52	±1.40	±1.27	±1.35
Wjets_norm [%]	±1.30	±1.29	±1.26	±1.23	±1.20	±1.19	±1.15	±1.15	±1.19
Zjets_norm [%]	±0.47	±0.47	±0.47	±0.44	±0.43	±0.40	±0.38	±0.37	±0.38
SingleTop_tW_DS [%]	∓0.44	∓0.42	∓0.40	∓0.40	∓0.38	∓0.33	∓0.26	< 0.05	±0.45
Modelling [%]	$^{+1.90}_{-1.91}$	±1.97	±1.96	±1.73	±1.45	±1.20	±0.91	$^{+0.67}_{-0.71}$	$^{+1.34}_{-1.38}$
Hadronization [%]	±1.83	±1.91	±1.89	±1.65	±1.33	±1.03	±0.63	±0.16	∓0.34
mtop [%]	$^{+0.46}_{-0.49}$	$^{+0.47}_{-0.49}$	±0.49	$^{+0.50}_{-0.51}$	$^{+0.49}_{-0.51}$	±0.52	$^{+0.56}_{-0.55}$	$^{+0.55}_{-0.59}$	$^{+0.69}_{-0.78}$
HardScattering [%]	∓0.25	< 0.05	±0.16	±0.06	∓0.28	∓0.31	±0.35	±0.35	∓1.09
Leptons [%]	$^{+0.62}_{-0.61}$	$^{+0.62}_{-0.61}$	$^{+0.63}_{-0.62}$	$^{+0.64}_{-0.63}$	±0.65	$^{+0.70}_{-0.69}$	$^{+0.80}_{-0.79}$	$^{+0.97}_{-0.96}$	$^{+1.12}_{-1.11}$
weight_leptonSF_EL_SF_ID [%]	±0.38	±0.38	±0.38	±0.38	±0.39	±0.42	±0.48	±0.64	±0.79
weight_leptonSF_MU_SF_Trigger_SYST [%]	$^{-0.30}_{+0.31}$	∓0.31	$^{-0.31}_{+0.32}$	$^{-0.32}_{+0.33}$	$^{-0.34}_{+0.35}$	∓0.37	$^{-0.40}_{+0.41}$	$^{-0.41}_{+0.42}$	$^{-0.41}_{+0.42}$
weight_leptonSF_MU_SF_Isol_SYST [%]	±0.32	±0.32	±0.32	±0.32	±0.33	±0.33	±0.33	±0.30	±0.28

Table B.5: Table of systematics for the differential cross-section at the parton level for the $|y^{t\bar{t}}|$ observable.

B.2 Double differential cross-sections

Bins [GeV] x [GeV]	0–60	60–150	150–280	280–410	410–1000	1000–1060	1060–1150	1150–1280	1280–1410	1410–2000	2000–2080	2080–2180	2180–2300	2300–2430	2430–3000	3000–3080	3080–3190	3190–3320	3320–4000	4000–4080	4080–4190	4190–4400	4400–5000
$d^2\sigma/dp_T^{t\bar{t}}dm^{t\bar{t}}$ [pb/GeV x GeV]	$5.30 \cdot 10^0$	$1.39 \cdot 10^0$	$2.55 \cdot 10^{-1}$	$4.78 \cdot 10^{-2}$	$3.41 \cdot 10^{-3}$	$2.40 \cdot 10^0$	$7.32 \cdot 10^{-1}$	$1.51 \cdot 10^{-1}$	$3.12 \cdot 10^{-2}$	$2.41 \cdot 10^{-3}$	$6.36 \cdot 10^{-1}$	$1.71 \cdot 10^{-1}$	$4.33 \cdot 10^{-2}$	$1.15 \cdot 10^{-2}$	$1.13 \cdot 10^{-3}$	$1.51 \cdot 10^{-1}$	$4.21 \cdot 10^{-2}$	$1.09 \cdot 10^{-2}$	$9.55 \cdot 10^{-4}$	$2.47 \cdot 10^{-3}$	$7.75 \cdot 10^{-4}$	$1.54 \cdot 10^{-4}$	$1.24 \cdot 10^{-4}$
Total Uncertainty [%]	±0.7	±1.4	±0.5	±0.3	±0.3	±1.2	±2.7	±0.5	±1.3	±0.5	±0.5	±0.5	±0.5	±0.4	±0.3	±0.5	±0.7	±0.5	±0.3	±0.5	±0.4	±0.6	±0.6
Statistics [%]	±0.1	±0.1	±0.2	±0.5	±0.9	±0.1	±0.1	±0.2	±0.5	±0.9	±0.2	±0.2	±0.4	±0.8	±1.3	±0.5	±0.5	±0.8	±1.5	±3.7	±3.4	±4.4	±9.7
Systematics [%]	±0.7	±1.4	±0.4	±0.3	±0.1	±1.2	±2.7	±0.4	±1.2	±0.1	±0.4	±0.4	±0.1	±0.1	±0.1	±0.4	±0.5	±0.1	±0.1	±2.1	±1.2	±3.1	±6.1
Modelling [%]	±0.83	±10.0	±8.19	±4.41	±5.49	±4.61	±7.87	±3.62	±4.58	±4.65	±7.43	±6.00	±8.00	±6.22	±6.22	±12.7	±9.61	±7.46	±11.2	±28.0	±16.2	±23.1	±30.4
HardScattering [%]	±0.50	±0.21	±0.45	±1.62	±0.36	±0.46	±0.88	±1.67	±0.62	±0.81	±1.06	±1.58	±4.18	±4.93	±0.49	±3.20	±1.95	±6.89	±11.2	±2.78	±4.73	±2.54	±29.2
Hadronisation [%]	±0.43	±10.0	±8.13	±4.04	±5.49	±4.58	±7.61	±8.46	±4.54	±4.58	±7.36	±5.78	±6.81	±3.78	±3.02	±12.3	±1.71	±6.18	±3.25	±27.9	±9.91	±1.73	±8.46
mtop [%]	±0.6	±0.6	±0.6	±0.7	±0.6	±0.7	±0.8	±0.6	±0.5	±0.6	±0.6	±0.7	±0.8	±0.26	±0.6	±0.6	±0.6	±0.6	±0.6	±0.6	±0.6	±0.6	±0.6
Background [%]	±1.13	±1.10	±1.33	±1.39	±1.05	±1.44	±1.53	±1.78	±1.95	±2.26	±2.81	±2.98	±3.48	±3.87	±5.04	±6.79	±7.07	±8.29	±11.9	±22.0	±22.6	±25.3	±33.4
SingleTop_tW_DS [%]	±0.31	< 0.05	±0.21	±0.36	±1.05	±0.08	±0.36	±0.54	±0.71	±1.43	±1.28	±1.68	±1.89	±2.10	±3.65	±4.73	±5.48	±6.24	±8.57	±18.6	±19.9	±22.3	±29.1
Wjets_norm [%]	±0.87	±0.70	±0.89	±1.04	±1.12	±1.18	±0.96	±1.27	±1.37	±1.37	±1.60	±2.13	±1.87	±2.31	±3.02	±3.31	±4.48	±3.85	±4.96	±6.71	±11.2	±9.74	±11.1	±15.8
Zjets_norm [%]	±0.47	±0.32	±0.25	±0.23	±0.21	±0.45	±0.33	±0.30	±0.31	±0.27	±0.59	±0.48	±0.51	±0.54	±0.51	±0.94	±0.82	±0.92	±1.02	±1.69	±1.65	±1.82	±1.97
JES/JER [%]	±1.62	±0.55	±0.47	±0.45	±0.51	±0.71	±0.75	±0.85	±0.95	±1.08	±1.22	±1.45	±1.67	±1.84	±2.41	±3.25	±3.39	±3.97	±5.71	±10.5	±10.8	±12.1	±15.9
CategoryReduction_JET_Pileup_RhoTopology [%]	±1.05	±0.36	±0.28	±0.29	±0.33	±0.46	±0.49	±0.55	±0.62	±0.70	±0.79	±0.94	±1.08	±1.19	±1.56	±2.11	±2.19	±2.57	±3.70	±6.82	±7.00	±7.85	±10.3
CategoryReduction_JET_EtaIntercalibration_Modelling [%]	±0.85	±0.31	±0.24	±0.25	±0.59	±0.39	±0.41	±0.46	±0.52	±0.59	±0.66	±0.79	±0.90	±0.99	±1.30	±1.76	±1.83	±2.14	±3.09	±5.69	±5.84	±6.55	±8.61
CategoryReduction_JET_Flavor_Response [%]	±0.65	±0.27	±0.15	±0.16	±0.22	±0.30	±0.32	±0.37	±0.41	±0.47	±0.53	±0.63	±0.72	±0.79	±1.04	±1.41	±1.47	±1.71	±2.47	±4.55	±4.68	±5.24	±6.89
IFSR + PDF [%]	±2.15	±0.73	±0.62	±0.59	±0.68	±0.59	±0.54	±0.57	±0.63	±0.72	±0.84	±1.00	±1.15	±1.27	±1.72	±2.33	±2.42	±2.74	±3.95	±7.28	±7.48	±8.38	±11.0
for_muR_syst [%]	±0.26	±0.29	±0.06	±0.08	±0.19	±0.26	±0.29	±0.33	±0.36	±0.40	±0.46	±0.56	±0.64	±0.71	±0.96	±1.30	±1.34	±1.52	±2.19	±4.04	±4.16	±4.65	±6.11
for_muRmuR_VarSc_syst [%]	±1.14	±0.47	±0.46	±0.49	±0.07	±0.27	±0.27	±0.31	±0.36	±0.40	±0.46	±0.56	±0.64	±0.71	±0.96	±1.30	±1.34	±1.52	±2.19	±4.04	±4.16	±4.65	±6.11
scale_muR_syst [%]	±0.47	±0.46	±0.46	±0.49	< 0.005	±0.07	±0.06	±0.06	±0.06	±0.06	±0.06	±0.06	±0.06	±0.06	±0.06	±0.06	±0.06	±0.06	±0.06	±0.06	±0.06	±0.06	±0.06
Flavour tagging [%]	±1.12	±0.47	±0.46	±0.49	±0.07	±0.27	±0.27	±0.31	±0.36	±0.40	±0.46	±0.56	±0.64	±0.71	±0.96	±1.30	±1.34	±1.52	±2.19	±4.04	±4.16	±4.65	±6.11
weight_bTagSF_DLlr_70_eigenvars_B_6 [%]	±0.4	±0.3	±0.3	±0.3	±0.3	±0.3	±0.3	±0.3	±0.3	±0.3	±0.3	±0.3	±0.3	±0.3	±0.3	±0.3	±0.3	±0.3	±0.3	±0.3	±0.3	±0.3	±0.3
weight_bTagSF_DLlr_70_eigenvars_B_4 [%]	±0.2	±0.2	±0.2	±0.2	±0.2	±0.2	±0.2	±0.2	±0.2	±0.2	±0.2	±0.2	±0.2	±0.2	±0.2	±0.2	±0.2	±0.2	±0.2	±0.2	±0.2	±0.2	±0.2
Leptons [%]	±0.5	±0.70	±0.67	±0.6	±0.74	±0.6	±0.6	±0.64	±0.6	±0.6	±0.6	±0.6	±0.6	±0.89	±0.6	±0.6	±0.6	±0.6	±0.6	±0.6	±0.6	±0.6	±0.6
weight_leptonSF_EL_SF_ID [%]	±0.35	±0.34	±0.36	±0.42	±0.56	±0.38	±0.38	±0.42	±0.49	±0.65	±0.50	±0.52	±0.58	±0.67	±0.86	±0.83	±0.84	±0.92	±1.12	±1.72	±1.72	±1.96	±2.16
weight_leptonSF_MU_SF_Trigger_SYST [%]	±0.33	±0.32	±0.32	±0.3	±0.37	±0.33	±0.33	±0.33	±0.32	±0.37	±0.32	±0.35	±0.35	±0.32	±0.31	±0.41	±0.37	±0.37	±0.32	±0.33	±0.33	±0.35	±0.36
weight_leptonSF_MU_SF_Isol_SYST [%]	±0.37	±0.35	±0.30	±0.26	±0.23	±0.30	±0.29	±0.27	±0.25	±0.23	±0.26	±0.26	±0.25	±0.25	±0.25	±0.28	±0.27	±0.27	±0.29	±0.37	±0.35	±0.35	±0.38

Table B.6: Table of systematics for the differential cross-section at the parton level for the observable $p_T^{t\bar{t}}$ in bins of $m^{t\bar{t}}$.

Bins [GeV]	0–0.30	0.30–0.65	0.65–1	1–1.45	1.45–2.50	2.50–2.70	2.70–2.95	2.95–3.15	3.15–3.40	3.40–3.65	3.65–5	5–5.20	5.20–5.40	5.40–5.60	5.60–5.85	5.85–6.05	6.05–6.40	6.40–7.50
$d^2\sigma/d\|y^{t\bar{t}}\|dm^{t\bar{t}}$ [pb/GeV]	$4.52 \cdot 10^2$	$4.29 \cdot 10^2$	$3.75 \cdot 10^2$	$2.85 \cdot 10^2$	$1.16 \cdot 10^2$	$7.25 \cdot 10^1$	$6.93 \cdot 10^1$	$6.30 \cdot 10^1$	$5.44 \cdot 10^1$	$4.32 \cdot 10^1$	$1.35 \cdot 10^1$	$5.16 \cdot 10^1$	$4.93 \cdot 10^1$	$4.37 \cdot 10^1$	$3.60 \cdot 10^1$	$2.72 \cdot 10^1$	$1.74 \cdot 10^1$	$3.10 \cdot 10^0$
Total Uncertainty [%]	±1.25	±1.24	±1.20	±1.30	±1.80	±2.82	±3.37	±4.48	±4.50	±4.84	±10.0	±12.0	±11.8	±12.0	±12.3	±12.6	±13.6	±15.0
Statistics [%]	±0.7	±0.7	±0.8	±0.9	±1.4	±2.3	±2.4	±2.7	±3.0	±3.2	±9.9	±11.5	±11.3	±11.2	±11.5	±12.0	±13.5	±15.0
Systematics [%]	±0.1	±0.1	±0.1	±0.1	±0.2	±0.3	±0.2	±0.2	±0.3	±0.3	±0.4	±0.4	±0.3	±0.4	±0.4	±0.5	±0.7	±1.4
Systematics [%]	±1.24	±1.23	±1.19	±1.29	±1.78	±2.82	±3.37	±4.48	±4.50	±4.84	±10.0	±12.0	±11.8	±12.0	±12.3	±12.6	±13.6	±15.0
JES/JER [%]	±3.42	±3.40	±3.40	±4.05	±5.10	±5.96	±5.92	±5.87	±5.89	±5.99	±5.38	±5.49	±5.03	±5.08	±5.28	±5.89	±5.98	±6.00
CategoryReduction_JET_Pileup_RhoTopology [%]	±3.15	±3.15	±3.49	±3.46	±3.31	±3.99	±3.72	±3.70	±3.72	±3.43	±3.25	±3.31	±3.28	±3.28	±3.33	±3.21	±3.96	±3.84
CategoryReduction_JET_EtaIntercalibration_Modelling [%]	±1.63	±1.70	±1.66	±1.41	±2.12	±1.35	±1.80	±1.62	±1.75	±2.25	±3.39	±1.68	±1.66	±1.86	±2.05	±2.25	±3.04	±3.09
CategoryReduction_JET_Flavor_Response [%]	±1.45	±1.44	±1.42	±1.78	±2.96	±1.68	±1.67	±1.77	±1.74	±1.75	±1.96	±1.99	±1.67	±1.85	±1.99	±2.39	±2.47	±1.96
IFSR + PDF [%]	±1.29	±1.38	±1.49	±1.64	±1.80	±2.82	±1.76	±1.77	±1.80	±1.84	±2.04	±1.62	±1.59	±1.69	±1.72	±1.63	±1.73	±2.15
for_muR_syst [%]	±1.17	±1.18	±1.28	±1.26	±2.52	±4.04	±2.30	±2.23	±3.57	±2.96	±2.60	±3.95	±4.26	±4.21	±4.29	±4.18	±3.93	±3.76
for_muRmuR_VarSc_syst [%]	±1.14	±1.07	±1.24	±1.23	±2.40	±3.95	±2.08	±2.09	±3.49	±2.10	±2.35	±3.43	±3.40	±3.46	±3.70	±3.73	±3.88	±2.69
scale_muR_syst [%]	±0.10	±0.23	±0.31	±0.41	±0.58	±0.46	±0.63	±0.66	±0.58	±0.98	±1.27	±1.36	±1.34	±1.36	±1.64	±1.65	±1.77	±6.48
IntraPDF [%]	±0.27	±0.21	±0.12	±0.17	±1.28	±0.43	±0.33	±0.24	±0.16	±0.32	±1.71	±0.40	±0.34	±0.24	±0.22	±0.47	±0.96	±4.08
scale_muF_syst [%]	±0.29	±0.27	±0.23	±0.12	±0.17	±0.07	±0.07	±0.13	±0.11	±0.16	±0.69	±0.18	±0.12	±0.11	±0.09	±0.61	±1.13	±4.08
Modelling [%]	±3.52	±3.38	±2.93	±1.96	±1.16	±1.04	±0.96	±0.82	±1.30	±2.15	±3.89	±4.95	±4.43	±4.50	±4.92	±5.32	±6.97	±9.46
Hadronisation [%]	±3.48	±3.34	±2.79	±1.92	±0.77	±0.64	±0.82	±0.68	±1.25	±1.97	±3.84	±4.54	±4.31	±4.45	±4.89	±5.30	±6.73	±9.03
HardScattering [%]	±0.28	±0.15	±0.19	< 0.05	±0.52	±0.76	±0.29	±0.36	±0.15	±0.78	±0.42	±1.96	±0.89	±0.32	±0.13	±0.73	±1.65	±0.78
mtop [%]	±0.45	±0.46	±0.45	±0.52	±0.69	±0.20	±0.29	±0.37	±0.33	±0.45	±0.39	±0.43	±0.27	±0.52	±0.58	±0.71	±0.59	±0.56
Flavour tagging [%]	±1.60	±1.60	±1.36	±1.76	±1.04	±1.17	±1.17	±1.06	±2.29	±2.47	±2.41	±2.93	±2.82	±2.81	±2.78	±2.72	±2.56	±2.79
weight_bTagSF_DLlr_70_eigenvars_B_0 [%]	±2.82	±2.80	±2.73	±2.61	±3.32	±2.81	±2.68	±2.69	±2.87	±2.82	±2.09	±2.00	±1.96	±1.96	±1.78	±1.72	±1.79	±1.93
weight_bTagSF_DLlr_70_eigenvars_B_1 [%]	±1.81	±1.80	±1.74	±1.61	±3.37	±2.72	±2.69	±2.61	±2.59	±2.34	±2.09	±1.91	±1.97	±1.92	±1.84	±1.74	±1.58	±1.45
weight_bTagSF_DLlr_70_eigenvars_B_2 [%]	±0.78	±0.78	±0.80	±0.84	±0.94	±1.22	±1.32	±1.28	±1.35	±1.40	±1.24	±1.85	±1.86	±1.88	±1.93	±1.94	±2.06	±2.16
weight_bTagSF_DLlr_70_eigenvars_B_3 [%]	±0.89	±0.89	±0.90	±0.89	±0.84	±0.81	±0.83	±0.81	±0.78	±0.70	±0.60	±0.59	±0.57	±0.54	±0.49	±0.97	±0.41	±0.32
Background [%]	±1.20	±1.22	±1.25	±1.28	±1.26	±2.25	±2.23	±2.18	±2.16	±2.28	±2.40	±5.27	±5.19	±5.04	±5.01	±4.97	±4.99	±3.96
Wjets_norm [%]	±0.89	±0.89	±0.93	±0.99	±1.12	±1.62	±1.63	±1.61	±1.58	±1.63	±1.74	±3.44	±3.38	±3.29	±3.19	±3.09	±3.05	±2.96
SingleTop_tW_DS [%]	±0.09	±0.09	±0.08	±0.05	< 0.05	±0.73	±0.78	±0.81	±0.94	±1.18	±1.35	±3.44	±3.41	±3.35	±3.50	±3.58	±3.72	±2.43
Zjets_norm [%]	±0.43	±0.42	±0.41	±0.39	±0.37	±0.49	±0.49	±0.47	±0.44	±0.41	±0.38	±0.71	±0.71	±0.70	±0.67	±0.63	±0.59	±0.53
Leptons [%]	±0.59	±0.60	±0.64	±0.72	±0.94	±0.70	±0.72	±0.67	±0.81	±0.84	±0.95	±0.96	±1.00	±1.07	±1.13	±1.18	±1.22	±1.40
weight_leptonSF_EL_SF_ID [%]	±0.34	±0.33	±0.33	±0.38	±0.57	±0.39	±0.40	±0.42	±0.45	±0.51	±0.71	±0.60	±0.62	±0.66	±0.71	±0.77	±0.88	±1.12
weight_leptonSF_MU_SF_Trigger_SYST [%]	±0.29	±0.31	±0.34	±0.38	±0.42	±0.33	±0.33	±0.33	±0.34	±0.35	±0.39	±0.38	±0.38	±0.37	±0.37	±0.36	±0.38	±0.42
weight_leptonSF_MU_SF_Isol_SYST [%]	±0.33	±0.34	±0.35	±0.35	±0.32	±0.28	±0.28	±0.27	±0.26	±0.25	±0.24	±0.26	±0.26	±0.25	±0.24	±0.23	±0.22	±0.22

Table B.7: Table of systematics for the differential cross-section at the parton level for the observable $|y^{t\bar{t}}|$ in bins of $m^{t\bar{t}}$.

Bins [GeV] x [GeV]	0–90	90–180	180–300	300–600	600–1200	1200–1250	1250–1300	1300–1350	1350–1500	1500–1800	1800–2400	2400–2480	2480–2570	2570–2690	2690–3000	3000–3600	3600–3690	3690–3770	3770–3870	3870–3970	3970–4270	4270–4800	4800–4900	4900–5090	5090–5170	5170–5470	5470–6000
$d^2\sigma/dp_T^{t,\mathrm{had}}dm^{t\bar{t}}$ [pb/GeV x GeV]	$2.94 \cdot 10^0$	$2.25 \cdot 10^0$	$1.53 \cdot 10^{-1}$	$5.09 \cdot 10^{-2}$	$5.35 \cdot 10^{-3}$	$4.35 \cdot 10^{-1}$	$1.36 \cdot 10^0$	$5.74 \cdot 10^{-1}$	$1.59 \cdot 10^{-1}$	$1.22 \cdot 10^{-2}$	$1.48 \cdot 10^{-3}$	$2.77 \cdot 10^{-1}$	$2.16 \cdot 10^{-1}$	$4.92 \cdot 10^{-2}$	$1.74 \cdot 10^{-2}$	$2.96 \cdot 10^{-3}$	$5.75 \cdot 10^{-4}$	$4.68 \cdot 10^{-4}$	$3.09 \cdot 10^{-4}$	$1.37 \cdot 10^{-4}$	$3.62 \cdot 10^{-5}$	$5.74 \cdot 10^{-6}$	$1.92 \cdot 10^{-6}$	$7.70 \cdot 10^{-7}$	$4.78 \cdot 10^{-7}$	$1.99 \cdot 10^{-7}$	$3.44 \cdot 10^{-8}$
Total Uncertainty [%]	±0.1	±0.0	±0.6	±0.2	±1.4	±0.1	±0.1	±0.1	±0.3	±0.9	±0.3	±0.2	±0.2	±0.3	±0.6	±0.5	±0.5	±0.5	±0.6	±0.7	±3.1	±1.2	±1.4	±2.3	±3.5	±4.5	±12
Statistics [%]	±0.1	±0.0	±0.1	±0.1	±0.2	±0.1	±0.1	±0.1	±0.2	±0.4	±0.1	±0.1	±0.1	±0.2	±0.4	±0.3	±0.4	±0.4	±0.4	±0.5	±2.1	±0.7	±0.9	±1.5	±2.1	±2.7	±9.1
Systematics [%]	±0.1	±0.0	±0.6	±0.2	±1.4	±0.1	±0.1	±0.1	±0.3	±0.9	±0.3	±0.2	±0.2	±0.3	±0.6	±0.5	±0.5	±0.5	±0.6	±0.7	±3.1	±1.2	±1.4	±2.3	±3.5	±4.5	±12
Background [%]	±1.34	±1.03	±1.48	±3.29	±16.9	±2.42	±1.62	±0.78	±2.08	±8.87	±5.48	±4.38	±4.69	±1.43	±8.42	±9.59	±9.07	±7.92	±7.88	±6.87	±18.5	±14.6	±15.5	±17.7	±29.0	±24.3	±45.3
SingleTop_tW_DS [%]	±0.24	±0.13	±0.67	±2.46	±10.1	±0.27	±0.24	±0.15	±1.36	±7.93	±1.38	±1.58	±1.51	±0.11	±7.55	±3.55	±4.14	±4.96	±5.62	±6.39	±17.6	±7.06	±9.65	±11.5	±15.4	±23.9	±44.8
Wjets_norm [%]	±1.06	±0.71	±1.07	±1.89	±3.60	±2.24	±1.21	±0.42	±1.31	±3.56	±4.83	±3.52	±1.75	±0.65	±3.69	±8.34	±7.42	±5.52	±3.96	±2.23	±4.46	±2.60	±2.12	±2.17	±2.73	±3.60	±9.42
SingleTop_norm [%]	±0.17	±0.16	±0.23	±0.39	±0.86	±0.30	±0.24	±0.17	±0.32	±0.79	±0.55	±0.52	±0.40	±0.25	±0.94	±0.84	±0.68	±0.59	±0.62	±0.59	±1.30	±1.32	±1.28	±1.52	±1.73	±1.99	±3.45
IFSR + PDF [%]	±2.6	±1.6	±1.6	±0.7	±3.6	±3.0	±2.5	±1.5	±1.1	±1.6	±0.6	±0.6	±0.6	±0.5	±1.1	±1.6	±1.6	±1.6	±1.6	±1.7	±3.7	±2.6	±2.6	±2.7	±3.2	±3.4	±5.1
scale_muR_syst [%]	±0.0	±0.0	±0.0	±0.0	±0.0	±0.0	±0.0	±0.0	±0.0	±0.0	±0.0	±0.0	±0.0	±0.0	±0.0	±0.0	±0.0	±0.0	±0.0	±0.0	±0.0	±0.0	±0.0	±0.0	±0.0	±0.0	±0.0
scale_muRmuR_syst [%]	±0.0	±0.0	±0.0	±0.0	±0.0	±0.0	±0.0	±0.0	±0.0	±0.0	±0.0	±0.0	±0.0	±0.0	±0.0	±0.0	±0.0	±0.0	±0.0	±0.0	±0.0	±0.0	±0.0	±0.0	±0.0	±0.0	±0.0
for_muR_syst [%]	±0.2	±0.2	±0.2	±0.2	±0.2	±0.2	±0.2	±0.2	±0.2	±0.2	±0.2	±0.2	±0.2	±0.2	±0.2	±0.2	±0.2	±0.2	±0.2	±0.2	±0.2	±0.2	±0.2	±0.2	±0.2	±0.2	±0.2
Modelling [%]	±4.59	±3.2	±1.0	±0.64	±2.73	±0.62	±1.16	±1.2	±0.3	±0.63	±1.2	±1.67	±1.1	±0.74	±1.7	±1.6	±1.6	±1.6	±4.63	±4.6	±11.3	±11.3	±14.9	±444	±14.7	±14.3	±14.3
Hadronisation [%]	±4.54	±3.23	±4.87	±7.54	±12.3	±2.73	±3.53	±1.03	±3.12	±3.98	< 0.05	±1.43	±1.54	±1.99	±5.39	±5.05	±5.03	±4.92	±2.73	±2.62	±1.27	±11.0	±11.8	±13.9	±14.3	±14.0	±12.1
HardScattering [%]	±0.37	±0.19	±0.12	±2.89	±15.1	±0.29	±0.32	±0.52	±0.14	±2.65	±0.25	±0.39	±0.27	±0.71	±4.08	±0.80	±0.80	±0.93	±0.74	±0.55	±0.76	±2.34	±1.69	±1.48	±3.97	±1.82	±7.09
mtop [%]	±0.1	±0.1	±0.2	±0.1	±0.7	< 0.05	±0.1	±0.1	±0.1	±0.62	±0.1	±0.2	±0.2	±0.1	±0.3	±0.2	±0.2	±0.2	±0.2	±0.2	±0.2	±0.2	±0.43	±0.4	< 0.05	±0.2	±0.7
JES/JER [%]	±0.71	±0.5	±0.9	±0.6	±1.3	±0.6	±0.6	±0.6	±0.6	±0.6	±0.6	±0.6	±0.6	±0.6	±0.6	±0.6	±0.6	±0.6	±0.6	±0.6	±0.6	±0.6	±0.6	±0.6	±0.6	±0.6	±0.6
CategoryReduction_JET_Pileup_RhoTopology [%]	±0.6	±0.5	±0.8	±0.6	±1.3	±0.6	±0.6	±0.6	±0.6	±0.6	±0.6	±0.6	±0.6	±0.6	±0.6	±0.6	±0.6	±0.6	±0.6	±0.6	±0.6	±0.6	±0.6	±0.6	±0.6	±0.6	±0.6
CategoryReduction_JET_EtaIntercalibration_Modelling [%]	±0.6	±0.5	±0.8	±0.6	±1.3	±0.6	±0.6	±0.6	±0.6	±0.6	±0.6	±0.6	±0.6	±0.6	±0.6	±0.6	±0.6	±0.6	±0.6	±0.6	±0.6	±0.6	±0.6	±0.6	±0.6	±0.6	±0.6
CategoryReduction_JET_Flavor_Response [%]	±0.6	±0.5	±0.8	±0.6	±1.3	±0.6	±0.6	±0.6	±0.6	±0.6	±0.6	±0.6	±0.6	±0.6	±0.6	±0.6	±0.6	±0.6	±0.6	±0.6	±0.6	±0.6	±0.6	±0.6	±0.6	±0.6	±0.6
Flavour tagging [%]	±1.6	±1.2	±1.2	±1.2	±2.6	±1.2	±1.2	±1.2	±1.2	±1.2	±1.2	±1.2	±1.2	±1.2	±1.2	±1.2	±1.2	±1.2	±1.2	±1.2	±1.2	±1.2	±1.2	±1.2	±1.2	±1.2	±1.2
weight_bTagSF_DLlr_70_eigenvars_B_6 [%]	±0.2	±0.2	±0.2	±0.2	±0.2	±0.2	±0.2	±0.2	±0.2	±0.2	±0.2	±0.2	±0.2	±0.2	±0.2	±0.2	±0.2	±0.2	±0.2	±0.2	±0.2	±0.2	±0.2	±0.2	±0.2	±0.2	±0.2
weight_bTagSF_DLlr_70_extrapolation [%]	< 0.05	< 0.05	< 0.05	±0.03	±0.04	< 0.05	< 0.05	±0.08	±0.1	< 0.05	< 0.05	< 0.05	< 0.05	< 0.05	±0.1	±0.09	±0.1	±0.1	±0.07	±0.23	±0.59	±0.4	±0.4	±0.4	±2.85	±1.2	±1.2
weight_bTagSF_DLlr_70_eigenvars_B_1 [%]	±0.64	±0.5	±3.02	±1.6	±1.6	±0.85	±1.01	±0

Appendix B. Systematic tables

Bins [GeV]	0–75	75–170	170–300	300–500	500–1000	1000–1075	1075–1170	1170–1300	1300–1500	1500–2000	2000–2075	2075–2170	2170–2300	2300–2500	2500–3000	3000–3075	3075–3180	3180–4000
$d^2\sigma/dp_T^{t\bar{t}}d\|y^{t\bar{t}}\|$ [pb/GeV]	$2.63 \cdot 10^0$	$6.59 \cdot 10^{-1}$	$1.42 \cdot 10^{-1}$	$2.47 \cdot 10^{-2}$	$1.80 \cdot 10^{-3}$	$2.62 \cdot 10^0$	$6.34 \cdot 10^{-1}$	$1.31 \cdot 10^{-1}$	$2.18 \cdot 10^{-2}$	$1.44 \cdot 10^{-3}$	$1.64 \cdot 10^0$	$3.68 \cdot 10^{-1}$	$7.07 \cdot 10^{-2}$	$1.02 \cdot 10^{-2}$	$5.25 \cdot 10^{-4}$	$8.00 \cdot 10^{-1}$	$1.39 \cdot 10^{-1}$	$3.76 \cdot 10^{-3}$
Total Uncertainty [%]	±8.24	±14.4	±12.0	±9.11	±3.26	±6.47	±12.0	±12.2	±9.16	±9.76	±6.96	±12.1	±12.4	±9.96	±13.8	±7.26	±12.2	±12.6
Statistics [%]	-7.44	-13.9	-11.4	-8.97	-3.06	-7.52	-13.1	-13.0	-10.1	-9.58	-8.21	-12.7	-13.2	-10.0	-13.3	-8.31	-12.6	-13.1
	±0.1	±0.1	±0.3	±0.6	±1.5	±0.1	±0.1	±0.3	±0.6	±1.6	±0.2	±0.2	±0.4	±0.9	±2.8	±0.5	±0.4	±0.9
Systematics [%]	±4.32	±13.4	±12.0	±9.09	±8.19	±6.48	±13.0	±12.5	±9.07	±8.59	±6.85	±12.5	±12.4	±9.60	±11.2	±7.74	±12.5	±12.3
	-7.44	-13.9	-11.4	-9.05	-3.45	-7.52	-13.1	-13.0	-10.1	-9.42	-8.21	-12.7	-13.2	-10.0	-13.3	-8.29	-12.6	-13.1
JES/JER [%]	±2.24	±2.06	±2.24	±2.52	±1.09	±1.97	±2.23	±2.30	±2.17	±1.61	±1.22	±2.30	±3.13	±1.17	±3.21	±1.39	±2.25	±2.25
CategoryReduction_JET_Pileup_RhoTopology [%]	±2.16	±0.96	±0.43	±0.68	±2.17	±2.22	±0.97	±2.30	±2.35	±2.03	±2.39	±2.30	±0.23	±2.36	±2.60	±2.21	±2.36	±2.12
CategoryReduction_JET_Flavor_Response [%]	-2.23	-3.16	-2.98	-2.31	-2.04	-1.27	-1.05	-2.06	-3.19	-2.07	-1.28	-1.99	-3.09	-2.32	-2.67	-1.27	-1.89	-1.86
	±0.67	±2.62	±3.22	±3.05	±1.51	±0.77	±2.51	±3.29	±3.02	±1.61	±1.01	±2.75	±3.42	±3.26	±1.99	±1.45	±2.07	±3.09
CategoryReduction_JET_EtaIntercalibration_Modelling [%]	-0.89	-2.61	-2.51	-1.42	-1.07	-0.51	-2.28	-2.12	-1.95	-1.32	-1.33	-2.04	±3.35	-1.22	-1.81	-1.21	-1.66	-2.21
	±0.12	-1.91	-2.13	-1.05	-1.26	-0.56	-2.28	-2.72	-1.57	-1.50	-1.13	-2.08		-1.57	-2.02	-1.05	-1.40	-2.15
Modelling [%]	±1.72	±9.76	±8.66	±3.60	±1.86	±1.97	±9.20	±7.92	±3.41	±5.30	±1.64	±8.15	±7.25	±1.76	±9.27	±2.30	±6.92	±6.16
Hadronization [%]	±1.59	±9.72	±8.40	±4.28	±4.11	±1.76	±9.15	±7.75	±3.72	±4.38	±2.47	±8.03	±7.14	±4.51	±7.15	±2.20	±6.60	±5.17
HardScattering [%]	±0.50	∓0.78	∓2.03	∓1.28	±1.07	±0.77	∓0.80	∓1.54	±1.71	∓2.93	±0.85	∓1.28	∓1.45	∓1.24	∓4.88	±0.33	∓1.92	∓3.48
mtop [%]	±0.42	±0.50	±0.45	±0.45	±0.42	±0.45	±0.39	±0.52	±0.49	±0.27	±0.45	±0.48	±0.48	±0.60	±0.45	±0.59	±0.62	±0.42
	-0.41	-0.73	-0.58	-0.46	-0.40	-0.41	-0.38	-0.49	-0.48	-0.26	-0.44	-0.47	-0.47	-0.58	-0.44	-0.58	-0.59	-0.41
IFSR + PDF [%]	±2.60	±3.76	±3.30	±2.66	±1.69	±1.81	±3.36	±3.50	±2.59	±2.99	±1.51	±3.02	±2.97	±1.69	±2.46	±1.32	±3.06	±3.83
fsr_muR_syst [%]	±2.16	±2.16	±2.98	±2.66	±2.02	±1.21	±2.28	±2.26	±2.11	±2.82	±2.44	±2.01	±2.84	±2.23	±2.25	±1.10	±2.84	±2.38
	±1.44	±2.16	±2.98	±2.66	±2.02	±1.21	±2.28	±2.26	±2.11	±2.82	±2.44	±2.01	±2.84	±2.23	±2.25	±1.10	±2.84	±2.38
scale_muR_syst [%]	-0.84	-0.84	-0.61	-0.47	-0.86	< 0.05	-0.28	-0.66	-0.70	-0.65	-0.86	-0.65	-0.85	-0.86	-0.67	-0.65	-0.96	-0.85
	±0.05	±0.41	±0.79	±0.79	±0.40		±0.38	±0.76		±0.05	±0.36	±0.64	±1.44	±0.97	±0.45	±0.44	±1.04	±1.89
IntraPDF [%]	±0.22	±0.25	±0.33	±0.33	±0.23	±0.08	±0.12	±0.25	±0.28	±0.17	±0.35	±0.44	±0.28	±0.19	±0.47	±2.01	±2.71	±2.50
Flavour tagging [%]	-3.96	-3.37	-3.18	-2.69	-2.35	-3.82	-3.55	-3.26	-2.68	-2.21	-2.31	-3.51	-3.25	-2.38	-2.24	-2.37	-3.47	-3.20
	-3.82	-3.22	-3.19	-2.89	-2.73	-3.77	-3.59	-3.36	-2.91	-2.72	-2.46	-3.46	-3.22	-2.95	-2.73	-2.52	-3.42	-3.20
weight_bTagSF_DL1r_70_eigenvars_B_0 [%]	-2.61	-2.47	-2.90	-2.61	-2.00	-3.12	-2.24	-2.86	-2.59	-2.02	-1.48	-2.19	-2.56	-2.21	-2.10	-2.42	-3.13	-2.89
	±2.62	±2.47	±2.90	±2.61	±2.00	±3.12	±2.24	±2.86	±2.59	±2.02	±1.48	±2.19	±2.56	±2.21	±2.10	±2.42	±3.13	±2.89
weight_bTagSF_DL1r_70_eigenvars_B_1 [%]	±0.95	±0.94	±1.01	±1.29	±1.78	±0.96	±0.85	±1.03	±1.48	±1.76	±0.98	±0.95	±1.02	±1.23	±1.65	±1.00	±0.97	±1.08
weight_bTagSF_DL1r_70_eigenvars_B_2 [%]	±0.80	±0.81	±0.74	±0.64	±0.29	±0.90	±0.82	±0.75	±0.65	±0.33	±0.90	±0.82	±0.77	±0.68	±0.40	±0.89	±0.83	±0.76
Background [%]	±1.66	±1.68	±2.07	±2.42	±3.54	±1.53	±1.60	±2.00	±2.34	±3.31	±1.34	±1.49	±1.87	±2.22	±2.65	±1.25	±1.30	±1.83
Wjets_norm [%]	±1.32	±1.10	±1.46	±1.83	±1.97	±1.24	±1.03	±1.43	±1.86	±2.13	±1.15	±1.02	±1.42	±1.91	±2.26	±1.10	±1.08	±1.60
SingleTop_tW_DS [%]	±0.22	∓0.59	±0.89	±1.30	∓2.85	∓0.21	∓0.54	±0.75	±1.04	∓2.40	±0.10	∓0.46	±0.63	±0.74	±1.22	±0.35	∓0.14	±0.35
Zjets_norm [%]	±0.55	±0.38	±0.32	±0.31	±0.30	±0.49	±0.36	±0.32	±0.33	±0.31	±0.41	±0.33	±0.33	±0.36	±0.34	±0.37	±0.35	±0.36
Leptons [%]	-0.67	±0.60	±0.61	±0.67	-0.46	-0.62	-0.61	-0.64	-0.66	±0.71	±0.60	-0.71	±0.78	±0.78	±0.85	-0.66	±1.01	±1.07
	±0.67				-0.46	-0.62	-0.61	-0.64	-0.66		-0.60	-0.71				-0.66		
weight_leptonSF_EL_SF_ID [%]	±0.36	±0.36	±0.40	±0.50	±0.73	±0.38	±0.38	±0.42	±0.52	±0.75	±0.46	±0.46	±0.53	±0.64	±0.81	±0.69	±0.65	±0.78
weight_leptonSF_MU_SF_Trigger_SYST [%]	±0.31	-0.37	±0.30	-0.39	-0.28	-0.33	-0.31	±0.33	-0.37	±0.32	-0.40	-0.39	-0.38	-0.36	-0.38	-0.42	-0.41	±0.41
		±0.37		±0.39	±0.29	±0.33	±0.31		±0.37		±0.40	±0.39	±0.38	±0.36	±0.38	±0.42	±0.41	
weight_leptonSF_MU_SF_Isol_SYST [%]	±0.33	±0.31	±0.27	±0.24	±0.22	±0.34	±0.32	±0.28	±0.25	±0.23	±0.34	±0.32	±0.29	±0.26	±0.24	±0.30	±0.30	±0.27

Table B.9: Table of systematics for the differential cross-section at the parton level for the observable $p_T^{t\bar{t}}$ in bins of $|y^{t\bar{t}}|$.

Appendix C

Update of the EvtGen decay models and branching ratios, together with mass tables for heavy flavour hadrons decay

C.1 Introduction

Final states that include heavy flavour (bottom and charm) hadrons are important for the study of many processes at the LHC [157]. Examples of these processes include top quark pair ($t\bar{t}$) production, Higgs production and searches for physics beyond the Standard Model (SM). To fully exploit the large data samples that have been collected during Run II at the LHC, a reduction in systematic uncertainties associated with the modelling of heavy flavour (HF) hadron production and decay will be needed. Although data-driven methods are likely to play a major part in the effort to reduce these uncertainties, improvements in the Monte Carlo (MC) models used to determine reconstruction efficiencies will also be necessary.

The BELLE II [158] collaboration has provided new models and updated decay tables, with major updates pertaining HF hadrons, therefore the focus of this work has been studying distributions that could give detailed info on how these changes affect Monte Carlo samples. These new models have been compiled into a modified version of EvtGen 1.7 [159] and compared to the results obtained using the default ATLAS tables as well as other MC generators. The BELLE II collaboration also provided updated mass tables with the most recent measurements from the PDG [160].

C.2 Monte Carlo samples and Rivet routine

The versions of the generators studied here were PYTHIA 8.244 [79] and PYTHIA 8.3 [161], HERWIG 7.2.1 [162], POWHEG [163] and SHERPA 2.2.11 [81]. In all samples except SHERPA, EVTGEN has been used to redecay the heavy flavour hadrons. All pp samples have been generated at the center-of-mass energy of $\sqrt{s} = 13$ TeV. The studied process is inclusive top-pair production, therefore no requirements are made for the W bosons decay channel.

The Rivet [164] routine, prepared to validate the new EVTGEN decay tables from the BELLE II collaboration, includes the following HF jets and hadrons related observables:

- Stable and charged stable particle multiplicities for B^+, B^0, B_s^0, Λ_b^0, D^0, D^+, D_s^+, Λ_c^+.
- Production fractions for HF hadrons.
- Stable charged particle multiplicity in b- and c-jets.
- Fragmentation functions (FFs) for HF jets, calculated as a function of

$$z \equiv \frac{\vec{p}_{\text{hadron}} \cdot \vec{p}_{\text{jet}}}{p_{\text{jet}}^2}, \tag{C.1}$$

  where $\vec{p}_{\text{hadron}}$ and $\vec{p}_{\text{jet}}$ are the 3-momentum of the HF hadron and of the reconstructed jet, respectively.

  In this study z was measured for anti-k_t (R=0.4) jets with rapidity $|\eta^{\text{jet}}| < 2.5$ and transverse momentum $p_T^{\text{jet}} > 25$ GeV. Jets are defined to be heavy flavour jets if there is a HF hadron with momentum $p_T > 5$ GeV within $\Delta R = \sqrt{\Delta\phi^2 + \Delta\eta^2} <$ 0.3 of the jet direction.

  The following distributions were included in the routine:

- FFs for HF jets in the region 500 GeV $< p_T <$ 1000 GeV.
- FFs for HF jets with exactly 1 HF hadron.
- p_T and $p_{T_{\text{rel}}}$ distributions for leptons in b- and c-jets, where $p_{T_{\text{rel}}}$ is calculated as

$$p_{T_{\text{rel}}} \equiv \frac{|\vec{p}_{\text{lep}} \times \vec{p}_{\text{jet}}|}{|\vec{p}_{\text{jet}}|}. \tag{C.2}$$

  Here again $\vec{p}_{\text{jet}}$ is the 3-momentum of the considered jet, while $\vec{p}_{\text{lep}}$ is the one associated with the lepton.

- Differential and integrated jet shapes. The differential jet shape $\rho(r)$ in an annulus of inner radius $r - \Delta r/2$ and outer radius $r + \Delta r/2$ from the axis of a given jet [1] is defined as

$$\rho(r) \equiv \frac{1}{\Delta r} \frac{p_T(r - \Delta r/2, r + \Delta r/2)}{p_T(0, R)}, \tag{C.3}$$

  where $p_T(a, b)$ is the total p_T of the particles found in an annulus of inner radius a and outer radius b. In a similar way, the integrated jet shape is defined to be:

$$\Psi(r) \equiv \frac{p_T(0,\ r)}{p_T(0, R)},\ 0 \leq r \leq R. \tag{C.4}$$

- Jet width W, obtained as a distribution of the distance ΔR from the center of the jet weighted by the jet constituent (stable) particles' p_T in the following way:

$$W \equiv \frac{\sum_i p_{T_i} \Delta R_i}{\sum_i p_{T_i}}. \tag{C.5}$$

- Jet p_T and p_T^{had}. Here p_T is the transverse momentum of the jet, while p_T^{hadron} is the transverse momentum of the HF included in the jet.

The routine also includes the distributions of the following observables:

- differential jet shape,
- lepton $p_{T_{\text{rel}}}$ for b- and c-jets,
- stable charged particle multiplicity in HF jets,

divided in the following jet p_T bins:

$$\{25,\ 30,\ 50,\ 70,\ 100,\ 150,\ 300,\ 500,\ 1000\}\ \text{GeV}.$$

In this study, only jets with a $p_T > 25$ GeV were considered. The routine has been added to the Rivet repository under the name MC_HFDECAYS.

C.3 Results

A good agreement was found between the new BELLE II models/decay tables and the standard ATLAS ones. Herwig and Sherpa, on the other hand, while in reasonable agreement in the b-jet fragmentation function and in the core of the c-jet one ($0.2 < z < 0.9$), showed a difference of $\sim 40\%$ in the

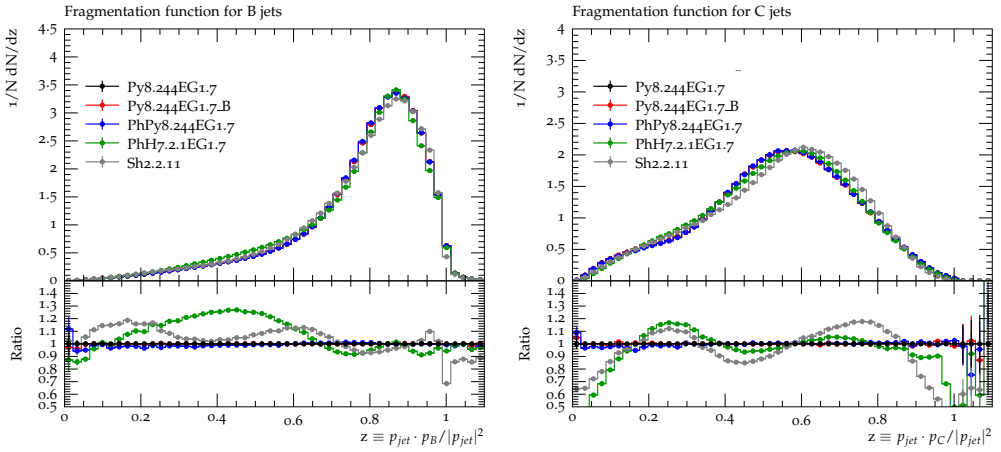

(a) (b)

Figure C.1: Fragmentation functions for b- (a) and c-jets (b).

low- and high-z regions, as can be seen in Fig. C.1. The $p_{T_{\mathrm{rel}}}$ distribution of the leptons contained in the HF jets, shown in Fig. C.2, showed a good overall agreement between different generators, except for SHERPA 2.2.11, which differed from the others by more than 40% in most of the bins. As

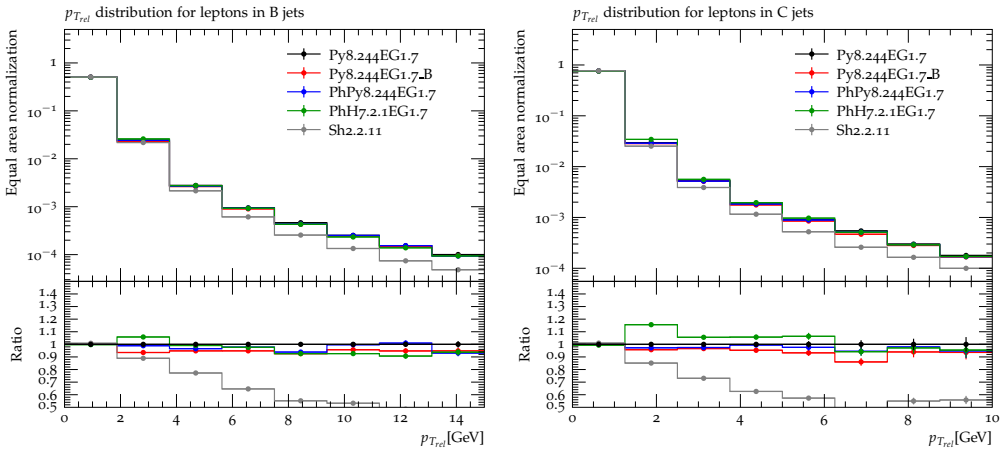

(a) (b)

Figure C.2: $p_{T_{\mathrm{rel}}}$ distributions for leptons in b- (a) and c-jets (b).

[1]The jet axis is defined to be the direction of the momentum of the jet from the anti-k_t (R=0.4) algorithm

for the differential jet shape (Fig. C.3), for both b- and c-jets the agreement was very good between all the considered MC samples, reaching differences not bigger than $\sim 10\%$ in all the bins. Comparing the results obtained with

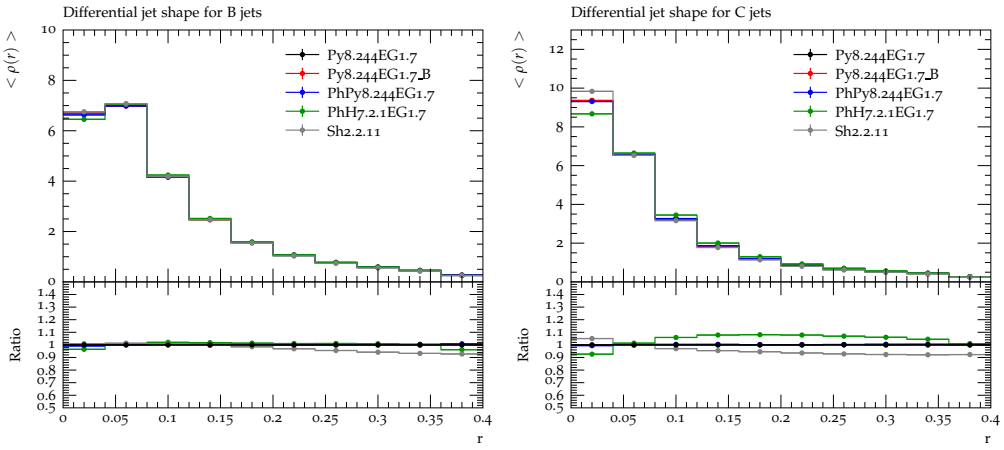

(a) (b)

Figure C.3: Differential jet shape (ρ) distributions for b- (a) and c-jets (b).

different generators for distributions divided in p_T bins (e.g. the $p_{T_{\text{rel}}}$ of the leptons in the HF jet), all the generators were in good agreement, even in low-statistics bins considering the large uncertainties. SHERPA was the only one which differed by more than 40% in most of the $p_{T_{\text{rel}}}$ bins. However, as shown in Fig. C.5, in the high-p_T bins ($p_T > 300$ GeV), this difference became smaller and disappeared in the last one, where 500 GeV $< p_T <$ 1000 GeV Fig. C.5(h).

Since the biggest changes in the EVTGEN tables were made in the HF hadrons decays, part of the study has been dedicated to investigate how these changes affect the production fractions and multiplicities of neutral stable and stable charged decay products of these hadrons.

Charged multiplicities and decay multiplicities showed quite clearly the differences between the default and updated tables, together with some differences with other generators. In particular SHERPA, which however has not been interfaced with EVTGEN, differed by $\sim 40\%$ with respect to other generators in the low-multiplicity bins of the charged multiplicity distribution when looking at b-jets (Fig. C.4), while HERWIG differed by $\sim 50\%$ in the high-multiplicities region.

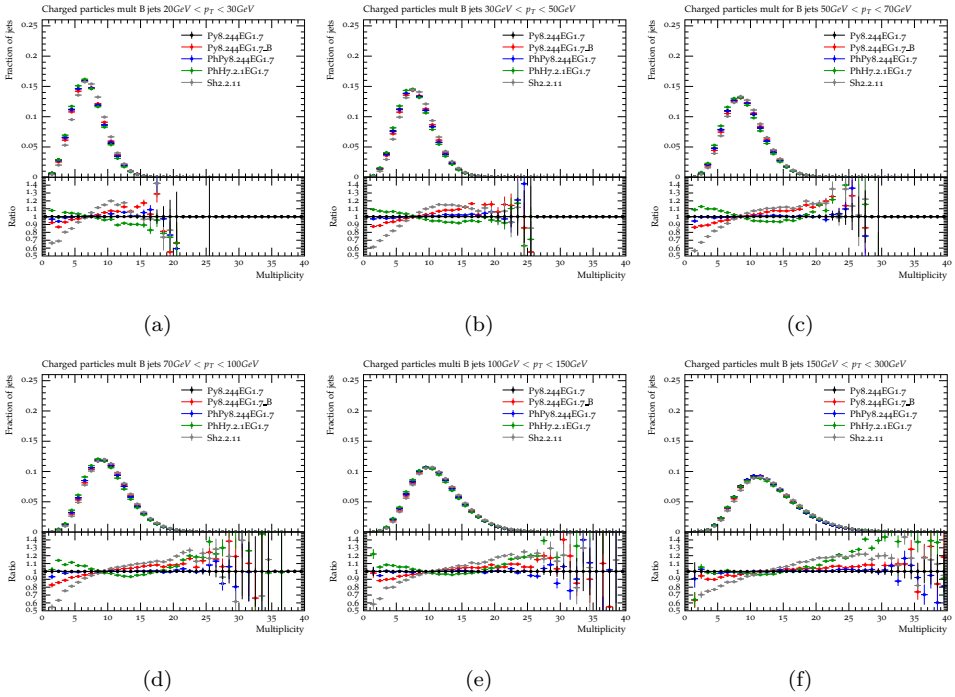

Figure C.4: Charged particle multiplicities for b-jets in different p_T regions.

C.4 Conclusion

The differences between the standard ATLAS decay tables used by EvtGen and an updated version of them made available by the BELLE II collaboration were studied, together with new decay models. Since the changes were mostly important in heavy flavour hadrons decays, the studied distributions refer to either b- or c-jets. No major change was observed in fragmentation functions, jet width/shape, nor $p_{T_{\text{rel}}}$ distributions, while it was clear (and expected) that the updated tables affect the neutral stable and charged stable decay products multiplicities for HF hadrons.

Some differences have been observed between Herwig, Sherpa and Pythia, in particular in distributions like fragmentation functions, where differences ranged from 10 to 40% for both Sherpa and Herwig, and $p_{T_{\text{rel}}}$ distributions where Sherpa differed from the other generators by as much as 50%. Large differences were also observed in the production fractions of heavy flavour hadrons.

To investigate the difference between different generators and versions of both decay models and tables, a Rivet routine was prepared which contains most of the distributions shown in a previous work [165] and more were

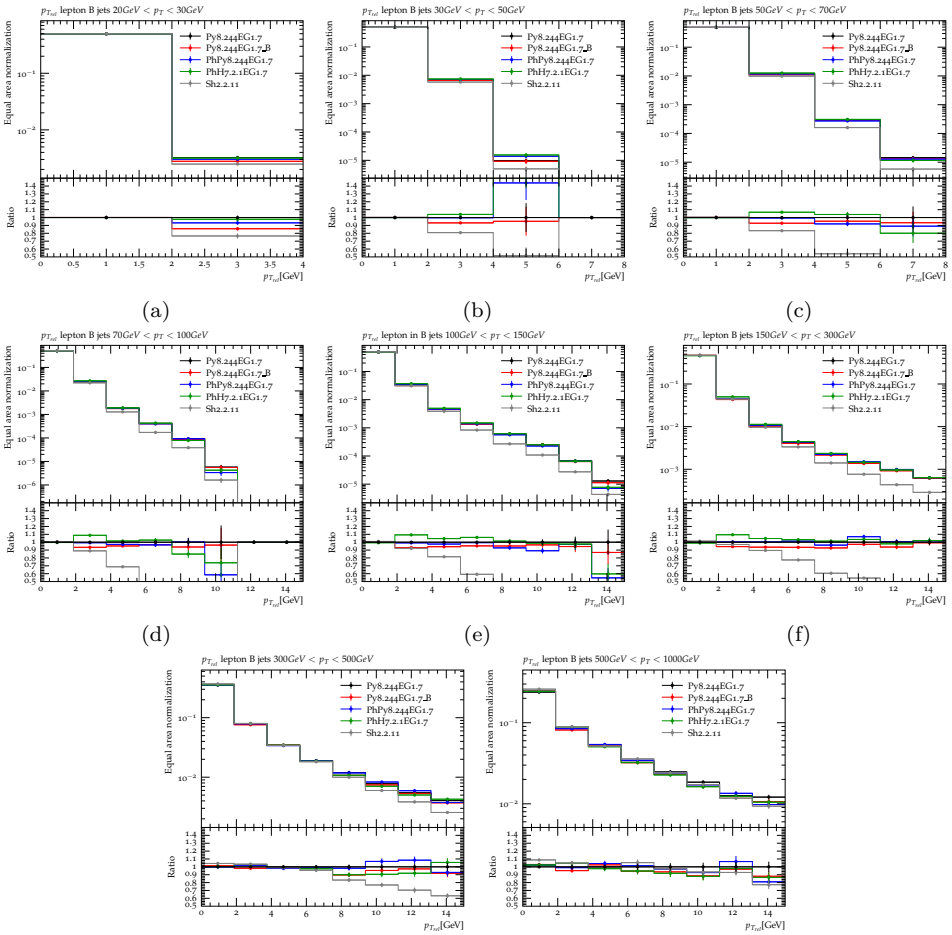

Figure C.5: $p_{T_{\text{rel}}}$ for leptons contained in b-jets, in different p_T regions.

added.

Bibliography

[1] Sheldon L. Glashow. 'Partial-symmetries of weak interactions'. In: *Nuclear Physics* 22.4 (1961), pp. 579–588. ISSN: 0029-5582. DOI: https://doi.org/10.1016/0029-5582(61)90469-2 (cit. on p. 5).

[2] Abdus Salam. 'Weak and Electromagnetic Interactions'. In: *Conf. Proc.* C680519 (1968), pp. 367–377 (cit. on p. 5).

[3] Steven Weinberg. 'A Model of Leptons'. In: *Phys. Rev. Lett.* 19 (21 Nov. 1967), pp. 1264–1266. DOI: 10.1103/PhysRevLett.19.1264 (cit. on p. 5).

[4] Gerard 't Hooft and M. J. G. Veltman. 'Regularization and Renormalization of Gauge Fields'. In: *Nucl. Phys. B* 44 (1972), pp. 189–213. DOI: 10.1016/0550-3213(72)90279-9 (cit. on p. 5).

[5] Chen-Ning Yang and Robert L. Mills. 'Conservation of Isotopic Spin and Isotopic Gauge Invariance'. In: *Phys. Rev.* 96 (1954). [,150(1954)], pp. 191–195. DOI: 10.1103/PhysRev.96.191 (cit. on p. 7).

[6] Toichiro Kinoshita. 'Mass Singularities of Feynman Amplitudes'. In: *Journal of Mathematical Physics* 3.4 (1962), pp. 650–677. DOI: 10.1063/1.1724268. eprint: https://doi.org/10.1063/1.1724268 (cit. on p. 9).

[7] T. D. Lee and M. Nauenberg. 'Degenerate Systems and Mass Singularities'. In: *Phys. Rev.* 133 (6B Mar. 1964), B1549–B1562. DOI: 10.1103/PhysRev.133.B1549 (cit. on p. 9).

[8] Vardan Khachatryan et al. 'Measurement of the inclusive 3-jet production differential cross section in protonproton collisions at 7 TeV and determination of the strong coupling constant in the TeV range'. In: *Eur. Phys. J.* C75.5 (2015), p. 186. DOI: 10.1140/epjc/s10052-015-3376-y. arXiv: 1412.1633 [hep-ex] (cit. on p. 13).

[9] Gavin P. Salam. 'Elements of QCD for hadron colliders'. In: *High-energy physics. Proceedings, 17th European School, ESHEP 2009, Bautzen, Germany, June 14-27, 2009*. 2010. arXiv: 1011.5131 [hep-ph] (cit. on p. 14).

[10] Guido Altarelli and G. Parisi. 'Asymptotic Freedom in Parton Language'. In: *Nucl. Phys. B* 126 (1977), pp. 298–318. DOI: 10.1016/0550-3213(77)90384-4 (cit. on p. 17).

[11] V. N. Gribov and L. N. Lipatov. 'Deep inelastic e p scattering in perturbation theory'. In: *Sov. J. Nucl. Phys.* 15 (1972), pp. 438–450 (cit. on p. 17).

[12] Yuri L. Dokshitzer. 'Calculation of the Structure Functions for Deep Inelastic Scattering and e+ e- Annihilation by Perturbation Theory in Quantum Chromodynamics.' In: *Sov. Phys. JETP* 46 (1977), pp. 641–653 (cit. on p. 17).

[13] S. Moch, J. A. M. Vermaseren and A. Vogt. 'The Three loop splitting functions in QCD: The Nonsinglet case'. In: *Nucl. Phys.* B688 (2004), pp. 101–134. DOI: 10.1016/j.nuclphysb.2004.03.030. arXiv: hep-ph/0403192 [hep-ph] (cit. on p. 17).

[14] A. Vogt, S. Moch and J. A. M. Vermaseren. 'The Three-loop splitting functions in QCD: The Singlet case'. In: *Nucl. Phys.* B691 (2004), pp. 129–181. DOI: 10.1016/j.nuclphysb.2004.04.024. arXiv: hep-ph/0404111 [hep-ph] (cit. on p. 17).

[15] Tancredi Carli et al. 'A posteriori inclusion of parton density functions in NLO QCD final-state calculations at hadron colliders: theăAPPLGRIDăproject'. In: *The European Physical Journal C* 66.3 (2010). DOI: 10.1140/epjc/s10052-010-1255-0 (cit. on p. 19).

[16] T. Kluge, K. Rabbertz and M. Wobisch. 'Fast pQCD calculations for PDF fits'. In: *Deep Inelastic Scattering DIS 2006*. World Scientific, 2007. DOI: 10.1142/9789812706706_0110 (cit. on p. 19).

[17] F. Abe et al. 'Observation of top quark production in $\bar{p}p$ collisions'. In: *Phys. Rev. Lett.* 74 (1995), pp. 2626–2631. DOI: 10.1103/PhysRevLett.74.2626. arXiv: hep-ex/9503002 (cit. on p. 22).

[18] R. Blair et al. 'The CDF-II detector: Technical design report'. In: (Nov. 1996) (cit. on p. 22).

[19] S. Aronson et al. 'Design Report: The D0 Experiment at the Fermilab Antiproton - Proton Collider'. In: (Oct. 1984) (cit. on p. 22).

[20] S. Abachi et al. 'Observation of the top quark'. In: *Phys. Rev. Lett.* 74 (1995), pp. 2632–2637. DOI: 10.1103/PhysRevLett.74.2632. arXiv: hep-ex/9503003 (cit. on p. 22).

[21] Particle Data Group et al. 'Review of Particle Physics'. In: *Progress of Theoretical and Experimental Physics* 2022.8 (Aug. 2022). 083C01. ISSN: 2050-3911. DOI: 10.1093/ptep/ptac097. eprint: https://academic.oup.com/ptep/article-pdf/2022/8/083C01/45434166/ptac097.pdf (cit. on p. 22).

[22] R.E. Marshak. *Conceptual Foundations Of Modern Particle Physics*. World Scientific Publishing Company, 1993. ISBN: 9789813103368. URL: https://books.google.it/books?id=i%5C_47DQAAQBAJ (cit. on p. 22).

[23] Makoto Kobayashi and Toshihide Maskawa. 'CP Violation in the Renormalizable Theory of Weak Interaction'. In: *Prog. Theor. Phys.* 49 (1973), pp. 652–657. DOI: 10.1143/PTP.49.652 (cit. on p. 22).

[24] ATLAS. *Top working group mass and properties summary plots - November 2022*. URL: https://atlas.web.cern.ch/Atlas/GROUPS/PHYSICS/PUBNOTES/ATL-PHYS-PUB-2022-050/ (cit. on p. 23).

[25] P. Nason, S. Dawson and R. Keith Ellis. 'The Total Cross-Section for the Production of Heavy Quarks in Hadronic Collisions'. In: *Nucl. Phys. B* 303 (1988), pp. 607–633. DOI: 10.1016/0550-3213(88)90422-1 (cit. on p. 26).

[26] P. Nason, S. Dawson and R.K. Ellis. 'The total cross section for the production of heavy quarks in hadronic collisions'. In: *Nuclear Physics B* 303.4 (1988), pp. 607–633. ISSN: 0550-3213. DOI: https://doi.org/10.1016/0550-3213(88)90422-1 (cit. on p. 27).

[27] Peter Bärnreuther, Micha Czakon and Alexander Mitov. 'Percent-Level-Precision Physics at the Tevatron: Next-to-Next-to-Leading Order QCD Corrections to $q\bar{q} \to t\bar{t}+X$'. In: *Phys. Rev. Lett.* 109 (13 Sept. 2012), p. 132001. DOI: 10.1103/PhysRevLett.109.132001 (cit. on p. 27).

[28] Michal Czakon and Alexander Mitov. 'NNLO corrections to top-pair production at hadron colliders: the all-fermionic scattering channels'. In: *Journal of High Energy Physics* 2012.12 (2012), p. 54. DOI: 10.1007/JHEP12(2012)054 (cit. on p. 27).

[29] Michal Czakon and Alexander Mitov. 'NNLO corrections to top pair production at hadron colliders: the quark-gluon reaction'. In: *JHEP* 01 (2013), p. 080. DOI: 10.1007/JHEP01(2013)080. arXiv: 1210.6832 [hep-ph] (cit. on pp. 27, 55).

[30] Michal Czakon, Paul Fiedler and Alexander Mitov. 'Total Top-Quark Pair-Production Cross Section at Hadron Colliders Through $\mathcal{O}(\alpha_S^4)$'. In: *Phys. Rev. Lett.* 110 (25 June 2013), p. 252004. DOI: 10.1103/PhysRevLett.110.252004 (cit. on p. 27).

[31] Matteo Cacciari et al. 'Top-pair production at hadron colliders with next-to-next-to-leading logarithmic soft-gluon resummation'. In: *Physics Letters B* 710.4 (2012), pp. 612–622. ISSN: 0370-2693. DOI: https://doi.org/10.1016/j.physletb.2012.03.013 (cit. on p. 27).

[32] Michal Czakon and Alexander Mitov. 'Top++: A program for the calculation of the top-pair cross-section at hadron colliders'. In: *Computer Physics Communications* 185.11 (2014), pp. 2930–2938. ISSN: 0010-4655. DOI: https://doi.org/10.1016/j.cpc.2014.06.021 (cit. on p. 27).

[33] Michal Czakon, David Heymes and Alexander Mitov. 'High-Precision Differential Predictions for Top-Quark Pairs at the LHC'. In: *Phys. Rev. Lett.* 116 (8 Feb. 2016), p. 082003. DOI: 10.1103/PhysRevLett.116.082003 (cit. on p. 27).

[34] Stefano Catani et al. 'Top-quark pair production at the LHC: Fully differential QCD predictions at NNLO'. In: *JHEP* 07 (2019), p. 100. DOI: 10.1007/JHEP07(2019)100. arXiv: 1906.06535 [hep-ph] (cit. on p. 27).

[35] Stefano Catani et al. 'Top-quark pair hadroproduction at NNLO: differential predictions with the $\overline{\text{MS}}$ mass'. In: *Journal of High Energy Physics* 2020.8 (Aug. 2020). DOI: 10.1007/jhep08(2020)027 (cit. on p. 27).

[36] Stefano Catani et al. 'Top-quark pair production at the LHC: fully differential QCD predictions at NNLO'. In: *JHEP* 2019.7 (2019), p. 100. DOI: 10.1007/JHEP07(2019)100 (cit. on pp. 27, 100).

[37] Pier Francesco Monni et al. 'MiNNLOPS: a new method to match NNLO QCD to parton showers'. In: *JHEP* 2020.5 (2020), p. 143. DOI: 10.1007/JHEP05(2020)143 (cit. on pp. 27, 50, 55).

[38] Javier Mazzitelli et al. 'Next-to-Next-to-Leading Order Event Generation for Top-Quark Pair Production'. In: *Physical Review Letters* 127.6 (Aug. 2021). DOI: 10.1103/physrevlett.127.062001 (cit. on pp. 27, 55).

[39] Paolo Nason. 'A new method for combining NLO QCD with shower Monte Carlo algorithms'. In: *JHEP* 11 (2004), p. 040. DOI: 10.1088/1126-6708/2004/11/040. arXiv: hep-ph/0409146 (cit. on pp. 27, 53, 55).

[40] Paolo Nason and Giovanni Ridolfi. 'A positive-weight next-to-leading-order Monte Carlo for Z pair hadroproduction'. In: *Journal of High Energy Physics* 2006.08 (Aug. 2006), pp. 077–077. DOI: 10.1088/1126-6708/2006/08/077 (cit. on p. 27).

[41] Stefano Frixione, Paolo Nason and Carlo Oleari. 'Matching NLO QCD computations with parton shower simulations: the POWHEG method'. In: *JHEP* 11 (2007), p. 070. DOI: 10.1088/1126-6708/2007/11/070. arXiv: 0709.2092 [hep-ph] (cit. on pp. 27, 53).

[42] K. Aamodt et al. 'The ALICE experiment at the CERN LHC'. In: *JINST* 3 (2008), S08002. DOI: 10.1088/1748-0221/3/08/S08002 (cit. on p. 29).

[43] G. Aad et al. 'The ATLAS Experiment at the CERN Large Hadron Collider'. In: *JINST* 3 (2008), S08003. DOI: 10.1088/1748-0221/3/08/S08003 (cit. on pp. 29, 31, 34, 38).

[44] S. Chatrchyan et al. 'The CMS Experiment at the CERN LHC'. In: *JINST* 3 (2008), S08004. DOI: 10.1088/1748-0221/3/08/S08004 (cit. on p. 29).

[45] A. Augusto Alves Jr. et al. 'The LHCb Detector at the LHC'. In: *JINST* 3 (2008), S08005. DOI: 10.1088/1748-0221/3/08/S08005 (cit. on p. 29).

[46] O. Adriani et al. 'The LHCf detector at the CERN Large Hadron Collider'. In: *JINST* 3 (2008), S08006. DOI: 10.1088/1748-0221/3/08/S08006 (cit. on p. 30).

[47] J. L. Pinfold. 'The MoEDAL Experiment at the LHC a New Light on the Terascale Frontier'. In: *J. Phys. Conf. Ser.* 631.1 (2015), p. 012014. DOI: 10.1088/1742-6596/631/1/012014 (cit. on p. 30).

[48] G. Anelli et al. 'The TOTEM experiment at the CERN Large Hadron Collider'. In: *JINST* 3 (2008), S08007. DOI: 10.1088/1748-0221/3/08/S08007 (cit. on p. 30).

[49] A. Airapetian et al. 'ATLAS detector and physics performance: Technical Design Report, 1'. In: Technical design report. ATLAS (1999). URL: https://cds.cern.ch/record/391176 (cit. on pp. 31, 35).

[50] ATLAS Outreach. 'ATLAS Fact Sheet : To raise awareness of the ATLAS detector and collaboration on the LHC'. 2010. DOI: 10.17181/CERN.1LN2.J772 (cit. on p. 34).

[51] Fabian Hügging. 'The ATLAS Pixel Insertable B-Layer (IBL)'. In: *Nucl. Instrum. Meth. A* 650 (2011). Ed. by Roland Horisberger, Danek Kotlinski and Andrey Starodumov, pp. 45–49. DOI: 10.1016/j.nima.2010.12.113. arXiv: 1012.2742 [physics.ins-det] (cit. on p. 35).

[52] B. Abbott et al. 'Production and Integration of the ATLAS Insertable B-Layer'. In: *JINST* 13.05 (2018). 90 pages in total. Author list: ATLAS IBL Collaboration, starting page 2. 69 figures, 20 tables. Published in Journal of Instrumentation. All figures available at: https://atlas.web.cern.ch/Atlas/GROUPS/PHYSICS/PLOTS/PIX-2018-001, T05008. DOI: 10.1088/1748-0221/13/05/T05008. arXiv: 1803.00844 (cit. on p. 36).

[53] G. Aad et al. 'ATLAS pixel detector electronics and sensors'. In: *JINST* 3 (2008), P07007. DOI: 10.1088/1748-0221/3/07/P07007 (cit. on p. 35).

[54] Georges Aad et al. 'Operation and performance of the ATLAS semiconductor tracker'. In: *JINST* 9 (2014), P08009. DOI: 10.1088/1748-0221/9/08/P08009. arXiv: 1404.7473 [hep-ex] (cit. on p. 35).

[55] Adrian Vogel. 'ATLAS Transition Radiation Tracker (TRT): Straw tube gaseous detectors at high rates'. In: *Nuclear Instruments and Methods in Physics Research A* 732 (Dec. 2013), pp. 277–280. DOI: 10.1016/j.nima.2013.07.020 (cit. on p. 36).

[56] A. Hrynevich. 'Performance of the ATLAS Tile Calorimeter'. In: *Journal of Instrumentation* 12.06 (June 2017), pp. C06021–C06021. DOI: 10.1088/1748-0221/12/06/c06021 (cit. on pp. 37, 39).

[57] J P Archambault et al. 'Energy calibration of the ATLAS Liquid Argon Forward Calorimeter'. In: *Journal of Instrumentation* 3.02 (Feb. 2008), P02002–P02002. DOI: 10.1088/1748-0221/3/02/p02002 (cit. on p. 39).

[58] ATLAS Collaboration. *ATLAS Detector and Physics Performance: Technical Design Report, Volume 1*. ATLAS-TDR-14; CERN-LHCC-99-014. 1999. URL: https://cds.cern.ch/record/391176 (cit. on p. 40).

[59] Georges Aad et al. 'Improved luminosity determination in pp collisions at sqrt(s) = 7 TeV using the ATLAS detector at the LHC'. In: *Eur. Phys. J. C* 73.8 (2013), p. 2518. DOI: 10.1140/epjc/s10052-013-2518-3. arXiv: 1302.4393 [hep-ex] (cit. on p. 41).

[60] V. Cindro et al. 'The ATLAS beam conditions monitor'. In: *JINST* 3 (2008), P02004. DOI: 10.1088/1748-0221/3/02/P02004 (cit. on p. 42).

[61] Marco A. L. Leite. 'Performance of the ATLAS Zero Degree Calorimeter'. In: *2013 IEEE Nuclear Science Symposium and Medical Imaging Conference and Workshop on Room-Temperature Semiconductor Detectors*. 2013. DOI: 10.1109/NSSMIC.2013.6829811 (cit. on p. 42).

[62] Maciej Trzebiski. 'Towards a Total Cross Section Measurement with the ALFA Detector at ATLAS'. In: *Acta Phys. Polon. B* 44.7 (2013). Ed. by Maciej Skrzypek, Adam Trzupek and Mariusz Witek, pp. 1623–1628. DOI: 10.5506/APhysPolB.44.1623. arXiv: 1409.4866 [physics.ins-det] (cit. on p. 42).

[63] ATLAS. *Standard Model Summary Plots February 2022*. URL: https://atlas.web.cern.ch/Atlas/GROUPS/PHYSICS/PUBNOTES/ATL-PHYS-PUB-2022-009/ (cit. on p. 43).

[64] ATLAS. *Data Acquisition and Trigger System*. URL: https://www.fsp103-atlas.de/e17619/e17626/ (cit. on p. 44).

[65] A. Dewhurst and F. Legger. 'Distributed analysis in ATLAS'. In: *Journal of Physics: Conference Series* 664 (Dec. 2015), p. 032020. DOI: 10.1088/1742-6596/664/3/032020 (cit. on p. 44).

[66] 'LHC computing Grid. Technical design report'. In: Technical design report. LCG (June 2005). Ed. by I. Bird et al. URL: https://cds.cern.ch/record/840543 (cit. on p. 44).

[67] 'ATLAS computing: Technical design report'. In: Technical design report. ATLAS (June 2005). Ed. by G. Duckeck et al. URL: https://cds.cern.ch/record/837738 (cit. on p. 44).

[68] ATLAS. *The LHCs worldwide computer*. URL: https://cerncourier.com/a/the-lhcs-worldwide-computer/ (cit. on p. 45).

[69] Walter Lampl. 'A new approach for ATLAS Athena job configuration'. 23rd International Conference on Computing in High Energy and Nuclear Physics, CHEP 2018, Sofia, Bulgaria, 9 - 13 Jul 2018. June 2018. URL: https://cds.cern.ch/record/2627857 (cit. on p. 45).

[70] ATLAS. *Luminosity Public Results*. URL: https://twiki.cern.ch/twiki/bin/view/AtlasPublic/LuminosityPublicResultsRun2 (cit. on pp. 46, 48).

[71] Stefan Höche. 'Introduction to parton-shower event generators'. In: *Proceedings, Theoretical Advanced Study Institute in Elementary Particle Physics: Journeys Through the Precision Frontier: Amplitudes for Colliders (TASI 2014): Boulder, Colorado, June 2-27, 2014* (2015), pp. 235–295. DOI: 10.1142/9789814678766_0005 (cit. on p. 51).

[72] B.R. Webber. 'A QCD model for jet fragmentation including soft gluon interference'. In: *Nuclear Physics B* 238.3 (1984), pp. 492–528. ISSN: 0550-3213. DOI: https://doi.org/10.1016/0550-3213(84)90333-X (cit. on p. 51).

[73] B. Andersson et al. 'Parton fragmentation and string dynamics'. In: *Physics Reports* 97.2 (1983), pp. 31–145. ISSN: 0370-1573. DOI: https://doi.org/10.1016/0370-1573(83)90080-7 (cit. on p. 51).

[74] D. Amati and G. Veneziano. 'Preconfinement as a property of perturbative QCD'. In: *Physics Letters B* 83.1 (1979), pp. 87–92. ISSN: 0370-2693. DOI: https://doi.org/10.1016/0370-2693(79)90896-7 (cit. on p. 51).

[75] Ya.I. Azimov et al. 'The string effect and QCD coherence'. In: *Physics Letters B* 165.1 (1985), pp. 147–150. ISSN: 0370-2693. DOI: https://doi.org/10.1016/0370-2693(85)90709-9 (cit. on p. 51).

[76] S. Agostinelli et al. 'Geant4a simulation toolkit'. In: *Nuclear Instruments and Methods in Physics Research Section A: Accelerators, Spectrometers, Detectors and Associated Equipment* 506.3 (2003), pp. 250–303. ISSN: 0168-9002. DOI: https://doi.org/10.1016/S0168-9002(03)01368-8 (cit. on p. 52).

[77] Simone Alioli et al. 'A general framework for implementing NLO calculations in shower Monte Carlo programs: the POWHEG BOX'. In: *JHEP* 2010.6 (2010), p. 43. DOI: 10.1007/JHEP06(2010)043 (cit. on p. 53).

[78] J. Alwall et al. 'The automated computation of tree-level and next-to-leading order differential cross sections, and their matching to parton shower simulations'. In: *JHEP* 07 (2014), p. 079. DOI: 10.1007/JHEP07(2014)079. arXiv: 1405.0301 [hep-ph] (cit. on p. 53).

[79] Torbjörn Sjöstrand et al. 'An introduction to PYTHIA 8.2'. In: *Comput. Phys. Commun.* 191 (2015), p. 159. DOI: 10.1016/j.cpc.2015.01.024. arXiv: 1410.3012 [hep-ph] (cit. on pp. 53, 133).

[80] Johannes Bellm et al. 'Herwig 7.0/Herwig++ 3.0 release note'. In: *Eur. Phys. J. C* 76.4 (2016), p. 196. DOI: 10.1140/epjc/s10052-016-4018-8. arXiv: 1512.01178 [hep-ph] (cit. on pp. 53, 55).

[81] Enrico Bothmann et al. 'Event generation with Sherpa 2.2'. In: *SciPost Phys.* 7.3 (2019), p. 034. DOI: 10.21468/SciPostPhys.7.3.034. arXiv: 1905.09127 [hep-ph] (cit. on pp. 54, 56, 133).

[82] *Summary of ATLAS Pythia 8 tunes*. Tech. rep. Geneva: CERN, Aug. 2012. URL: https://cds.cern.ch/record/1474107 (cit. on p. 54).

[83] Richard D. Ball et al. 'Parton distributions with LHC data'. In: *Nuclear Physics B* 867.2 (2013), pp. 244–289. ISSN: 0550-3213. DOI: https://doi.org/10.1016/j.nuclphysb.2012.10.003 (cit. on p. 54).

[84] Richard D. Ball et al. 'Parton distributions for the LHC run II'. In: *JHEP* 04 (2015), p. 040. DOI: 10.1007/JHEP04(2015)040. arXiv: 1410.8849 [hep-ph] (cit. on p. 55).

[85] T. Sjöstrand, S. Mrenna and P. Skands. 'A brief introduction to PYTHIA 8.1'. In: *Comput. Phys. Commun.* 178 (2008), pp. 852–867. DOI: 10.1016/j.cpc.2008.01.036. arXiv: 0710.3820 [hep-ph] (cit. on p. 55).

[86] Richard D. Ball et al. 'Parton distributions with LHC data'. In: *Nucl. Phys. B* 867 (2013), p. 244. DOI: 10.1016/j.nuclphysb.2012.10.003. arXiv: 1207.1303 [hep-ph] (cit. on p. 55).

[87] *ATLAS Pythia 8 tunes to 7 TeV data*. Tech. rep. Geneva: CERN, Nov. 2014. URL: https://cds.cern.ch/record/1966419 (cit. on p. 55).

[88] *Studies on top-quark Monte Carlo modelling for Top2016*. Tech. rep. Geneva: CERN, Sept. 2016. URL: https://cds.cern.ch/record/2216168 (cit. on pp. 55, 56).

[89] Michal Czakon and Alexander Mitov. 'Top++: A program for the calculation of the top-pair cross-section at hadron colliders'. In: *Comput. Phys. Commun.* 185 (2014), p. 2930. DOI: 10.1016/j.cpc.2014.06.021. arXiv: 1112.5675 [hep-ph] (cit. on p. 55).

[90] M. Beneke et al. 'Hadronic top-quark pair production with NNLL threshold resummation'. In: *Nucl. Phys. B* 855 (2012), pp. 695–741. DOI: 10.1016/j.nuclphysb.2011.10.021. arXiv: 1109.1536 [hep-ph] (cit. on p. 55).

[91] Matteo Cacciari et al. 'Top-pair production at hadron colliders with next-to-next-to-leading logarithmic soft-gluon resummation'. In: *Phys. Lett. B* 710 (2012), pp. 612–622. DOI: 10.1016/j.physletb.2012.03.013. arXiv: 1111.5869 [hep-ph] (cit. on p. 55).

[92] Peter Bärnreuther, Michal Czakon and Alexander Mitov. 'Percent-Level-Precision Physics at the Tevatron: Next-to-Next-to-Leading Order QCD Corrections to $q\bar{q} \to t\bar{t} + X$'. In: *Phys. Rev. Lett.* 109 (2012), p. 132001. DOI: 10.1103/PhysRevLett.109.132001. arXiv: 1204.5201 [hep-ph] (cit. on p. 55).

[93] Michal Czakon and Alexander Mitov. 'NNLO corrections to top-pair production at hadron colliders: the all-fermionic scattering channels'. In: *JHEP* 12 (2012), p. 054. DOI: 10.1007/JHEP12(2012)054. arXiv: 1207.0236 [hep-ph] (cit. on p. 55).

[94] Michal Czakon, Paul Fiedler and Alexander Mitov. 'Total Top-Quark Pair-Production Cross Section at Hadron Colliders Through $O(\alpha_S^4)$'. In: *Phys. Rev. Lett.* 110 (2013), p. 252004. DOI: 10.1103/PhysRevLett.110.252004. arXiv: 1303.6254 [hep-ph] (cit. on p. 55).

[95] M. Bähr et al. 'Herwig++ physics and manual'. In: *Eur. Phys. J. C* 58 (2008), p. 639. DOI: 10.1140/epjc/s10052-008-0798-9. arXiv: 0803.0883 [hep-ph] (cit. on p. 55).

[96] M. H. Seymour and A. Siódmok. 'Constraining MPI models using eff and recent Tevatron and LHC Underlying Event data'. In: *JHEP* 2013.10 (2013), p. 113. DOI: 10.1007/JHEP10(2013)113 (cit. on p. 55).

[97] L.A. Harland-Lang et al. 'Parton distributions in the LHC era: MMHT 2014 PDFs'. In: *Eur. Phys. J. C* 75.5 (2015), p. 204. DOI: 10.1140/epjc/s10052-015-3397-6. arXiv: 1412.3989 [hep-ph] (cit. on p. 55).

[98] Stefano Frixione et al. 'Single-top hadroproduction in association with a W boson'. In: *JHEP* 07 (2008), p. 029. DOI: 10.1088/1126-6708/2008/07/029Next-to-next-to-leading-ordercollinear. arXiv: 0805.3067 [hep-ph] (cit. on p. 56).

[99] Nikolaos Kidonakis. 'Top Quark Production'. In: *Proceedings, Helmholtz International Summer School on Physics of Heavy Quarks and Hadrons (HQ 2013)* (JINR, Dubna, Russia, 15th–28th July 2013), pp. 139–168. DOI: 10.3204/DESY-PROC-2013-03/Kidonakis. arXiv: 1311.0283 [hep-ph] (cit. on p. 56).

[100] M. Aliev et al. 'HATHOR – HAdronic Top and Heavy quarks crOss section calculatoR'. In: *Comput. Phys. Commun.* 182 (2011), pp. 1034–1046. DOI: 10.1016/j.cpc.2010.12.040. arXiv: 1007.1327 [hep-ph] (cit. on p. 56).

[101] P. Kant et al. 'HatHor for single top-quark production: Updated predictions and uncertainty estimates for single top-quark production in hadronic collisions'. In: *Comput. Phys. Commun.* 191 (2015), pp. 74–89. DOI: 10.1016/j.cpc.2015.02.001. arXiv: 1406.4403 [hep-ph] (cit. on p. 56).

[102] Nikolaos Kidonakis. 'Next-to-next-to-leading-order collinear and soft gluon corrections for t-channel single top quark production'. In: *Phys. Rev. D* 83 (9 May 2011), p. 091503. DOI: 10.1103/PhysRevD.83.091503 (cit. on p. 56).

[103] Nikolaos Kidonakis. 'Next-to-next-to-leading logarithm resummation for s-channel single top quark production'. In: *Phys. Rev. D* 81 (5 Mar. 2010), p. 054028. DOI: 10.1103/PhysRevD.81.054028 (cit. on p. 56).

[104] Tanju Gleisberg and Stefan Höche. 'Comix, a new matrix element generator'. In: *JHEP* 12 (2008), p. 039. DOI: 10.1088/1126-6708/2008/12/039. arXiv: 0808.3674 [hep-ph] (cit. on p. 56).

[105] Fabio Cascioli, Philipp Maierhöfer and Stefano Pozzorini. 'Scattering Amplitudes with Open Loops'. In: *Phys. Rev. Lett.* 108 (2012), p. 111601. DOI: 10.1103/PhysRevLett.108.111601. arXiv: 1111.5206 [hep-ph] (cit. on p. 56).

[106] Steffen Schumann and Frank Krauss. 'A parton shower algorithm based on Catani–Seymour dipole factorisation'. In: *JHEP* 03 (2008), p. 038. DOI: 10.1088/1126-6708/2008/03/038. arXiv: 0709.1027 [hep-ph] (cit. on p. 56).

[107] S. Catani et al. 'QCD Matrix Elements + Parton Showers'. In: *JHEP* 11 (2001), p. 063. DOI: 10.1088/1126-6708/2001/11/063. arXiv: hep-ph/0109231 (cit. on p. 56).

[108] Charalampos Anastasiou et al. 'High precision QCD at hadron colliders: Electroweak gauge boson rapidity distributions at next-to-next-to leading order'. In: *Phys. Rev. D* 69 (2004), p. 094008. DOI: 10.1103/PhysRevD.69.094008. arXiv: hep-ph/0312266 (cit. on p. 56).

[109] *ATLAS simulation of boson plus jets processes in Run 2*. Tech. rep. Geneva: CERN, May 2017. URL: https://cds.cern.ch/record/2261937 (cit. on p. 56).

[110] Emanuele Re. 'Single-top Wt-channel production matched with parton showers using the POWHEG method'. In: *The European Physical Journal C* 71.2 (2011), p. 1547 (cit. on p. 57).

[111] T Cornelissen et al. *Concepts, Design and Implementation of the ATLAS New Tracking (NEWT)*. Tech. rep. Geneva: CERN, Mar. 2007. URL: https://cds.cern.ch/record/1020106 (cit. on pp. 58, 59).

[112] 'The Optimization of ATLAS Track Reconstruction in Dense Environments'. In: (Mar. 2015) (cit. on p. 58).

[113] M. Aaboud et al. 'Reconstruction of primary vertices at the ATLAS experiment in Run 1 proton–proton collisions at the LHC'. In: *The European Physical Journal C* 77.5 (2017), p. 332. DOI: 10.1140/epjc/s10052-017-4887-5 (cit. on p. 59).

[114] 'Performance of primary vertex reconstruction in proton-proton collisions at $\sqrt{s}$ =7 TeV in the ATLAS experiment'. In: (July 2010). URL: https://cds.cern.ch/record/1281344 (cit. on p. 59).

[115] ATLAS Collaboration. 'Electron and photon performance measurements with the ATLAS detector using the 2015–2017 LHC proton–proton collision data'. In: *JINST* 14 (2019), P12006. DOI: 10.1088/1748-0221/14/12/P12006. arXiv: 1908.00005 [hep-ex] (cit. on p. 59).

[116] *Electron efficiency measurements with the ATLAS detector using the 2015 LHC proton-proton collision data*. Tech. rep. Geneva: CERN, June 2016. URL: https://cds.cern.ch/record/2157687 (cit. on p. 60).

[117] M. Aaboud et al. 'Measurement of the $t\bar{t}$ production cross-section using $e\mu$ events with b-tagged jets in pp collisions at $\sqrt{s}$ = 13TeV with the ATLAS detector'. In: *Physics Letters B* 761 (2016), pp. 136–157. ISSN: 0370-2693. DOI: https://doi.org/10.1016/j.physletb.2016.08.019 (cit. on p. 60).

[118] J. Illingworth and J. Kittler. 'A survey of the hough transform'. In: *Computer Vision, Graphics, and Image Processing* 44.1 (1988), pp. 87–116. ISSN: 0734-189X. DOI: https://doi.org/10.1016/S0734-189X(88)80033-1 (cit. on p. 61).

[119] Georges Aad et al. 'Muon reconstruction performance of the ATLAS detector in protonproton collision data at $\sqrt{s}$ =13 TeV'. In: *Eur. Phys. J. C* 76.5 (2016), p. 292. DOI: 10.1140/epjc/s10052-016-4120-y. arXiv: 1603.05598 [hep-ex] (cit. on pp. 61, 62, 95).

[120] John E. Huth et al. 'Toward a standardization of jet definitions'. In: *1990 DPF Summer Study on High-energy Physics: Research Directions for the Decade (Snowmass 90)*. Dec. 1990, pp. 0134–136 (cit. on p. 63).

[121] Georges Aad et al. 'Topological cell clustering in the ATLAS calorimeters and its performance in LHC Run 1'. In: *Eur. Phys. J. C* 77 (2017), p. 490. DOI: 10.1140/epjc/s10052-017-5004-5. arXiv: 1603.02934 [hep-ex] (cit. on p. 64).

[122] Matteo Cacciari, Gavin P. Salam and Gregory Soyez. 'The anti-k_t jet clustering algorithm'. In: *JHEP* 04 (2008), p. 063. DOI: 10.1088/1126-6708/2008/04/063. arXiv: 0802.1189 [hep-ph] (cit. on p. 64).

[123] *Monte Carlo Calibration and Combination of In-situ Measurements of Jet Energy Scale, Jet Energy Resolution and Jet Mass in ATLAS*. Tech. rep. Geneva: CERN, Aug. 2015. URL: https://cds.cern.ch/record/2044941 (cit. on p. 65).

[124] Matteo Cacciari and Gavin P. Salam. 'Pileup subtraction using jet areas'. In: *Physics Letters B* 659.1 (2008), pp. 119–126. ISSN: 0370-2693. DOI: https://doi.org/10.1016/j.physletb.2007.09.077 (cit. on p. 65).

[125] *Tagging and suppression of pileup jets with the ATLAS detector*. Tech. rep. ATLAS-CONF-2014-018. Geneva: CERN, May 2014. URL: https://cds.cern.ch/record/1700870 (cit. on p. 66).

[126] G. Aad et al. 'ATLAS b-jet identification performance and efficiency measurement with $t\bar{t}$ events in pp collisions at $\sqrt{s} = 13$ TeV'. In: *The European Physical Journal C* 79.11 (2019), p. 970. DOI: 10.1140/epjc/s10052-019-7450-8 (cit. on p. 66).

[127] R. Frühwirth. 'Application of Kalman filtering to track and vertex fitting'. In: *Nuclear Instruments and Methods in Physics Research Section A: Accelerators, Spectrometers, Detectors and Associated Equipment* 262.2 (1987), pp. 444–450. ISSN: 0168-9002. DOI: https://doi.org/10.1016/0168-9002(87)90887-4 (cit. on p. 67).

[128] ATLAS Collaboration. *Topological b-hadron decay reconstruction and identification of b-jets with the JetFitter package in the ATLAS experiment at the LHC*. ATL-PHYS-PUB-2018-025. 2018. URL: https://cds.cern.ch/record/2645405 (cit. on p. 67).

[129] Morad Aaboud et al. 'Measurements of b-jet tagging efficiency with the ATLAS detector using $t\bar{t}$ events at $\sqrt{s} = 13$ TeV'. In: *JHEP* 08 (2018), p. 089. DOI: 10.1007/JHEP08(2018)089. arXiv: 1805.01845 [hep-ex] (cit. on p. 67).

[130] *Calibration of the ATLAS b-tagging algorithm in $t\bar{t}$ semi-leptonic events*. Tech. rep. Geneva: CERN, Sept. 2018. URL: http://cds.cern.ch/record/2638455 (cit. on p. 67).

[131] *Simulation-based extrapolation of b-tagging calibrations towards high transverse momenta in the ATLAS experiment*. Tech. rep. Geneva: CERN, Mar. 2021. URL: https://cds.cern.ch/record/2753444 (cit. on p. 68).

[132] *Expected performance of missing transverse momentum reconstruction for the ATLAS detector at $\sqrt{s} = 13$ TeV*. Tech. rep. ATL-PHYS-PUB-2015-023. Geneva: CERN, July 2015. URL: https://cds.cern.ch/record/2037700 (cit. on p. 68).

[133] M. Aaboud et al. 'Performance of missing transverse momentum reconstruction with the ATLAS detector using proton–proton collisions at $$\sqrt{s}=13~\hbox {TeV}$$'. In: *The European Physical Journal C* 78.11 (2018), p. 903. DOI: 10.1140/epjc/s10052-018-6288-9 (cit. on p. 68).

[134] G. Aad et al. 'Measurement of the top quark pair production cross-section with ATLAS in the single lepton channel'. In: *Physics Letters B* 711.3 (2012), pp. 244–263. ISSN: 0370-2693. DOI: https://doi.org/10.1016/j.physletb.2012.03.083 (cit. on p. 71).

[135] G. Aad et al. 'Differential top-antitop cross-section measurements as a function of observables constructed from final-state particles using pp collisions at $$ \sqrt{s}=7 $$TeV in the ATLAS detector'. In: *JHEP* 2015.6 (2015), p. 100. DOI: 10.1007/JHEP06(2015)100 (cit. on p. 76).

[136] Georges Aad et al. 'Measurements of top-quark pair differential and double-differential cross-sections in the ℓ+jets channel with pp collisions at $\sqrt{s} = 13$ TeV using the ATLAS detector'. In: *Eur. Phys. J. C* 79.12 (2019). [Erratum: Eur.Phys.J.C 80, 1092 (2020)], p. 1028. DOI: 10.1140/epjc/s10052-019-7525-6. arXiv: 1908.07305 [hep-ex] (cit. on pp. 77, 82, 101).

[137] M. Aaboud et al. 'Measurements of inclusive and differential fiducial cross-sections of $t\bar{t}$ production with additional heavy-flavour jets in proton-proton collisions at $\sqrt{s} = 13$ TeV with the ATLAS detector'. In: *Journal of High Energy Physics* 2019.4 (Apr. 2019). DOI: 10.1007/jhep04(2019)046 (cit. on p. 77).

[138] Volker Blobel. *Unfolding methods in high-energy physics experiments*. Tech. rep. Dec. 1984, 40 p. DOI: 10.5170/CERN-1985-009.88 (cit. on p. 80).

[139] Andreas Höcker and Vakhtang Kartvelishvili. 'SVD approach to data unfolding'. In: *Nuclear Instruments and Methods in Physics Research Section A: Accelerators, Spectrometers, Detectors and Associated Equipment* 372.3 (1996), pp. 469–481. ISSN: 0168-9002. DOI: https://doi.org/10.1016/0168-9002(95)01478-0 (cit. on p. 81).

[140] G. D'Agostini. 'Improved iterative Bayesian unfolding'. In: *Alliance Workshop on Unfolding and Data Correction*. Oct. 2010. arXiv: 1010.0632 [physics.data-an] (cit. on p. 81).

[141] G. D'Agostini. 'A multidimensional unfolding method based on Bayes' theorem'. In: *Nuclear Instruments and Methods in Physics Research Section A: Accelerators, Spectrometers, Detectors and Associated Equipment* 362.2 (1995), pp. 487–498. ISSN: 0168-9002. DOI: https://doi.org/10.1016/0168-9002(95)00274-X (cit. on p. 81).

[142] Tim Adye. *Unfolding algorithms and tests using RooUnfold*. 2011. arXiv: 1105.1160 [physics.data-an] (cit. on p. 84).

[143] *Electron and photon energy calibration with the ATLAS detector using data collected in 2015 at* $\sqrt{s} = 13$ TeV. Tech. rep. Geneva: CERN, Aug. 2016. URL: https://cds.cern.ch/record/2203514 (cit. on p. 95).

[144] M. Aaboud et al. 'Jet energy scale measurements and their systematic uncertainties in proton-proton collisions at $\sqrt{s} = 13$ TeV with the ATLAS detector'. In: *Phys. Rev. D* 96.7 (2017), p. 072002. DOI: 10.1103/PhysRevD.96.072002. arXiv: 1703.09665 [hep-ex] (cit. on p. 95).

[145] Georges Aad et al. 'Jet energy measurement with the ATLAS detector in proton-proton collisions at $\sqrt{s} = 7$ TeV'. In: *Eur. Phys. J. C* 73.3 (2013), p. 2304. DOI: 10.1140/epjc/s10052-013-2304-2. arXiv: 1112.6426 [hep-ex] (cit. on p. 95).

[146] Georges Aad et al. 'ATLAS b-jet identification performance and efficiency measurement with $t\bar{t}$ events in pp collisions at $\sqrt{s} = 13$ TeV'. In: *Eur. Phys. J. C* 79.11 (2019), p. 970. DOI: 10.1140/epjc/s10052-019-7450-8. arXiv: 1907.05120 [hep-ex] (cit. on p. 95).

[147] *Measurement of b-tagging Efficiency of c-jets in* $t\bar{t}$ *Events Using a Likelihood Approach with the ATLAS Detector*. Tech. rep. Geneva: CERN, Mar. 2018. URL: https://cds.cern.ch/record/2306649 (cit. on p. 95).

[148] 'Calibration of light-flavour b-jet mistagging rates using ATLAS proton-proton collision data at $\sqrt{s} = 13$ TeV'. In: (Apr. 2018). URL: https://cds.cern.ch/record/2314418 (cit. on p. 95).

[149] Morad Aaboud et al. 'Performance of missing transverse momentum reconstruction with the ATLAS detector using proton-proton collisions at $\sqrt{s} = 13$ TeV'. In: *Eur. Phys. J. C* 78.11 (2018), p. 903. DOI: 10.1140/epjc/s10052-018-6288-9. arXiv: 1802.08168 [hep-ex] (cit. on p. 95).

[150] ATLAS Collaboration. 'Luminosity determination in pp collisions at $\sqrt{s} = 13$ TeV using the ATLAS detector at the LHC'. In: (2022). DOI: 10.48550/ARXIV.2212.09379. arXiv: 2212.09379 [hep-ex] (cit. on p. 96).

[151] G. Avoni et al. 'The new LUCID-2 detector for luminosity measurement and monitoring in ATLAS'. In: *JINST* 13.07 (2018), P07017. DOI: 10.1088/1748-0221/13/07/P07017 (cit. on p. 96).

[152] Stefan Höche et al. 'A Study of QCD Radiation in VBF Higgs Production with Vincia and Pythia'. In: *SciPost Phys.* 12 (2022), p. 010. DOI: 10.21468/SciPostPhys.12.1.010 (cit. on p. 96).

[153] ATLAS Collaboration. *Studies on top-quark Monte Carlo modelling with Sherpa and MG5_aMC@NLO*. ATL-PHYS-PUB-2017-007. 2017. URL: https://cds.cern.ch/record/2261938 (cit. on p. 97).

[154] Jon Butterworth et al. 'PDF4LHC recommendations for LHC Run II'. In: *J. Phys. G* 43 (2016), p. 023001. DOI: 10.1088/0954-3899/43/2/023001. arXiv: 1510.03865 [hep-ph] (cit. on p. 97).

[155] M. Aaboud et al. 'Measurement of the top quark mass in the $t\bar{t} \to$ lepton + jets from $\sqrt{s} = 8$ TeV ATLAS data and combination with previous results'. In: *The European Physical Journal C* 79.4 (Mar. 2019). DOI: 10.1140/epjc/s10052-019-6757-9 (cit. on p. 98).

[156] Michal Czakon et al. 'Top-pair production at the LHC through NNLO QCD and NLO EW'. In: *JHEP* 10 (2017), p. 186. DOI: 10.1007/JHEP10(2017)186. arXiv: 1705.04105 [hep-ph] (cit. on p. 100).

[157] Lyndon Evans and Philip Bryant. 'LHC Machine'. In: *Journal of Instrumentation* 3.08 (Aug. 2008), S08001. DOI: 10.1088/1748-0221/3/08/S08001 (cit. on p. 132).

[158] T. Abe et al. *Belle II Technical Design Report*. 2010. DOI: 10.48550/ARXIV.1011.0352 (cit. on p. 132).

[159] D. J. Lange. 'The EvtGen particle decay simulation package'. In: *Nucl. Instrum. Meth. A* 462 (2001), p. 152. DOI: 10.1016/S0168-9002(01)00089-4 (cit. on p. 132).

[160] P.A. Zyla et al. 'Review of Particle Physics'. In: *PTEP* 2020.8 (2020), p. 083C01. DOI: 10.1093/ptep/ptaa104 (cit. on p. 132).

[161] Christian Bierlich et al. *A comprehensive guide to the physics and usage of PYTHIA 8.3*. 2022. DOI: 10.48550/ARXIV.2203.11601 (cit. on p. 133).

[162] Johannes Bellm et al. 'Herwig 7.2 release note'. In: *The European Physical Journal C* 80.5 (2020), p. 452. DOI: 10.1140/epjc/s10052-020-8011-x (cit. on p. 133).

[163] Stefano Frixione, Paolo Nason and Giovanni Ridolfi. 'A positive-weight next-to-leading-order Monte Carlo for heavy flavour hadroproduction'. In: *JHEP* 09 (2007), p. 126. DOI: 10.1088/1126-6708/2007/09/126. arXiv: 0707.3088 [hep-ph] (cit. on p. 133).

[164] Christian Bierlich et al. 'Robust Independent Validation of Experiment and Theory: Rivet version 3'. In: *SciPost Physics* 8.2 (Feb. 2020). DOI: 10.21468/scipostphys.8.2.026 (cit. on p. 133).

[165] ATLAS Collaboration. *Comparison of Monte Carlo generator predictions for bottom and charm hadrons in the decays of top quarks and the fragmentation of high p_T jets*. ATL-PHYS-PUB-2014-008. 2014. URL: https://cds.cern.ch/record/1709132 (cit. on p. 137).